Numerically Modelling Skin-Product Interaction: Applications to Tactile Perception and Skin Injury

Author: Rikeen Dhanvantray Jobanputra

Supervisor: Dr M. A. Masen
Co-supervisor: Prof. D. Dini

Submitted for the degree of Doctor of Philosophy
23 January 2023

Department of Mechanical Engineering
Imperial College London

Statement of Originality

I confirm that the work in this thesis is my own, and that information derived from other sources is appropriately referenced.

Copyright Declaration

The research presented in this thesis was funded by UKRI (EPSRC Project 2149494) in collaboration with L'Oréal Research & Innovation. Industrial supervisors for this project were Dr Gustavo Luengo and Dr Roberto Santoprete. The work concerning PPE-induced skin injury was also financially supported by the Imperial College COVID Response fund. No animal studies were conducted.

Acknowledgements

I would like to thank my supervisor, Dr Marc Arthur Masen, for his professional and personal support over the last four years. He provided me with an optimal balance of guidance and autonomy in order for this research to be conducted as efficiently and enjoyably as possible. He encouraged me to take on every opportunity, which has enabled me to grow as a person. The combination of his experimental, subject specific knowledge, in conjunction with the theoretical, computational perspective provided by my secondary supervisor, Prof. Daniele Dini, is what made this thesis possible. I would also like to take a moment to thank Dr Gustavo Luengo and Dr Roberto Santoprete from L'Oréal Research & Innovation for their advice in the fields of tactile perception and skin research over the duration of this project.

Alongside, the support I have received academically, I am incredibly fortunate to have been encouraged personally by a large, exceptional group of friends and colleagues, all of whom have helped me persevere, grow and indeed laugh a lot over the last few years. Whilst there are many individuals I wish to acknowledge, I would like to take this opportunity to personally express my gratitude to Aakeen Parikh, Abhinav Gandhi, Stephen Titus and Thushaan Rajaratnam. For almost a decade, in the simplest of terms, you have made me better.

Last, but certainly not least, I would like to thank my family. To my mother, Gita, and father, Dhanvant, your support and belief in my abilities is what kept me on the right path. I would be nothing without your guidance and I count you amongst my closest friends. To my older brother Shamil, from an early age I was lucky enough to have you as a mentor. You set the benchmark to which I should measure myself. Finally, to my twin brother, Rishi, the greatest friend and rival a man could ask for. I love you all and this thesis is dedicated to you.

"My greatest asset has always been the company that I keep.
To all of my family, friends, and colleagues,
I wouldn't be where or indeed who I am,
without you."

R. D. Jobanputra

Abstract

As we interact with objects and surfaces, mechanical stimuli propagate from the skin surface towards our receptors, after which neurological impulses are sent to the central nervous system, thereby initiating our psychological and behavioral response. Due to the skin's complexity, cutaneous biotribological phenomena are not fully understood. The objective of this study is to use computational skin models to help deliver insight into skin-product interaction.

Through collaboration with L'Oréal Research & Innovation, numerical models were utilized to better understand tactile perception. Parameterized finite element finger skin models were developed to simulate the transmission of stresses, strains and energy from the skin-surface boundary to the tactile mechanoreceptors. Three parametric studies were conducted to understand the effects of skin ageing, counter surface topography and cosmetic film properties on receptor excitation.

Key findings include:

- Age-related biomechanical skin changes reduce the magnitude of mechanical stimuli being transmitted to the receptor sites, offering an additional explanation for tactile perceptive degradation amongst the elderly.
- When in contact with rigid sinusoidal counter surfaces, the similarity of the fingerprint and counter surface wavelength plays a dominant role in influencing mechanoreceptor excitation.
- Contact between the finger and facial skin generates mechanical signals at the receptor sites which exhibit three characteristic behaviours. Through including and modifying the properties of interfacial cosmetic polymer films, it is possible to influence each of these behaviours and thus modulate tactile perception.

During the COVID-19 pandemic, healthcare workers wearing high-grade personal protective equipment for extended periods experienced facial skin irritation and injury. Therefore, research efforts were briefly focused on a final parametric study, where the effect of altering the properties of respirator masks on the skin's damage propensity was investigated. It was found that soft, low friction materials should be utilized, contact area should be maximized and the use of soft, incompressible materials should be avoided.

Overall, this thesis describes the use of computational models to analyse the propagation of subsurface mechanical stimuli within soft tissue during skin-product interaction. Product designers could use the outputs of this thesis in conjunction with existing experimental data to enhance sensorial experiences amongst consumers.

Contents

List of Figures

List of Tables

1. Introduction

Touch, one of our most fundamental senses, is a complex biotribological process which is initiated upon skin-surface contact, prompting the propagation of mechanical stimuli to our receptors. Through gripping, lifting, sliding, rotating or simply tapping against counter surfaces, we are able to interact with the world around us through cutaneous interactions.

The skin is our largest organ which accounts for approximately 16 % of our mass and occupies a surface area of up to 2 square meters[1]. The properties of skin play an instrumental role in how humans perceive surfaces. The skin exhibits large variations in its structural properties between individuals, due to both biological and environmental factors including age, race, sex, hydration and occupation. From a mechanics point of view, skin is an inhomogeneous, anisotropic, non-linear, time-dependent solid comprising three distinct layers supported by the subcutis[1–6]. From outermost to innermost, our skin comprises the stratum corneum, viable epidermis, dermis and hypodermis/subcutis, each with different mechanical and structural properties.

Partially due to the skin's heterogeneity, certain cutaneous biomechanical phenomena, such as our sense of touch, are not fully understood. Passive touch refers to scenarios in which the finger is stationary whilst external stimuli are applied to it. Conversely, active touch describes the process in which subjects proactively explore a counter surface, a process often used when investigating sensations associated with tactile perception[7,8]. Tactile perception is essential for proprioception, kinesthesia and cutaneous functions including the detection of pressure, vibrations, temperature and pain[9–11]. The combination of both discriminative and affective touch helps describe the psychophysical processes and responses of tactile perception. Historically, discriminative touch has been more widely investigated and refers to our ability to perceive the physical characteristics of objects, such as their roughness, slipperiness, compliance, as well as distinguish surface contours (including edges and curvatures). Affective touch describes how contact affects the internal state of the body, eliciting emotions, sensations and experiences[9,12–15].

Our sense of touch is critical for cognitive development during childhood and has significant effects on mental health, social behaviour, and emotional wellbeing throughout our lives[15]. Furthermore, tactile perception has become a key area of focus for product design engineers and ergonomists who wish to distinguish their premium products by provoking desirable feelings upon contact (e.g., cosmetic applications, product surfaces and packaging). Developments in our understanding of touch can lead to the improvement of skin injury treatments and artificial skins for rehabilitation purposes and robotics. Through investigating how factors such as ageing, gender and humidity affect our skin and sense of touch, products and methods could be developed to help enhance or counteract these changes to improve tactile sensation. Finally, in addition to further medical technologies (e.g., artificial sensors for intelligent prostheses), a better understanding of tactile perception can also help reproduce or enhance human perception through virtual and augmented reality respectively[16].

Conventionally, tactile perception studies are conducted through panel testing which, by nature, generate subjective results. However, with the rise in computational power over the last few decades, the use of Finite Element (FE) models to simulate soft tissue interaction has become increasingly popular. These numerical models enable the definition of objective, quantitative metrics to provide more insight into the effects of relevant parameters on our sense of touch, thereby aiding the development of consumer products, such as cosmetics. Whilst unable to fully simulate the intricacies of soft tissue, numerical analysis hosts a number of advantages over experimental methods. These numerical investigations are typically:

- Relatively inexpensive – hardware and software licenses are typically cheaper than experimental procedures requiring test rigs, laboratory conditions and trained specialists.
- Much faster – simulation speed scales with model simplicity and high-performance computation.
- Easily repeatable – the mechanical, geometric, and interfacial properties of soft tissue show high degrees of variations amongst individuals. Therefore, in experimental investigations where multiple samples are often required, natural biological variations can obscure results and trends. In computational investigations, these parameters can be isolated and fixed or varied at will.
- Non-invasive – as the properties of tissue differ considerably between in and ex vivo samples, experimental procedures may require invasive testing.
- Able to simulate subsurface stress, strain, and energy fields.

Together with our industrial sponsors, L'Oréal Research & Innovation, the focus of this investigation and thesis is on computationally analyzing subsurface biomechanical tissue phenomena associated with skin-product interaction. The global skin care market was valued at 155.8 billion USD in 2021[17]. This thesis focusses on parametric computational investigations aimed at studying the effects of altering the properties of cosmetic products on tactile perception in order to develop more premium, desirable experiences amongst consumers.

1.1. Research Objectives

The objective of this thesis is to use computational models to help deliver insight into skin-product interaction. Initially this thesis was focused on using numerical methods across three investigations to develop our understanding of our sense of fine (high spatial resolution) touch. The first two investigations involved modifying the properties of the skin and the counter surface respectively to study the effect on the stimulation of our tactile mechanoreceptors. In the third investigation, we aimed to explore the effect of introducing and altering the properties of a cosmetic intermediary on our sense of touch. However, during the PhD, our division was drafted by the Imperial College COVID-19 Response team to help reduce skin injuries amongst healthcare workers with prolonged exposure to high-grade Personal Protective Equipment (PPE). Therefore, an unexpected fourth investigation involved developing finite element models to investigate the effect of mask modifications on the damage propensity of facial tissue. This still falls in line with the overarching theme of our study and was thus included in this thesis. The research objectives are summarized below:

1) Improve understanding of tactile perception through the utilization of computational models
    - Develop a finite element finger-skin model (Chapter 3).
    - Conduct parametric studies to understand the effect of biomechanical skin ageing (Chapter 4), surface topography (Chapter 5) and cosmetic products (Chapter 6) on tactile perception.

2) Suggest design changes to PPE to reduce skin injuries after prolonged usage
    - Develop face mask and facial tissue models
    - Investigate the effect of modifying the mask's material, geometric and interfacial properties on the skin's damage propensity (Chapter 7).

1.2. Thesis Structure

This thesis begins with a literature review into the mechanical and neurological properties of our skin, before examining the effects of various internal, external and system parameters on tactile perception and skin damage (Chapter 2). Chapter 3 then gives a brief overview of modelling techniques and existing soft tissue models, before describing the development of the finite element models used in this thesis. Chapters 4, 5, 6 and 7 summarize the four parametric studies conducted (3 for tactile perception, 1 for PPE-induced skin injury), before a brief summary concludes the thesis.

2. Skin-Product Interaction

This thesis focuses on computationally analyzing skin product interaction with particular emphasis on our sense of touch and PPE-induced facial skin injury. This chapter provides an overview of literature surrounding the two processes, including background information on the skin and the microscale mechanisms and contributing factors involved in tactile perception and skin damage.

2.1. Tactile Perception

Our skin is an inhomogeneous, multi-layered, anisotropic, non-linear, time dependent solid whose parameters vary considerably depending on anatomical site. During tactile perception, the plantar, glabrous (hairless) skin that lines our hands makes contact with counter surfaces. Plantar skin is generally thicker than non-plantar skin (which surrounds the rest of the body) due to the presence of a thicker stratum corneum (see 2.1.1.1. Stratum Corneum), enabling our fingers to bear considerably higher loads as we touch and grip surrounding objects. As the finger is compressed and translated against a counter surface, on the microscale, the fingerprint ridges make contact with the counter surface asperities. The material, geometric and interfacial properties of the finger, counter surface and system can affect the tribological state of the contact. The relative geometries and stiffnesses of both the finger pad and the counter surface will define their conformability, and thus the contact area and friction. Furthermore, the interaction of the finger against surfaces is influenced by mechanical parameters (such as applied load and sliding velocity), biological phenomena (such as skin ageing) and environmental parameters (which can affect either of the contacting bodies or the interface e.g., natural moisture, applied lubricants and moisturizers). This section details the structure and morphology of plantar skin, the mechanisms involved in tactile perception and the factors influencing our sense of touch (Figure 1[18]).

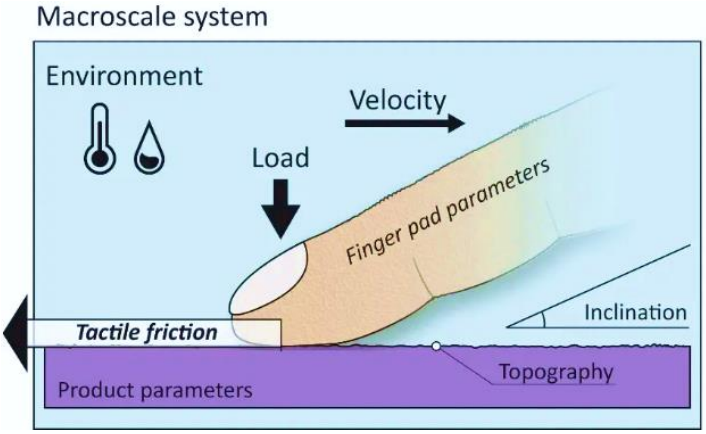

Figure 1: Tactile perception is a complex biotribological problem which is a function of biological, mechanical, interfacial and environmental parameters[18].

2.1.1. Skin Structure and Morphology

The stratum corneum and viable epidermis are often jointly referred to as the epidermis, the upper avascular cellular layer of the skin (Figure 2). The boundary between the epidermis and the dermis has an irregularly undulated structure and is called the dermal epidermal junction (DEJ). The dermis is of particular importance, as in addition to having a large contribution to the non-linear behavior of the skin due to its fiber-matrix structure[2,3,19–21], it houses the mechanoreceptors that convert local mechanical stimuli into a sequence of action potentials that trigger our neurological, psychological and behavioral response to touch.

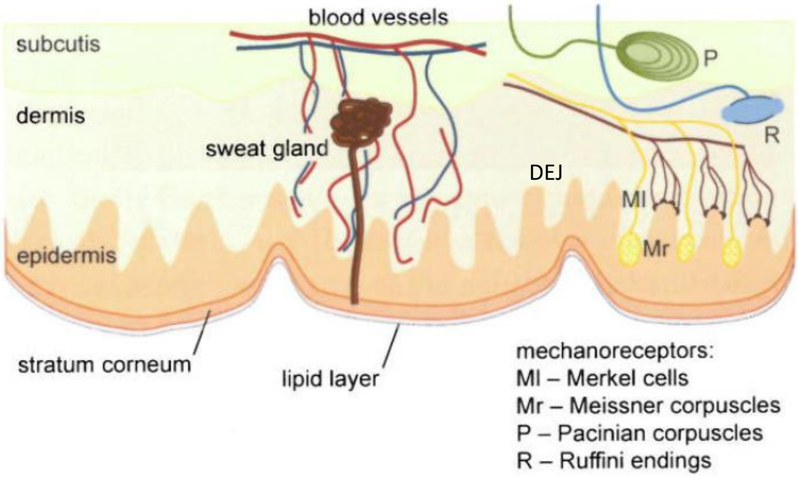

Figure 2: Illustration of the finger skin and dermal mechanreceptors[2].

The skin layers have distinctly different mechanical properties which can vary considerably between individuals, anatomical sites and due to environmental factors (Figure 3, left)[2]. The mechanical behavior of the skin as a whole is also a function of length scale (Figure 3, right). This change in mechanical behavior affects the contact area within the skin-surface interface, thus playing an important role in tactile perception. On the microscale, at the scale of surface roughness and asperities, the effective elastic modulus is predominantly affected by the stratum corneum. At the meso-scale, when the lower, more compliant skin layers are considered, the overall effective modulus of the skin decreases. Finally, at the macroscale, the much stiffer bone of the distal phalanx results in an increase in the effective modulus[2].

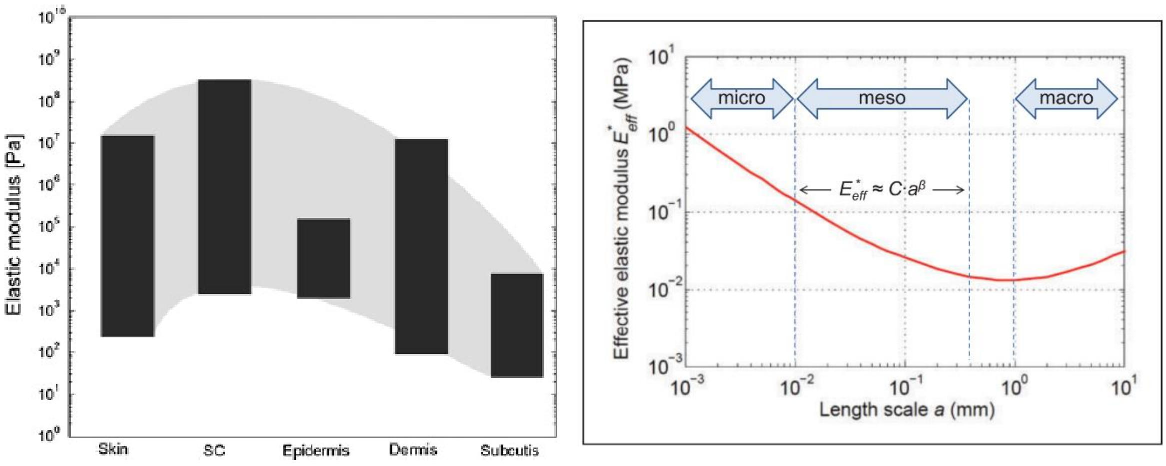

Figure 3: Elastic modulus of the individual skin layers[22] (left – note vertical axis is logarithmic) and the effective modulus of volar forearm skin for different length scales[23] (right) SC = stratum corneum.

2.1.1.1. Stratum Corneum

The stratum corneum is the outermost and thickest layer of the epidermis, acting as a protective barrier to the outside world. It is largely composed of layers of keratinised corneocyte cells[24]. These corneocytes are embedded in lamellar epidermal lipids in a brick-and-mortar style structure. Over time, the outermost layer of corneocytes is cyclically removed and another layer is generated at the bottom of the viable epidermis in order to maintain overall thickness. The stratum corneum typically varies from 8-20 µm in thickness, except at key contact points such as the palms and soles, where the layer can be up to ten times thicker[25]. The stratum corneum is a major load-bearing component of the skin. As opposed to stretching with the other skin layers when macroscopically loaded, the stratum corneum flattens via folding and unfolding[26]. The effective modulus of this layer has been shown to vary considerably from 6 MPa (wet) up to 4 GPa (dry)[4]. This is because the mechanical properties of the stratum corneum are heavily dependent on hydration levels. Water breaks down the hydrogen bonds in the stratum corneum and results in the swelling of its constituent corneocytes, thereby plasticizing the layer, increasing its Poisson's ratio and decreasing its modulus[27]. The behaviour of the stratum corneum under strain can be subdivided into three phases. The first (elastic) phase consists of linear behaviour until up to 10 % elongation. At high humidity levels, the stratum corneum undergoes the plastic phase between 25-125 % elongation, during which irreversible elongation happens. Finally, the strain hardening phase occurs before rupture until 200 % extension (Figure 4)[28]. Compared to the dermis (see 2.1.1.3. Dermis), stress relaxation in the response of the stratum corneum was found to be negligible. The presence of the fingerprint ridges on the surface of the stratum corneum contributes its anisotropy. The ridges and furrows have widths of approximately 200 µm and 120 µm respectively, whilst their depth is approximately 100 µm[2,5,29–33].

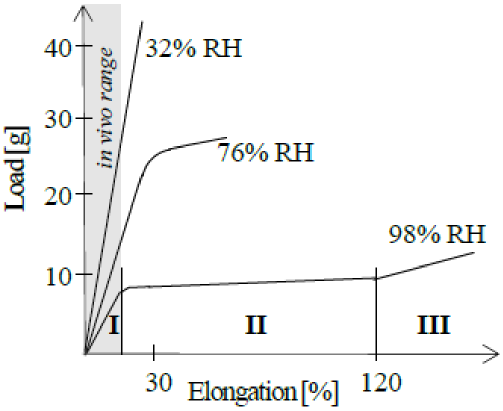

Figure 4: Typical force-extension curve for the elastic (I) plastic (II) and strain-hardening (III) phase for different humidities[28].

Whilst the presence of fingerprints has been found to have negligible effect on tactile perception during static loading, they are fundamental during finger sliding against rough surfaces[34]. As the finger slides against a surface, collisions between the fingerprint ridges and topological features of the counter surface result in the propagation of vibrations to the mechanoreceptor sites. It is thought that fingerprints aid the spectral filtering and amplification of the transmitted vibrations[34,35]. When our fingerprints are orientated perpendicularly to the scanning direction, spectral analysis of the vibrations has shown dominant peaks that are a function of the scanning speed and inter-ridge ratio[35,36]. Whilst fingerprints vary considerably between individuals, common traits within certain demographics exist. Our fingerprints develop until into early adulthood, after which point they are constant[37,38]. Anthropometrically, males have been found to have statistically larger fingers than females. The number of fingerprint ridges are approximately constant amongst individuals' fingers, this results in a higher density amongst females. These fingerprints are thought to improve vibratory transmission and thus offer an explanation as to the increase in perceptive ability amongst females, compared to males; a disparity that has been found to increase with age[39–45].

2.1.1.2. Viable Epidermis

Below the stratum corneum is the viable epidermis which consists of the stratum lucidum (closest to the skin surface), granulosum, spinosum and basale (deepest epidermal layer). Within the viable epidermis, keratinocytes are formed at the stratum basale before differentiating and migrating towards the skin surface over time, changing their size, shape and composition as they gradually transform into corneocytes within the stratum corneum. Due to the elevated levels of hydration in the living cells, molecular diffusion through the viable epidermis is far faster than the stratum corneum[46]. Additionally, the viable epidermis is responsible for many of the cellular processes of the entire epidermis.

The viable epidermis typically varies from 50-100 µm in thickness, except at key contact points such as the palms and soles, where it can reach up to 1 mm[25]. Due to the high number of cellular layers within the viable epidermis, it possesses a high cell density which results in the layer possessing a comparable stiffness to the stratum corneum and being considerably stronger than the dermis or hypodermis[4,24,28]. However, at present there are relatively few results obtained from human testing to accurately describe the mechanical behaviour of just the viable epidermis under applied loads [25].

2.1.1.3. Dermis

The thickness of the dermis varies considerably depending on anatomical site, ranging from 0.6mm in the eyelids to up to 3 mm on people's backs. Approximately 75 % of the dry weight dermal tissue is attributed to collagen fibres, whilst the reticulin fibres, elastin fibres, and gel-like matrix account for the other 25 %. The matrix comprises interstitial fluids (e.g. hyaluronic acid), fibroblasts, proteoglycans and water. As a result of its fibre-matrix like structure, the dermal layer (and by extension the skin) exhibits an anisotropic, highly non-linear stress-strain response due to its ability to expel bound water under pressure, and reincorporate it during unloading[6,27,47–53]. Dermal behaviour can be subdivided into 3 phases (Figure 5). Phase one (at low loads) is characterised by low stiffness as the crimped, unaligned collagen fibres provide little resistance. As the load increases, the fibres begin to align within the matrix in the direction of the applied load, providing resistance and thus increasing stiffness (phase 2). This relative movement between the collagen network and the gel matrix allows skin to exhibit a viscoelastic stress strain response. Finally, once the majority of the fibres are aligned, any further extension of the dermis will require extension of the collagen fibres themselves (phase 3). This provides the dermis with a higher stiffness, whilst the recoil provided by the elastin fibres allows the skin to exhibit a degree of elasticity[6,53].

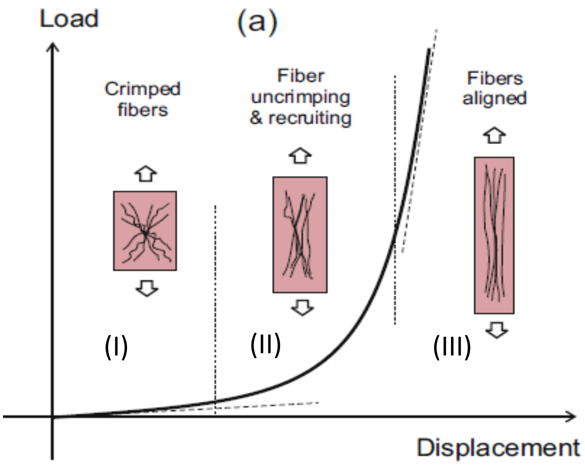

Figure 5: Force-Displacement curve of dermal tissue[53].

2.1.1.4. Hypodermis (Subcutaneous Tissue)

The hypodermis lies underneath the dermis and is interlaced by connective tissue and fibres that anchor the skin to the bone and muscle below. The hypodermis constitutes for approximately 10 % of our mass, whilst its thickness varies considerably over our body[6,25]. The primary functions of the hypodermal layer are to store nutrients and energy (attributed to its high fat content), and provide thermal insulation and impact resistance. The lipid-filled cells are embedded in a loose network of collagen fibres, which connect the layer to the dermis. The hypodermal modulus has been quoted to range from a few kPa to 500 kPa[4,28,53]. Whilst information regarding mechanical behaviour of the hypodermis is scarce, it has been found via compressive testing that the layer exhibits non-linear, viscoelastic properties. Though the results of the test did not show any directionality, it expected that the hypodermis will exhibit anisotropic properties when shear-loaded due to the alignment of collagen fibers within the layer[27,54].

2.1.2. Mechanoreceptors & Mechanotransduction

2.1.2.1. Receptor Function

Mechanoreceptors are densely packed within the distal phalanx and result in the heightened tactile sensitivity (ability to detect changes in stimulus magnitude) and acuity (ability to distinguish spatially distributed surface features). Upon the skin’s contact with a counter surface, mechanical spatiotemporal stimuli such as stresses, strains and vibrations, propagate through the skin layers as mechanical waves to the sites of our mechanoreceptors. These receptors are activated by the skin stress-state variations and convert the applied mechanical stimuli into action potentials. The space-time variation of stresses throughout the skin causes the mechanoreceptors to deform and respond with appropriate space-time variations in their discharge rates. Our neurological response is subsequently triggered in response to this skin-surface interaction during process of mechano-electrical transduction. It is known that mechanical stimuli cause an influx of ions into the receptors via voltage and stretch-gated channels within the axon[55,56]. This influx is a prerequisite for the release of synaptic transmitters which prompt the receptors to fire action potentials to the central (peripheral) nervous system (CNS). The exact method of conversion between the initial mechanical stimulus and the resulting firing of action potentials is not fully understood[57] due to limited literature surrounding the topic. However, it is known that resulting neural signals are mapped onto the outer areas of the brain corresponding to the primary cerebral sensory cortices[58]. Initial psychophysical/sensorial judgements are made as a precursor to emotion, before being transmitted to other areas of the brain, where they may be compared to memories and expectations, in order to form affective judgements.

Mechanoreceptors can be functionally and neurophysiologically distinguished by their adaptive rates and receptive fields, in addition to the stimuli and frequencies they respond to (Figure 6)[59–62]. In the absence of relative movement between skin and surface, slowly adapting (SA) mechanoreceptors respond continuously to the magnitude of sustained stimuli with sustained discharges. Whilst these action potentials occur throughout the entire duration of the stimulus, they do so at a decreasing rate. Conversely, when relative movement occurs, rapidly adapting (RA) receptors are activated by the onset or offset of an applied stimulus, such as the vibrations resulting from dynamic contact[20]. When vibrations are applied for extended periods, rapidly adapting mechanoreceptors can undergo vibrotactile adaptation, in which the receptors sensitivity threshold can change of be inhibited[63]. Therefore, during static contact, the ability to perceive of surface roughness characteristics is reduced due to the absence of vibrations generated from the contact of fingerprint ridges with surface asperities. Receptive fields are typically round or ovular in shape and represent areas of tissue over which an afferent is most easily excited[64]. Type I receptors have smaller receptive fields and higher spatial resolutions for pinpoint precision. This is due to the way in which Type I afferents branch out as they enter the skin and terminate in multiple small mechanoreceptor endings, resulting in distinct borders and multiple small local hotspots. Alternatively, Type II afferents innervate relatively large mechanoreceptors without branching out, resulting in larger receptive fields and lower spatial resolutions. They can be further classified by their indiscriminate borders and a single large zone of maximal sensitivity[64]. Type 1 receptors are typically located within the dermis along the dermal-epidermal junction (DEJ relatively close to the skin surface to promote higher spatial resolution, whilst type II receptors are located deeper within the dermis.

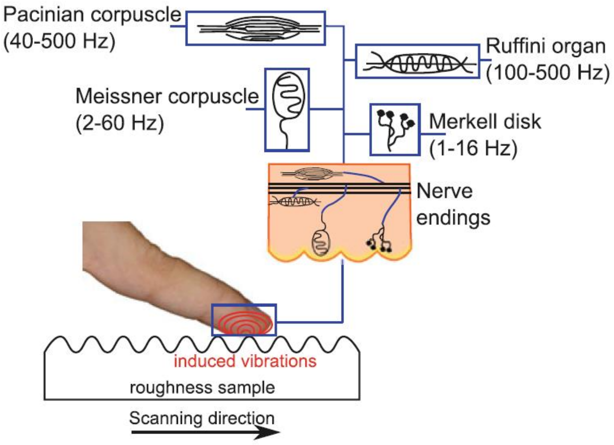

Figure 6: Frequency ranges that the mechanoreceptors respond to during sliding[59].

2.1.2.2. Types of Receptors

The four principal mechanoreceptors used for surface characterization during tactile perception are the Meissner Corpuscles (RAI), Merkel Discs (SAI), Pacinian Corpuscle (RAII) and Ruffini Endings (SAII). Together they enable the discrimination stresses through the transmission of stresses, strains, and vibrations with approximate frequencies of 2-500 Hz. The existence of mechanoreceptors with unique adaptive rates and receptive fields allows each cutaneous afferent class to provide unique contact information to the central nervous system (CNS) during tactile perception. These four mechanoreceptive channels primarily react to changes in strain energy density and the deviatoric component of the applied local strain tensor fields and maintain their independence as high within the central nervous system as the primary somatosensory cortex[57,61,65–69]. Their responses can interact and linearly amalgamate during skin-surface contact in order to create a more robust tactile experience.

Meissner (RAI)

Each primary RAI afferent terminates in up to 17 Meissner Corpuscles, resulting in a density of approximately 150 per mm^2 of skin, higher than that of the Merkel receptors[63,64,70]. Meissner Corpuscles are partially encapsulated, coil-like structures which are ovoid-shaped with axial dimensions of approximately 100 x 500 µm, with the longer axis lying perpendicularly to the skin surface[63]. The unmyelinated terminal branches of the primary RAI afferent are integrated through modified epithelial cells, which form flattened laminar layers within each Meissner Corpuscle. During skin motion/deformation, these cells within the laminar layers can shear past one another, distorting and depolarizing the afferent terminals[64]. The Meissner Corpuscles are located within the dermal papillae of glabrous skin along the dermal epidermal junction at a depth of approximately 0.5-0.7 mm[63]. The receptors produce the sensation of flutter and are fundamental to the perception of skin motion, which is essential for precise grip control, edge detection and object handling. They are sensitive to transient skin deformation/strain and low frequency vibrations (2-60 Hz)[63]. They are most sensitive to applied tangential/shear forces applied in the radial and proximal directions[71].

Merkel (SAI)

The Merkel complex is associated with the SAI afferent (density approximately 1 per mm^2) and is situated along the dermal-epidermal junction (DEJ) with its long axis orientated parallel to the skin surface. It comprises an unencapsulated receptor, the Merkel cell, which encloses the Merkel discs, the primary afferent terminal[63,64]. The Merkel cells are ovular in shape and have an approximate diameter of 10 µm. The SAI afferents innervate 10-100 neighbouring Merkel Cells which, in response to surrounding tissue deformation, release neuropeptides and depolarize the primary afferent. The rate and duration of neuropeptide release is related to the magnitude and time of tissue distortion[63,64]. The Merkel complex responds to static stimuli and enable the detection of an object’s spatial structure and form. Due to their sensitivity to local stress/SED fields, they aid in the detection of surface curvatures, edges and corners and are able to define the overall contact shape, area and load intensity to the brain. They have fine spatial resolutions which are minimally influenced by scanning speeds up to 80 mm/s and forces between 0.2 and 1 N[55,57,61,72]. Merkel receptors are particularly sensitive to normal loads, tangential loads in the distal direction and very low frequency vibrations (1-16 Hz)[63]. The firing rate of pressure-related information to the brain increases linearly with increasing contact pressures up to indentations of 1.5 mm[73].

Pacinian (RAII)

Each primary RAII afferent terminates within the core of a single encapsulated Pacinian Corpuscle, which owing to its large size, possesses large receptive fields with single hotspots and undefined borders; however, they have poor spatial resolution[56,61,63,64]. They are located deeper within the dermis and subcutaneous tissue in both hairy and glabrous skin. Geometrically, Pacinian Corpuscles are ellipsoidal in shape with lengths between 0.3-2 mm and diameters between 0.2-0.7 mm[63]. Structurally, they consist of 20-70 fluid filled laminar cell layers that contribute elastic and viscous properties to the receptor[64]. These layers help filter and protect the receptor from very large stresses and strains. Furthermore, the viscoelastic properties rapidly attenuate low velocity, sustained indentations whilst transmitting high velocity skin deformation components to the receptor core. The low velocity or sustained deformations are transmitted through to the elastic laminar layers, which generate negligible viscous forces. In contrast, high velocity deformations displace the viscous fluid within the laminar cells, transmitting and propagate forces to the afferent terminal resulting in discharge[64]. The receptors responsiveness to mechanical transients results in its sensitivity to high frequency vibrations (40-500 Hz) and its ability to detect skin motions as small as 10 nm[59,73].

Ruffini (SAII)

Each SAII afferent innervates a single, encapsulated, spindle-shaped Ruffini ending[63,64]. They are located deep within the dermis of both hairy and glabrous skin. Ruffini afferents possess large receptive fields with a single hotspot and undefined borders; however, they too have low spatial resolution. The Ruffini organ is 0.5 - 1 mm in length and 0.2 mm in diameter with their long axis orientated parallel to the skin surface[63]. As the receptor is anchored by collogen fibres into the dermal connective tissue, they have a very high sensitivity to lateral skin-stretch. This is due to the collagen fibres intertwining with the unmyelinated terminal branches of the SAII afferent, transmitting any skin deformation directly to the receptor, resulting in its depolarisation. Furthermore, Ruffini Endings are sensitive to vibrations between 100 – 500 Hz, inducing a buzzing sensation[73]. The combination of the receptor's sensitivities additionally render it instrumental for proprioception and kinaesthesia[10,74].

2.1.3. Factors Affecting Tactile Perception

Our sense of touch is modulated by the tribological state of the skin-surface interface, which itself is influenced by mechanical, biological and environmental parameters. In this discussion, we review literature describing the effect of skin ageing, skin hydration, friction, applied normal load, translational velocity on receptor excitation and sensorial experience.

2.1.3.1. Effects of Ageing on Tactile Perception

It is estimated that the global proportion of people over the age of 60 will almost double between 2015 and 2050[1]. This demographic increase necessitates a better understanding of the process of physiological degradation to be able develop tailored products and treatments aimed at improving quality of life. Tactile sensitivity and acuity develop very quickly during early childhood, before becoming further optimized during adolescence and early adulthood. However, as we age further, it has been found that our sense of touch deteriorates significantly over time[11,75–80]. This tactile perceptive degradation manifests itself amongst the elderly through a reduction in accuracy and increases in variability, discrimination thresholds and response times, when performing tasks that require high spatial resolution. This suggests that changes at the peripheral receptor level, in addition to those at the central processing level, may play a significant role in the reduction of fast, efficient pattern recognition amongst the elderly. Tactile degradation is typically associated with neurological changes such as decreases in mechanoreceptor density and increases in detection thresholds[81–85]. Furthermore, changes in the geometry of the receptors themselves have been to contribute to the reduction in their sensitivities. It has been shown that age and skin surface roughness are positively correlated[84,86,87]. Therefore, due to the change in contact mechanics, vibrational transmissions are distorted. The vibrational acceleration increases resulting in frequencies that are higher than the field of human perception, thereby contributing to tactile perceptive degradation[76]. Researchers have reported that the elderly, who have less moisture in their skin, have lower coefficients of friction upon skin surface interaction than younger individuals[40,78]. Friction, which is strongly correlated with perceptive ability, is heavily dependent on hydration[2]. Hydrated skin better facilitates pressure stress transmission to the mechanoreceptors and central nervous system[78]. As a result, this potentially further contributes to temporal tactile perceptive degradation.

Figure 7: Structural comparison of young vs old skin [88].

As we age, the skin also undergoes biomechanical and geometric changes (Figure 7). The ability of the skin to withstand deformation and recoil changes with age[1,76]. The increase in stiffness is often attributed to a decrease in the hydration of the epidermis and an increase in the stiffness of dermal fibroblasts, whilst the decrease in recoil-ability is associated with the reduction of collagen and elastin fibre density within the dermis[1,79,89–93]. Whilst the skin thickens for the first 20 years of our lives, the subsequent decrease in fibre density weakens the infrastructure of the dermis resulting in skin thinning at an increasing rate, leading to an overall reduction of approximately 20 % over time[1,76]. Within the epidermis, the size and rate of production of keratinocytes reduces over time[75,79,94]. This, in conjunction with the retraction of the epidermal rete pegs over time, results in a thinner epidermal layer. Finally, the subcutaneous hypodermis (which has a high fat composition) thins with age too. As a result, the overall thinning of the integumentary system results in a loss of insulative properties and a higher risk of damage and skin tears[75]. Ageing also results in a flattening of the DEJ of 20 to 35 %, as fibres that anchor the dermis to the viable epidermis degrade and the density of dermal papillae reduces[1,75,79]. Flattening of the DEJ is a key contributor to the decrease in thickness of the viable epidermis[1,75]. The thinner dermal and epidermal skin layers, in conjunction with the flattening of the DEJ results in a lower opposition to shear forces and increased exposure to mechanical insult. This is because separation/delamination of the two layers from the intermediate basement layers can increase the risk of wrinkles and blisters too[75]. It has been shown that skin roughness, furrow spacing and anisotropy increase with age. Furthermore, as we age, the reduction in the skin's elasticity results in a decrease in the density of primary lines and contributes to increases in skin friction[22]. The reduction in viscoelastic recovery and skin turgor further reduces the skins ability to withstand shear forces.

Overall, age-related tactile perceptive degradation has typically been associated with neurological changes. Presently, there are few investigations studying the effect of age-related material and morphological skin changes on the excitation of mechanoreceptors. A better understanding of the extent to which biomechanical skin changes affect tactile perception aid the development of products specifically designed to enhance tactile sensations amongst the elderly.

2.1.3.2. Effects of Friction on Tactile Perception

Friction is well known to play a dominant role in the perception of surface roughness, slipperiness and warmth[2,23]. It facilitates surface discrimination and, through minimizing slip, indicates the degree of grip required for object manipulation[95]. The proportionality constant associated with surface slipperiness and normal loading is the coefficient of friction. Slipperiness can be perceived statically when adjusting applied forces to optimise grip, and dynamically when assessing the tackiness of a surface[7,23,96]. Friction can be subdivided into static and kinetic/dynamic friction[22,97]. Static friction describes the force required to initiate motion on a body, whilst kinetic friction describes the force required to maintain motion. Studies have shown that the static friction coefficient of human skin can be between 10 and 40% higher than dynamic[22]. During tactile exploration tests, significant positive correlations between perceived roughness and mean kinetic friction have been found. Furthermore, the rate of change of tangential stroking force was found to be a significant determinant of perceived subjective roughness[97].

The propensity to deform of both the skin's and counter surfaces microgeometries have a direct effect on the local coefficient of friction, which in turn influences the global macroscopic coefficient of friction affecting both propagated mechanical vibrations and perceived roughness[98]. It has been shown that roughness perceived by one finger is affected by simultaneous contact with another finger against smoother or rougher surfaces. Furthermore, counter surfaces can feel rougher following prior contact with smoother surfaces, than if the surfaces were explored independently[7]. This indicates that whilst tactile exploration originates at the skin surface boundary of individual fingers, it can neurologically assimilate information from multiple sources into a higher order response.

It is known that within sliding contacts, the maximum tensile stress at the surface and the maximum subsurface shear stress are both proportional to the interfacial friction coefficient[99–102]. The duplex friction model describes how friction can be subdivided into adhesive and deformation components (Figure 8). The latter of which can be characterized by the effects of interlocking and hysteresis friction[21,23,103]. Adhesive friction describes the resistance to motion generated by surface energies and intermolecular forces associated with interacting bodies. It is a system property that depends on the material combination, surface topography, intermediate substance (e.g. lubricants) and environmental and operational conditions. Adhesive friction can be defined as the product of the interfacial shear strength and contact area. The interfacial shear stress is a function of contact pressure and intrinsic shear strength, and can be strongly influenced by the viscosity and thickness of the lipid film on the skin surface[22]. Experimental methods have typically yielded interfacial shear strengths with an order of magnitude of 10-100kPa[23]. The resistance to motion generated by adhesive friction can cause smoother, flatter surfaces to be perceived as rougher[104]. Deformation friction occurs upon contact of the finger pad against geometrically rough surfaces. During sliding, energy is dissipated due to hysteresis losses in the skin, which is proportional to the degree of indentation of the surface topography. Furthermore, surface asperities can interlock against the fingerprint ridges during relative sliding, providing further resistance to motion. Whilst the adhesive component of friction is the dominant mechanism for smooth dry surfaces[105–107]. An increase in surface roughness results in a decreased contact area and thus a decrease in the adhesive contribution to the overall frictional force. This increase in roughness increases the deformation component of friction. It is worth noting here that surfaces with very high asperity densities can be perceived as smooth due to large contact areas, whilst conversely, surfaces with low asperity densities can be perceived as rough.

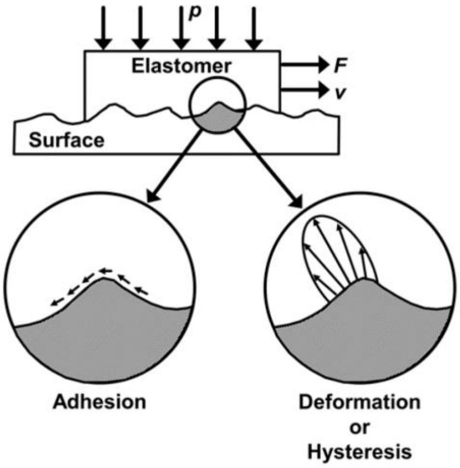

Figure 8: The difference between adhesive and deformation friction, illustrated here for an elastomer making contact with a rigid surface[108].

Generally, smoother, more compliant surfaces are perceived as being more pleasurable or desirable[2]. More specifically, individuals have been reported to experience desirable feelings when their fingers slide over surfaces that are smoother than the fingertip[104]. The converse is true for surfaces that are rougher. As a result, increases in perceived roughness and frictional forces are generally correlated with decreases in pleasantness[14,109,110]. Ridges and surface features are often added to surfaces to improve grip e.g. sports equipment, handlebars[101]. It has been shown that humans can detect single asperities down to at least 1 µm, whilst applying wave-like surface textures with amplitude of as little as 10 nm is enough to distinguish it from smooth surfaces with otherwise identical chemistry[104].

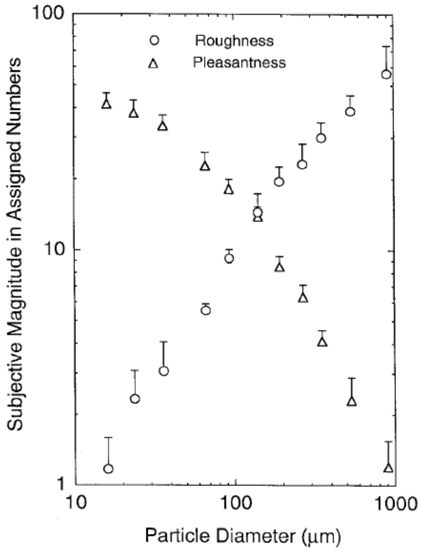

Figure 9: The relationship between particle diameter and perceived pleasantness and perceived roughness[109].

With regards to topological features, our ability to perceive roughness is a function of the height, width, and separation of the surface features[103,111,112]. Increases in ridge width or asperity diameter increases contact area and thus decreases deformation friction and perceived roughness (Figure 9)[103,109,113]. Conversely, as groove width or feature spacing increases, deformation friction plays an increasingly important role in increasing perceived roughness and unpleasentness (Figure 10)[8,13,97,113]. This is largely driven by interlocking friction; for asperities exceeding 250 µm, hysteresis friction can contribute up to 10-20 % of total friction[101].

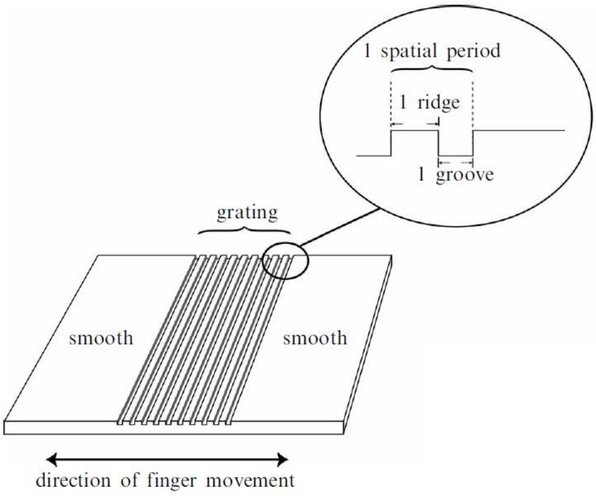

Figure 10: Perceived roughness is strongly dependent on both ridge and groove width. Image adapted from Lawrence et. al[113].

The friction generated within the skin-surface interface during sliding fluctuates depending on the degree of contact and indentation between the skin surface and the counter surface raised features (Figure 11). Maximum ploughing friction is achieved when the skin tissue dips within the groove between two adjacent surface features[103]. In contrast, maximum adhesive friction is achieved as the contact area between the finger and both the feature surface and the grooves is maximized. The amplitude of frictional oscillations is a function of the microgeometries of the contacting bodies, whilst first and second order kinetics describe how friction is dependent on hydration, normal loading and sliding velocity[33].

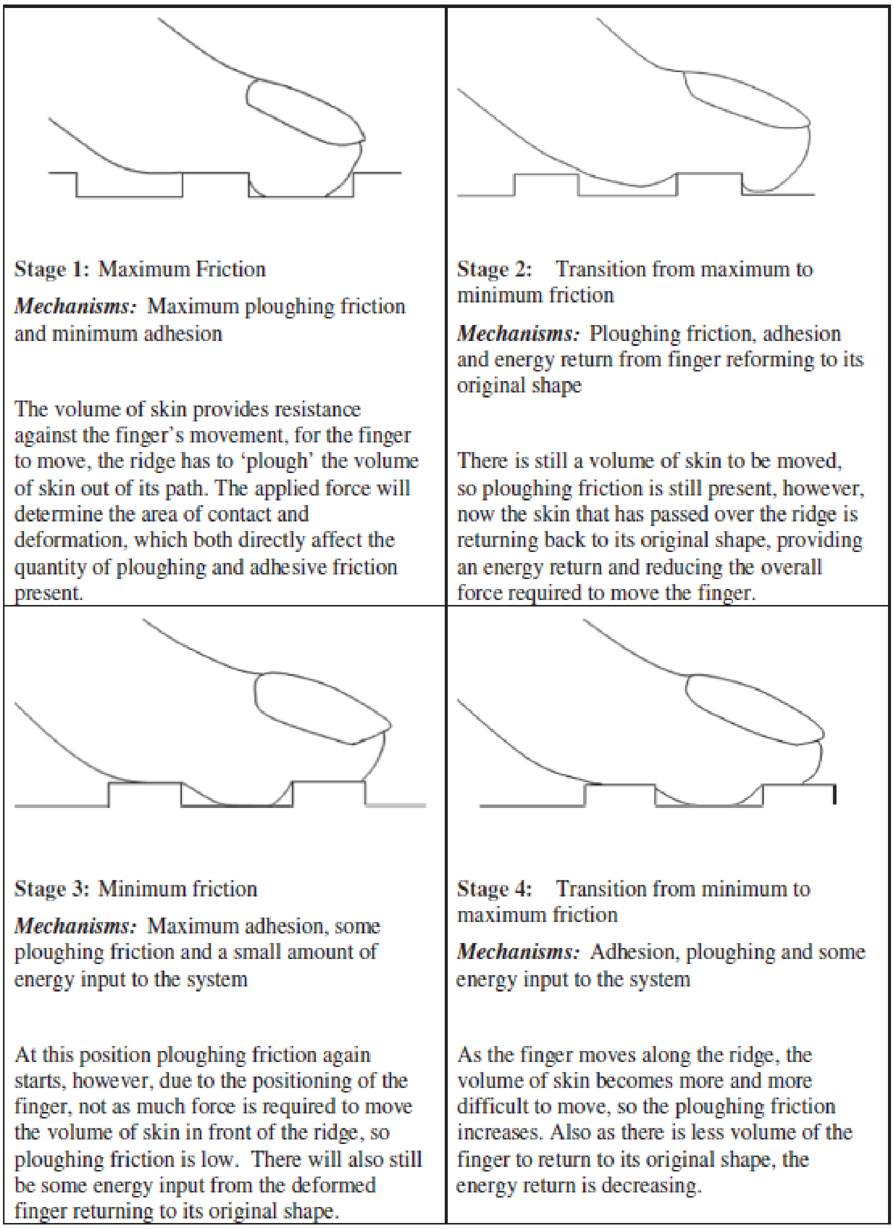

Stage 1: Maximum Friction

Mechanisms: Maximum ploughing friction and minimum adhesion

The volume of skin provides resistance against the finger's movement, for the finger to move, the ridge has to 'plough' the volume of skin out of its path. The applied force will determine the area of contact and deformation, which both directly affect the quantity of ploughing and adhesive friction present.

Stage 2: Transition from maximum to minimum friction

Mechanisms: Ploughing friction, adhesion and energy return from finger reforming to its original shape

There is still a volume of skin to be moved, so ploughing friction is still present, however, now the skin that has passed over the ridge is returning back to its original shape, providing an energy return and reducing the overall force required to move the finger.

Stage 3: Minimum friction

Mechanisms: Maximum adhesion, some ploughing friction and a small amount of energy input to the system

At this position ploughing friction again starts, however, due to the positioning of the finger, not as much force is required to move the volume of skin in front of the ridge, so ploughing friction is low. There will also still be some energy input from the deformed finger returning to its original shape.

Stage 4: Transition from minimum to maximum friction

Mechanisms: Adhesion, ploughing and some energy input to the system

As the finger moves along the ridge, the volume of skin becomes more and more difficult to move, so the ploughing friction increases. Also as there is less volume of the finger to return to its original shape, the energy return is decreasing.

Figure 11: Friction mechanisms deviate depending on relative location of the finger and protruding surface features[113].

The duplex theory of tactile perception describes how topological features of different magnitudes are distinguished and discriminated during sliding contact [7,16,20,23,33,59,63,73,104,110,114–116]. Fine textures with spatial periods below 100 µm are perceived by vibrations induced through contact against the fingerprint ridges, which propagate to our rapidly adapting afferents[16]. The amplitude of vibrations is positively correlated with perceived roughness, whilst the frequency determines how strongly the receptors respond[7]. Fingerprints are fundamental to the process of tactile perception, acting as biological filters and stress concentration sites to facilitate the amplification of induced vibrations[34,35]. Texture patterns with larger spatial periods than the finger are not perceived by vibrations. When shear forces are applied at the skin surface, maximum deviatoric stresses have been found to propagate towards the locations of the tactile mechanoreceptors[63]. Furthermore, it has been shown that higher frequency vibrations propagate deeper into the skin tissue, consistent with the location of the Pacinian Corpuscles, whilst lower frequency vibrations only penetrate superficially, consistent with the location of Meissner Corpuscles[62,117,118]. It is worth noting that even if the topologies of two surfaces are similar, differences in mechanical properties can affect the compliance of the counter surface upon contact with the finger and thus effect friction and perception[119]. As vibrations are required to perceive fine textures, they can only be perceived dynamically i.e. during sliding. Conversely, coarse textures can be perceived statically as uneven pressure distributions[7,23]. Coarser textures with spatial periods above 200 µm are perceived by spatial code generated by the firing variation of slowly adapting afferents. Within the characteristic region of 100 – 200 µm, both spatial and temporal mechanisms play an important role in tactile perception[16].

With respect to larger surface textures, researchers have investigated four main categories of ridge design: criss-cross patterns, dimples, pimples and ridges[101]. The most common category was a ridge pattern, either triangular or rectangular in cross-section and between 0.1 to 5.0 mm in height. Increases in spatial period up to 8.5 mm have resulted in approximately linear increases in perceived roughness[97]. Tactile information on regarding surface roughness is based upon the integration of spatial and temporal information generated during sliding[13]. Psychophysical experiments to determine the link between varying the spacing of embossed dots on plastic surfaces and perceived roughness magnitude yielded an inverted-U relationship[66,120–122]. Up to approximately 2.0 mm, perceived roughness increased monotonically with increasing spatial period[120]; however, the inverted U then peaks between 2-4 mm, whilst further increases in spatial period decreased perceived roughness (Figure 12) [120,122]. This relationship is true for rigid surface features, whilst non-rigid surface features display increases in perceived roughness over a larger range of feature spacing.

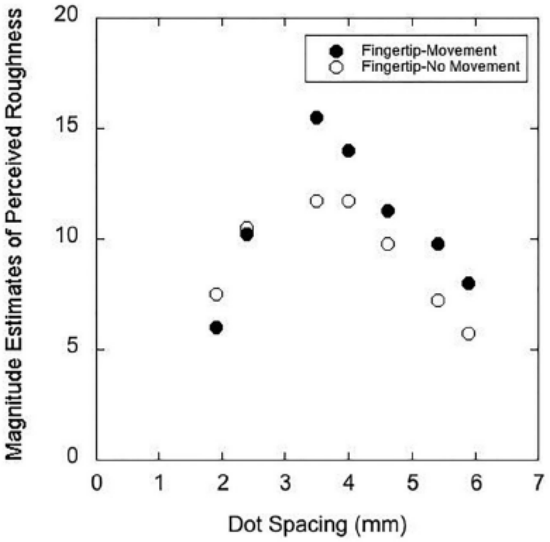

Figure 12: The magnitude of perceived roughness obeys an inverted U relationship under both static and dynamic conditions[122].

Neurologically, whilst researchers have found that temporal history of deviatoric stresses at the Type 1 receptor sites are more strongly correlated with the number of impulses generated than the nerve impulse firing rate[69], others have reported monotonic relationships between perceived roughness and average impulse/discharge rates[120]. Connor found that the average impulse rate also has an inverted U-shape relationship with dot spacing[120]. Recent studies also suggest that texture perception may be correlated with spatial or temporal variations in discharge rates[123]. Temporal variation describes the variation in firing rate of individual afferents as the skin is passed over rough surfaces over time, thereby transmitting information about the unevenness of the surface. Spatial variation refers to the firing of adjacent receptors as the skin is irregularly indented whilst passing over uneven surfaces. This generates a two-dimensional pattern of firing rates beneath the skins surface, which transmits roughness information to the brain[120,123]. In both cases, the size and sharpness/height of raised topological features affect the amplitude and periodicity of temporal and spatial variation. Whilst some believe that the integration of both spatial and temporal information facilitates textural perception, others have found, following psychological and neurophysiological testing, that the spatial variation theory was more closely correlated with perceived roughness than the temporal variation model. However, these spatial mechanisms alone can only account for the perception of coarser textures[124].

For periodic surfaces, the frequency peaks of the acceleration spectra generated from skin-surface contact is shown to be a function of spatial period ratio of the fingerprint and surface, and the scanning velocity[73,125]. Lower surface feature spatial periods are associated with a higher collision rate and are thus inversely proportional to the principal frequency of the elicited mechanical vibration[114]. When the surface textures are finer than that of the fingerprint, the frequency peaks are multiples of the fundamental frequency and are predominantly a function of surface roughness alone. As the spatial period of the counter surface geometry increases and becomes comparable to that of the fingerprint, the spectrum is a function of mutual roughness ratio. Surfaces with wavelengths that are multiples of the fingerprint wavelength results in larger excitation frequency peaks[63,126]. Finally, further increase in surface wavelength generates a spectrum which is a function of the fingerprint wavelength. As a result, the surface can only be perceived by spatial mechanisms as a quasi-static pressure distribution on the finger, whilst vibratory/temporal mechanisms have a much lower contribution to tactile perception. Therefore, it can be concluded that the elicited vibration spectrum is at the very least always a function of the smallest wavelength[16]. Isotropic surfaces textiles exhibited a both a characteristic frequency peak and a larger frequency distribution attributed to the surface scale texture roughness and microscale fibre roughness respectively[114].

Overall, friction plays a substantial role in modulating tactile perception. Whilst adhesive friction dominates upon contact with smooth dry surfaces, deformation friction becomes more significant when perceiving rougher and textured surfaced through the use of both spatial and temporal mechanisms. The geometry of the counter surface can significantly influence the frictional regime at the skin-surface boundary. Investigating the effect of altering surface topography on tactile perception could offer designers insight into the development of products designed to elicit specific sensations amongst consumers.

2.1.3.3. Effect of Translational Velocity on Tactile Perception

During tactile exploration sliding speeds between 0-200 mm/s are most relevant; however, typical surface scanning speeds fall between 10-30 mm/s when performing tasks where tactile acuity is required[33,73]. Additionally, individuals have been found to vary scanning speed in response to changes in surface topography, potentially related to psychological cues such as pleasantness and aversiveness, in additional to mechanical cues such as maintaining friction[127]. It has been found that maximum friction coefficients are experienced within the velocity ranges commonly used for tactile exploration[33]. Coulomb's law describes how kinetic friction is independent of applied velocity; however, some researchers have found skin friction coefficient tends to decrease with increasing scanning speed for both smooth and rough surfaces[23,33,128], whilst others have found the opposite[22,129].

Perceived roughness is relatively insensitive to changes in speed over a large range; however, our afferent responses are[124]. Faster speeds have been found to elicit less pleasant sensations when the finger is traversed over rough surfaces (Figure 13)[13]. It has been shown that texture specific spiking patterns contract and dilate in conjunction with changes in scanning speed ratio[124]. For low speeds, dominant vibration frequencies exhibited low strain energy values, whilst the converse was true for high sliding speeds[125,128]. Increases in scanning speed result in increases in vibration magnitude, peak spectral frequency, frequency distribution and tactile accuracy during exploratory tasks. These higher frequency vibrations are more likely to be detected and processed by the Pacinian Corpuscles deeper within the skin, as opposed to the Meissner Corpuscles, which are more superficially located.

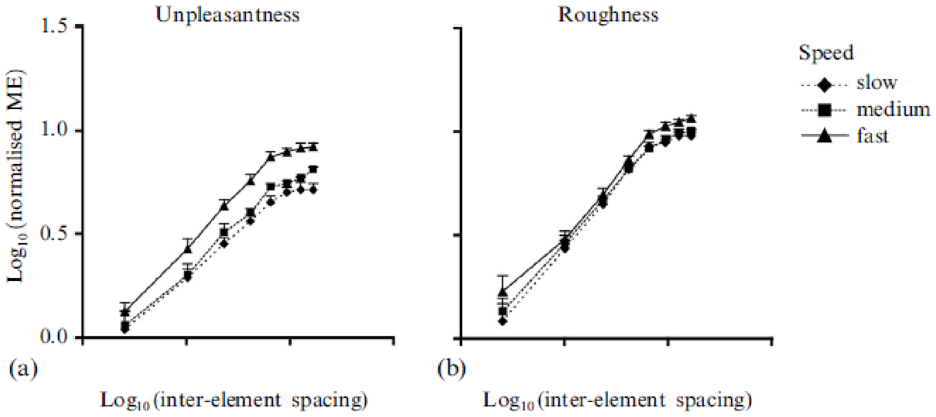

Figure 13: The effect of interelement spacing and sliding speed on log$_{10}$ normalised magnitude estimates of perceived unpleasantness (left) and roughness (right). Here, faster speeds had a more pronounced effect on unpleasantness than roughness[13].

Whilst some researchers have found the magnitude of vibration acceleration signals to be higher at the fingertip than the finger pad, others have found that at lower speeds, the finger pad was more effective than the fingertip at surface discrimination[128]. This is due to the stick slip phenomenon being more prominent at the fingertip than the finger pad at lower speeds. Stick-slip friction occurs when the friction coefficient decreases with increasing velocity, resulting in intermittent sliding motion when localized stick occurs at the center of the contact Zone whilst the periphery of the contact regions remains in slip state[128]. This typically occurs at low speeds on smooth materials and thus has load-dependencies closely corresponding to those described for the adhesive friction model. Stick-slip friction has been found to interrupt perceptive cues and is associated with unpleasantness[128].

With respect to directionality of the finger pad, researchers have experimentally found that participants of tactile exploration tasks exhibited higher accuracy along the distal-proximal direction than the radial-ulnar direction. Whilst the distal surface exploration was found to be the most sensitive, it exhibited significant stick-slip at slower speeds[129]. As a result, the proximal direction was found to be more favourable as sliding speed can be easily moderated in this direct. Furthermore, subjects exhibited no significant difference in accuracy along the proximal direction when sliding speed was varied, whilst distal performance was improved at higher speeds.

Overall, both the finger sliding velocity plays an important role in our ability to perceive surfaces. Controlling, sliding speed enables optimal friction levels for perception to be reached. Furthermore, the sliding speed is related to propagated vibrations and perceived pleasantness. Further investigation into the effect of sliding speed on receptor excitation may help engineers better understand the operating conditions under which different surface textures.

2.1.3.4. Effect of Applied Load on Tactile Perception

Normal forces typically modulate friction for optimal grip and tactile experience; therefore, applied forces are typically a function of the weight of the object, the friction between the skin-surface boundary and the safety margin set by individuals based on prior experience (e.g., for sharp or slippery surfaces). Whilst exerted grip forces can reach up to 50 N, normal forces generated through the distal phalanx during texture perception typically approximate to 1 N[23]. Amonton's empirical law of dry friction states that friction is directly proportional to applied normal load and is independent of apparent contact area. Due to the skin's complexity (non-linearity, viscoelasticity and anisotropy), this relationship does not hold true as the real contact area itself is a function of normal load, hydration and temporal effects[22,33,59,104]. As a result, more relevant models have typically been derived from the tribological performance of elastomers.

For finger-surface interaction, the association of frictional force and normal loading (N) obeys a power law relationship (Figure 14) [23,130]. For scenarios of pure adhesion, the adhesive component of frictional force is proportional to $N^{2/3}$. On the other hand, considering scenarios of pure deformation and hysteresis friction yields frictional force components that are proportional to $N^{4/3}$. Adhesive friction has been found to dominate in dry to moist environments, at low loads, with relatively smooth surfaces ($Rq < 6$ µm)[22]. Conversely, in wet environments or those with larger applied loads against rougher surfaces, the deformation and hysteresis components start to become more significant. Through dividing the frictional forces by normal load, we obtain the coefficient of friction for each of the components. Therefore, the adhesive coefficient of friction is proportional to $N^{-1/3}$, whilst the deformation coefficient of friction is proportional to $N^{1/3}$[130].

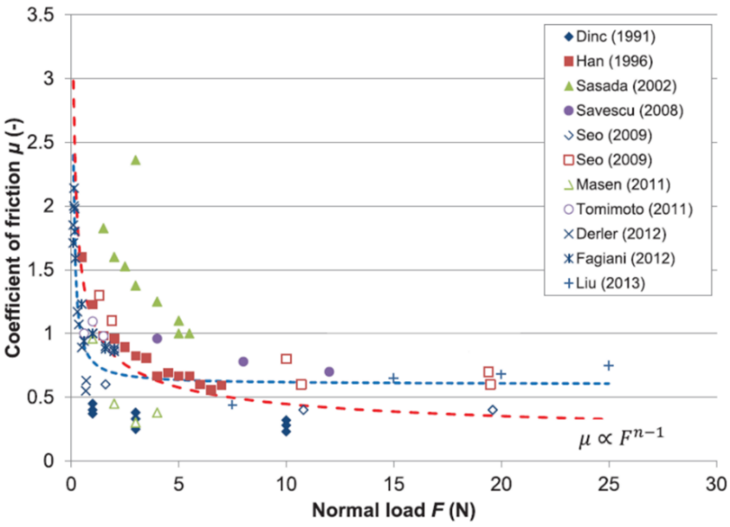

Figure 14: Coefficient of friction of the index finger as a function of normal load[59,105,130–137]. Image adapted from Kuilenburg et al[23].

Through tactile perception experiments, studies have found that frictional force increases with normal force (which typically approximates 1 N), until a critical value is reached, after which skin friction is mostly insensitive to further increases in applied load[22,23,104]. This is likely due to a maximum value of contact area being established as the skins effective modulus has been found to increase with applied load. Similarly, the coefficient of friction is found to decrease with normal load until a threshold value is reached, after which it is insensitive for further increases in contact pressure[22,98,101]. In scenarios where the deformation component is more prevalent (e.g. at higher loads), scientists have reported varying results, with some stating that the coefficient of friction seems less sensitive to increases in contact pressure, whilst others have reported that overall friction coefficient starts to increase with further increases in normal loading[33,98]. These differences may be attributed to material, interfacial or environmental parameters affecting the extent to which deformation and hysteresis mechanisms compete over one another to dominate the overall frictional behaviour[22,23,130].

With regards to tactile perception, neurophysiological experiments have established that tactile pattern recognition is relatively insensitive to changes in low normal loading (0.2-1 N)[63]. This corroborates findings that at low loads, elicited mechanical vibrations are relatively constant. However, larger forces correspond to larger perceived roughnesses due to both larger vibration magnitudes and higher contact areas and tissue deformation, contributing to increases in frictional forces[8,59]. Exceeding user specific threshold loads results in excessive tissue deformation, reductions in spectral amplitude and decreases in perceptive ability. As low friction environments tend to elicit desirable sensations during surface exploration, it has been found that larger normal loads result in less pleasant tactile experiences. However, it is worth noting that as tactile perceptive degradation occurs temporally, the elderly have been found to apply higher contact pressures than younger individuals[78]. This is likely done to increase frictional forces to enhance their tactile experience.

Overall, applied load has been shown to have significant effects on both the magnitude of friction and the friction regime (i.e., the relative contributions of each mechanism). Friction itself is a function of material, interfacial and environmental parameters. Further investigation into the relationship between applied load and surface topography may help designers understand why users may vary applied load to elicit specific sensations in specific applications.

2.1.3.5. Effect of Hydration on Tactile Perception

Changes in the hydration level of the skin occur due to fluctuations in ambient relative humidity, the introduction of hydrants onto the skin surface (e.g. water), or sweat production, the primary evaporative cooling mechanism for the human body. Hydration levels have been shown to have a substantial effect on friction and by extension, tactile perception[138,139]. It has been found that increases in relative humidity have positive correlations with perceived smoothness[109].

A U-shaped relationship between skin hydration and friction has been attributed to changes within the lubrication regime (Figure 15)[22,109,140]. At low levels of moisture, boundary lubrication may exist characterized by molecular surface films which can influence the interfacial coefficient of friction[109]. At low to mid-levels of moisture, the lubrication regime can shift towards mixed lubrication, characterized by the coexistence of a dry and wet contact Zone[33,109]. Within this region, occlusion of the skin will have occurred[23,33]. In this process, sweat is exuded from pores located on fingerprint ridges when in contact with impermeable surfaces. The presence of moisture can vary the elastic modulus of the stratum by up to three orders of magnitude from 6 MPa (wet) to 4 GPa (dry)[4]. Water disintegrates the hydrogen bonds in the stratum corneum and results in the swelling of its constituent corneocytes, thereby plasticizing the layer, increasing its Poisson’s ratio and decreasing its modulus.

This increase in compliance increases the contact area against counter surfaces, thereby affecting the adhesive coefficient of friction, and elevating the deformability of the skin against harder rough surfaces, resulting in an increase in friction[22,23,100,104]. The increase in the overall coefficient of friction persists as contact and occlusion time increases (in which friction can increase by an order of magnitude after approximately 10 seconds of contact time) until a steady state value is reached. In its fully hydrated and occluded state, friction between the skin and counter surfaces can be 2-4 times higher than in dry sliding conditions[138].

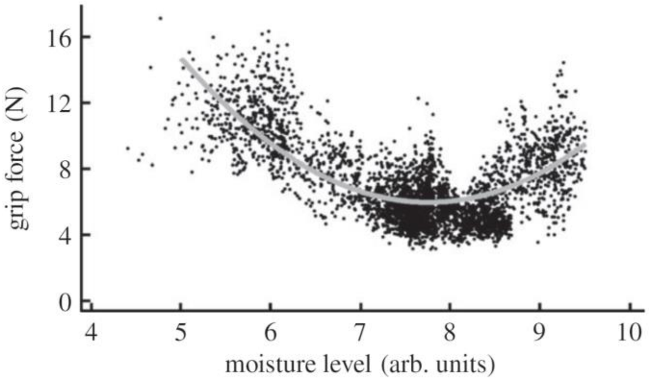

Figure 15: Static grip force as a function of moisture level. The line of best fit exhibits a minimum at approximately 7.75 arbitrary units, indicating an optimal moisture level for grip[33].

Upon the saturation of the skin surface, excess moisture can build up within the interface and generate adhesive capillary forces[22,33,101,119]. These are the result of surface tension and reduced Laplace pressure within liquid junctions that have a concave meniscus. Within skin-surface contacts, this mechanism has a less pronounced effect on friction than occlusion[33]. At this intermediate level of friction, optimal levels of sweat are produced to maximize friction and grip, thus requiring a minimal level of applied normal force[7,22,141]. Thus, it has been suggested that sweat regulation mechanisms may exist to ensure optimal levels are produced to help control friction. Whilst multiple mechanisms have been proposed, the simplest explanation involves hydrostatic pressure within the sweat pores being blocked by counter surface contact. Additional suggested mechanisms include evaporation of excessive sweat or the channeling of excessive sweat through the valleys of the fingerprint ridges via two-dimensional Darcy flow[33].

It has been found that application of skin creams has resulted in decreased vibration amplitudes, leading to smoother perception of rough surfaces, which are generally categorized as being more pleasant or desirable[111]. However, it has been found that for the perception of smooth surfaces, the inclusion of moisture can increase friction and lead to less pleasant perceptions. In the event of excessive moisture build up within the skin contact, the film thickness can reach levels at which the surfaces are completely separated by the lubricating film. This regime is referred to as (elasto)hydrodynamic lubrication and typically results in an overall reduction in friction[142]. In this regime, the adhesive intermolecular forces that generate friction are disrupted by the presence of the moisture film and replaced by viscous friction, the force required to shear the lubricating film within the interface[33]. The properties of the lubricating layer and thus the overall frictional response will be dependent on a variety of tribological parameters such as film thickness, contact pressure and viscosity (which itself is a function of attributes such as temperature and sliding velocity). It has been found that efficient aqueous lubrication of the skin can lead to friction coefficients below 0.1 at high contact pressures[22]. Finally, it is worth noting some researchers have reported that the presence of moisture can lead subjects experiencing stick-slip sensations[101]. This could result in negative implications for both perceptive ability and pleasantness.

Overall, the moisture and hydration of the skin and within the contact itself strongly influence friction and by extension tactile perception. Further investigation in the field could enable cosmetics companies to develop premium products that may optimize friction levels in order to improve the pleasantness of their consumer’s cutaneous interactions.

2.2. PPE-Induced Facial Tissue Damage

During the COVID-19 pandemic, healthcare professionals globally have been using personal protective equipment (PPE) for increased durations. The prolonged use of facial PPE, such as respirator masks, visors and face shields, may lead to the development of a range of skin issues, including irritation and injuries such as skin tears, pressure injuries and urticaria (Figure 16) [143–148]. This section details the structure and morphology of facial skin, the microscale mechanisms under which it is damaged, and methods to prevent skin injury.

Figure 16: Images displaying skin damage induced by excessive usage of high-grade PPE amongst healthcare workers during the COVID-19 pandemic[149]. Source: Instagram @dermguru

2.2.1. Skin Structure and Morphology

Non-glabrous skin is located around the majority of the body. It is characterized by the presence of hair follicles, being considerably thinner than plantar skin, which is thick, hairless and surrounds the palms and soles of the human body. The stratum corneum and viable epidermis of non-glabrous skin are considerably thinner than plantar skin (Figure 17), thereby reducing its load bearing capacity [5]. Furthermore, the interlayer junctions of facial skin possess considerably less tortuosity than their glabrous equivalents[5]. Whilst non-glabrous possesses a lower mechanoreceptor density than finger skin, the receptor density within facial still exceeds the majority of anatomical sites[150]. Information describing the geometric and material properties for each of the facial skin layers are scarce relative to that of finger skin. Like finger tissue, facial skin properties vary considerably amongst individuals; however, on the face they also differ considerably by testing mode (e.g. torsion, indentation and extension) and anatomical region[6,151–155]. Typically, mechanical parameters are characterized as linear elastical and homogenous; fewer studies detail the mechanical behavior of each individual facial skin layer[6,151,153,156,157].

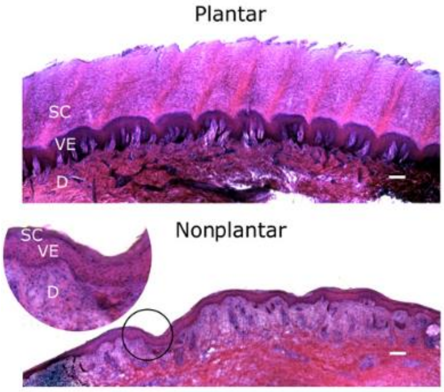

Figure 17: The difference in structure between plantar and non-plantar skin. Scale bar (bottom right) is 200 μm[5]*.*

2.2.2. Skin Damage Mechanism

Respiratory protective equipment has been widely reported to cause skin reactions such as contact dermatitis, acne, facial itch and rash[158–160]. Lan et al report skin damage related to general protective measures occurring in up to 97 % of health care workers, of which the nasal bridge has the highest prevalence[161]. Yen et al report that up to 71 % of healthcare workers who wear PPE experience burning and itching sensations[162]. Discomfort and irritation may lead to the improper use of PPE, whilst skin injury might result in lost hours with medical and care staff being absent from work. In addition, a compromised skin barrier adds a potential entry route for COVID-19 infection[163]. Jiang et al correlated PPE-induced skin injury with heavy sweating, the use of higher-grades of PPE and the duration of continued use of PPE[164].

A key feature of tight-fitting or sealing PPE is that there is a close contact between the PPE and the skin, resulting in the skin being subjected to a combination of normal and shear forces. Manifestations of these loads acting on the skin range from indentation marks at the locations of PPE-skin contact to deep-tissue bruising across a larger area. Excessive loading of the skin can result in lesions at the skin surface, which can develop into erythema and mild irritations [163,165–167]. Various causative pathways to severe skin injuries have been presented in literature[168]. Loading of the skin may result in occlusion of the capillaries and restricted lymph flow, which will set off a cascade of biochemical processes. The resulting ischaemic response of the cell includes hypoxia, lack of nutrients and the build-up of metabolic waste products and will lead to a breakdown of cell organelles, triggering apoptosis or necrosis[160,169–171]. These effects at the cellular level, caused by applied external forces and local tissue deformation, result in macroscopic tissue injury at the sites of bony prominences, such as the nasal bridge, cheekbones and forehead [164,172].

It has long been established that shear forces acting on the skin result in damage occurring at significantly lower pressures than when only a normal load is applied [173–176]. In the contact between skin and PPE, three primary mechanisms can be identified that generate shear stresses at the skin interface. Firstly, static friction, sometimes also referred to as 'shear' or 'stiction', which prevents sliding of the PPE. Secondly, local relative motion between the PPE and skin, e.g. as a result of speaking when wearing PPE, causing rubbing of the PPE against the skin. Finally, upon compression, the skin and PPE will deform perpendicular to the direction of loading by different amounts due to their respective Poisson's ratios, resulting the development of shear forces at the interface[174–176].

Preventing PPE-related skin injury requires a better understanding of the interaction between the PPE and the skin, in addition to the effects of this interaction on the strains and stresses inside the tissue. Common treatments to alleviate friction-related injuries involve the application of hydrocolloid dressings [177,178] and the use of moisturisers. However, it was found that incorrect applications of moisturisers before and after PPE application may increase infection risk[179]. Wax-oil compounds have been found to be effective in reducing both short- and long-term friction.

Overall, it has been found that prolonged exposure to high-grade PPE results in skin irritations and injuries which can disrupt the ability of healthcare professionals to perform optimally. Previous investigations on PPE have mainly focused on modelling the pressure that acts on the surface of the skin, with the objective of ensuring an appropriate seal and maintaining a level of user comfort[180–183]. However, the effects of PPE-skin interaction on subsurface stresses and strains within the tissue have not previously been investigated. Further investigation into the effect of PPE-design on subsurface mechanical stimuli within the skin could enable mask manufacturers to design PPE with targeted modifications to reduce specific injuries.

2.3. Conclusion

Tactile perception is a complex multi-dimensional bio-tribological process that is influenced by mechanical, biological and environmental parameters. Developing our understanding of how these parameters influence the sense of touch will enable the development of products designed to enhance tactile sensation. Furthermore, a better understanding of tactile perception can also contribute to the fields of affective and kansei engineering, where products are designed to evoke specific psychological responses amongst consumers. Experimental approaches are frequently used to understand more about tactile perception. However, the skin is highly individualized, and the analysis of in vivo subsurface mechanical stimuli is currently not possible on the receptor level. Therefore, this thesis focusses on a computational approach in order to develop more generalized conclusions on how alterations of the skin, counter surfaces and interstitial compounds influence the excitation of Type 1 (high-spatial resolution) mechanoreceptors and by extension our sense of fine touch. More specifically, this thesis will describe the development of a parameterized finite element model which will be used to assess the effect of skin ageing, surface topography and cosmetic products on tactile perception.

PPE-induced skin injury has been seen across the globe in response to excessive usage of high-grade masks during the COVID-19 pandemic. In this thesis the effect of mask modifications on the skin's damage propensity will also be investigated. Parametric studies will be conducted on finite element respirator mask models in order to better understand the effect of altering the geometric, material and interfacial parameters of PPE on the subsurface mechanical stimuli within facial skin.

3. Numerical Modelling - Background Theory & Model Development

3.1. Introduction

In each of the studies included in this thesis, finite element skin models are utilized to assess the effects and trends of:

1) Skin ageing
2) Surface topographies
3) Cosmetic properties
4) PPE properties

on the propagation of mechanical stimuli within the skin.

Investigation 1 (4. Investigating the Effect of Biomechanical Skin Ageing on Tactile Perception) comprised the development of a soft finger skin model to be compressed and translated against a rigid smooth surface. Biomechanical manifestations of skin ageing are then applied to the finger skin in order to observe their effect on Type 1 mechanoreceptor stimulation and thus fine (high spatial resolution) touch. In investigation 2 (5. Effect of Surface Textures on Tactile Perception), the same soft finger model was compressed and translated against a range of rigid rough surfaces. This parametric study was conducted to simulate the contact of the finger against surfaces with different textures. In Investigation 3 (6. Investigating the Effects of Cosmetic Polymer Film Properties on Tactile Perception), a soft finger skin model was compressed against soft facial tissue, whilst an intermediate cosmetic layer was applied between the two surfaces. The properties of this cosmetic layer were then altered in order to better understand the effect polymer film properties on mechanoreceptor excitation. Finally, in Investigation 4 (7. Investigating the Effects of Respirator Mask Design on Facial Skin's Damage Propensity), contact between a respirator mask and facial tissue was simulated. A parametric study was then conducted to understand the effect of altering the properties of the PPE on skin's damage propensity.

This section will summarise relevant finite element (FE) theory, commonly used material models and existing FE skin models in order to provide justifications for a subsequently developed numerical finger skin model. This finger skin model is used throughout the majority of this thesis. Details surrounding development of the facial tissue models included in Investigations 3 and 4 can be found in their respective chapters.

3.2. Finite Element Method and Software

This section aims to describe the background and rationale required to develop effective finite element models. Background theory is first discussed, before outlining considerations surrounding software and solver selection.

3.2.1. Background

In the sphere of computational modelling, finite element methods (FEM) are amongst the most common for solid simulation. Whilst boundary element methods (BEM) are typically quicker as they reduce dimensionality by 1, FEM is more compatible with transient and non-linear problems[184]. Finite element analysis works by first discretizing a structure into small elements[185]. Simple functions are developed to describe the stress, strain, and displacement variations across each element. These variations propagate to adjacent elements via nodes along the boundary of each element. Each of these nodes can possess up to 6 degrees of freedom (DoF) for a three-dimensional analysis (three translational and three rotational) and 3 DoF for a two-dimensional analysis (two translational and one rotational). The stiffness of each element is calculated by analyzing the force-displacement relationship at each node for each element. By assembling the stiffness equations of each element, a larger matrix equation is developed describing the force-displacement relationship for the macroscale structure. The solution to this matrix equation for applied mechanical loads yields nodal displacements across the structure, enabling the resolution of stresses and strains for any element within the object. Broadly speaking, this process can be described in 7 distinct steps listed below.

1) Discretise structure into elements
2) Select nodal point variables and shape functions to help describe
    a. Nodal variables describe the number of DoF (rotational, translational) attributed to each element.
    b. Shape function describes displacements anywhere within the element.
3) Derive element stiffnesses
    a. Describes force (F) – displacement (δ) relationship for each DoF within the element.
    b. Calculated by integrating across the volume of the element using The Principle of Virtual Work (work done within element = external work done by forces at nodes)

4) Assemble global stiffness matrix, $[K]$, for the overall structure.
    a. Symmetric square matrix with positive or zero leading-diagonal coefficients.
    b. For compatibility, the displacement at each node must be the same for all elements meeting at that node.
    c. For equilibrium, the sum of all the forces at each DoF/node within the global system must balance.
5) Apply the boundary conditions
    a. Helps prevent rigid body motion
    b. Simplifies and helps resolve matrix equations.
6) Solve the overall equations
    a. Yields all nodal displacements due to applied forces.
    b. Algebraically invert the stiffness relationship e.g. $\{F\} = [K]\{\delta\}$ to $\{\delta\} = [K]^{-1}\{F\}$
    c. In practice, FE packages use variants of Gauss Elimination to simplify analysis.
7) Calculate, analyse, and interpret field outputs (stress, strain, displacement etc…) based on displacement results of each element for regions of interest.

3.2.2. Software

Hard coding this process into compilers is often considered very time consuming. Therefore, FEA software packages are commonly used. The pre-processor (or Graphical User Interface – GUI) of most finite element packages is where the user is able to develop and visualise their model before the simulation begins. Following the submission of the job, the software runs the simulation and outputs the results in the post-processor, from which the user can visualise and interpret the results through use of a variety of analysis tools. During the analysis steps, the solver tries to achieve convergence through fulfilling certain criteria e.g., achieving equilibrium between internal and external forces within specific thresholds. In this investigation, Abaqus CAE (Complete Abaqus Environment) was chosen as the GUI in which the tissue models would be developed. This choice was made based on the stability and compatibility of Abaqus CAE with the installed operating system relative to other tested programs.

3.2.3. Solvers

Abaqus CAE provides users with two solvers to choose from, Abaqus/Standard (Implicit) and Abaqus/Explicit. This section details the rationale behind solver selection using information provided from the Abaqus software and user manual[186,187]. Both solvers offer distinct advantages and disadvantages depending on the simulation requirements. Abaqus/Standard offers efficient solutions to slower, static or dynamic non-linear problems. Furthermore, quasistatic problems can also be conducted in Abaqus/Standard, where inertial effects are negligible for time-dependent material behavior. Abaqus/Explicit is the preferred choice for high-speed dynamic analysis of extremely non-linear problems. Typical examples involve high-speed stress wave propagation, applied vibrations, impact and material failure.

Following the application of mechanical loads, the displacements (and therefore deformations) of each element are calculated using its stiffness at each timestep. For implicit analysis, equilibrium is enforced between the externally applied load and internally generated reaction forces at every time step. To ensure accuracy and minimize the impact of errors, Abaqus employs stringent convergence criteria whereby the model will not converge to equilibrium if the force residuals and displacement corrections are greater than 0.5% and 1% respectively. Abaqus/Standard uses a second-order accurate, implicit Hilber-Hughes-Taylor rule by default and solves simultaneous nonlinear dynamic equilibrium equations using an incremental-iterative solution based on Newton's method, enabling variable time steps. These time-integration operators are unconditionally stable for linear systems. However, due to the inherent iterative approach utilized in the implicit method, there is often a larger computational cost associated with the implicit approach per time increment. Furthermore, due to the large numbers of iterations possible in an increment, disk space and memory usage can be large. On the other hand, through using explicit methods, no equilibrium is enforced, resulting in a conditionally stable methodology.

Abaqus/Explicit uses a second order accurate explicit integration scheme. Whilst Abaqus/Standard iterates to solve non-linear problems, Abaqus/Explicit solves the problem by explicitly advancing the kinematic state from the previous increment. Explicit methods use conditionally stable integration operators which can sometimes lead to impractically small-time steps, as they must be below a critical value to avoid divergence. This sometimes results in large computational expenditure. However, as no iterations or large simultaneous equations are involved, this is often less computationally expensive and takes up less storage than implicit methods (Figure 18). Furthermore, unlike in Abaqus/Standard, the solution is still affected by increment size, by increasing the number of solution steps (i.e., reducing the timestep size), the deviation from equilibrium can be controlled.

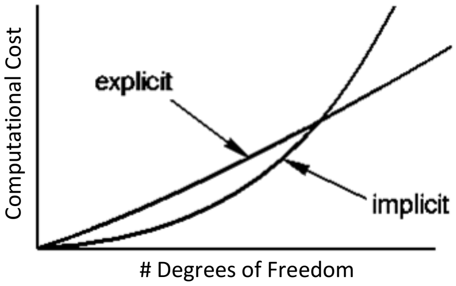

Figure 18: Graph depicting relationship between model complexity and computational cost for explicit and implicit solvers[186]*. Where the total number of degrees of freedom is equal to the product of the number of nodes within the model and the degrees of freedom per node.*

Therefore, choosing between implicit and explicit methods often involves choosing between fewer, larger increments (implicit) or many smaller time increments (explicit). Using Abaqus/Standard, computational cost is approximately equal to the square of the number of DoF. Disk space and memory requirements scale in a similar manner. Using Abaqus/Explicit, computational expenditure is proportional to the number of elements and inversely proportional to the smallest element dimension. In order to simulate skin-surface interaction on the receptor scale, the size of elements in this study would be small, potentially increasing overall expenditure through using explicit analysis.

Overall, as the applications of this study do not require high-speed dynamic analysis, Abaqus/Standard was used to simulate mechanical behavior in this thesis. Whilst this method offers unconditional stability, it is acknowledged that it may come at the expense of computational expenditure and storage.

3.3. Modelling Considerations

This section details the factors considered when choosing the elements that were applied to the model. The type of elements applied to the model geometry have a substantial effect on the way in which mechanical stimuli are propagated throughout the structure. Furthermore, this section will describe the different type of material models commonly used to describe the force – displacement relationship of the nodes within each finite element.

3.3.1. Element Selection

Approximations within FEA are assigned at the element level due to the properties of the elements themselves (e.g., shape functions) and mesh distributions within the structure. The global assembly and solution are exact. Therefore, element selection and distribution should be considered carefully.

3.3.1.1. Dimensionality

Abaqus CAE offers users a variety of two-dimensional and three-dimensional elements for users to choose from. Where possible, two-dimensional analysis is often preferred compared to three-dimensional analysis due to computational expenditure, which scales with the number of DoF and nodes included in the model. This reduction in dimensionality is often achieved through the use of axisymmetric, plane stress, or plane strain elements. This allows Abaqus CAE to simplify the model's geometry and still taking any boundary conditions into account, thereby reducing computational expenditure. Axisymmetric elements are typically used when there is rotational symmetry within the geometry, allowing the user to just simulate a cross-section of the geometry instead of the overall shape. Plane stress elements generally require users to enter a value for the thickness of the model that is typically much smaller than its height and width, thus stresses in the third dimension can be ignored. In contrast, the use of plane strain elements implies the direction normal to the plane is infinite and thus strain in the third dimension can be ignored.

3.3.1.2. Shape

For 2-dimensional analysis, triangular or rectangular element geometries are frequently chosen. Simple linear triangular elements possess 3 nodes, each with two translative degrees of freedom (DoF) in the x and y directions (Figure 19). These elements are frequently referred to as Constant Strain Triangles (CSTs), whose corresponding shape functions describe displacements varying linearly with respect to x and y. Therefore, the elemental strain (which is a derivative of the displacements with respect to direction), and thus stress, is constant throughout the element[185]. As a result, variations within the element are not possible to evaluate accurately.

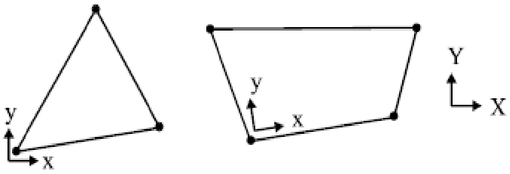

Figure 19: A linear triangular (left) and quadrilateral (right) elements[185].

Linear rectangular elements possess 4 nodes and two translative DoF in the x and y directions. In contrast to CSTs, their displacement (shape) function is bilinear, often referred to as in incomplete quadratic function with respect to x and y i.e. (C1 + C2 x + C3 y + C4 xy), where C_i are constants. Therefore, the strain function varies linearly with respect to direction and is non-constant. As a result, in general, rectangular elements perform better than triangular elements when analyzing higher order intra-element stress and strain fields. The main exception to this rule is when triangular elements may suit acute angles in a structure better than poorly shaped quadrilateral elements with high distortions or aspect ratios.

3.3.1.3. Order

Quadratic elements have at least twice as many nodes as their linear equivalents, this enables them to model non-linear deformations more easily at the cost of computational expenditure (Figure 20). This is done by increasing the order of the shape functions with respect to their displacement in the x and y directions.

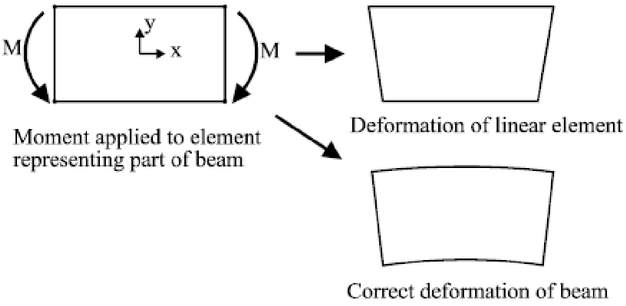

Figure 20: Quadratic elements are capable of non-linear deformations[185].

Quadratic triangular elements possess 6 nodes and two translative DoF in the x and y directions (Figure 21). The increase in shape function order enables non-constant stresses and strains to be interpreted across the element. However, as with linear elements, the quadratic quadrilateral elements are able to simulate displacements of a higher order with respect to direction (quadratic in both x and y). These elements possess 8 nodes and two translative DoF in the x and y directions.

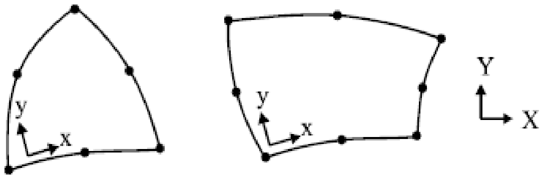

Figure 21: Quadratic triangular (left) and rectangular (right) elements[185].

3.3.1.4. Other Selection Criteria

As only a limited number of polynomial coefficients are used within the shape functions to describe the displacement field, elements are often slightly stiffer than intended, resulting in the underestimation of displacement. Therefore, by not performing the full integration (often referred to as “reduced integration”, these elements are artificially softened.

It is not possible to solve FE problems for fully incompressible materials (Poisson’s ratio = 0.5) as the application of hydrostatic stresses will cause no change in volume and thus no change in nodal displacement. When a nearly incompressible element (Poisson’s ration > 0.475) is exposed to hydrostatic stresses, it will experience negligible change in volume and thus negligible nodal displacement. The element thus behaves with a higher stiffness in response to hydrostatic stresses, known as volumetric locking. Therefore, for nearly incompressible materials, nodal displacements are only be used to calculate deviatoric stresses and strains, not the hydrostatic components. For extreme values of Poisson’s ratio (v > 0.4999), very small changes in nodal displacement can produce very large changes in pressure, therefore a purely displacement-based solution is too sensitive to be useful numerically as simple computer rounding errors can cause the method to fail. Hybrid elements provide additional degrees of freedom to describe the pressure variation over nearly and fully incompressible elements directly, enabling the evaluation of the overall stress state of the element. Whilst this helps avoid volumetric locking by establishing the stress state using methods that are independent nodal displacements the additional degrees of freedom result in the elements being more computationally expensive. Further details of hybrid elements and the formulation of their additional degrees of freedom can be found in literature[188–190].

3.3.2. Material Behaviour

Finite Element Analysis (FEA) is an efficient tool to model and visualise the local subsurface stress and strain levels within the tissue[191]. Numerical models of soft tissue typically differ in scale and complexity. The following section describes common material models used to characterise the stress-strain response of skin using theory from undergraduate courses[192], user manuals[187,193], and literature[194,195].

3.3.2.1. Linear Elasticity

Linear elastic models are amongst the simplest of the constitutive models in which the stiffness, (described by the Elastic or Young’s Modulus, E) is characterized by the quotient of stress and strain (denoted σ and ε respectively).

$$E = \frac{\sigma}{\varepsilon} \qquad \textbf{\textit{Eq. 1}}$$

Similarly, the shear modulus can be described by:

$$G = \frac{\tau}{\gamma} = \frac{E}{2(1+v)} \qquad \textbf{\textit{Eq. 2}}$$

Where:

- τ is the shear stress
- γ is the shear strain
- v is the Poisson (contraction) ratio

Due to their simplicity, linear elastic data is easily extracted from simple mechanical tests and is thus abundant in existing research. However, it is known that within soft tissue, stress does not vary linearly within strain, prompting the use of more complex models.

3.3.2.2. Hyperelasticity

In continuum mechanics, linear elasticity can be encompassed by the infinitesimal strain theory, in which the deformation of solid body involves the displacement of a material's particles being substantially smaller than the dimensions of the body itself. However, soft tissues (which are highly incompressible) frequently undergo more complex, larger, non-linear deformations that are better analysed through the use of hyperelastic models, encompassed by the finite (or large) strain theory. These hyperelastic models are characterised by strain energy density equations and are conservative, thus assuming that deformations are fully recovered upon unloading[51,53,194–196]. The strain energy functions represent the energy per volumetric unit stored in the material upon deformation. To derive these strain energy functions from first principles, it is first necessary to consider the deformation gradient, F, sometimes referred to as Jacobian matrix of deformation. The deformation gradient is a tensor that is a function of both spatial and temporal variables and is used to describe the deformation of a body in the current configuration (x) relative to that in the initial or reference configuration (X).

$$F = \frac{\partial x}{\partial X} \qquad \textbf{\textit{Eq. 3}}$$

The left (C) and right (b) Cauchy-Green deformation tensors can be subsequently defined as:

$$C = F^T . F \qquad \textbf{\textit{Eq. 4}}$$

$$b = F . F^T \qquad \textbf{\textit{Eq. 5}}$$

The first two invariants of the deviatoric component of the left Cauchy-Green deformation tensor (*C*) are frequently used to derive the strain energy potential (*U*) equations that characterise the behaviour of hyperelastic materials. The third invariant is used less frequently. These invariants are defined by:

$$I_1 = tr(C) = {\lambda_1}^2 + {\lambda_2}^2 + {\lambda_3}^2 \qquad \textbf{\textit{Eq. 6}}$$

$$I_2 = \frac{1}{2}\left(tr(C)^2 - tr(C^2)\right) = {\lambda_1}^2{\lambda_2}^2 + {\lambda_2}^2{\lambda_3}^2 + {\lambda_1}^2{\lambda_3}^2 \qquad \textbf{\textit{Eq. 7}}$$

$$I_3 = det(C) = (\det(F))^2 = J^2 = {\lambda_1}^2{\lambda_2}^2{\lambda_3}^2 \qquad \textbf{\textit{Eq. 8}}$$

Where λ represents the principal stretches of the tested material and J is the volume ratio and is the product of the three principal stretches. Four popular polynomial strain energy models are the Neo-Hookean, Mooney Rivlin, Yeoh and Ogden models[50]. The Neo-Hookean model (***Eq. 9***) is contingent on only one stress invariant from the left (material) Cauchy-Green deformation tensor. Its strain energy density equation is the simplest out of the three models, however, the model is only valid for small to moderate strains[196,197]. The Neo-Hookean potential represents the Helmholtz free energy of a molecular network with Gaussian chain-length distribution[187]. The model is frequently used for stiffer layers of the skin and the matrix for more complex biological structures.

$$U = C_{10}(I_1 - 3) + \frac{1}{D_1}(J-1)^2 \qquad \textbf{\textit{Eq. 9}}$$

Where C_{10} is a material property relating to the Gaussian mechanics of chains and is thus correlated with the shear modulus μ. D_1 is inversely related to K (the bulk modulus) and thus is correlated with compressibility. Increasing in complexity, the Mooney-Rivlin model (***Eq. 10***) is based on two stress invariants and is able to more accurately describe the responses to higher strains (up to 200%)[28,197]. The second invariant is particularly important when modelling plasticity. The Mooney Rivlin has been proven to demonstrate a high degree of accuracy with isotropic rubber-like material and can be defined as:

$$U = C_{10}(I_1 - 3) + C_{01}(I_2 - 3) + \frac{1}{D_1}(J-1)^2 \qquad \textbf{\textit{Eq. 10}}$$

Where the linear elastic shear modulus $\mu = 2(C_{10}+C_{01})$. Presently, research has not focussed on the plastic deformation of tissue, furthermore, the 2nd invariant has proven to be typically harder to obtain for elastomers than the 1st [198].

As a result, the Yeoh model (***Eq. 11***) is often used for soft tissue, whose behaviour is characterised by a third order strain energy equation based purely on the 1st invariant[199]. A disadvantage of the model is that more material parameters are required. After obtaining the required material parameters, the model can then be fitted to experimental data to provide a more accurate fit than the former two models. The strain energy potential is described by[6]:

$$U = \sum_{i=1}^{N} C_{i0}(I_i - 3)^i + \sum_{i=1}^{N} \frac{1}{D_i}(J - 1)^{2i} \qquad \textbf{Eq. 11}$$

Where *N,* defines the number of terms or order of the Yeoh model. This model has been frequently applied to biological tissues, however, data on human skin has been found to be scarce compared to the Ogden model[50] (***Eq. 12***). The Ogden model may be simplified into the Neo-Hookean or Mooney-Rivlin model; however, more complex forms are often used[187]. Whilst the former models make use of the invariants of the deformation tensor, the Ogden model makes direct use of the principal stretches of the material to describe the changes in these stretches from reference to the current orientation[200]. When fitted to test data, the Ogden model provides a better fit on the stress-strain curve across a larger strain range when compared to the Neo-Hookean and Mooney-Rivlin models (Figure 22)[197,201,202]. However, it should be noted that data from more than one mode of testing (e.g., compression, uniaxial tension etc.) is required to uniquely fit the model[203]. The strain energy potential is given by:

$$U = \sum_{i=1}^{N} \frac{2\mu_i}{{\alpha_i}^2}({\lambda_1}^{\alpha_i} + {\lambda_2}^{\alpha_i} + {\lambda_3}^{\alpha_i} - 3) + \sum_{i=1}^{N} \frac{1}{D_i}(J - 1)^{2i} \qquad \textbf{Eq. 12}$$

Where μ relates to shear modulus and α relates to the degree of non-linearity of the stress strain curve.

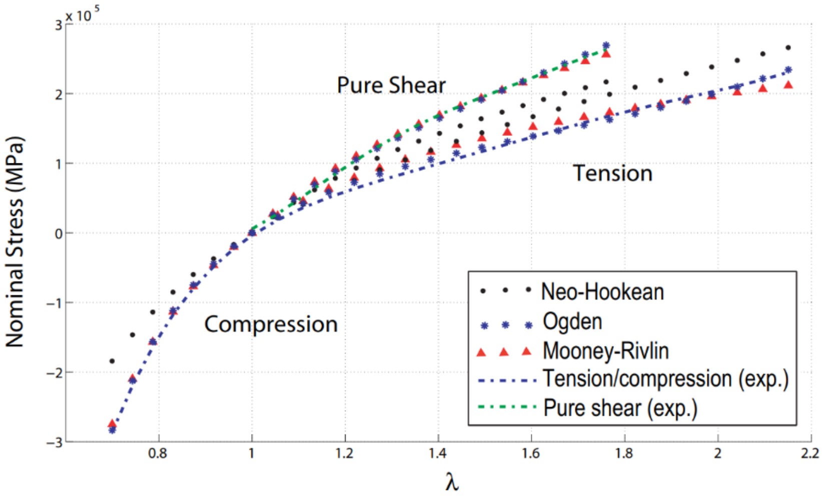

Figure 22: Nominal stretch vs. strain data and models for the uniaxial compression, tension and pure shear of rubber-like polymers[202].

The advantages and disadvantages of each model are summarised in (Table 1).

Table 1: A summary of the advantages and disadvantages of each hyperelastic model.

Model	***Advantages***	***Disadvantages***
Neo-Hookean	• A relatively simple model • A lot of human skin data available in literature	• Cannot accurately model non-linear behaviour at high strains
Mooney-Rivlin	• Can model non-linearity to higher strains than Neo-Hookean	• Data on human skin more scarce than Neo-Hookean • Requires the 2nd stress invariant • Model can be unstable at finite strains in different loading modes[198]
Yeoh	• Shown to model non-linear behaviour accurately within a wide range	• Data on human skin scarce • Requires 4+ material properties
Ogden	• Models non-linearity accurately over a wide range • Skin data more abundant than Yeoh Model	• Requires data from at least two modes of loading

3.3.2.3. Time-dependent Behaviour

Time dependent material models describe the temporal behaviour of materials in response to the application of mechanical stimuli. There are different models used to characterise the time dependent material behaviour of skin, such as poroelastic and viscoelastic material models. Poroelasticity describes the relationship of fluid flow within a solid and the solid's deformation and mechanical properties. However, viscoelastic skin models are more commonly used to help characterise the time-dependent behaviour of skin and describe how materials exhibit dissipative losses primarily caused by internal damping and characteristically exhibit one or more of the following mechanical responses[204]:

- Stress-strain hysteresis – dependence on prior loading conditions
- Stress relaxation – decreasing stress with constant applied strain
- Creep – increasing strain for a constant applied stress
- Rate dependent modulus – stiffness is a function of strain or stress rate

Describing Viscoelastic Behaviour

Viscoelasticity is commonly described by decomposing material behaviour into its deviatoric and volumetric or hydrostatic responses. For small strains the time-dependent shear stress, $\tau(t)$, is defined as[187]:

$$\tau(t) = \int_0^t G_R(t-s) \cdot \dot{\gamma}(s)\, ds \quad \textbf{\textit{Eq. 13}}$$

Where, $G_R(t)$, is the time-dependent shear relaxation modulus and $\dot{\gamma}$ is the time-dependent shear strain rate applied to the material. The dimensionless shear relaxation modulus is obtained from the following:

$$g_R(t) = \frac{G_R(t)}{G_0} \quad \textbf{\textit{Eq. 14}}$$

Where G_0 is the instantaneous shear relaxation modulus. Therefore, ***Eq. 13*** may be written as:

$$\tau(t) = G_0 \int_0^t g_R(t-s) \cdot \dot{\gamma}(s)\, ds \quad \textbf{\textit{Eq. 15}}$$

For larger strains, ***Eq. 15*** can be integrated by parts and rearranged to obtain:

$$\tau(t) = \tau_0(t) - \int_0^t \dot{g}_R(s) \cdot \tau_0(t-s)\, ds \quad \textbf{\textit{Eq. 16}}$$

Similar derivations for bulk material properties yield the time-dependent volumetric response for viscoelastic materials:

$$p(t) = -K_0 \int_0^t k_R(t-s) \cdot \dot{\varepsilon}^{vol}(s)\, ds \quad \textbf{\textit{Eq. 17}}$$

Where:

- $p(t)$ is the time dependent hydrostatic or volumetric stress
- K_0 is the instantaneous bulk modulus
- k_R is the dimensionless bulk relaxation modulus
- $\dot{\varepsilon}^{vol}$ is the volumetric strain rate

Measuring Viscoelasticity

In order to experimentally study viscoelasticity dynamic mechanical analysis (DMA) is often used, in which sinusoidal or vibratory loads are applied to a material whilst any extension or displacement is measured. This enables the calculation of the dynamic (or complex) modulus.

For strains applied to viscoelastic solids:

$$\varepsilon(t) = \varepsilon_0 \sin(\omega t) \quad \textbf{\textit{Eq. 18}}$$

$$\sigma(t) = \sigma_0 \sin(\omega t + \delta) \quad \textbf{\textit{Eq. 19}}$$

Where:

- ω is the frequency of strain oscillation
- t is the time of applied strain
- δ is the phase lag between stress and applied strain

In the case of perfectly elastic solids:

$$\sigma(t) = E\varepsilon(t) \quad \textbf{\textit{Eq. 20}}$$

$$\sigma_0 \sin(\omega t + \delta) = E\varepsilon_0 \sin(\omega t) \quad \textbf{\textit{Eq. 21}}$$

Therefore, $\delta = 0$ and thus stresses and strains are perfectly in phase with one another.

However, in the case of a purely viscous substance:

$$\sigma(t) = K\frac{\delta\varepsilon}{\delta t} \quad \textbf{\textit{Eq. 22}}$$

$$\sigma_0 \sin(\omega t + \delta) = K\varepsilon_0\omega \cos(\omega t) \quad \textbf{\textit{Eq. 23}}$$

Therefore, stresses and strains are 90° out of phase. The storage modulus measures the stored energy within the elastic portion of the viscoelastic behavior, whilst the loss modulus represents the heat energy dissipated during the viscous portion. For tensile loading, the storage (E') and loss (E'') modulus and phase angle can be defined by:

$$E' = \frac{\sigma_0}{\varepsilon_0}\cos\delta \quad \textbf{\textit{Eq. 24}}$$

$$E'' = \frac{\sigma_0}{\varepsilon_0}\sin\delta \quad \textbf{\textit{Eq. 25}}$$

$$\delta = \tan^{-1}\left(\frac{E''}{E'}\right) \quad \textbf{\textit{Eq. 26}}$$

Therefore, the dynamic (or complex) tensile modulus (E*) can be defined as:

$$E^* = E' + iE'' = \frac{\sigma_0}{\varepsilon_0}(\cos\delta + i\sin\delta) = \frac{\sigma_0}{\varepsilon_0}e^{i\delta} \quad \textbf{\textit{Eq. 27}}$$

A similar expression can be derived for the shear storage (G') and loss (G'') moduli:

$$\frac{\tau(t)}{\gamma(t)} = \frac{\tau_0}{\gamma_0}\cos(\delta)\sin(\omega t) + \frac{\tau_0}{\gamma_0}\sin(\delta)\cos(\omega t) \quad \textbf{\textit{Eq. 28}}$$

$$\frac{\tau(t)}{\gamma(t)} = G' \sin(\omega t) + G'' \cos(\omega t) \qquad \textbf{\textit{Eq. 29}}$$

Where:

- $\tau(t)$ is the time dependent shear stress
- $\gamma(t)$ is the time dependent shear strain

Therefore, the dynamic shear modulus can be defined as:

$$G^* = G' + iG'' = \frac{\tau_0}{\gamma_0}(\cos\delta + i\sin\delta) = \frac{\tau_0}{\gamma_0}e^{i\delta} \qquad \textbf{\textit{Eq. 30}}$$

Kelvin-Voigt model

A common model to describe the viscoelasticity of polymers under loading is the Kelvin-Voigt model[205,206]. The elastic components of the model are described using springs whilst the viscous components are described using dashpots (Figure 23).

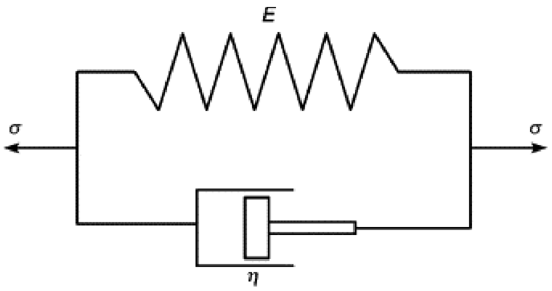

Figure 23: Kelvin-Voigt spring-dashpot system used to model viscoelasticity[207].

In this parallel system:

$$\varepsilon = \varepsilon_1 = \varepsilon_2 \qquad \textbf{\textit{Eq. 31}}$$

$$\sigma = \sigma_1 + \sigma_2 \qquad \textbf{\textit{Eq. 32}}$$

Where the numbers 1 and 2 refer to the spring and dashpot system respectively. The stress within dashpot models is proportionate to their strain rate and viscosity, η, therefore:

$$\sigma = E\varepsilon_1 + \eta\frac{\delta\varepsilon_2}{\delta t} = E\varepsilon + \eta\dot{\varepsilon} \qquad \textbf{\textit{Eq. 33}}$$

Solving this equation leads to an expression for time-dependent strain (Figure 24):

$$\varepsilon(t) = \frac{\sigma}{E}\left(1 - e^{\frac{-Et}{\eta}}\right) = \frac{\sigma}{E}\left(1 - e^{\frac{-t}{T}}\right) \qquad \textbf{\textit{Eq. 34}}$$

Where the viscoelastic time constant is given by:

$$T = \frac{\eta}{E} \qquad \textbf{Eq. 35}$$

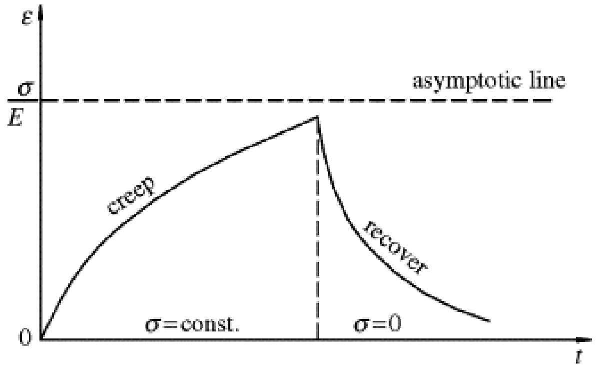

Figure 24: Strain-time graph of a Kelvin-Voigt material. Image adapted from Wang[208].

The model possesses a complex dynamic modulus equivalent to:

$$E^* = E' + iE'' = E_2 + i\eta\omega \qquad \textbf{Eq. 36}$$

Implementing Viscoelasticity into Abaqus

The Prony series is frequently used to describe the long and short-term viscoelastic effects on deviatoric (shear) and volumetric (bulk) material properties[186,187]. The time-dependent shear relaxation modulus, $G_R(t)$, can be defines as:

$$G_R(t) = G_\infty + \sum_{i=1}^{N} G_i \cdot e^{-\frac{t}{T_i}} \qquad \textbf{Eq. 37}$$

Where:

- G_∞ represents the long-term shear relaxation modulus
- N is the number of terms or order of the equation
- T_i are the characteristic relaxation times (or time constants) of the material

Furthermore, the instantaneous shear relaxation modulus, G_0, may be defined as:

$$G_R(t=0) = G_0 = G_\infty + \sum_{i=1}^{N} G_i \qquad \textbf{Eq. 38}$$

Combining ***Eq. 37*** & ***Eq. 38*** yields the time-dependent shear relaxation modulus as a function of its instantaneous value:

$$G_R(t) = G_0 - \sum_{i=1}^{N} G_i \cdot \left[1 - e^{-\frac{t}{T_i}}\right] \qquad \textbf{\textit{Eq. 39}}$$

Within Abaqus CAE, this equation is used in its dimensionless form to characterise deviatoric viscoelastic behaviour:

$$g_R(t) = g_0 - \sum_{i=1}^{N} g_i \cdot \left[1 - e^{-\frac{t}{T_i}}\right] \qquad \textbf{\textit{Eq. 40}}$$

Where g_i and T_i are material input parameters. g_0 is frequently normalised to 1. A similar Prony series expansion is used for the volumetric viscoelastic response, which is valid for small and large strain applications:

$$p = K_0\left(\varepsilon^{vol} - \sum_{i=1}^{N} \varepsilon_i^{vol}\right) \qquad \textbf{\textit{Eq. 41}}$$

These viscoelastic parameters are then applied to the coefficients of linear or hyperelastic functions or inserted into the functions directly in Abaqus CAE. For a first order (N=1) deviatoric Prony series curve described by ***Eq. 40***, in the short term ($t \ll T$) $g_R(t) = g_0$, whilst in the long term ($t \gg T$) $g_R(t) = g_0 - g_1$. Therefore, it was found that changing the time constant had greater influence on the concavity of the curve, whilst changes in changes in g_1 have a more dominant effect on the long-term relaxation value and thus the x-asymptote (Figure 25).

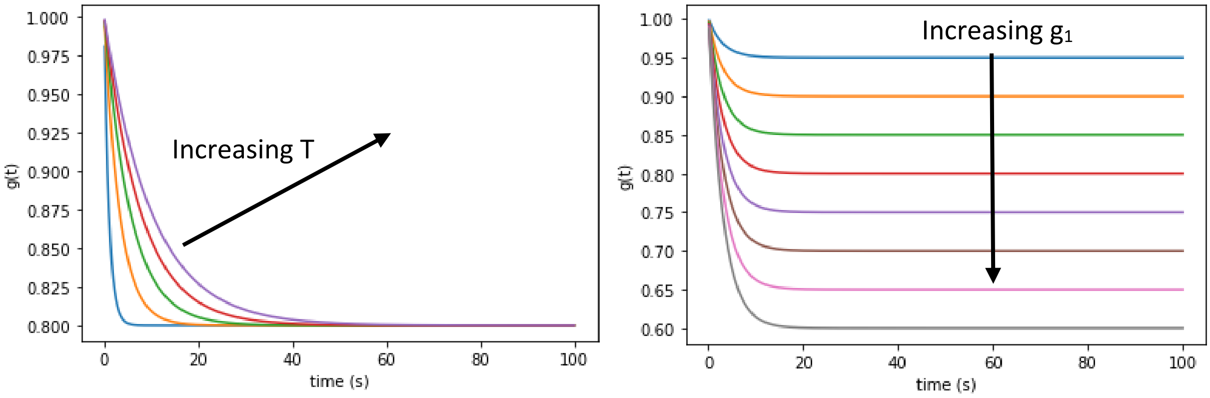

Figure 25: The effect of altering the material input parameters (time constant - left, dimensionless shear modulus - right) on the dimensionless time-dependent shear relaxation modulus of the first order Prony series.

Overall, element and material model selection have a large influence on our ability to accurately model the skin's complex mechanical performance. Existing materials models have proven capable of describing the stress-strain response of skin accurately within finite strain intervals and are described in the next section.

3.4. Finite Element Skin Models in Literature

This section aims to summarise existing skin models in literature. The geometry and material behaviours utilized within these finite element simulations differ in complexity. Microscale models offer an advantage over macroscale models as they enable the observation of stimulus propagation on the receptor level, in order to better understand tissue response and tactile perception. Whilst there is much research on the numerical modelling of skin, few models are solely based on humans, with many models making use of experimental data from other species (e.g., rats and pigs) in order to develop or validate their models. Even fewer investigations have focussed on the skin of the fingertip and face, many focus on other easily-testable anatomical regions of the body e.g. forearms[52,172,209]. Of the literature on the numerical modelling of skin, many of these focus on material characterisation and do not extend to changes in the structure and geometry of the skin[210,211]. Many of these studies have characterised skin homogenously or as linearly elastic. For the fingertip, few, more complex hyperelastic models exist both on the micro and macro-scale to help better characterise non-linear tissue response[3,4]. Complex material models of facial tissue are not as abundant as they are for the fingertip.

When modelling soft tissue, researchers typically choose between single-layered or multi-layered models, depending on the outcome they require. Phenomenological models are typically homogenous (i.e., single layered) and are used to characterise the overall behaviour of the skin to an external force. Structural models treat skin as a composite-like heterogenous solid. This can help explicitly characterise the interactions between each of the layers. Single layer skin models have been created using different hyperelastic equations (e.g., Mooney Rivlin, Figure 26).

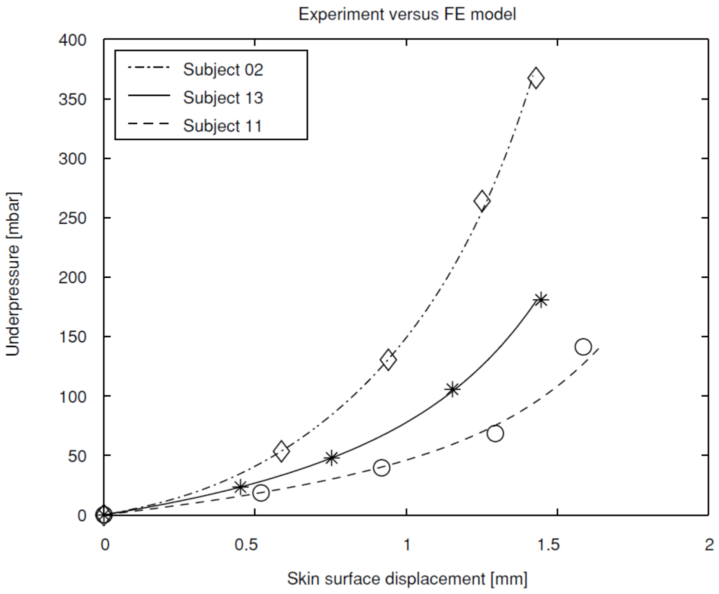

Figure 26: Mooney-Rivlin models (lines) simulating experimental data (shapes) obtained from three subjects during a skin suction test[210].

Many recent models have used Ogden parameters to characterise the skins behaviour (Table 2). The coefficients and exponents used show a wide range.

$$U = \sum_{i=1}^{N} \frac{2\mu}{{\alpha_i}^2}({\lambda_1}^{\alpha_i} + {\lambda_2}^{\alpha_i} + {\lambda_3}^{\alpha_i} - 3) + \sum_{i=1}^{N} \frac{1}{D_i}(J-1)^{2i}$$

Table 2: Ogden coefficients and exponents used to characterise human skin as a homogenous material.

μ_1 (kPa)	**α_1**	**μ_2 (kPa)**	**α_2**	**Primary Author**	**Year**
110	9			Shergold[212]	2004
49.8	2.1	0.0003	35.24	Flynn[213]	2013
0.008	10			Oomens[172]	2011
0.01	40			Manan[214]	2012
0.01	110			Mahmud[215]	2012

Regarding multi-layered models, due to the relative linearity of the stiffer layers of the skin compared to the dermis and hypodermis, many studies are able to characterise the mechanical behaviour of the stratum corneum and epidermis with a Neo-Hookean function (Figure 27). Note that some of these values at small strains were calculated via the use of linear elastic parameters (Youngs' Modulus and Poisson's ratio)[26]. When derived from experimental results, these values can differ significantly (Table 3).

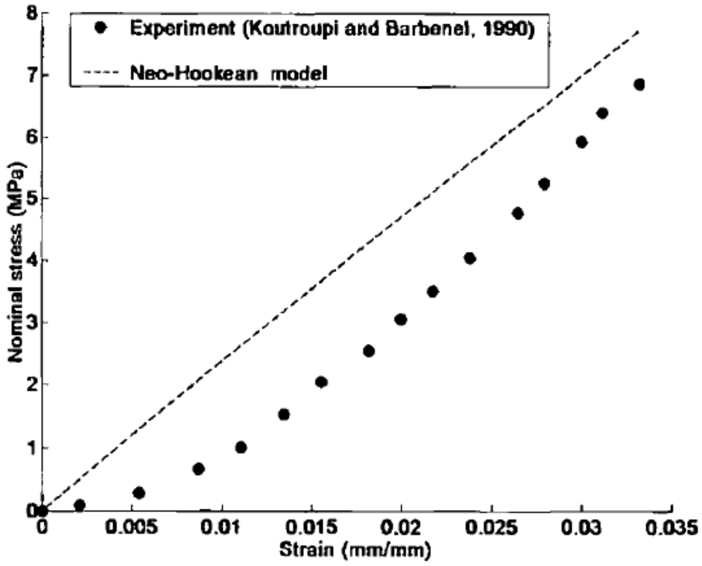

Figure 27: Neo-Hookean model[27] plotted against experimental uniaxial tensile data of the human stratum corneum[216].

Table 3: Neo-Hookean coefficients obtained from the stratum corneum and the viable epidermis.

	C10 (MPa)	***D1 (MPa^{-1})***	***Primary Author***	***Year***
SC	0.115	4.000	Geerligs[217]	2011
	0.231	2.000	Geerligs	2011
	1.003	0.010	Magnenat-Thalmann[218]	2002
	1.923	0.240	Lévêque[219]	2013
	2.007	0.005	Magnenat-Thalmann	2002
	2.596	0.178	Wu[220]	2006
	2.500	0.185	Delalleau[221]	2007
	11.115	0.042	Delalleau	2007
	19.231	0.024	Delalleau	2007
	33.712	0.014	Wu	2006
	192.308	0.002	Delalleau	2007
VE	0.000	4,195.804	Hendriks[210]	2006
	0.010	48.000	Lévêque	2013
	0.008	1.200	Magnenat-Thalmann	2002
	0.008	1.200	Magnenat-Thalmann	2002
	0.115	4.000	Geerligs	2011
	1.500	0.308	Delalleau	2007

For less stiff, highly non-linear soft tissues such as the dermis and hypodermis, Ogden models are more frequently used. For example, Boyle fitted a two parameter Ogden model to compression and simple shear data to obtain exponents and coefficients for each layer of plantar foot skin (Table 4)[5,172,222].

Table 4: The mechanical properties of plantar foot-skin[5].

Layer	***Modulus (kPa)***	***Exponent***
Hypodermis	25	5
Dermis	2.55	-14.53
Viable Epidermis	61.75	-14.53
Stratum Corneum	86.76	-14.53

Overall, finite element models have proven useful in characterizing the stress-strain behaviour of skin in specific applications. Due to the complexity of the skin and how much its properties vary between individuals, almost all models make use of simplifications when characterizing both the geometry of the skin, and its mechanical response. When used properly, multi-layered, non-linear, time-dependent models have the potential to simulate the behavior of skin more accurately than simpler models.

3.5. Model Development

This section contains work that has been published by Jobanputra et al in a peer reviewed journal[223]*.*

Finite element models of the finger and facial tissues were required in order to simulate the tactile perception of textures and cosmetics. In this chapter, the development of the finger skin model used in Investigations 1 – 3 is detailed here, whilst any additional investigation specific models are detailed in their respective chapters.

The purpose of the finger skin model was to simulate the propagation of mechanical stimuli to the sites of the Type 1 mechanoreceptors in order to simulate fine (high spatial resolution) touch. The model was developed in ABQUS CAE and run using the implicit solver via Full Newton numerical integration due to its stability and convergence rate. Biologically, skin layers have complex geometries that are highly variable between individuals. Therefore, a mechanical representation was used in this investigation in order to perform parametric studies on the skin's geometric, material and interfacial properties. Furthermore, because skin is highly individualized, the use of a parameterized model enables generation of more wide-ranging conclusions.

Challenges regarding the accurate validation of finite element models simulating tactile perception on the receptor level include the need for invasive studies on living tissue and the balance of penetration depth and resolution associated with different optical methods (e.g., OCT, ultrasound). Furthermore, presently no clear link has been made between the mechanical response of the skin, the neurological response of the receptors and individual's psychological or behavioral response. Therefore, the purpose of the model was to establish the effects and trends of the various skin and surface alterations on the stimuli magnitudes recorded at the Type 1 receptor sites, rather than attempting to obtain biologically exact values.

In order to improve accuracy, implement the vastly different geometric and material properties of different skin layers and the different ways in which phenomena such as ageing affect them, a multi-layered finite element model was developed. Anisotropic data for each layer of skin is scarce in literature and can only be established via *in vivo* studies. Additionally, the data is likely to be highly variable depending on anatomical site and subject. Therefore, an isotropic model was developed, thus inherently assuming there is no significant change in material properties with respect to direction.

In order to examine the stress-state of the microscale mechanoreceptors, which were to be embedded in a millimetre scale skin mode, many small elements would be required. It is known that simulation time scales in proportion to N^x, where N is the number of nodes within the model and $x > 1$. Therefore, a 3D dimensional model would possess substantially more elements and nodes than a 2D model, and thus take substantially longer to solve. As a result, 2-dimensional model was developed to reduce computational expenditure. Furthermore, due to the parameterized nature of the model, a three-dimensional model would still be unable to model skin layer inhomogeneity on the microscale. Therefore, 2D plane strain finite elements are used to simulate the thickness of the skin, thereby assuming no significant change in material, geometric and interfacial property occurs with depth. Due to the incompressibility of the skin and to avoid volumetric locking, hybrid, reduced integration elements were used.

The model is schematically shown in Figure 28 and consists of the stratum corneum (SC), the viable epidermis (VE), the dermis (D) and the subcutaneous tissue (S). The model geometry was developed as a single geometry before being partitioned into individual skin layers with assigned material properties, thus simulating perfect adhesion between the layers. This assumption was made as delamination of the skin layers during skin tearing or blister formation is outside the scope of this thesis. Biologically, interlayer junctions in the skin are irregular waveforms, whilst in the model they are parameterized as regular waveforms with amplitudes and wavelengths taken from literature[2,5,29–32]. Reported values for the thickness of the stratum corneum range from 130 to 795 µm[5,224,225], and a mid-range value of 425 µm was implemented into the model. In palmoplantar skin, the viable epidermis is relatively thin compared to the stratum corneum and was modelled with a thickness of 175 µm[5,224]. The dermis was modelled with a thickness of 1.4 mm[4,93], supported by a 1 mm subcutaneous tissue layer that provides a compliant boundary condition for the dermis by representing underlying tissue[4,93,210]. The model was made 14.4 mm wide in order to mitigate any edge effects on the centre of model, where analysis was to be done, and allow complete interlayer junction wavelengths to form. The dimensions are summarised in Table 5 and Table 6.

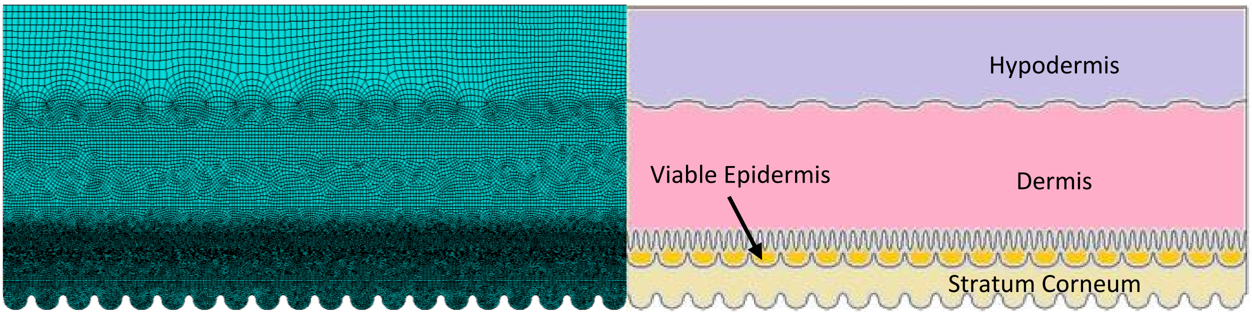

Figure 28: The mesh (left) and geometry (right) of the developed numerical finger skin model.

Owing to the high degree of non-linearity attributed to the deeper layers of the skin, the mechanical response for each layer was characterised using a first order Ogden model (shown below), for which the full strain energy potential is described by ***Eq. 12***[198,202]. The coefficients were obtained from experiments on plantar foot skin by Boyle et al[5] and are summarized in Table 5.

$$U = \frac{2\mu_1}{{\alpha_1}^2}({\lambda_1}^{\alpha_1} + {\lambda_2}^{\alpha_1} + {\lambda_3}^{\alpha_1} - 3) + \frac{1}{D_1}(J - 1)^2$$

In which:

- λ represents the material's principal stretches
- J is the volume ratio is equivalent to the product of the three principal stretches
- D_1 is a material parameter that defines compressibility
- μ_1 is the Ogden shear modulus
- α_1 is the Ogden exponent and relates to the degree of non-linearity of the stress-strain curve

Viscoelastic parameters were implemented in Abaqus CAE via a second order Prony series (***Eq. 40*** and expanded below) from data used by Wu et al[62,187] in tactile perception simulations. These values were determined by fitting constitutive models to the stress-strain relationships and stress relaxation curves of skin obtained from experimental data[226–228] and are summarized in Table 5. This was implemented into the finger skin models in Chapter 5 and Chapter 6 to enable it to more accurately respond to the complex, time-dependent loading conditions associated with rough surface contact (5. Effect of Surface Textures on Tactile Perception) and a deforming counter surface or substrate in the form of facial tissue (6. Investigating the Effects of Cosmetic Polymer Film Properties on Tactile Perception).

$$g_R(t) = g_0 - g_1 \cdot \left[1 - e^{-\frac{t}{T_1}}\right] - g_2 \cdot \left[1 - e^{-\frac{t}{T_2}}\right]$$

Where:

- $g_R(t)$ is the time-dependent dimensionless shear relaxation modulus
- g_0 is the initial dimensionless shear relaxation modulus, usually normalised to 1
- g_i is the dimensionless shear relaxation modulus of the material
- T_i are the characteristic relaxation times of the material

The geometric and material parameters of the model are summarised in Table 5 and Table 6.

Table 5: Model skin layer characteristics and material properties[5,62].

Skin Layer	**Thickness (µm)**	**µ (kPa)**	**α (-)**	**g_1**	**$T_1(s)$**	**g_2**	**$T_2(s)$**
Subcutis (S)	1,000	25	5	0.2566	0.3834	0.2225	4.6731
Dermis (D)	1,400	2.55	-14.53	0.0864	0.2136	0.2136	8.854
Viable Epidermis (VE)	175	61.75	-14.53	0.0864	0.2136	0.2136	8.854
Stratum Corneum (SC)	425	86.76	-14.53	0.0864	0.2136	0.2136	8.854

Table 6: Waveform dimensions of the interlayer junctions.

Junction	Peak to peak amplitude (μm)	Wavelength (μm)
S-D	75	720
D-VE	200	120
VE-SC	150	360
Fingerprint Ridges	150	360

Choosing the shape and order of elements within a mesh is critical in finite element modelling. In Abaqus/Standard's 2D element library, quadrilateral, quadratic elements offer higher stability and are able to model higher order deformations than constant strain triangles. This is due to their inherent shape functions and the number of nodes they possess. However, it is worth noting that this comes at a cost of increased computational expenditure. Quadratic, quadrilateral, hybrid plane strain finite elements (CPE8RH) were chosen to populate the geometry (Figure 29A).

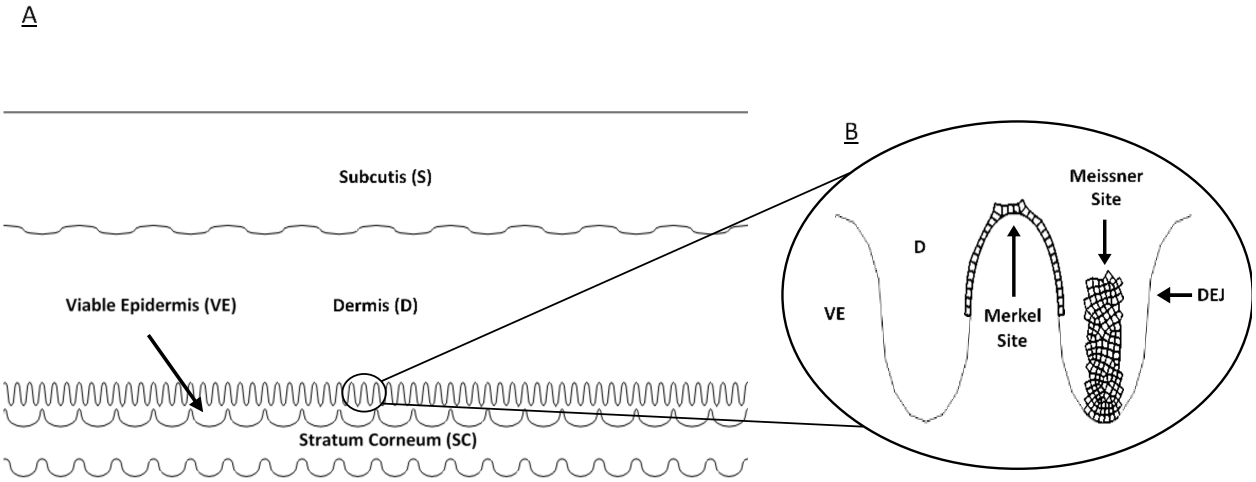

Figure 29: Schematic diagram of the numerical skin model developed (A) and the DEJ (B – inset) illustrating the Merkel and Meissner sites where the stress, strain and SED were recorded during the investigation.

In order to improve computational efficiency without compromising model accuracy, a convergence study was performed to optimize the mesh distribution. In this study, the skin model was compressed and translated against a rigid, flat counter surface. This convergence study involved independently altering the number of elements within each skin layer whilst the deviatoric stress was measured within elements in the outer, middle and inner regions of the layer along the central axis (Figure 30). Inner refers to increasing depth of the skin (towards the base of the hypodermis), whilst outer refers toward the exterior of the model (towards the edge of the stratum corneum).

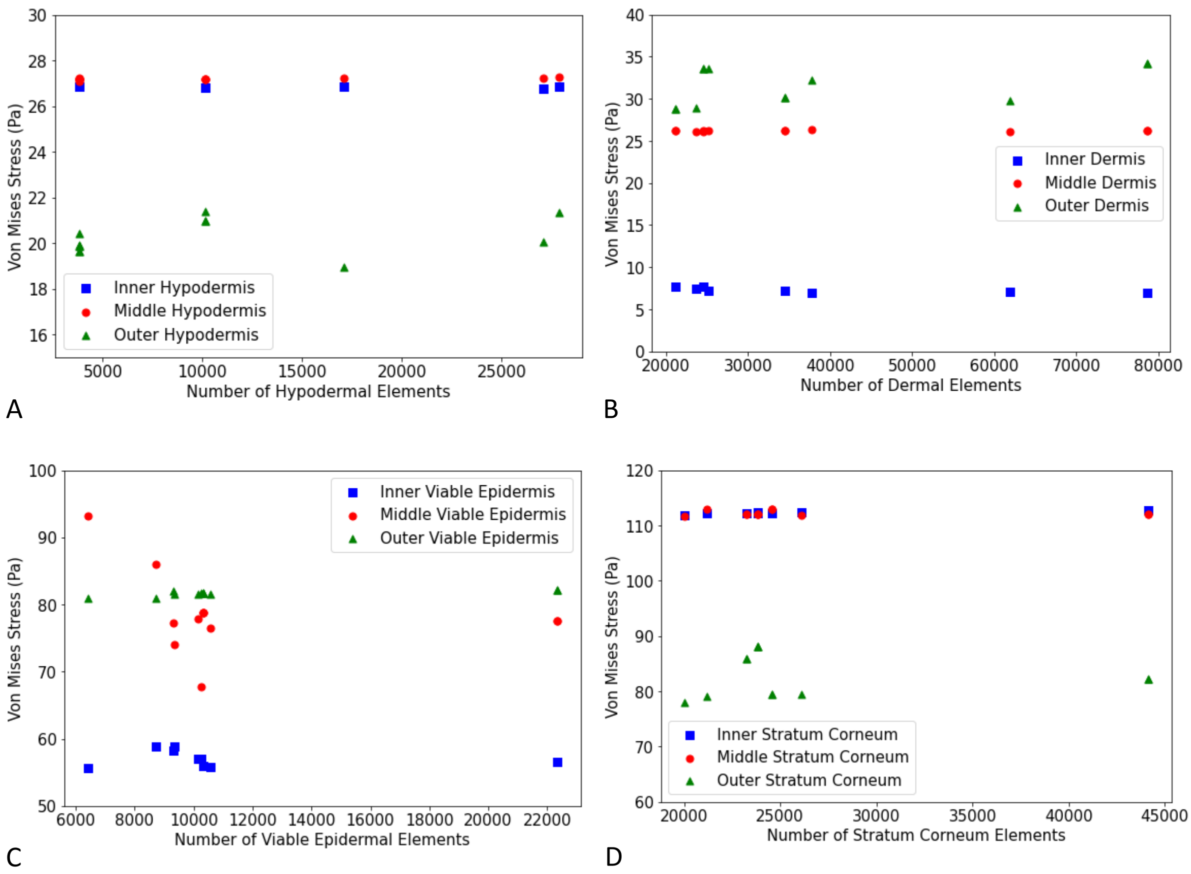

Figure 30: Convergence studies performed on (from innermost to outermost) the hypodermis (A), dermis (B), viable epidermis (C) and stratum corneum (D).

From Figure 30A, it was found that changes in the number of elements between the 3,825 and 27,857 had negligible effect on stresses in the inner and middle of the hypodermis, whilst only having a modest effect on the outer hypodermis. Therefore, only 5,865 elements were required. Whilst changes in mesh density had negligible effect on the inner and middle dermal von mises stress (Figure 30B), small fluctuations were experienced at the outer dermis within the vicinity of the Type 1 dermal mechanoreceptor sites, where the results of the simulations will be extracted from (Figure 29B). Therefore, in order to increase sensitivity in the region, mesh refinement was performed in the region, leading to decrease the local seed size to 7.5 µm. This smaller mesh size better represents the volume of the mechanoreceptor sites and provides a satisfactory compromise in terms of accuracy and computational resources. A total of 38,194 dermal elements were included in this layer in order to balance accuracy with computational efficiency.

With respect to the viable epidermis (Figure 30C), it was found that increasing the number of elements from 6,399 to 10,574 generally resulted in decreases in stress at the middle of the layer. In order to ensure the model was able to more accurately output the correct stresses within the viable epidermal skin layer, the number of elements was doubled to over 22,000. This was done to test for a lower bound value. However, it was found that doubling the element number did not lead to any substantial difference in the stresses recorded within the layer. Due to the refinement in seed size at the dermal epidermal junction (Figure 29B), the total number of elements in the viable epidermis was 24,071. There was no significant change in inner or outer epidermal stresses following mesh refinement. Finally in the stratum corneum (Figure 30D), initial increases in the number of elements to approximately 25,000 yielded little change in the stresses observed within the skin layer. Therefore, to test an extreme value, the number of elements was increased to almost 45,000, after which the stratum corneum still experienced similar stress levels. Therefore 25,934 were implemented into the layer to ensure compatibility with adjacent layers and follow the skin layer’s contours. For each layer, the number of elements is summarized in Table 7.

Table 7: The number of elements allocated to each layer of the finger skin model.

Layer	***# Elements (CPE8RH)***
Hypodermis	5,865
Dermis	38,194
Viable Epidermis	24,071
Stratum Corneum	25,934

3.6. Conclusion

This chapter details the background theory and rationale concerning the development of a computational finger skin model designed to help us better understand our sense of fine touch. In Abaqus CAE, a 2-dimensional, parametrized finite element model was developed in order reduce computational expenditure and enable the conduction of parametric studies on the finger skin's geometric and material properties. As in reality the skin is highly individualized, a parameterized model gives the opportunity to form more wide-ranging, generalized conclusions on the isolated effects of exposing the skin to biological, mechanical and environmental changes on tactile perception. The multi-layered model was prescribed with hyperelastic and viscoelastic material properties in order to more accurately simulate the mechanical behavior of the finger skin. This model will be used to evaluate the effect of skin ageing (4. Investigating the Effect of Biomechanical Skin Ageing on Tactile Perception), surface topography (5. Effect of Surface Textures on Tactile Perception) and cosmetic film properties (6. Investigating the Effects of Cosmetic Polymer Film Properties on Tactile Perception) on the excitation of the Type 1 (high spatial resolution) mechanoreceptors.

4. Investigating the Effect of Biomechanical Skin Ageing on Tactile Perception

This section contains work that has been published by Jobanputra et al[223].

4.1. Introduction

The two primary objectives of this study were to:

- Test the developed finger skin model against rigid flat surfaces.
- Better understand the relationship between age-related biomechanical skin changes and tactile perceptive degradation amongst the elderly.

Currently, to the best of our knowledge, there exists no ageing-related, microscale numerical skin model that focuses on varying the tissue geometrical and mechanical properties in order to describe the effect on perception. A better understanding of the relationship between the geometric and mechanical properties of the skin and tactile perception, and how touch deteriorates with age, would provide insight into possible pathways for more efficient mechanotransduction and help counteract tactile degradation. This chapter details how ageing manifestations were implemented into the model, and how these changes affect stimuli magnitudes at the sites of the high resolution, fine touch mechanoreceptors (Merkel and Meissner Receptors). The use of the model as a tool to assist the development of measures aimed at preserving and enhancing tactile sensation will be discussed. These measures include targeted skin treatments and the design of specific surface textures for optimised mechanoreceptor stimulation.

4.2. Methods

4.2.1. Simulating Skin Ageing

Material and geometric changes associated with ageing skin manifest themselves by changes to the stiffness of the various skin layers, thinning of the dermis and the flattening or decreasing tortuosity of the DEJ. Changes to the skin layer stiffnesses were modelled independently by incrementally increasing the Ogden shear modulus μ from half that of the reference model to 150%. The dermis is the thickest layer in the skin and the thickness was reduced incrementally to half the thickness of the reference model, this represents an approximate 20% decrease of the thickness of the entire skin[76]. Table 3 provides an overview of the various skin ageing parameters modelled in this study. Mathematically, the flattening of the DEJ can be interpreted as a combination of an increased wavelength and a decreased amplitude of the interface. In the present study these two phenomena were modelled separately: the amplitude was reduced incrementally to 75% of the original value whilst keeping the wavelength constant. In order to avoid any edge effects influencing the calculation results, the DEJ wavelength can only be increased to certain specific values, as the sinusoidal DEJ should only comprise complete waves. Therefore, the wavelength was increased incrementally to twice the reference value, whilst keeping the amplitude constant.

In addition to these individual manifestations of ageing, a combined aged skin model was developed in which the stiffnesses of all three skin layers were increased to 120% of the reference values mentioned in Table 8, the dermal thickness was reduced to 80% of the original value, whilst the DEJ's tortuosity was decreased by reducing the amplitude to 85% and the increasing wavelength to 125% of their respective values in the reference model. As the various manifestations of ageing vary strongly between people, it should be noted that, just like the reference model, this general aged model is for indicative purposes only and is not intended to be representative for a specific degree of ageing.

Table 8: The ageing manifestations tested in this investigation. All variations were tested incrementally and independently of one another.

Ageing Manifestation	Reference Model Parameters	Variations in Study
Changes in Skin Layer Stiffness (Ogden Moduli)	Stratum Corneum - μ: 86.76 kPa	43.38 – 130.14 kPa (50-150%)
	Viable Epidermis - μ: 61.75 kPa	30.875 – 92.625 kPa (50-150%)
	Dermis - μ: 2.55 kPa	1.275 – 3.825 kPa (50-150%)
Flattening of the DEJ	Wavelength: 120 µm	120 – 240 µm (100-200%)
	Peak to Peak Amplitude: 200 µm	150 – 200 µm (75-100%)
Thinning of the Dermis	*Thickness: 1400 µm*	*700 – 1400 µm (50-100%)*

4.2.2. Simulating Sliding and Observing Mechanoreceptor Response

To model fine touch, normal contact is initiated during the finger and the counter surface, followed by sliding between the two surfaces. Adhesive friction is considered to be the main cause of macroscopic friction for unlubricated skin contacts [20,106] and is caused by intermolecular forces between the contacting bodies. Therefore, the counter surface was kept geometrically smooth and deformation friction was ignored. The simulation comprises a compressive phase with a uniformly distributed load of 1 N, and a translation phase with the adhesive friction coefficient, f_{adh}, set to 0.2 using a penalty formulation. The top of the subcutaneous tissue was constrained in the horizontal direction (Figure 31A). A rigid counter surface for the skin model to be compressed and translated on was defined and constrained in all directions.

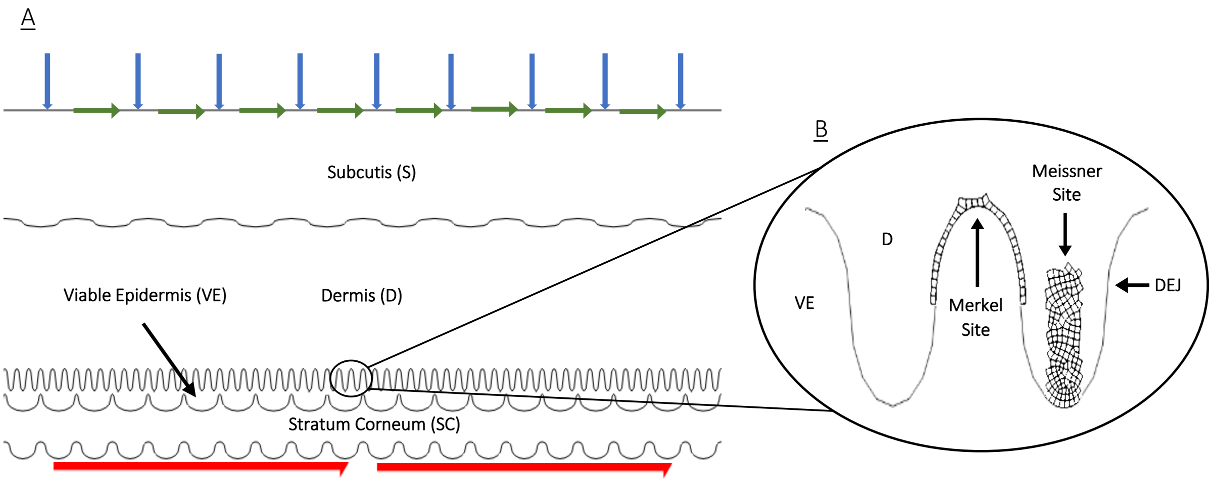

Figure 31: Schematic diagram of the numerical skin model developed (A). Image illustrates the translational lock (green horizontal arrows) implemented on the top of the subcutaneous tissue to prevent rigid body motion, and the compressive (blue vertical arrows) and shear (red horizontal half-arrows) forces experienced during sliding against a rigid counter surface. Schematic diagram of the DEJ (B) illustrating the Merkel and Meissner sites where the stress, strain and SED were recorded during the investigation.

The stimuli magnitude was measured at the receptor sites at the centre of the model. The deviatoric stress and SED experienced at the Merkel site were extracted from the elements along the DEJ, across the so-called "touch dome" that comprises the inner section of the dermal papillae as shown in Figure 31B. For the Meissner Corpuscle, strain data was extracted across elements within the central section of the dermal papillae, corresponding to the area of the receptor[229]. Statistical data regarding age-related geometrical changes to the mechanoreceptors are not extensively described in literature[83], and therefore the receptor analysis area was kept constant throughout the investigation.

For each ageing manifestation tested, point-clouds are generated to represent the stimuli magnitude for each element at each receptor site. Each data points represents the arithmetic mean of the four nodal integration points in an element. Then to summarise the effect of each ageing manifestation on stimuli magnitude at the receptor sites, the average stimuli magnitude over all elements contained in each receptor site is displayed. To assess and quantify the relative impact of each manifestation of skin ageing, the average values presented are normalised against the reference model.

4.3. Results

Figure 32 displays a typical maximum principal logarithmic strain distribution at the dermal mechanoreceptor analysis site, as calculated for the reference model, following the compression and shear against a rigid counter surface. Note that the epidermis and the corresponding strains are removed for clarity. At the site of the Meissner corpuscle the principal strain shows a gradual increase from bottom right to top left, whilst the arc shaped Merkel cell experiences a minimum strain at the left-hand side and maximum strains at both the right-hand side and the apex. Other measures for the internal strain field, such as shear strain and minimum principal strain, showed identical trends and therefore only the maximum principal strain is shown here.

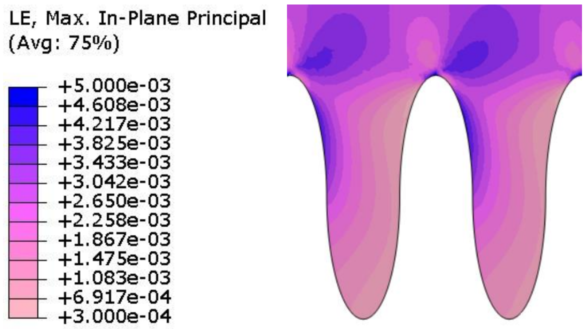

Figure 32: Contour plot of the reference model's maximum principal logarithmic strain field at the mechanoreceptor sites following compression and translation against a smooth surface.

4.3.1. Skin Layer Stiffness

The stiffness of the dermis, viable epidermis and stratum corneum were altered independently to values deviating ±50% of those of the reference model, in 10% increments. The stimuli response at each receptor site was recorded.

4.3.1.1. Dermal Stiffness

Figure 33 shows the effect of dermal stiffening on the elemental and overall stimuli magnitude at each receptor site. Figure 33A & B illustrate the effect of dermal stiffening on the Von Mises stress and the SED, respectively. Both the average Von Mises stress and the range of stresses experienced across the Merkel receptor increase with increasing stiffness, whilst the SED and the range of SED in the elements representing the Merkel disk decreased. Figure 33C demonstrates how a stiffer dermis reduces the range of strains across the elements at the Meissner site and reduces the average value. In the majority of the elements a reduced strain value is calculated. The observed changes in strains and stresses in the mechanoreceptors, which were represented on the element level in Figure 33A, B and C, can be summarised in terms of their average values. Figure 33D shows these average values in response to dermal stiffening, a decreasing the average strain (green triangles) in the Meissner corpuscle, an increasing Von Mises stress (red squares) and a decreasing SED (blue stars) in the Merkel discs.

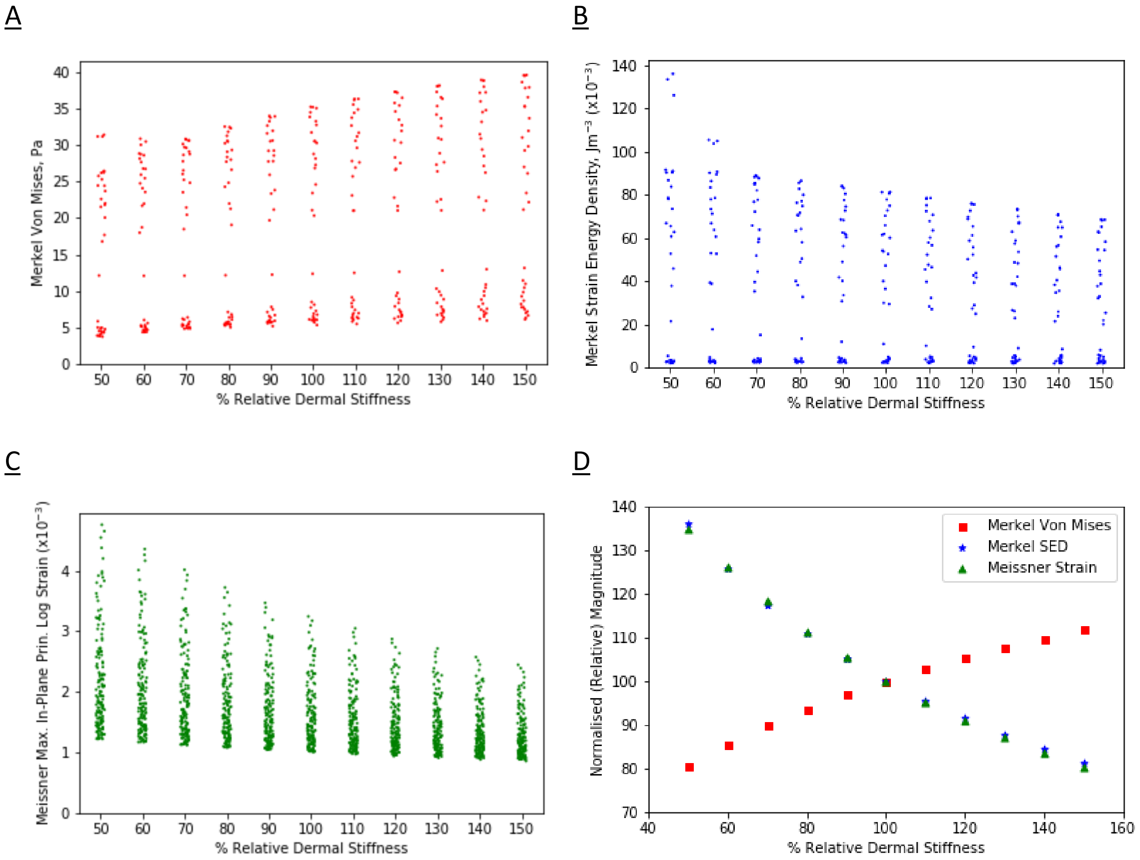

Figure 33: (A) The mean elemental Von Mises stress at the Merkel site at different relative dermal stiffnesses. (B) The mean elemental SED at the Merkel site. (C) The mean elemental maximum principal logarithmic strain at the Meissner site. (D) The mean stimuli magnitude across all data points at each site for dermal stiffening relative to the reference model.

4.3.1.2. Epidermal Stiffness

Figure 34 shows the effect of stiffening the viable epidermis on the elemental and overall stimuli magnitude at each receptor site. From Figure 34A, whilst the average value of Von Mises stresses at the Merkel disc site decreased with increasing epidermal stiffness, the range of values experienced at the site increased. This was driven by a fall in the minimum values of deviatoric stress experienced at the site. Figure 34B, describes how elemental SED values within the Merkel disc site fall slightly as epidermal stiffness increases. From Figure 34C, stiffening the viable epidermis results in decreases average elemental maximum principle logarithmic strain values at the Meissner site, whilst the range of values increases due to falls in the minimum strain values. Figure 34D summarises how stiffening the viable epidermis results in a decrease in stimulus magnitudes experienced at both mechanoreceptor sites, with the decrease in strain at the Meissner corpuscle more pronounced than the stimuli at the Merkel cells.

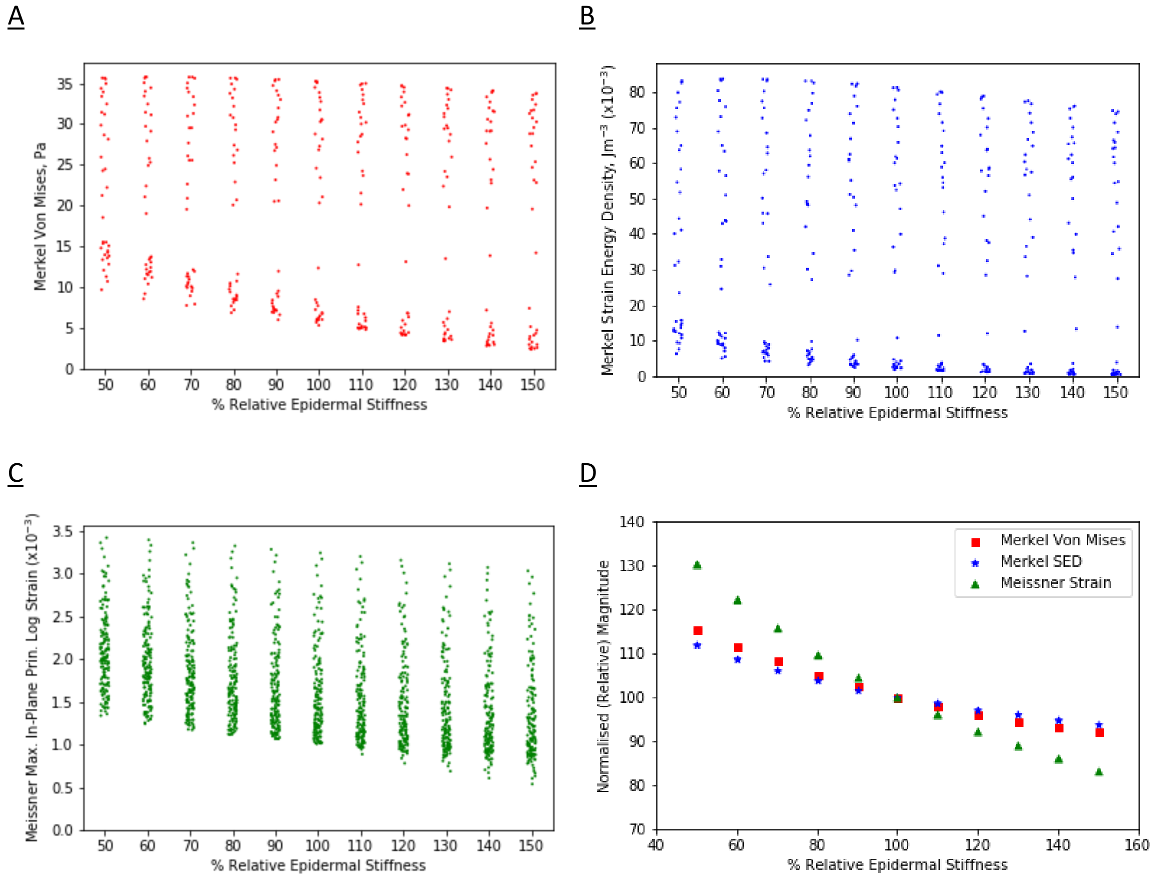

Figure 34: (A) The mean elemental Von Mises stress at the Merkel site at different relative epidermal stiffnesses. (B) The mean elemental SED at the Merkel site. (C) The mean elemental maximum principal logarithmic strain at the Meissner site. (D) The mean stimuli magnitude across each site for epidermal stiffening relative to the reference model.

4.3.1.3. Stratum Corneum

Figure 35 shows the effect of stiffening the stratum corneum on the elemental and overall stimuli magnitude at each receptor site. Figure 35A displays how stratum corneum stiffening results in a pronounced decrease in elemental deviatoric stress range at the Merkel receptor site, whilst having a less pronounced effect on the average stress level. Stratum corneum stiffening results in a decrease in Merkel elemental SED range and average SED values as shown in Figure 35B. This decrease in range is driven by a fall in maximum SED values at the site. The elemental maximum principal logarithmic stress range at the Meissner site falls with increasing stratum corneum stiffness (Figure 35C), whilst the effect on the average strain value is less pronounced. Figure 35D summarises how stiffening the stratum corneum results in a relatively strong decrease of Merkel SED, whilst the Merkel Von Mises stress and Meissner strain show a modest decrease on average.

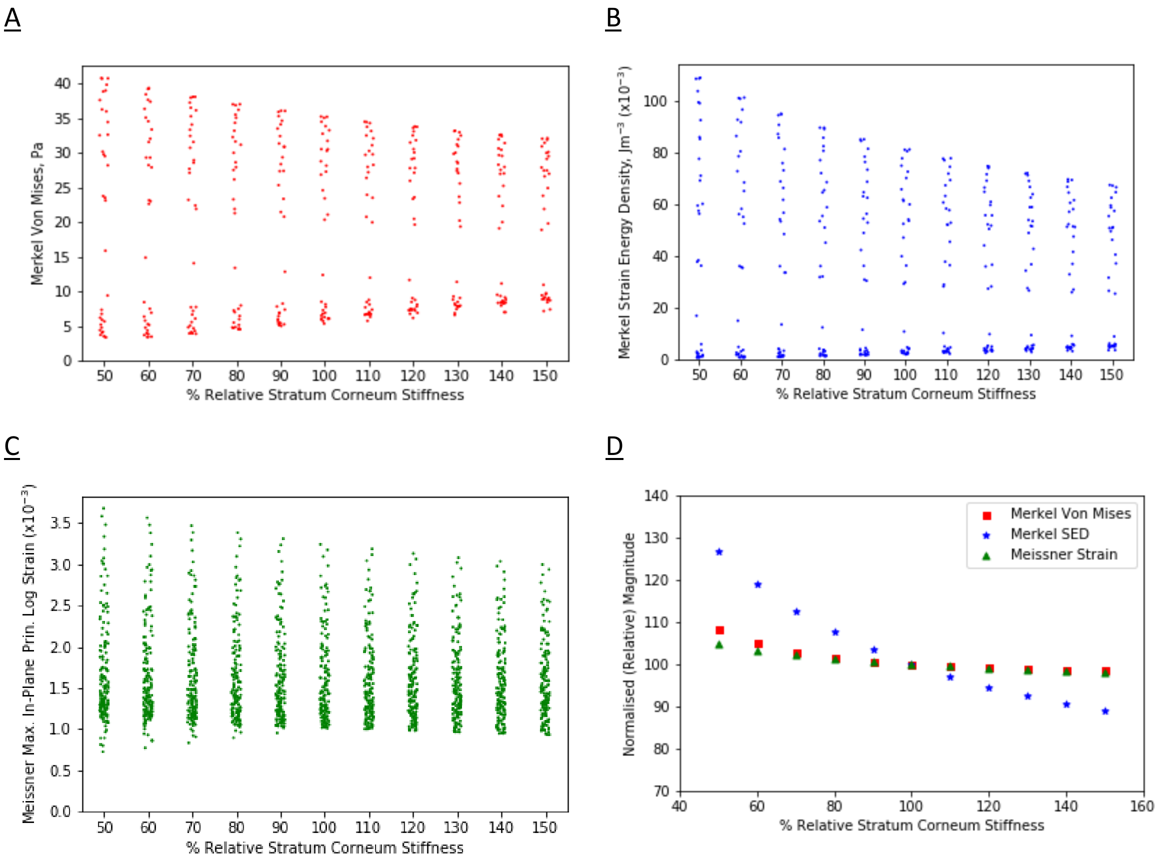

Figure 35: (A) The mean elemental Von Mises stress at the Merkel site at different relative stratum corneum stiffnesses. (B) The mean elemental SED at the Merkel site. (C) The mean elemental maximum principal logarithmic strain at the Meissner site. (D) The mean stimuli magnitude across each site for stratum corneum stiffening relative to the reference model.

Overall, except for the Von Mises stresses resulting from dermal stiffening, stiffening of skin layers causes a reduction of the stimulus magnitudes at both mechanoreceptor sites.

4.3.2. Dermal Thickness

The bulk thickness of the dermis was incrementally reduced to 50% of the thickness in the reference model. Figure 36 shows the results for the stimulus magnitudes experienced at the receptor sites. From Figure 36A, dermal thinning reduces the elemental deviatoric stress range experienced at the Merkel site, whilst having a less pronounced effect on the average value. In contrast, dermal thinning results in decreases in both average SED and SED range for the Merkel site (Figure 36B). For the Meissner site, dermal thinning results in a modest decrease in average strain values whilst having a small effect on the range of strain values experienced at the site (Figure 36C). Overall, Figure 36D describes how dermal thinning reduces the strain at the Meissner Corpuscle site, but this effect is modest: halving the thickness of the dermis results in a 7% reduction of the strain. The effects on the Merkel cell are more pronounced and non-monotonic; maximum values for the Von Mises stress and SED are observed when the dermal thicknesses are reduced to respectively 80% and 90% of the reference values. Further thinning causes a decrease of the stimuli at the Merkel cell, which in the case of the SED amounts to approximately 18% when the thickness of the dermis reaches half the original value.

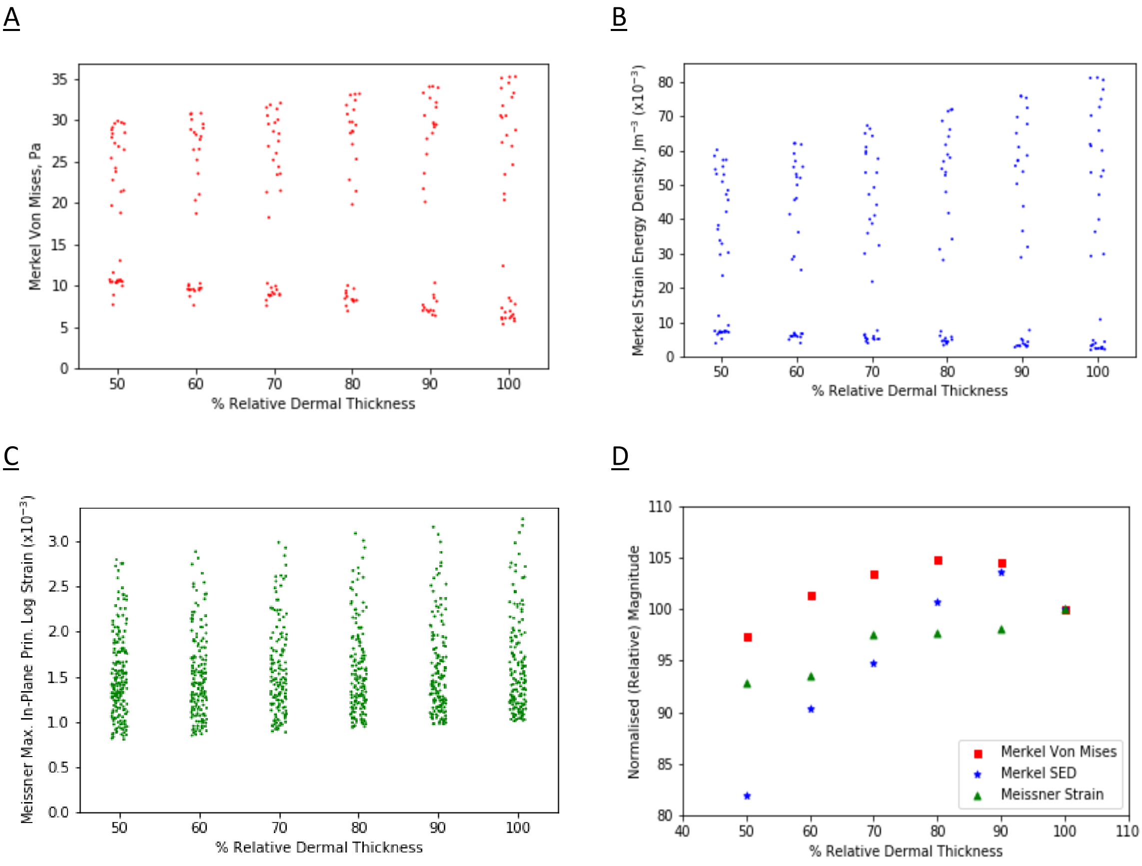

Figure 36: (A) The mean elemental Von Mises stress at the Merkel site at different relative dermal thicknesses. (B) The mean elemental SED at the Merkel site. (C) The mean elemental maximum principal logarithmic strain at the Meissner site. (D) The mean stimuli magnitude across each site for dermal thickening relative to the reference model.

Figure 37 shows SED contours along the DEJ for four different dermal thicknesses, from which it can be seen that a thinner dermis reduces the differences in SED between the two ‘legs’ of the Merkel cells, whilst also reducing the stress peak observed at the apex of the touch dome.

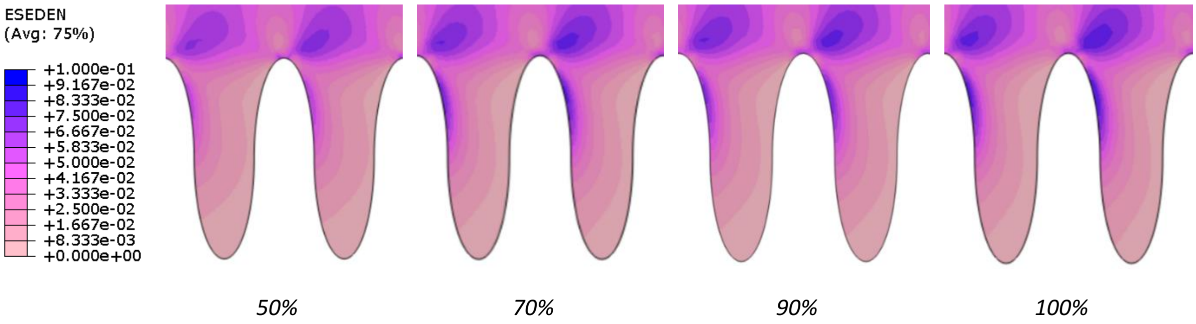

Figure 37: Strain energy density at different dermal thickness values. Note the reduced value of SED along both sides of the dermal papilla at the Merkel site, particularly when the dermal thickness is reduced to 50%.

4.3.3. DEJ Flattening

As discussed previously, ageing results in a reduced tortuosity of the DEJ, which can be modelled either by decreasing the amplitude or by increasing the wavelength. Figure 38 illustrates the effect of decreasing DEJ amplitude on the stimuli magnitudes experienced at the receptor sites. From Figure 38 A & B, it is clear that decreasing DEJ amplitude has little effect on the elemental stimuli experienced at the Merkel site. However, this is not the case for the Meissner site (Figure 38 C & D). It should be noted that, as the analysis areas for the mechanoreceptors shown in Fig. 1 were kept constant. Therefore, when reducing the amplitude of the DEJ to 80% of its original value (i.e. a reduction of 20%), the height of the Meissner corpuscles becomes comparable to the height of the dermal papillae. In that case the Meissner mechanoreceptor would incorrectly be partially contained in the bulk of the dermis which affects the obtained results. As a result, DEJ amplitudes reduced by greater than 20% are affected by this artefact. For DEJ amplitudes larger than 80% the geometric validity of the model is maintained and for these values a decreased amplitude gives a consistent reduction in stimulus magnitudes recorded at the Meissner site, as indicated by the diagonal green dotted line. Reducing the amplitude by 15% results in a 7% reduction of the strain.

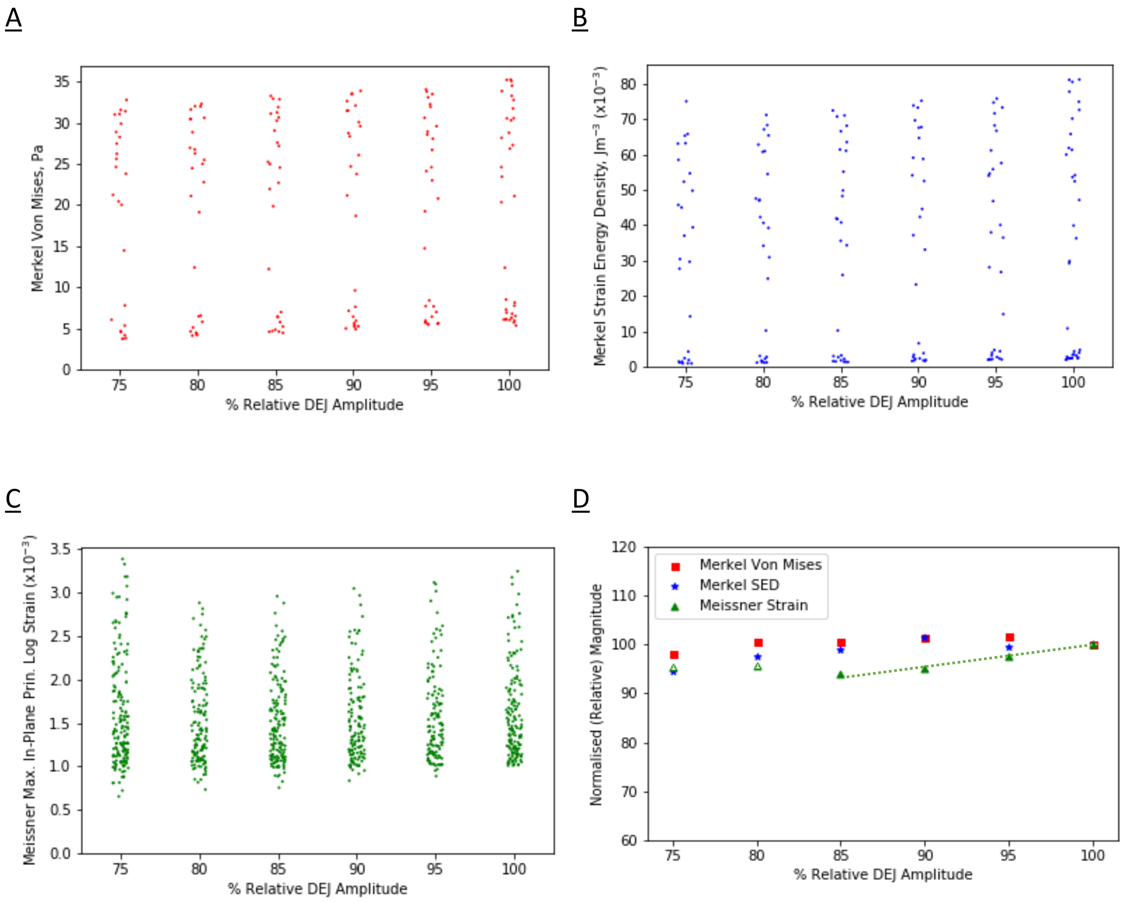

Figure 38: The mean elemental Von Mises stress at the Merkel site at different relative DEJ amplitudes. (B) The mean elemental SED at the Merkel site. (C) The mean elemental maximum principal logarithmic strain at the Meissner site. (D) The mean stimuli magnitude across each site for different relative DEJ amplitudes compared to the reference model. Note: the mean strain values at the Meissner site at 75-80% normalised magnitude are hollowed out due to area of the site being influenced by stimuli in the bulk of the dermis.

Figure 39 illustrates the effect of increasing the wavelength of the DEJ up to double its original length. From Figure 39A, whilst increasing DEJ increases the elemental deviatoric stress range experienced at the Merkel site, it has little effect on the average value. The same was found for Merkel SED (Figure 9B). However, the average elemental strain and strain range experienced across the Meissner site decreased considerably across the modelled range (Figure 39 C & D). A 30% increase of the wavelength of the dermal-epidermal junction yields an almost 20% decrease in strain response at the site of the Meissner corpuscle. Overall, it was found that DEJ flattening had a more substantial effect on the Meissner site than the Merkel site.

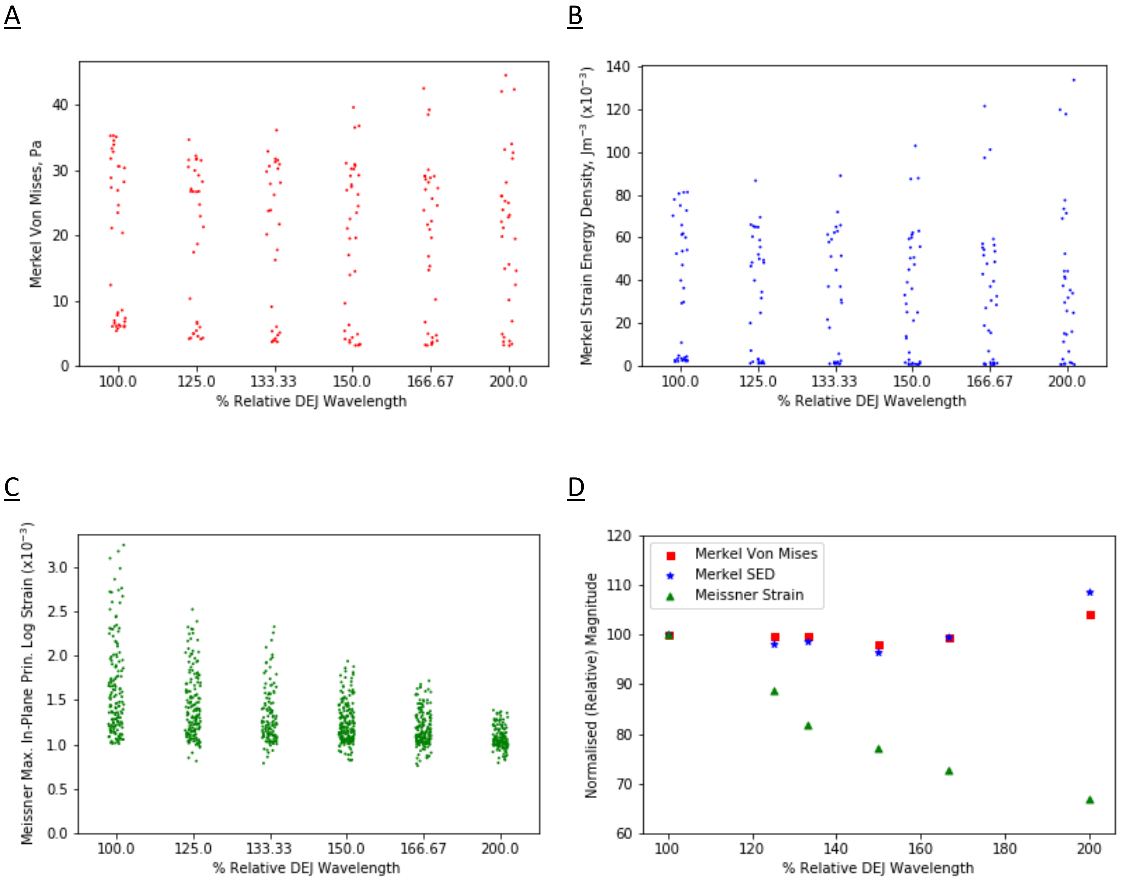

Figure 39: (A) The mean elemental Von Mises stress at the Merkel site at different relative DEJ wavelengths. (B) The mean elemental SED at the Merkel site. (C) The mean elemental maximum principal logarithmic strain at the Meissner site. (D) The mean stimuli magnitude across each site for different relative DEJ wavelengths compared to the reference model.

4.3.4. Combined Effects

Figure 40 shows the effects of the combined ageing model, in which all manifestations of ageing were simultaneously modelled. The stiffness of the stratum corneum, viable epidermis and dermis were increased, the thickness of the dermis was reduced, and the tortuosity of the DEJ was decreased by both reducing the amplitude and increasing the wavelength. Figure 40A shows the local strain field in the dermis of the aged skin, showing a similar pattern as previously presented in Figure 32 for the reference skin model. Comparing Figure 32 and Figure 40A shows that the aged skin experiences a reduced level of strain across the entirety of the dermal papillae, as illustrated by the dark blue high strain area that fans out diagonally rightwards from the apex of the touch dome, and along the “legs” of the Merkel disc. However, the apex of the touch dome, which is the centre of the Merkel disc, remains an area of high local strain. The reduction in strain across the dermal papillae is reflected in Figure 40B, showing that the strain across the Meissner corpuscle both in terms of the element distribution and the average value as indicated by the horizontal dashed lines site, are significantly reduced for aged skin. Figure 40C shows the deviatoric stress magnitudes at the Merkel site for both models, indicating a mild increase of the range of stresses calculated and a slight decrease of the average stress calculated in the mechanoreceptor. The aged skin also experiences a decrease in Merkel SED, both in terms of range and average value (Figure 40D).

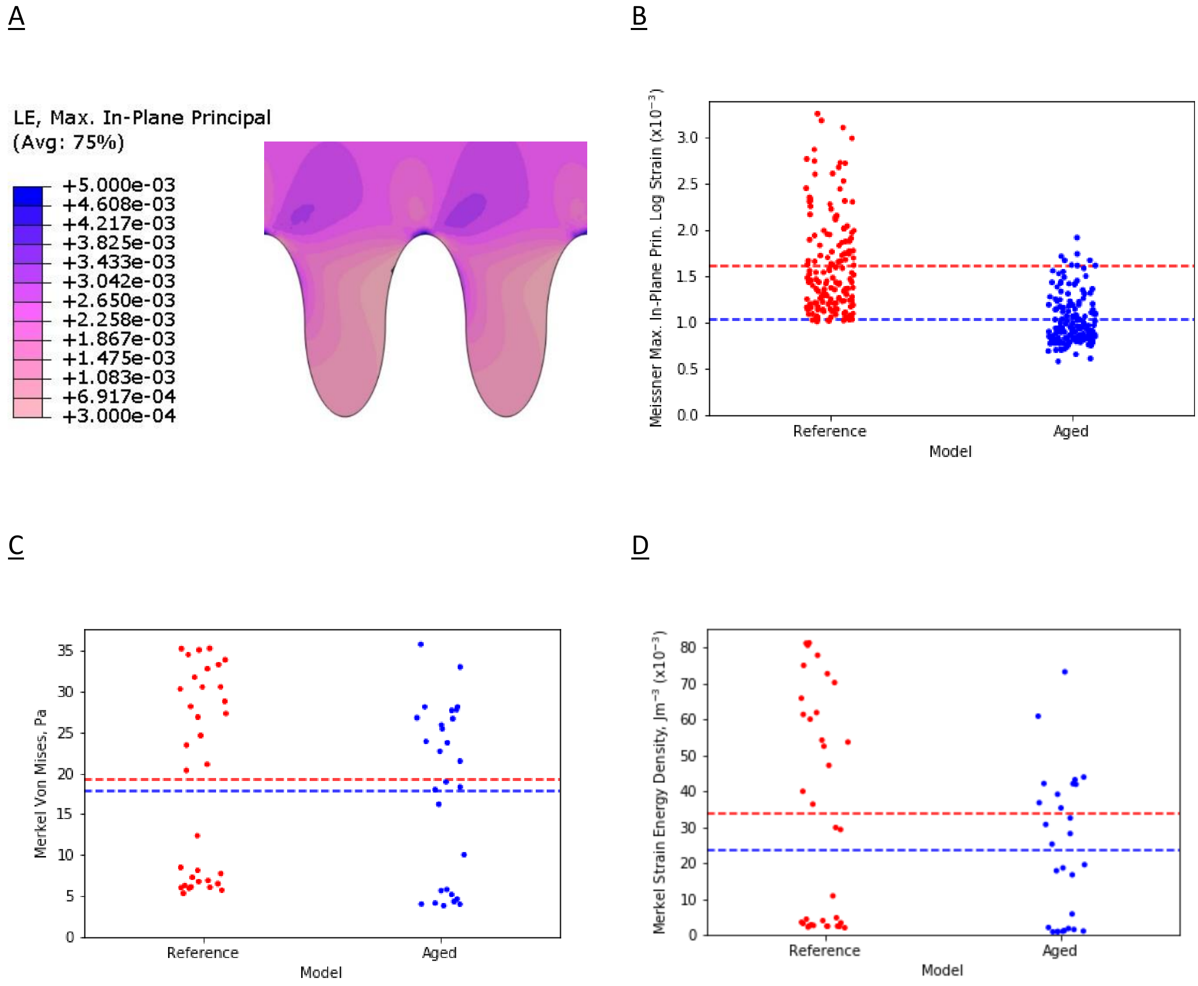

Figure 40: Contour plot of the aged skin model (A). Elemental strip plots illustrating that combining the ageing manifestations results in a decrease in strain at the Meissner (B) and deviatoric stress (C) and SED (D) at the Merkel site relative to the reference model. The horizontal broken lines illustrate the mean stimuli magnitude in the model at the respective site.

4.4. Discussion

The results presented in Figures 33-40 illustrate how individual ageing-related mechanical and geometrical changes to the skin strongly affect the stimulus magnitudes experienced by the mechanoreceptors under the same external loading conditions. Presently, the effect of differences in the elemental stimulus magnitude within each receptor site (indicated by the range of data points within the clouds of graphs A-C in Figures 33-39) on tactile perception is not fully understood. Future studies could focus on the effect of differences in stimulation within mechanoreceptor sites on the discharge of neurological impulses. By reviewing the effect of age-related skin changes on the average stimuli magnitude across each site (indicated by graph D in Figures 33-39), the simulations show that all age-related changes modelled resulted in a decrease of the strains at the Meissner site. The Merkel SED reduced in all cases except for the dermal thickness, which shows a maximum stimulus intensity at 90% dermal thickness. The decrease of the stimulus magnitudes could result in a higher proportion of stimuli not meeting the detection thresholds of the mechanoreceptors and thus offer an additional explanation for the reduction in perceptive fine touch ability amongst the elderly. The deviatoric stresses at the Merkel cell site are less clearly affected by ageing, both in terms of the absolute values and the relative trends. An increase of the dermal stiffness results in an increased local deviatoric stress, which differs from the other ageing manifestations tested. Whilst it could be hypothesised that this means that, mechanically, the stiffer dermis appears to dampen the other observed effects of ageing, in a biological sense the net effect on the Merkel site of the deviatoric stress and the SED responding differently is not understood. Empirically, literature suggests that static touch, which is detected at the Merkel sites, is more significantly impacted by ageing than the Meissner Corpuscle's dynamic touch[230]. However, our results suggest that age-related material and geometric changes affect dynamic touch to a greater extent, indicating that perhaps the Merkel's response is more influenced by neurological changes.

4.4.1 Relative Effects of Age-Related Geometrical and Mechanical Skin Changes

The main affecting factors for the Meissner corpuscle are the stiffness of the dermal and epidermal layers and the wavelength of the DEJ. For the Merkel site the three largest impetuses on the value of the SED are the stiffness of the dermis and stratum corneum, and the thickness of the dermis. As the applied force in the simulations is kept constant at 1 N, a stiffer dermis leads to lower strains at the sites of the fine touch mechanoreceptors. Overall, both the Meissner and Merkel sites are strongly affected by increased stiffness of the various skin layers (Figures 33-35). The relatively stiff stratum corneum and viable epidermis cover the much more compliant dermis, and the further stiffening of these two layers with increasing age means that local stress variations will be distributed more evenly in the dermis, and consequently the local deformations will be reduced. This results in a reduction of the peak strains at the receptor sites and, as the strain energy depends on the product of local stress and strain values, also directly affects the SED. The exact effect of stiffer skin surface layers depends on the interplay of mechanical and geometrical properties, which both have a marked effect.

The effect of the tortuosity of the DEJ can be explained by looking at the epidermal rete pegs. These act as stiff protrusions that interdigitate with the more compliant dermis. This geometrical structure facilitates the efficient transfer of shear stresses from one layer to the other, thereby protecting the interface between the two layers: if the epidermis and dermis were not interdigitated, the DEJ would be directly subjected to these shear stresses. Both a decrease in amplitude (Figure 38) and an increase in wavelength (Figure 39) of the DEJ reduce the interdigitation meaning that the DEJ, which is modelled as a perfectly adhered layer, would be subjected to elevated levels of shear. The calculated results indicate that the overall effect of the reduced interdigitation on the Merkel discs is relatively small, as the increased stress at the apex is offset by the reduced stress along the two legs of the mechanoreceptor. The stimulus at the Meissner site is strongly affected by the changed tortuosity of the DEJ as the lower stresses acting on the sides of the dermal papillae reduce the strain in the dermal papillae. Physiologically, excessive flattening of the DEJ leads to elevated peak stresses acting along the DEJ and, if these exceed the value for delamination to occur, can potentially cause blisters or skin tears. Because the geometry of the mechanoreceptor analysis sites in the model was kept constant, a reduction of the DEJ amplitude of more than 20% would cause the Meissner site being partially contained in the dermis, skewing the calculated results. A better understanding of age-related effects on mechanoreceptor geometry, as discussed by Garcia-Piqueras[83], would allow analysis over a more precise area. As previously discussed, maximum values for the SED and deviatoric stress were observed at slightly reduced values of the dermal thickness. This suggests that there may be an optimal bulk dermal thickness that amplifies the stimuli response at the sites of the mechanoreceptors and thus improves tactile perceptiveness (Figure 36), perhaps counteracting the negative effects of the other manifestations of ageing at the initial stages of ageing.

4.4.2. Aged Skin Model

The results obtained using the combined ageing model are shown in Figure 40, indicating that the strains at the Meissner Corpuscle are particularly affected by ageing. In more detail, for the aged skin model the average strain in the Meissner corpuscles reduced by 36%, the SED in the Merkel cells reduced by 30% and the deviatoric stresses in the Merkel cells reduced by 7% compared to the reference model. Table 9 compares these values to the superposed results calculated for the various individual manifestations of ageing. Their superposition adds up to a 38% reduction of Meissner strain, a 19% reduction of Merkel SED and a 5% increase of Merkel deviatoric stress, respectively. The differences between the sum of the effects of individual manifestations and the combined model indicates that the modelled effects of ageing on the mechanoreceptor sites cannot be linearly superimposed and that, in reality, there is significant coupling between the various aspects of ageing. This coupling particularly manifests itself at the Merkel mechanoreceptor sites. Future research could focus on how the effects of each individual ageing manifestation on tactile perception integrate with one another.

Table 9: A summary of the effects of ageing for the various individual manifestations as well as the combined aged skin model. Stimuli magnitude at the receptor sites are quantified relative to the values of the reference model.

Ageing Manifestation		**% Change from Reference Model**		
Characteristic	**Magnitude**	**Merkel VM**	**Merkel SED**	**Meissner Strain**
Dermal Stiffening	20%	5.26	-8.53	-9.04
Epidermal Stiffening	20%	-3.99	-2.81	-7.73
Stratum Corneum Stiffening	20%	-0.82	-5.39	-0.99
Dermal Thinning	20%	4.84	0.66	-2.38
DEJ Amplitude	-15%	0.58	-1.01	-6.08
DEJ Wavelength	25%	-0.34	-1.83	-11.36
Superposition of Individual Manifestations		5.53	-18.91	-37.58
Combined Ageing Model		-7.45	-29.98	-36.24
Difference		12.98	11.06	-1.34

4.4.3. Interventions

Most interventions aimed at mitigating the effects of age-dependent degradation of touch and tactile perception can be divided into two categories: those affecting the skin and its ageing manifestations, and those that concern surface and product engineering methods. With respect to the skin itself, it has been shown that hydration and, by extension, softening of the skin increases the perceptive ability amongst individuals[78]. Methods such as moisturising have a two-fold effect on the skin-surface interaction. Firstly, they plasticise the stratum corneum[138] thereby increasing the deformability and the contact area of the skin. Secondly, moisture in the skin-surface interface affects the intermolecular forces that cause adhesive friction, thereby potentially affecting perceptive ability[33,119]. However, the softening benefits of moisturisers are limited to the superficial layers as conventional moisturisers do not penetrate deeper towards the dermis. Additionally, due to the regeneration and cycling of the keratinocytes in the viable epidermis and stratum corneum these moisturisers offer only a temporary solution and require frequent reapplication. The results of this study indicate that the dermis plays a dominant role in transmitting tactile sensations, and its stiffness strongly affects this transmission. Methods to preserve the geometric and material integrity of the dermis include the administration of antioxidants, which are reported to reduce fibre degradation and thus slow the decomposition of the dermal matrix[231]. The maintenance of the dermis could slow the thinning of the layer and the flattening of the DEJ, helping to preserve our sense of touch. With respect to product design, the surfaces of objects can be optimised for tactile perception. This could involve changing the materials used, as the surface free energy directly relates to the grip and friction characteristics. It should, however, be noted this should be done with caution as the DEJ of aged skin is less able to support shear and deviatoric stresses[75,232] and increased friction could result in blisters and skin tears[233]. Product surfaces might also be optimised by changing the surface microgeometry, e.g. through texturing[234], to provide more prominent cutaneous sensations during touch. It is envisioned that the developed model can be used to analyse and improve measures aimed at preserving and enhancing tactile sensation. This includes modelling the effects of skin treatments and the design of specific surface textures for optimised mechanoreceptor stimulation.

5. Effect of Surface Textures on Tactile Perception

5.1. Introduction

Previously, a microscale finite-element finger skin model was developed to test the effects of biomechanical skin ageing on tactile perception[223]. This two-dimensional, hyperelastic model was employed to examine the stress, strain and energy fields at the locations of the Type-1 (high spatial resolution) mechanoreceptors in response to age-related mechanical and geometric skin alterations. Here, a parametric study was conducted to investigate the effect of altering the topography of the counter surface on the mechanical state of the high spatial resolution Merkel and Meissner receptors. The investigation focuses on the observation of the mechanoreceptors' stress, strain and energy fields in response to changing the amplitude and wavelength of rigid sinusoidal rough surfaces. By analysing the excitation of each of the receptor sites, we may better understand why different surfaces evoke specific sensations amongst individuals. In conjunction with perceptive data, surface design engineers could use the outputs of this investigation to aid the development of product surfaces and textures designed to elicit targeted sensations amongst consumers.

5.2. Materials & Methods

5.2.1. Analysing Skin-Surface Contact

In order to analyse the effect of rough surface topography on mechanoreceptor stimulation, an initial baseline was set by simulating the contact of the finger model against geometrically smooth surfaces for comparison. Friction coefficients against flat surfaces can vary considerably depending on variables such as the counter surface material and moisture in the contact. It has a marked effect on grip and tactile perception[95]. To simulate finger sliding and thus tactile perception, the viscoelastic finger skin model (Figure 41A) was first compressed against a rigid, smooth flat counter surface with a 1 N uniformly distributed load before being translated at a velocity of 20 mm/s. This is a load and speed typically exerted during tactile perception[73,95,127,138].

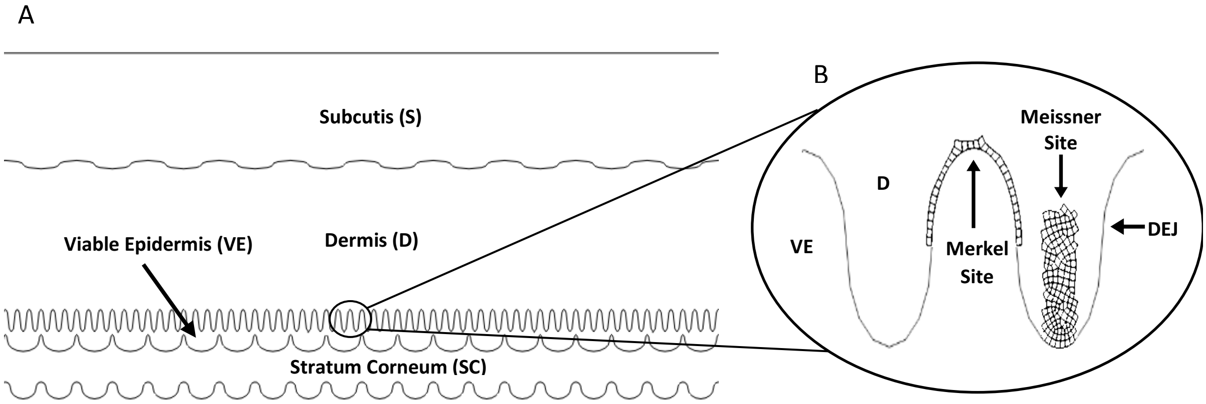

Figure 41: Schematic diagram of the numerical finger skin model (A). Schematic diagram of the Dermal Epidermal Junction (DEJ) (B) illustrating the Merkel and Meissner mechanoreceptor sites where the model outputs were recorded during this investigation. The Merkel site is located at the "touch dome" at the peak of the DEJ, whilst the Meissner site rests within the dermal papillae.

The effect of altering the adhesive friction coefficient on the stress-state of the Type 1 mechanoreceptor sites (Figure 41B) following contact of the finger skin model against a geometrically smooth counter surface was investigated by varying the applied interfacial friction coefficient at the skin-surface boundary between $\mu = 0.1$ and $\mu = 0.8$. Following this, in order to analyse the response of the skin model to textured surfaces, an intermediate value of the adhesive friction coefficient of 0.4 was applied and a parametric study was conducted in order to simulate the contact of the finger against a range of geometrically rough surfaces. These rough surfaces were represented as regular sinusoids whose wavelengths were independently varied between 80 µm and 500 µm, and amplitudes were independently varied between 10 µm and 100 µm. In order to explore the effect of commensurate fingerprint and counter surface wavelengths, an additional study was undertaken in which the surface amplitude was held at 40 µm, whilst the wavelength was varied between 350 µm and 450 µm.

To analyse the effect of surface topography on fine touch and tactile perception, the signals of mechanical stimuli generated at the Type 1 (Merkel and Meissner) mechanoreceptor sites were recorded. When translated against each surface, the average mechanical stimuli magnitude across each Type 1 receptor site was recorded over time. Furthermore, for each simulation, the average and range (max. – min.) values of the mechanical stimuli at each receptor site was also recorded.

Viscoelasticity was incorporated into the finger skin model due to the time-dependent loading associated with rough surface contacts. These viscoelastic parameters are summarised in section 3.5. Model Development. The first and second order time constants of the skin layers within the model were equal to 0.2136 and 8.854 seconds respectively. The model was maintained under compression for 10 seconds in order to allow the skin to reach a relaxed state before being translated. The finger was kept in a relaxed state prior to translation to ensure that only the temporal effects of sliding against the rigid surface asperities were recorded, as opposed to any residual viscoelastic effects from the compression stage.

5.2.2. Validation

As mentioned in section 3.5. Model Development, it is currently not possible to directly compare the energy fields generated at the receptor sites in vivo to the results obtained using the developed finite element model. It is possible; however, to compare the results of tactile experiments to the excitation of the mechanoreceptors in the developed computational model. During the COVID-19 pandemic, the ability to conduct physical tactile experiments using human subjects was reduced, whilst time was instead allocated to the work included in section 7. Investigating the Effects of Respirator Mask Design on Facial Skin’s Damage Propensity. Therefore, in order to validate the model, simulation results were instead compared to perception tests presented in literature by Skedung[78].

In these tests 60 individuals were asked to compress and translate their fingers against rigid sinusoidal surfaces (dimensions detailed in Figure 42). The participants were allowed to use any preferred load, speed and inclination angle of the index finger during the tests, so long as they tried to be consistent for each surface. Participants tested the surfaces in randomized order, before being asked to distinguish between each of the surfaces and a reference surface (Ref100). The percentage of correct responses was then recorded for each demographic. The success criterion was defined as when 80 % of a demographic could correctly distinguish between a test surface and the reference surface. Skedung found that individuals were unable to successfully distinguish the S60 and S80 surfaces from the reference surface, Ref100.

Surface	*Wavelength (μm)*	*Approx. Amplitude (μm)*
S0	0	0
S40	40	8
S60	60	13
S80	80	15
Ref100	100	10

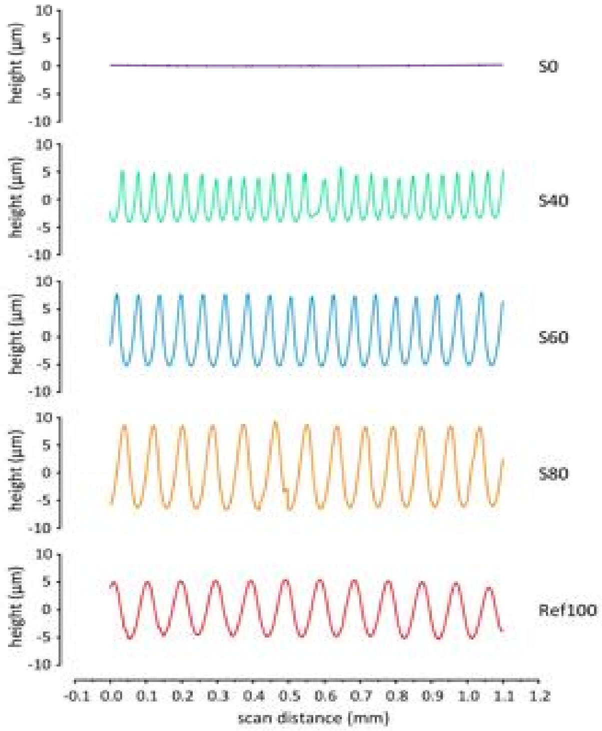

Figure 42: Dimensions (left) and diagrams (right) of the surfaces used by Skedung during tactile discrimination tests.

In order to test and validate the developed computational model, a finite element finger skin model was compressed with a 1 N load (typical value for perception tests) and translated against rigid surfaces with identical geometries to those used by Skedung. An arbitrary interfacial friction coefficient of 0.2 was applied between the surfaces. The excitation of the Type 1 mechanoreceptor sites were then compared to Skedung's experimental results.

Figure 43 illustrates the effect of translating the finger skin model against each the surfaces on the Von Mises stress at the Meissner site. The reference surface (Ref100 – blue line) generated an alternating waveform with two peaks at approximately 23 Pa and 18 Pa. The periodicity of the generated signal is a function of both the fingerprint and surface wavelength. Stresses propagated to the site of the receptor following multiple contacts of soft fingerprint ridges across the model against rigid surface asperities.

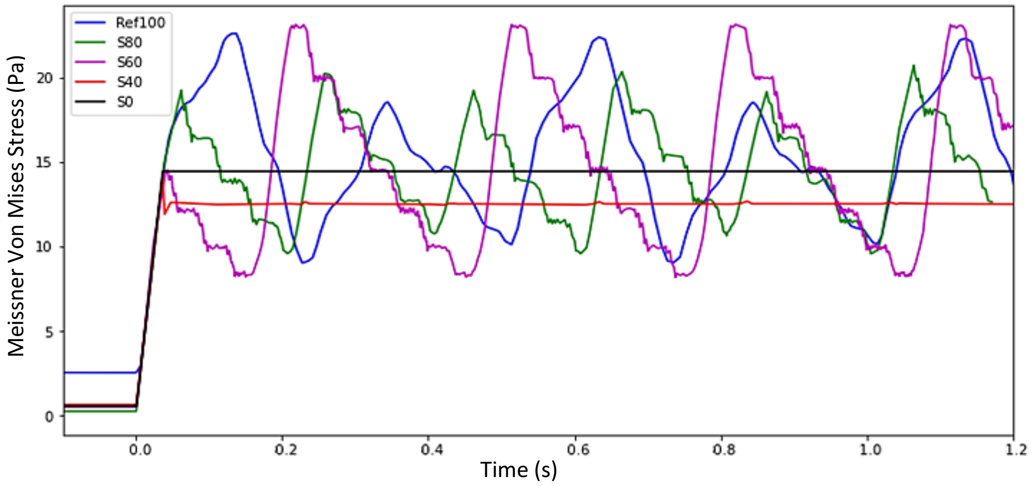

Figure 43: Deviatoric stresses at the Meissner site following the compression and translation of the skin model against surface geometries identical to those tested by Skedung.

The S0 (black line) and S40 (red line) both resulted in the propagation of uniform deviatoric stresses to the Meissner site for the majority of the translation time. Due to the small wavelengths associated with S40, multiple asperities were in contact with each stratum corneum ridge at any given time, resulting in an increase in contact area to the extent to which the oscillatory component of the stress signal was diminished. However, as the contact area between the finger model and the S40 surface was not as high as that of a flat surface (S0), the impact of adhesive friction was also reduced thus resulting in lower stresses being generated at the Meissner site from contact with the S40 surface, compared to the flat S0 surface.

S60 (magenta line), S80 (green line) and Ref100 (blue line) generated a regular waveform at the Meissner site. However, in contrast to larger surface wavelengths, the S60 surface wavelength was sufficiently small to enable multiple asperities to simultaneously make contact with the fingerprint ridges, generating a more complex stress field within the tissue (Figure 44).

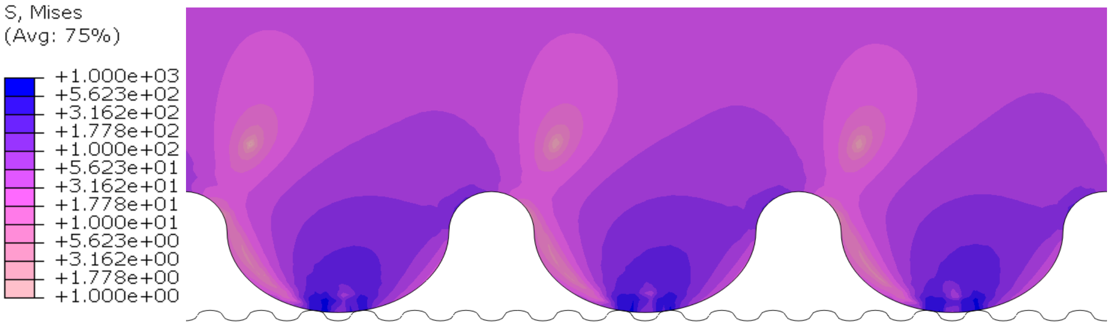

Figure 44: Multiple asperities of the S60 surface are able to make contact with a single fingerprint ridge at the edge of the stratum corneum, generating elevating deviatoric stresses.

Overall, the S60, S80 and Ref 100 surfaces produced similar Von Mises stress waveforms at the Meissner site, whilst the S0 and S40 surfaces generated distinctly different signals. Similar trends were found for the Merkel site. This finding corroborates those found by Skedung and offers an explanation as to why individuals were unable to distinguish the S60 and S80 surfaces from the reference surface.

5.2.3. Model Output

In literature, deviatoric stresses, strains, and strain energy density have previously been used to help characterise the stimulation of mechanoreceptors. Whilst in our previous study[223] each of these metrics were evaluated, it was found that the effect of surface topography on both deviatoric stresses (Von Mises) and strain energy density (SED) at the receptor sites were strongly correlated. Figure 45 illustrates the effect of translating the skin model against a surface geometry of wavelength 360 µm and amplitude 80 µm (denoted as W360A80) on the Meissner receptors deviatoric stress (Figure 45A) and SED (Figure 45B) value.

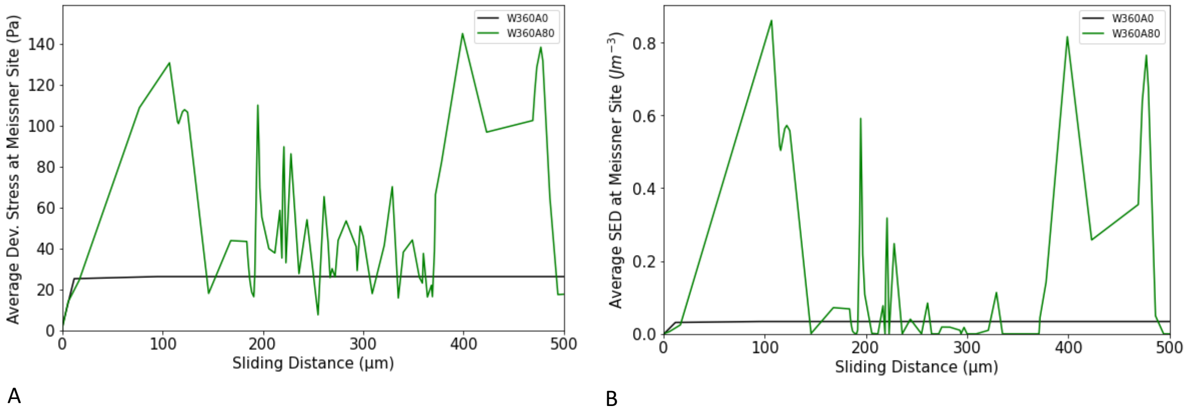

Figure 45: The deviatoric stress (A) and SED (B) signals generated as the finger skin model was translated against a surface with wavelength and amplitude of 360 µm and 80 µm respectively.

In this scenario, the periodicity of the fingerprint ridges and surface wavelength are both equal to 360 µm, therefore, it was possible for the two to interlock. Initially the fingerprint ridges lay embedded within the rough of the sinusoidal counter surface (Figure 46). Up to a sliding distance of approximately 150 µm, the skin model is traversing over the asperities. The peak in stimulus magnitude recorded at the receptor site following 100 µm of translation is the result of the fingerprint exhibiting physical resistance whilst traversing over the ridged counter surface texture. Between the sliding distance of 150 µm and 260 µm, the fingerprint ridges are translating almost horizontally over the tip of the surface asperities, after which it begins its decent back into the adjacent trough of the sinusoidal counter surface until a sliding distance of approximately 360 µm. From here, the cycle repeats and the fingerprint ridges ascend up counter surface texture once more. The difference between the initial peak (after approximately 100 µm of sliding) and the latter peak (corresponding to a sliding distance between approximately 400 and 480 µm) is attributed to stresses propagating through the model, initiating from contact of multiple soft adjacent fingerprint ridges against adjacent surface asperities. Both the deviatoric stress and strain energy density fields exhibit similar trends.

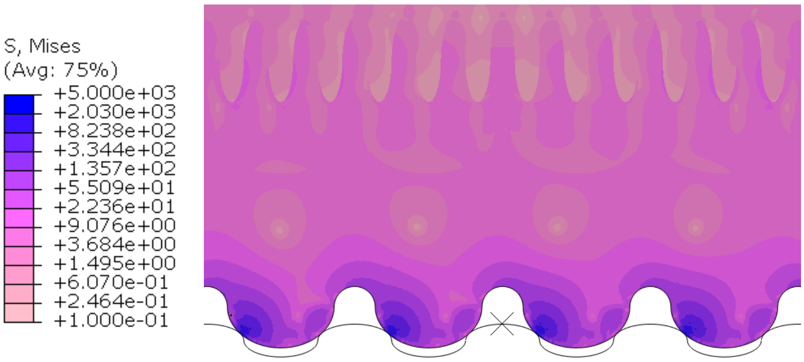

Figure 46: Deviatoric stresses within the superficial layers of the skin at the beginning of the translation stage. Note logarithmic contour scale.

As biologically representative values to describe mechanoreceptor stress-state in vivo cannot be easily obtained, the focus of this investigation is the effects and trends that topographical modifications have on receptor excitation. Due to their similarity, either of these metrics could have been chosen. Abaqus's standard deviatoric stress measure is Von Mises stress, which is conventionally used to describe the yield of ductile materials, such as many metals. In contrast, SED is a function of both stress and strain, and has been used to characterize critical loading conditions within soft tissue[167], in addition to the mechanical state and stimulation of both Type 1 mechanoreceptor sites[235–238]. Therefore, as both metrics were strongly correlated and exhibited the same trends, in this chapter SED will be used as the principal measure of mechanical stimulus magnitude at the receptor sites due to its prior biological connotations.

5.2.4. Static vs Dynamic Analysis

Viscoelasticity describes the time-dependent nature of mechanical properties of a material. It can only be implemented into dynamic finite element models and in doing so, enables the skin to exhibit creep and stress relaxation. However, within dynamic implicit analysis, Abaqus CAE implements default numerical damping in order to obtain convergence[239] which can result in the emergence of small, localised residual stresses being maintained from previous time steps. This effect was demonstrated at the edge of the stratum corneum (Figure 47). Here, the finger skin model was compressed and translated against a surface with a wavelength of 200 µm and amplitude of 60 µm (W200A60). During translation, despite some of the fingerprint ridges breaking contact with the counter surface geometry, localised residual stresses remain at the edge of the stratum corneum.

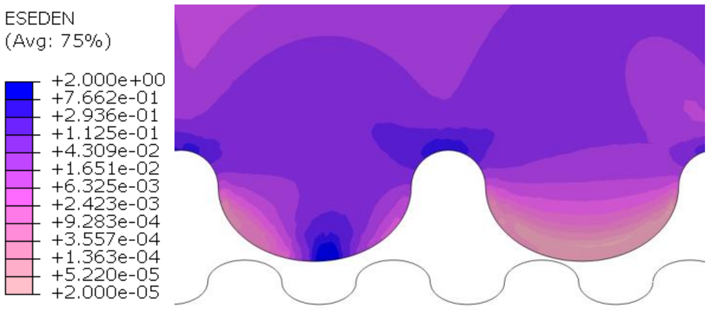

Figure 47: Residual SED values remained at the edge of the stratum corneum despite the fingerprint ridge no longer being in contact with the W200A60 surface during dynamic analysis.

In order to assess the impact of dynamic implicit analysis vs static analysis, the finger-skin model was translated against the W500A100 surface under both static (red line - no viscoelasticity) and dynamic (blue line - viscoelasticity) analysis methods at both receptor sites (Figure 48). The effect of using static simulations was found to exhibit similar trends and SED values compared to reducing the stiffness of the dynamic model by 30% (green line), which enabled more deformations and thus higher SED values. The original dynamic values (blue line) of SED were expectedly lower than that of static analysis (red line) due to the enablement of stress relaxation within the soft tissue. The stress relaxation offsets the very small potential SED increase at the receptor site caused by the residual stresses generated at the stratum corneum during dynamic analysis. Therefore, as the skin is a time-dependent material, dynamic analysis was still deemed the most appropriate method.

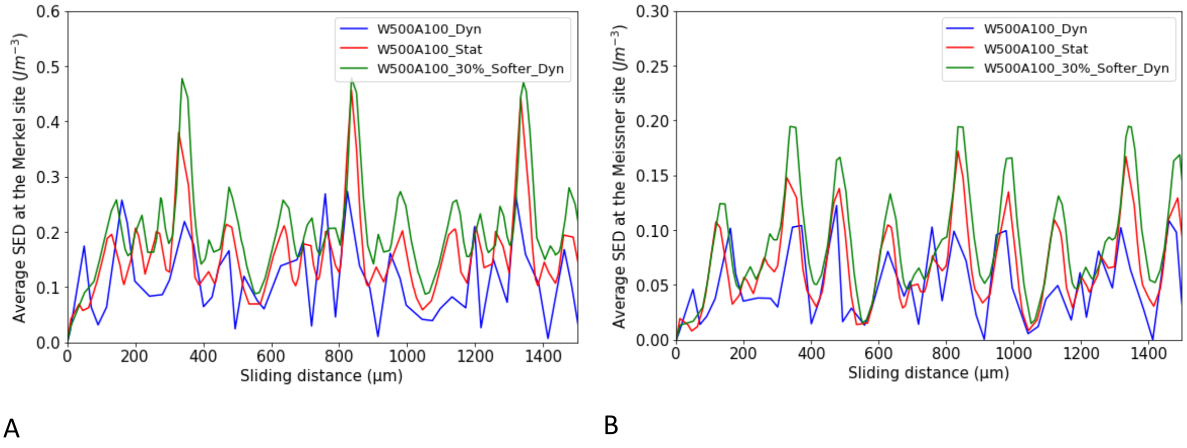

Figure 48: The SED at the Merkel (A) and Meissner (B) site following compression and sliding against surface W500A100 under static and dynamic conditions.

5.2.5. Standardising the Analysis

The majority of simulations within this investigation were completed after approximately 12-24 CPU hours. Due to the periodicity of the fingerprint and surface wavelength within the finite element models, the SED signals generated at the Type 1 mechanoreceptor sites were also periodic. However, due to software and licensing issues between Imperial College London and the Abaqus CAE software, automatic termination signals were randomly generated for simulations that ran for extensive periods of time and generated large output databases. This frequently occurred during the translation stage as, due to the complexity of simulating soft sliding contacts, this stage demanded the most computational expenditure. Therefore, random termination of the simulation during the translation stage would result in the distance travelled by the finger differing between simulations and not always being a multiple of the fingerprint or surface wavelength. Therefore, the SED signal generated at the receptor sites often included a non-integer value of SED cycles (partial or incomplete SED cycles).

If at least one cycle was recorded, any further partial cycles that were generated as a consequence of the simulations terminating prematurely have a more marked effect on the average SED recorded at the receptor site, than recorded maximum or minimum values. The analysis was therefore standardised to reduce the impact of partial cycles distorting the measured average stimuli and ensure that the effects of both the surface and fingerprint wavelength were accounted for. This was done by enforcing two truncation requirements resulting in the analysed translation distance being equivalent to the larger of the surface and fingerprint wavelength, i.e.:

1) For surface wavelengths smaller than the fingerprint (360 µm), the translation signal was analysed over the period of one fingerprint wavelength (360 µm).
2) For surface wavelengths greater than or equal to the fingerprint (360 µm), the translation signal was analysed over the period of one surface wavelength.

Figure 49 illustrates the effect of implementing the truncation requirements on the analysed Merkel SED signal following the finger model’s compression and translation against surfaces with wavelengths of 360 µm. The black line (W360A0) illustrates the receptor response to flat surfaces, whilst the red (W360A40) and green (W360A80) lines illustrate the SED signal generated at the Merkel site in response to surfaces with amplitudes of 40 µm and 80 µm respectively. Figure 49A illustrates the Merkel site SED signals over a sliding distance of 1000 µm, whilst Figure 49B shows the same SED signals over the truncated sliding distance, which in this case is equal to 360 µm.

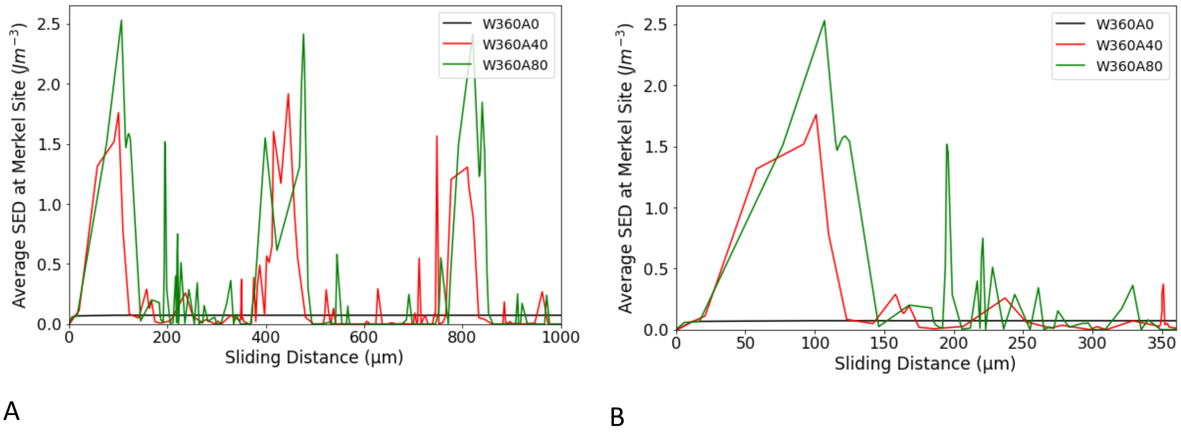

Figure 49: The change in analysed translation distance for surfaces with 360 µm wavelength before (A – 1000 µm) and after (B – 360 µm) truncation.

5.3. Results

Using a flat and geometrically smooth surface as a benchmark, the results obtained following contact against the various rough surfaces will be presented. Following the simulations, typical results are presented in three formats:

- As the local SED contours at the sites of the mechanoreceptors,
- As the time evolution of the average SED at each of the receptor sites.
- As the overall average and range SED values generated for each surface at each receptor site.

5.3.1. Effect of Adhesive Friction on Type 1 Mechanoreceptor Stimulation

Following compression, the finger skin was translated against a rigid, flat, geometrically smooth counter surface, with an applied interfacial (adhesive) friction coefficient, thereby inducing shear stresses at the interface which propagated to the receptor sites. Figure 50 illustrates the induced strain energy density (SED) distribution in the vicinity of the Type 1 mechanoreceptor sites (see Figure 41B) following the compression and translation of the finger skin model against a flat surface with an interfacial friction coefficient of 0.4.

Characteristically, the Type 1 receptor sites experience a SED gradient within the dermal papillae in the vicinity of the Meissner site, with higher SED values experienced along the dermal-epidermal junction (DEJ) towards the leading edge. This area has the potential to affect the SED recorded at both the Merkel and the Meissner site (see Figure 41B). Additionally, large SED peaks are found above the dermal papillae inclined towards the trailing edge, whilst a smaller SED peak is present at the apex of the DEJ (which acts as a stress concentration site) at the location of the Merkel's touch dome. High SED values were also found towards the upper left of the dermal papillae.

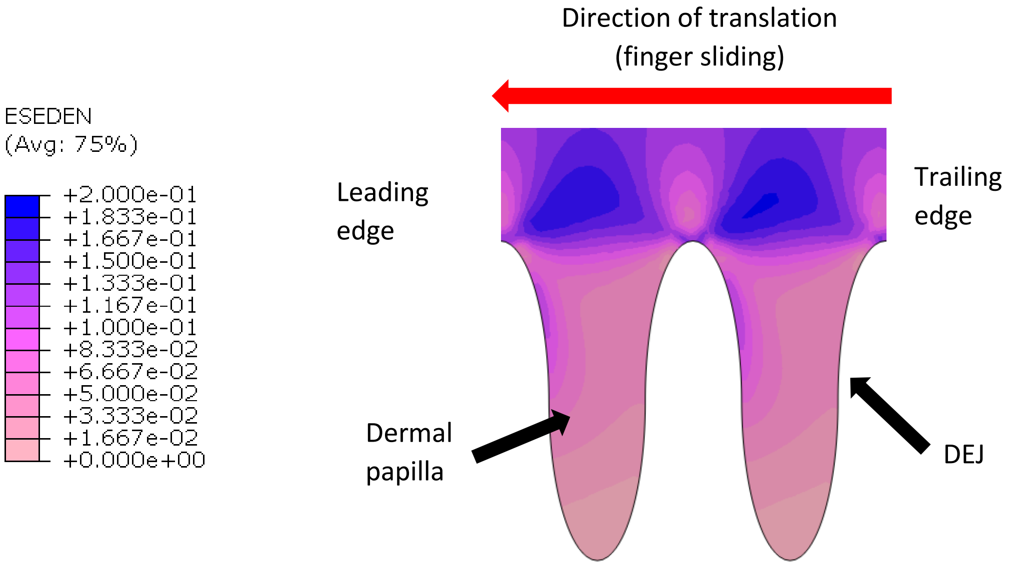

Figure 50: SED contour in the vicinity of the Type 1 receptor sites following translation of the finger skin model against flat surfaces with an interfacial friction coefficient of 0.4. Elemental SED values within the dermal papillae ranged from almost 0.0 Jm^{-3} at the bottom (indicated in light pink) of the dermal papillae to approximately 0.2 Jm-3 towards the peak (indicated with blue).

Figure 51 shows the average SED at each receptor site as the skin model is compressed (load 1 N) and translated against a flat, geometrically smooth, rigid surface with an intermediate applied friction coefficient of 0.4. The Merkel site experiences higher SED values than the Meissner site. The long-term average SED at the Merkel site, illustrated by the red line, is approximately 2.3 times larger (c. 0.07 Jm^{-3} vs. c. 0.03 Jm^{-3}) than that of the Meissner site, which is illustrated by the blue line. This is attributed to its position at the apex of the dermal epidermal junction, which acts as a stress concentration site.

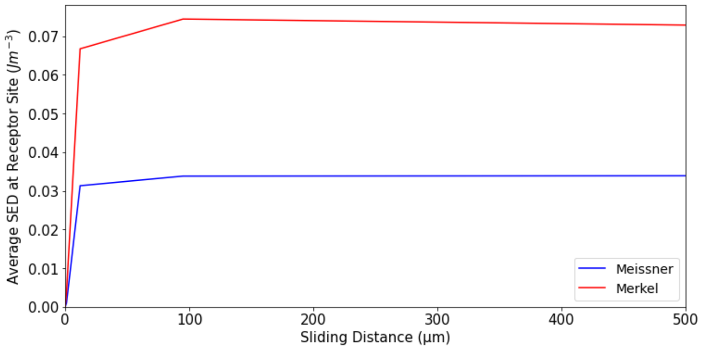

Figure 51: Average SED values at each receptor site following translation against a rigid, flat, geometrically smooth counter surface.

The SED distribution in the skin scales non-linearly with respect to interfacial friction coefficient. Figure 52 describes the effect of increasing the adhesive friction coefficient from μ = 0.1 to μ = 0.8 as the skin model was compressed and translated against flat, geometrically smooth surfaces. It was found that whilst changes in friction coefficient between μ = 0.1 and μ = 0.4 resulted in modest increases in SED at the receptor sites, further increases resulted in the emergence of large SED peaks, particularly above the dermal papillae.

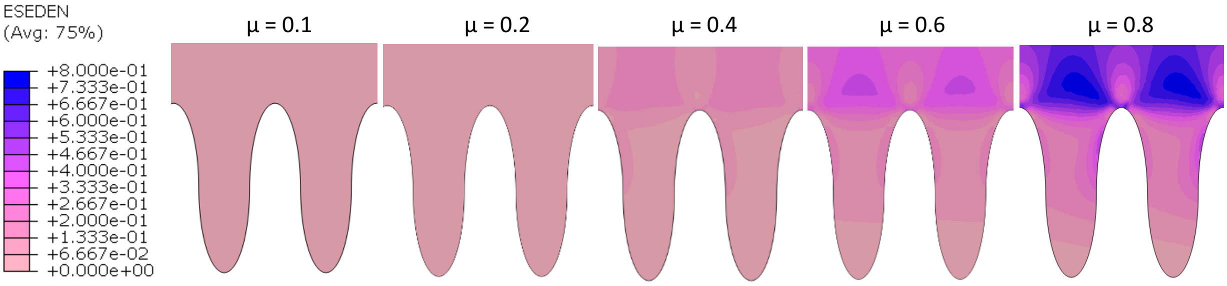

Figure 52: The effect of increasing the interfacial friction coefficient of the skin-surface interface on the SED distribution in the vicinity of the Type 1 mechanoreceptors.

The orientation of the SED contours within the vicinity of both receptors (i.e., above and within the dermal papillae) changed as the friction coefficient was increased from μ = 0.4 to μ = 0.8 (Figure 53). For μ = 0.4, the peak above the dermal papillae is inclined towards the trailing edge, whilst the peak within the dermal papillae is on the leading edge of the DEJ. However, the converse is true when the friction coefficient is increased to 0.8.

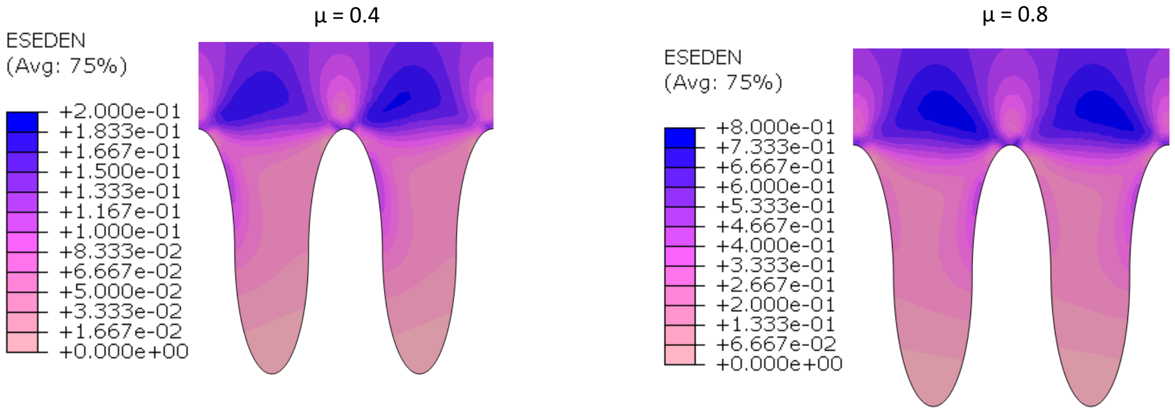

Figure 53: The SED contours change direction when the friction coefficient is elevated from μ = 0.4 (left) to μ = 0.8 (right).

5.3.2. Effect of Surface Topography on Type 1 Mechanoreceptor Excitation

After analysing the effect of adhesive friction on mechanoreceptor stimulation, the finger skin model was compressed and translated against ridged, sinusoidal surfaces. This was done to better understand the effect of surface textures and deformation friction on tactile perception. A representative intermediate value of interfacial friction coefficient of 0.4[23] was applied between the skin and counter surface, whilst topography of the surface was altered by independently varying wavelength and amplitude.

5.3.2.1. Merkel Site

Figure 54 illustrates the effect of altering surface topography on the strain energy density (SED) at the Merkel receptor site. Surface wavelengths approximating the fingerprint, such as 360 μm and 400 μm, will frequently be referred to as commensurate surfaces in this thesis. Figure 54A describes the effect of altering counter surface wavelength on the average SED at the Merkel site, following translation against surfaces with amplitudes of 40 μm (blue) and 80 μm (red). Characteristically, changes in surface amplitude and wavelength typically had a relatively small effect on the average SED at the Merkel site for surface wavelengths that did not approximate the fingerprint wavelength (360 μm). The average SED values generated at the Merkel site upon contact between the skin and non-commensurate surfaces were typically maintained between approximately 0.1 Jm^{-3} and 0.2 Jm^{-3}, which was generally higher than those achieved upon contact between the skin and geometrically smooth surfaces (0.07 Jm^{-3}). A similar trend was found for SED range (Figure 54B) which typically varied between 0.1 Jm^{-3} and 0.5 Jm^{-3} upon contact of the finger against non-commensurate surfaces.

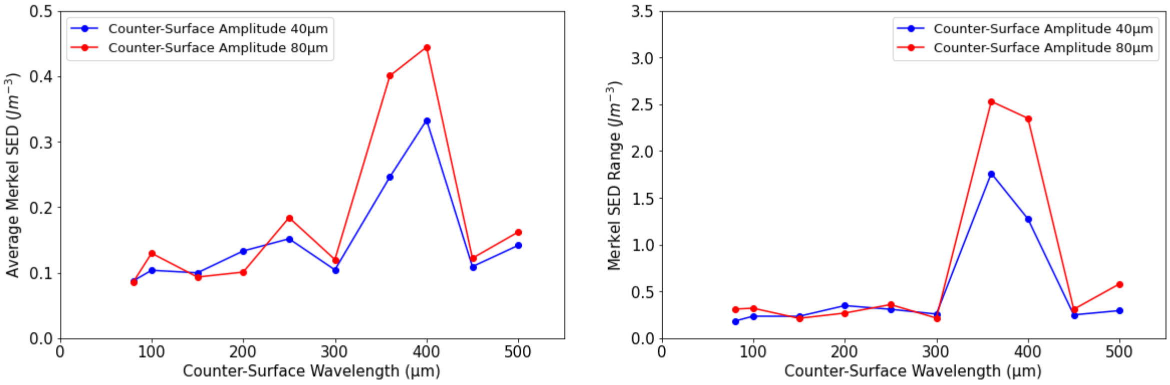

A B

Figure 54: The effect of surface topography on the average SED (A) and SED range (B) experienced at the Merkel site over the duration of sliding.

The general exception to the above is when the surface wavelength approximates the fingerprint wavelength (360 µm) and therefore, the ability of the fingerprint ridges to interlock against the counter surface topography increases (see Figure 46). From Figure 54A, contact of the finger skin model against surfaces with wavelengths of 360 µm and 400 µm result in significant increases in average SED recorded at the Merkel site, up to a peak of approximately 0.45 Jm^{-3} for the W400A80 surface. Furthermore, for these commensurate surfaces, it was found that increases in surface amplitude resulted in subsequent increases in SED recorded at the Merkel site. Figure 54B displays a similar trend between commensurate surfaces and the SED range experienced at the Merkel receptor site, which peaks at approximately 2.5 Jm^{-3} for surface W360A80. For commensurate surfaces, SED range is significantly higher than the average SED experienced at the Merkel site.

Figure 55A illustrates the SED signals generated at the Merkel site as the finger skin model is translated against different surfaces with wavelengths of 360 µm. Similar to Figure 45, the peaks and troughs of the signals can be attributed to the increase in contact area during interlocking (Figure 46) and the change in increased vertical motion of the skin as it traverses over the rigid asperities.

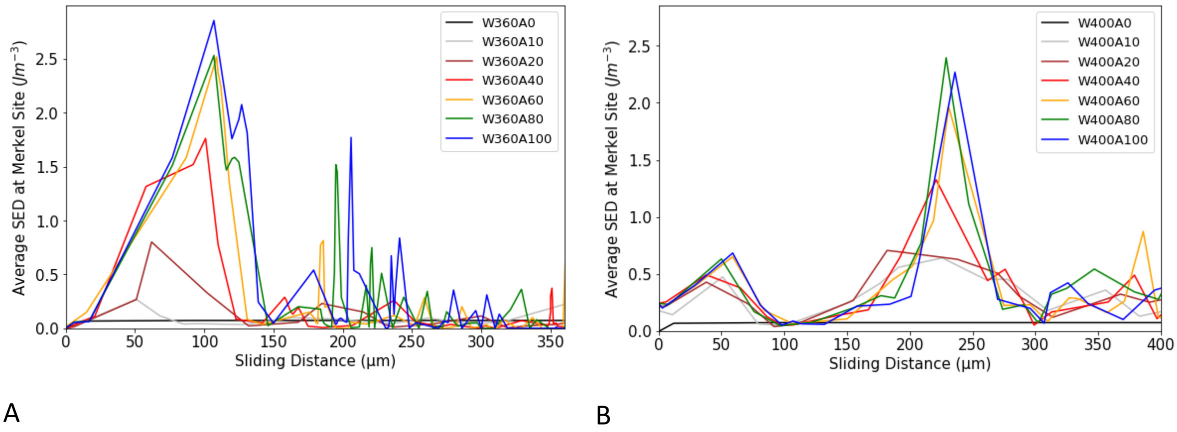

Figure 55: The Merkel SED signal generated by surfaces with wavelengths approaching that of the fingerprint. 360 µm counter surface wavelength (A), 400 µm counter surface wavelength (B).

Figure 55B illustrates the effect of translating the finger skin model against different surfaces with wavelengths of 400 µm on the excitation of the Merkel site. Larger surface wavelengths result in an increasing amount of fingerprint ridges that are no longer in contact with surface asperities. Therefore, each of the ridges that are in contact bear more load. The peak in SED signal generated after approximately 200 µm of sliding is the result of both the fingerprint ridges directly below the Type 1 receptor sites making contact with the surface asperities (Figure 56).

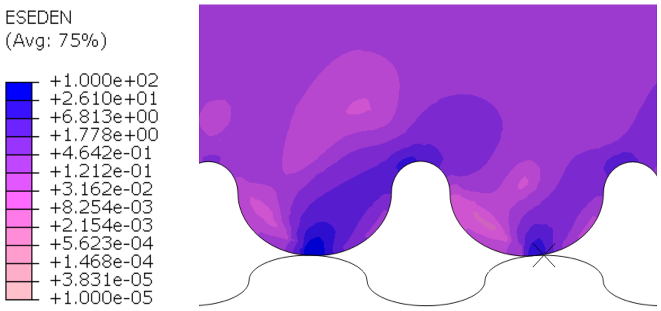

Figure 56: The fingerprint ridges directly below the Type 1 receptor sites making contact with surface asperities after approximately 200 µm of sliding.

For surfaces that do not approximate the fingerprint wavelength, increases in amplitude have generally been found to have negligible effects. This can be attributed to the fact that contact is generally made at the tip of the surface roughness. Therefore, a change in amplitude may only marginally alter the contact area by adjusting the width of the asperities. However, when exposed to a surface with 100 µm amplitude and 80 µm wavelength (W80A100), the Merkel site experienced elevated average SED values and a higher range of SED values. Figure 57 illustrates the effect of altering the amplitude of surfaces with wavelengths of 80 µm on the SED signal recorded at the Merkel site as the finger skin model was translated against the counter surfaces. It was found that for

W80A100 (blue line), the SED signal recorded at the Merkel site consistently exhibited a larger oscillatory behaviour than counter surfaces with lower magnitudes. This surface possesses the smallest wavelength and largest amplitude tested in this study, thereby reducing contact area against the stratum corneum and generating larger peak SED values which propagate through to deeper layers of the skin. This result suggests that the sharpness of surface asperities may play a significant role in defining our tactile experience.

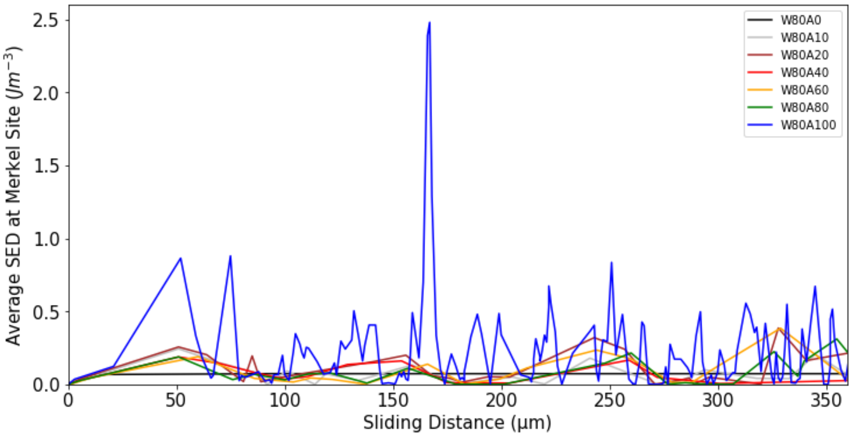

Figure 57: Graph illustrating the contact of the finger skin model against surfaces with wavelengths of 80 µm. The peak of the blue line displays the effect of the migration of the SED peak from the bulk of the dermis to the receptor sites.

After approximately 160 µm of sliding against surface W80A100, elevated SED levels were experienced in the region of the receptors. This was due to the migration of a SED peak from the bulk of the dermis to stress concentration sites along the dermal epidermal junction (DEJ) at the outermost edge of the dermis, which included the receptor sites (Figure 58). To the best of our knowledge, this specific situation has not been experimentally investigated in literature. Future work could focus on using identical surfaces in perceptive tests to better understand the effect of the W80A100 surface on tactile sensations.

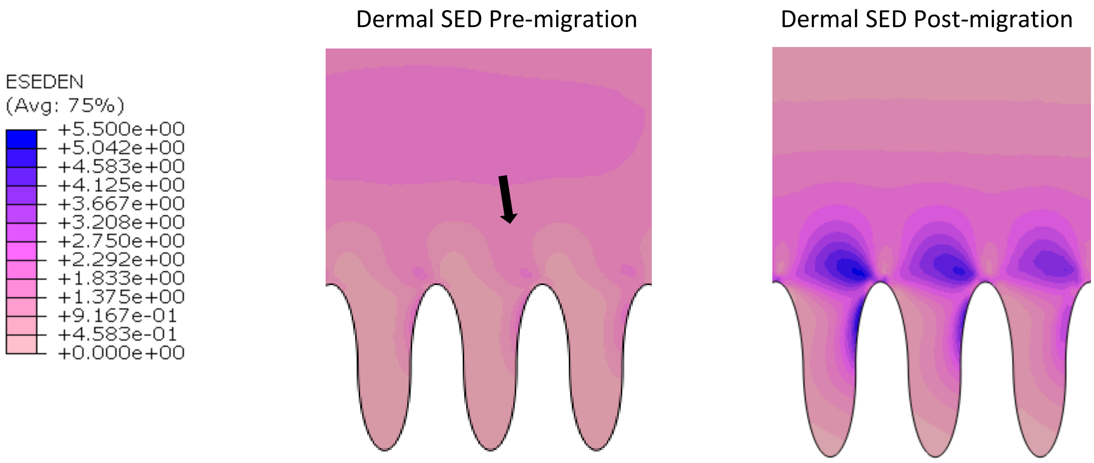

Figure 58: Diagram illustrating the migration (black arrow) and concentration of a small SED peak from within the bulk of the dermis to a much higher peak at the Type 1 mechanoreceptor site along the dermal-epidermal junction (DEJ) after the finger model was translated by approximately 160 µm against the W80A100 surface.

5.3.2.2. Meissner Site

Figure 59 illustrates the effect of altering surface topography on the strain energy density (SED) at the Meissner receptor site. Similar to the Merkel site, Figure 59A describes the effect of altering counter surface wavelength on the average SED at the Meissner site, following translation of the finger skin model against surfaces with amplitudes of 40 µm (blue) and 80 µm (red). In general, Merkel values of average SED and SED range were between 2 and 3 times higher than that of the Meissner site. For counter surface wavelengths that do not approximate the fingerprint wavelength (i.e., not 360 µm and 400 µm), changes in surface amplitude and wavelength typically have a relatively small effect on the average SED at the Meissner site. The average SED value was typically maintained between approximately 0.04 Jm^{-3} and 0.06 Jm^{-3}, which again is generally higher than the Meissner site experienced when in contact with geometrically smooth surfaces (approximately 0.03 Jm^{-3}). A similar trend was found for SED range which typically varied between 0.05 Jm^{-3} and 0.2 Jm^{-3} upon contact of the finger skin model with non-commensurate surface wavelengths (Figure 59B).

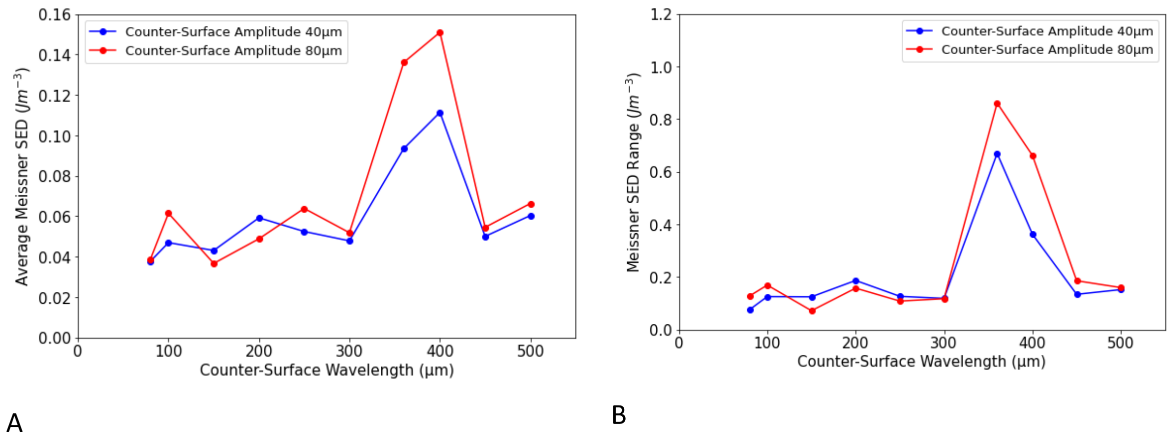

Figure 59: The effect of surface topography on the average SED (A) and SED range (B) experienced at the Meissner site over the duration of sliding.

Similar to the Merkel site, as the surface wavelength approached the fingerprint wavelength, elevated average and range SED levels were recorded at the Meissner site. For these commensurate surfaces, increases in surface amplitude generally resulted in subsequent increases in both average and range values of SED experienced at the Meissner receptor site. Figure 59A illustrates how surface W400A80 generated SED values of 0.15 Jm^{-3} at the Meissner site, significantly larger than values generated by non-commensurate surfaces. A similar trend was found to exist for SED range (Figure 59B), where surface W360A80 generated variations of approximately 0.8 Jm^{-3} at the Meissner site.

Figure 60A and Figure 60B show the SED signal generated at the Meissner site when the finger skin model is translated against surfaces with commensurate wavelengths; 360 µm and 400 µm respectively. As with the Merkel site, these wavelengths generate SED signals with significantly larger magnitudes than non-commensurate surfaces.

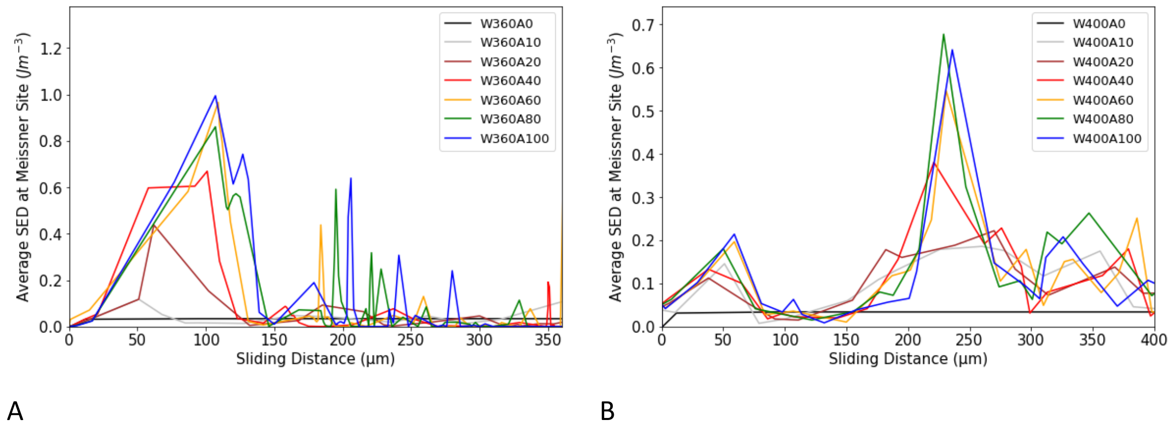

Figure 60: The Meissner SED signal generated by surfaces with wavelengths approaching that of the fingerprint. 360 µm counter surface wavelength (A), 400 µm counter surface wavelength (B).

Finally, increasing surface amplitudes between 10 µm and 80 µm appears to have negligible effects on average and range values of SED for wavelengths that do not approximate the fingerprint. However, as with the Merkel site, when exposed to surface W80A100, the Meissner site experienced elevated average and range SED values. This was due to the migration of a SED peak from the bulk of the dermis to the site of the receptor (Figure 57 & Figure 58 above).

5.3.2.3. The Effect of Commensurate Surfaces on Type 1 Receptor Stimulation

For both receptors there was a significant change in the SED profile when the counter surface wavelength approximated the fingerprint. The behaviour of the receptors within this region warranted further investigation. Therefore, in order to provide additional granularity, an intermediate amplitude of 40 µm was chosen whilst the surface wavelength was increased in 10 µm increments between 350 µm and 450 µm. Figure 61 illustrates the effect of counter surface wavelength on average (Figure 61A) and range (Figure 61B) SED values at the Merkel (red) and Meissner (blue) receptor sites. As before, it was found that both the average SED and SED range were consistently lower at the Meissner site than the Merkel site. At the Merkel site, it was found that as the surface wavelength approximated the fingerprint, there was a substantial increase in average and range SED values, indicating that the Merkel site may act as a focal point for SED signals for commensurate surfaces. Whilst the Meissner site exhibited similar patterns, this increase was less substantial, indicating that the Merkel site is more sensitive to strain energy density.

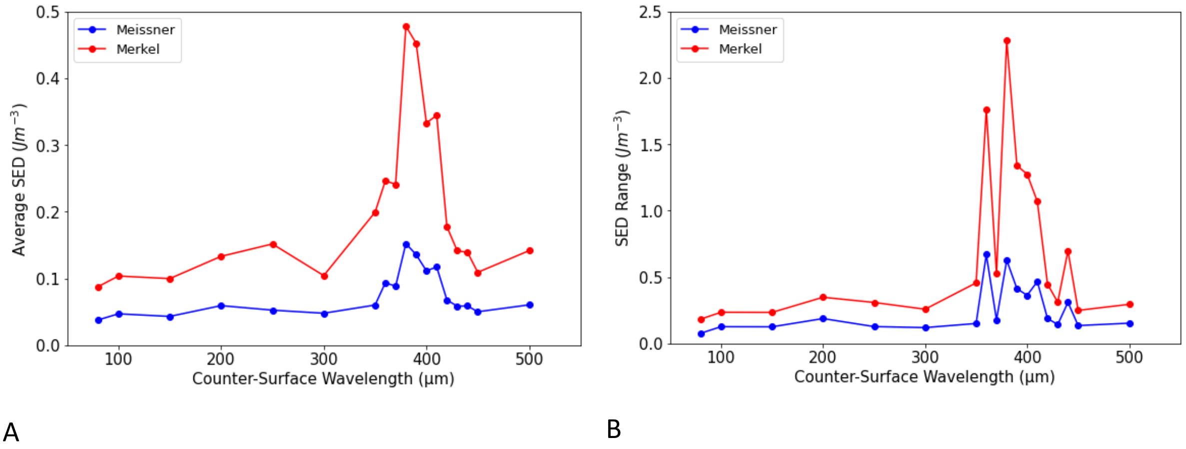

Figure 61: Average SED (A) and SED Range (B) for each receptor site. Further granularity has been provided for surface wavelengths between 350 and 450 µm in order to investigate the effects of the counter surface approximating the fingerprint wavelength.

For the Merkel site, average SED (Figure 61A) was elevated between 350 and 410 µm, reaching a peak of almost 0.5 Jm^{-3} at a surface wavelength of 380 µm. The SED range (Figure 61B) was elevated across a similar range of surface wavelengths; reaching a peak of almost 2.5 Jm^{-3} at a surface wavelength of 380 µm. It was found that the reduction in SED range for the W370A40 surface was the result of the SED peak falling outside of the analysed sliding distance and was thus an artefact of the implemented truncation requirements. Analysing over a larger translation distance beyond the truncation point yielded SED ranges with similar magnitudes to surrounding wavelengths (Figure 62). The impact of truncation was isolated to W370A40 and is considered further in section 5.4. Discussion.

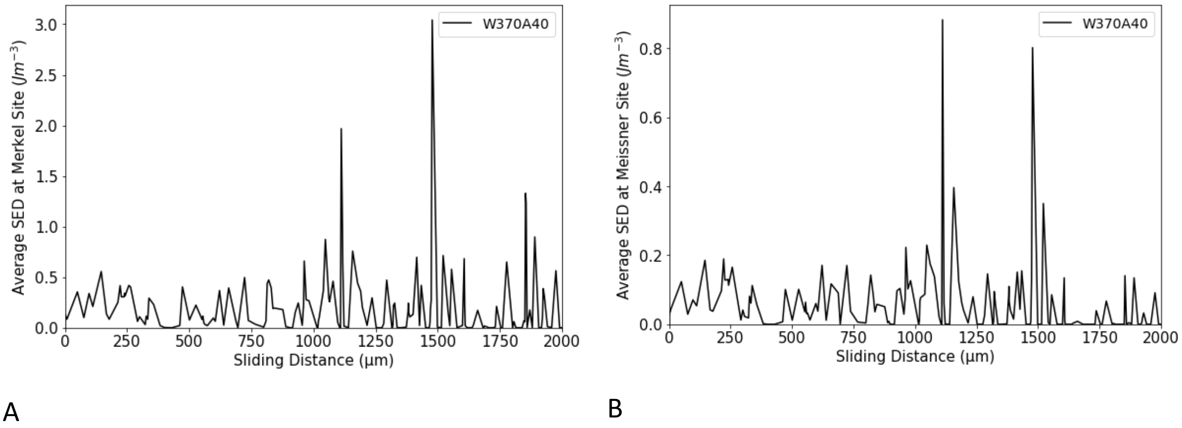

Figure 62: Merkel (A) and Meissner (B) SED signals beyond the truncation point for surface W370A40.

5.4. Discussion

Tactile perception can be considered to comprise four distinct processes.

1) Mechanical – The propagation of mechanical stimuli from the surface of the stratum corneum to our tactile receptors
2) Neurological – The transmission of impulses from the receptor level to our nervous system
3) Psychological – how the surfaces are perceived by the brain:
    a. Psychophysical - e.g., smooth, rough, hard, soft
    b. Affective – What emotions and memories do they evoke?
4) Behavioural – Our physical response e.g., increase or decrease pressure and speed of touch

The focus of this investigation was on the first, mechanical stage of tactile perception. Here, the effect of altering the adhesive friction coefficient on the SED at the Type 1 (high spatial resolution) mechanoreceptors sites was first analysed by compressing and sliding the finger skin model against various rigid, geometrically smooth surfaces. Following this, the effects of altering surface topography on the excitation of our Type 1 mechanoreceptors was then investigated. The amplitude and wavelength of periodic (sinusoidal), isotropic, rigid counter surfaces were independently varied to simulate the variation of a regular distribution of surface textures and asperities. The surfaces were then compressed and translated against the finger skin model whilst the SED at the receptor sites were recorded.

5.4.1. Adhesive Friction

Upon contact with flat surfaces, sites of maximum SED are found close to the trough of the dermal papillae (near the top of the Merkel's touch dome). This may be attributed to the peaks and troughs of the wave-like dermal epidermal junction (DEJ) acting as stress concentration sites, offering an explanation as to why the SED values of the Merkel site consistently exceed that of the Meissner site, which is located within the bulk of the papillae, a site of lower SED.

Similar to results found by Hamilton[240], it was found that the subsurface stress-state scales non-linearly with increases in friction coefficient (Figure 52). Modest changes in SED were recorded for initial increases in frictional coefficient from $\mu = 0.1$ to $\mu = 0.4$, whilst much more substantial increases were recorded from $\mu = 0.4$ to $\mu = 0.8$. During the latter interval, it was found that the maximum SED changed in both magnitude and orientation, as illustrated in Figure 53. Doubling the interfacial friction coefficient in the latter interval resulted in an approximate 4-fold increase in the SED distribution in the vicinity of the Type 1 receptors, reaffirming that adhesive fiction is a dominant parameter in modulating tactile perception and the discrimination of smooth surfaces[95,114,119]. It was found that the orientation of the SED contours changed as the coefficient of friction was increased from 0.4 to 0.8 (Figure 53). This may be attributed to the balance of tensile and compressive forces within the dermal skin layer as external applied shear stresses are increased. In general, it is known that when shear forces are applied to the finger surface, maximum deviatoric stresses have been found at the sites of the tactile mechanoreceptors[63]. However, presently, little is known about the effect of altering the orientation of the strain energy distribution within the receptor site itself on tactile perception. This opens up a potential avenue for further research. Changes in SED orientation at the receptor sites may be simulated by changes in the direction of sliding. The development of an anisotropic finger skin model that was able to consider joint dynamics and slip-stick[129] would be a crucial first step in better understanding the effect of sliding direction and SED orientation on receptor stimulation.

5.4.2. Rough Surfaces

A parametric study was conducted in which the skin model was compressed and translated against rough surfaces with varying sinusoidal dimensions, whilst the SED at the Type 1 receptor sites was recorded. This was done in order to gain insight into the effect of different surface textures on mechanoreceptor excitation and tactile perception.

Overall, it was found that the similarity of the fingerprint and counter surface wavelength plays a dominant role in modulating tactile experience during dynamic touch. Furthermore, texture spacing, or wavelength was found to be more significant than increasing the height or amplitude of the surface roughness features. These are consistent with findings from literature[13,63,101,103,111,241]. From Figure 54 & Figure 59, for surface wavelengths that did not approximate the fingerprint, average and range SED values at the sites of the Type 1 mechanoreceptors were slightly higher than those of flat surfaces with the same interfacial coefficient of friction (0.4), but did not change substantially. In contrast, for surface wavelengths that were commensurate to that of the fingerprint, it was found that average and range SED value at the Type 1 receptor sites were significantly elevated. This has been associated in literature with peaks in the spectral domain[63]. In these scenarios, there is an increased propensity for the interlocking of the fingerprint ridges against the troughs of the sinusoidal counter surface (Figure 46), increasing deformation friction. In these instances, increases in surface amplitude resulted in an increase in average SED and SED range, which can be attributed to the greater physical resistance encountered by the fingerprint as it traverses over taller surface features. Finally, the average SED and SED range experienced at the Merkel site were consistently greater than those experienced at the Meissner site. This difference was accentuated when the counter surface wavelength approximated that of the fingerprint. This is likely due to the presence of the stress concentration sites at the Merkel site. The results are summarised Figure 63.

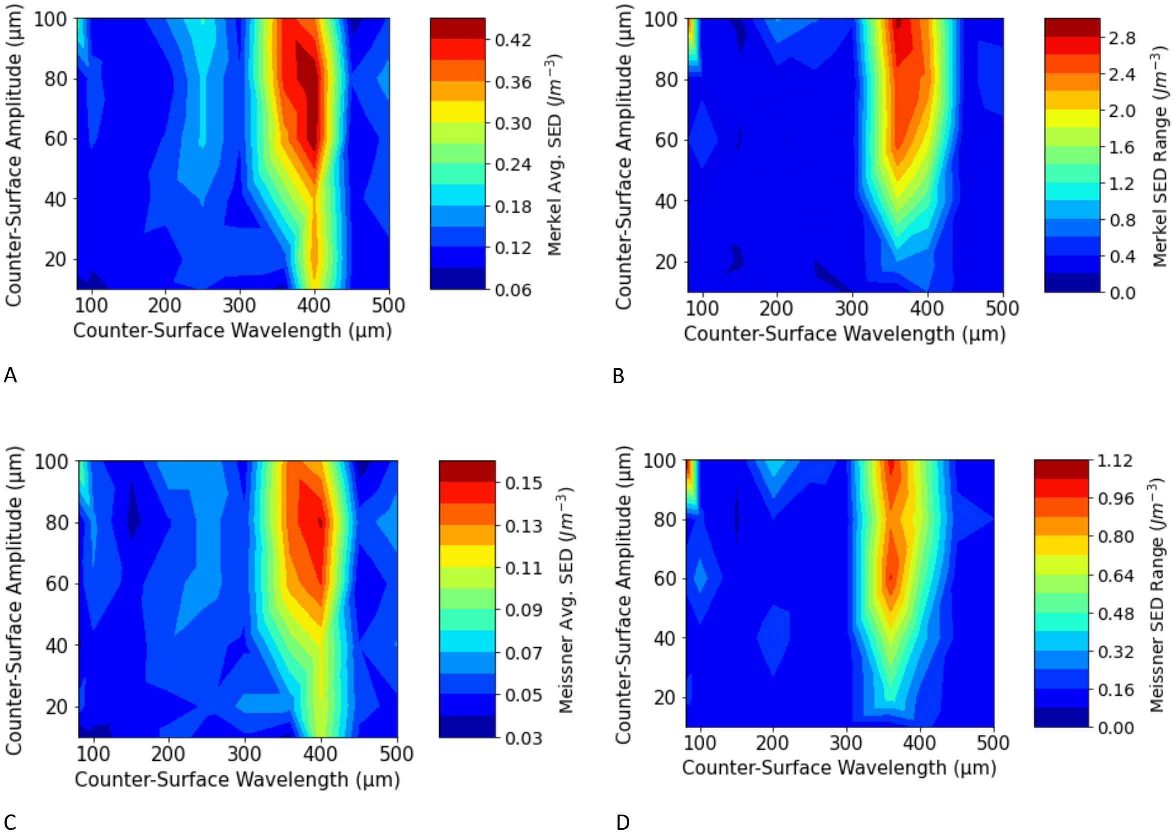

Figure 63: Surface plots illustrating the effects of altering surface topography on the Merkel cell's average SED (A), the Merkel cell's SED range (B), the Meissner receptor's average SED (C) and the Meissner receptor's SED range (D)

Whilst regular surface textures differ from most natural surfaces, they can be achieved synthetically. Based on the results of this study, the relative periodicity of the fingerprint and counter surface plays a very important role in modulating the average SED and SED range experienced at the mechanoreceptor sites. Surface topography can be augmented to create diminished or heightened sensations by fabricating surfaces which differ or approximate the fingertip respectively.

Surface design engineers and ergonomists can use this information to help target products towards specific demographics in order to elicit unique sensations. One would expect maximum stimulation to be achieved when the fingerprint and surface wavelengths are equal, thereby enabling maximum interlocking. However, from Figure 61, it is worth noting that peak average SED and SED range value can be achieved with surface wavelengths that are within the vicinity of the fingerprint wavelength, not just when they are exactly equal. Therefore, designers should be conscious of the range of values that fingerprint wavelengths can take amongst consumers when developing products.

5.4.3. Limitations

In order to measure the excitation of the mechanoreceptor sites on the microscale, very small finite element sizes were used, resulting in a finger skin model that consisted of over 94,000 elements, each with 8 nodes. Due to the model size, individual simulations could take over 24 CPU hours to complete. As a result, increasing the model's dimensionality from 2D to 3D would have resulted in a very large increase in simulation duration (exceeding a week per simulation). Therefore, in order to conduct the parametric study efficiently, a two-dimensional model was used to reduce computational expenditure; a methodology commonly used to numerically model tactile perception[34,63,69,241,242]. This inherently assumes that the mechanical and geometric properties of the model do not deviate with skin thickness. Whilst the fingerprint ridges are curved on the finger pad, they remain approximately parallel to one another on the fingertip (Figure 64), which is used extensively for tactile perception. Therefore, a 2D model was deemed appropriate.

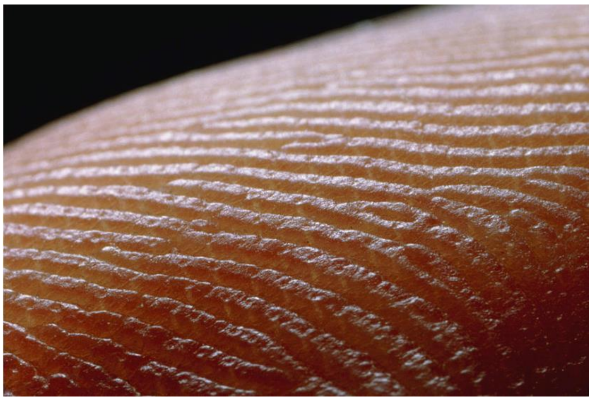

Figure 64: The fingerprint ridges are approximately parallel at the fingertip[243].

To help standardise the analysis of the SED signals generated at the receptor sites; the signals were truncated. This was done by only analysing the SED signal over a translation distance equal to the larger of the fingerprint or surface wavelength. For a surface with wavelength of 370 µm and amplitude of 40 µm, this requirement resulted in the omission of a large narrow SED peak from the analysis (Figure 56), resulting in a small underestimation of average SED, but a more significant underestimate of SED range. However, in general, the impact of the truncation requirements on the mean and range SED values did not affect the observed trends and derived conclusions of the study. Figure 65 illustrates how the surfaces approximating the fingerprint wavelength still generated significantly higher average and range SED values at both receptor sites, than surfaces which are less commensurate.

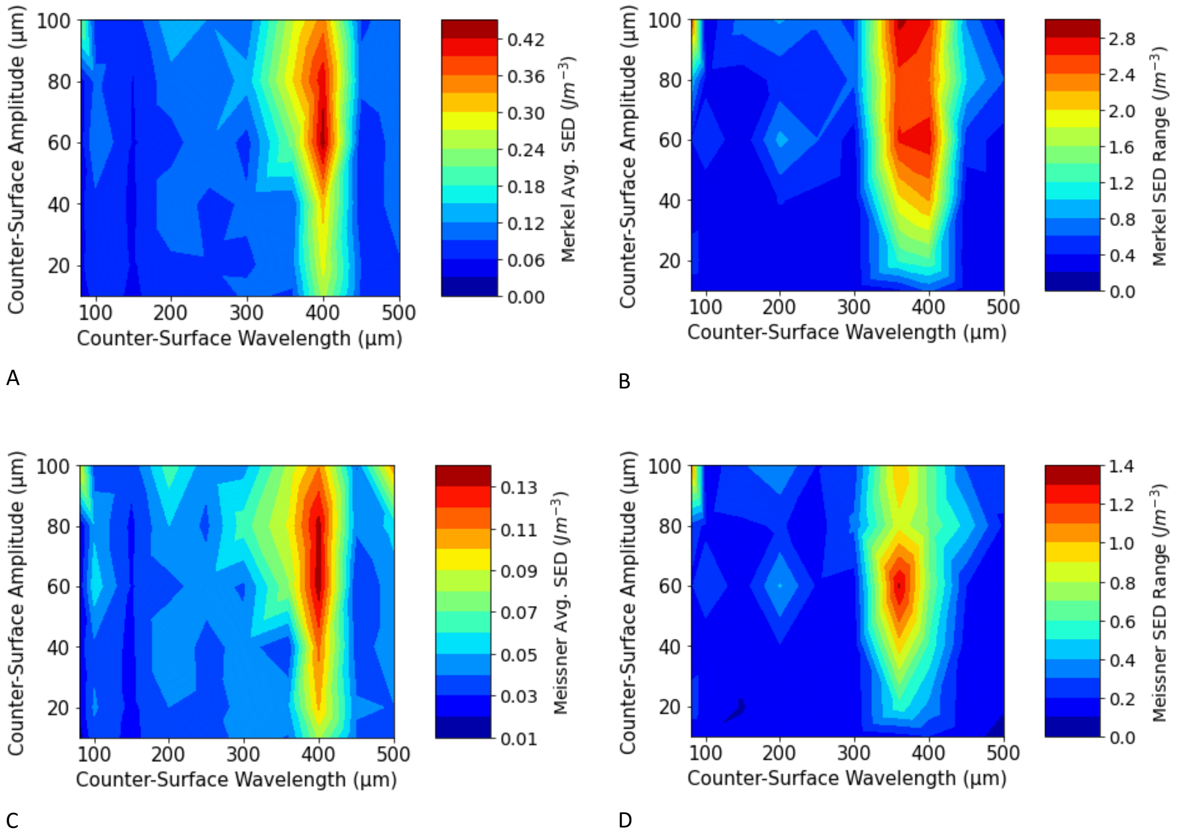

Figure 65: Surface plots illustrating the effects of altering surface topography on the average Merkel SED (A), Merkel SED range (B) average Meissner SED (C) and Meissner SED range (D) prior to truncating the signals.

To investigate the temporal effects of surface geometry on tactile perception, spectral analysis could be performed. Figure 66 illustrates the Fourier transforms of SED signals generated at the Meissner site following compression and translation against surfaces with wavelengths of 400 µm, prior to the signal’s truncation. It was found that peak frequencies were a function of translational velocity and surface geometry, as were subsequent harmonics. For example, with a surface velocity of 20 mm/s and a surface period of 400 µm, a peak frequency of 50 Hz is expected. However, the spectral signals generated presented secondary peaks that may have been related to incomplete and irregular SED cycles. Whilst the truncation requirements helped standardise the analysis of the SED signals, upon their enforcement the SED signals experienced at the receptor sites lose their periodicity and thus spectral analysis via Fourier transforms were no longer possible. If the software issues surrounding the auto-termination of simulations can be mitigated, full, standardised surface and fingerprint cycles could be guaranteed. This would generate longer, more uniform SED signals at the receptor sites, enabling more in-depth spectral analysis. The generated spectral responses could then be compared to the peak vibratory response of the receptors to determine the type of surfaces that provide the most stimulation.

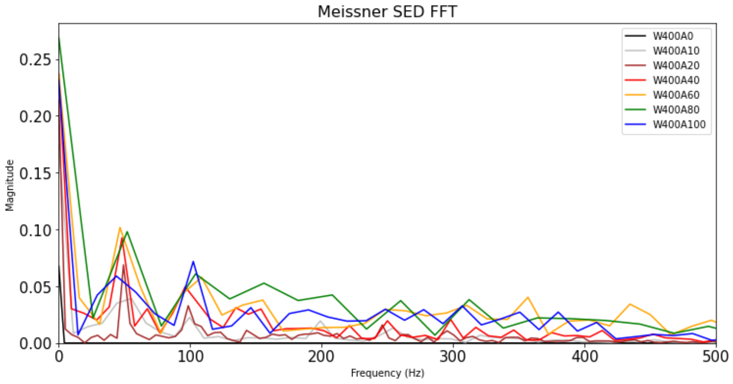

Figure 66: For the Meissner site, the Fast Fourier Transform (FFT) signals generated at each receptor site following compression and translation against surfaces with 400 µm wavelengths, pre-truncation.

5.4.4. Future Work

Future work could focus on comparing the results of our model with psychophysical experiments by translating the finger against periodic, isotropic, engineered surfaces in order to record users psychological and behavioral responses. Emphasis should be made on surfaces which possess periodicity that approximates that of the fingerprint ridges. Furthermore, the relative effect of spatial and temporal mechanisms on tactile perception could be investigated by analysing the effect of surfaces with smaller wavelengths on mechanoreceptor excitation. Through the use of surface profilers, finite element models representing the topography of day-to-day surfaces can be developed in order to analyse, on a microlevel, why some surfaces are more desirable than others. Fourier analysis can be performed to decompose the surface profile into its constituent sinusoids in order to assess the impact of specific topographical features on receptor stimulation. Finally, it is known that applied load and translational velocity affect tactile experiences (see section 2.1.3. Factors Affecting Tactile Perception). Future work could focus on both computationally and physically investigating the effect of load and velocity on the perception of different surface textures in order to take a step closer to understanding the necessary applied mechanical conditions required to enhance tactile sensations.

6. Investigating the Effects of Cosmetic Polymer Film Properties on Tactile Perception

6.1. Introduction

The global skin care market was valued at 155.8 billion USD in 2021 and is expected to increase to almost 190 billion USD by 2025[17]. Functionally, many of these skin care products involve the deposition of a polymer film against the skin surface (e.g., skin creams). Through optimizing the properties of the polymer film, it may be possible to develop products designed to elicit enhanced sensorial experiences amongst consumers. Currently, to the best of the authors knowledge, the effect of the presence and modification of cosmetic polymer films on tactile perception has scarcely been reported in literature[244]. This chapter details a pilot study in which the effect of modifying the properties of facial cosmetic films on their subsequent perception by the finger was investigated. Finite element models of the finger and facial skin were first developed before simulating the presence of a cosmetic polymer film at the interface. A parametric study was then conducted to establish the effect of modifying the mechanical, geometric and interfacial properties of the polymer film on Type 1 mechanoreceptor excitation within the finger skin model. Measures aimed at enhancing sensorial experience are then discussed before outlining key development points to improve the computational analysis of cosmetic products.

6.2. Methods

To simulate the tactile perception of a cosmetic product applied to the face, it was first necessary to design two new finite element models to represent the facial skin and interfacial polymer film. This section details the development of such models before describing the range of modifications applied to the interfacial polymer film during the parametric study.

6.2.1. Facial Skin Model Development

The purpose of this facial tissue was to provide a compliant boundary condition for the finger skin to translate across in order to simulate tactile perception of a cosmetic. Therefore, careful choice of the material properties of the facial tissue was required. Facial skin is typically less stiff than plantar skin, both macroscopically and on a layer-by-layer basis[5]. Therefore, upon contact between the finger and facial skin models, in the absence of any applied polymer film, the fingerprint ridges indent into the facial tissue.

6.2.1.1. Initial Model

A linear elastic, homogenous, non-time-dependent facial skin model was developed to help establish an initial approximation of the contact conditions between the finger and face. This single-layered skin model was prescribed a thickness of 1.98 mm[245] and given a width of 45 mm to mitigate any edge effects associated with translation against the 14.4 mm wide finger skin model. Mechanically, the facial tissue model was assigned an effective Young's modulus of 1.1 kPa and a Poisson's ratio of 0.48[6,246]. The finger skin model was then compressed with a load of 0.5 N against the facial skin model, before translating it for 10 mm at a velocity of 20 mm/s. Figure 67 illustrates how, upon compression and relative translation of the two skin surfaces, strain energy density (SED) propagates superficially across the softer facial substrate. Through varying the stiffness of the substrate, it was found that the lower the modulus of the facial skin, the higher the magnitude of the subsequent SED values in its superficial layers. Softer facial skin resulted in increased fingerprint ridge indentation, thereby increasing deformation friction and the magnitude of the SED field at the sites of the Type 1 receptors within the finger skin model.

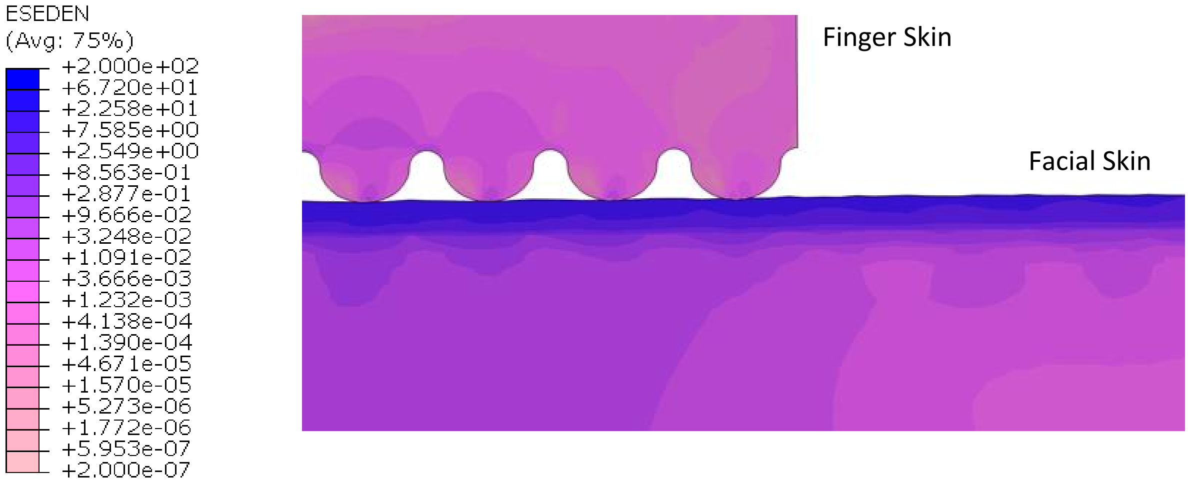

Figure 67: Stresses propagate near the surface of soft substrates following compression and translation against the finger skin model.

To provide a more representative boundary condition for the finger skin to make contact against, a refined facial skin model was developed in order to account for the layer's inhomogeneity and non-linearity.

6.2.1.2. Refined Model

To better represent the mechanical behavior of facial skin, a multi-layered, hyperelastic model was developed. This model was partitioned from a single geometry into individual layers, thereby inherently assuming no relative translation or delamination could occur between the skin layers. The developed facial skin model comprises an epidermal layer that combines the viable epidermis and stratum corneum. Combining the two individual layers increases the overall epidermal aspect ratio (60 µm thick and 45 mm wide) in order to prevent any simulation issues. The thickness of each layer of the facial skin model was assigned values from Chopra et al[155]. In the absence of specific mechanical data for multi-layered facial skin, each layer was assigned non-plantar hyperelastic properties to characterise the non-linearity of facial skin[5]. In non-plantar skin, the stratum corneum is 3 to 6 times thinner than the viable epidermis[4,156,245]. Therefore, a weighted average (or rule of mixtures approach) was used to prescribe a hyperelastic Ogden modulus to the epidermal skin layer with ratio 5:1 (viable epidermis modulus:stratum corneum modulus) from values in literature for each layer[5]. This resulted in an epidermal skin layer with an Ogden modulus of 21.69 kPa. The mechanical and geometric properties of the facial skin model are described in Table 10.

Table 10: Geometric and material properties of the three-layered facial skin model with a combined epidermis.

Skin Layer	Thickness (µm)	µ (kPa)	α (-)
Epidermis (E)	60	21.69	-13.04
Dermis (D)	1000	1.06	-13.04
Subcutis (S)	1000	25	5

The facial model comprised 55,463 quadratic plane strain elements (CPE8RH), with the finest seed size of 20 µm being located in the epidermis, whilst the coarsest was 80 µm within the hypodermis. As the purpose for this skin layer was to provide a compliant boundary condition for the finger skin model to slide against, this mesh was deemed sufficiently fine to characterise the deformation of the facial tissue.

6.2.2. Simulating Contact with Interfacial Polymer Films

In order to simulate the presence of a cosmetic polymer film, an additional FE layer was attached against the outer surface of the facial epidermal skin layer using tie constraints, thereby restricting displacement between the polymer film and the facial skin at their interface.

To conduct the parametric study, reference values were first established for the polymer film, before independently altering its material, geometric and interfacial parameters. With respect to material parameters, it is known that the elastic modulus of the film can vary considerably over 4 orders of magnitude (1 kPa and 10 MPa). Therefore, an intermediate modulus of 100 kPa was assigned to the reference model. The dry polymer film was assumed to be almost incompressible, thus the Poisson's ratio was set to 0.49. Dynamic mechanical analysis on polymer films during cycling loading at 1 Hz has resulted in tan(δ) within the range 0.05 – 1. In combination with the Kelvin-Voigt model, this yielded a viscoelastic time constant varying between 0.3 and 6 seconds. Therefore, an intermediate value of 3 seconds was chosen for the reference model. By comparing relaxation data from literature[247] with a first-order Prony series, a dimensionless shear modulus (g_1) value of 0.4 was assigned to the model and was varied between 0.1 and 0.4 in this study.

Geometrically, the cosmetic layer was given the same length as the facial skin to mitigate any edge effects. The thickness of cosmetic films can vary from 10 µm to 100 µm. The reference cosmetic layer was assigned a thickness of 50 µm. Finally, the reference model was assigned with an interfacial adhesive friction coefficient of 0.4, whilst being varied between 0.1 and 1 in the study. Table 11 describes the properties of the polymer film in the reference model and the variations included in this investigation.

Table 11: The polymer modifications tested in this study. All variations were tested incrementally and independently of one another.

Polymer Film Parameter	Reference Film Parameter	Variations in Study
Elastic Modulus, E [kPa]	100	1 – 10,000
Poisson's Ratio, ν [-]	0.49	-
Dimensionless Shear Modulus, g_1 [-]	0.4	0.1 – 0.4
Relaxation time constant, T [s]	3	0.3 – 6
Thickness, d [µm]	50	10 – 100
Adhesive Friction Coefficient, µ [-]	0.4	0.1 – 1

During touch, following the application of a normal load, the finger is compressed into a counter surface, before time-dependent effects within the finger and cosmetic layer result in the models undergoing differing degrees of stress relaxation. Therefore, three distinct loading stages were included in these simulations:

- Static Compression – Application of a 0.5 N uniformly distributed load to compress the finger skin model into the polymer film against the facial skin model
- Dynamic Rest – System held under constant conditions for 10 seconds to allow stress relaxation to occur. This enabled the finger skin to reach a relaxed state prior to translation, ensuring that only the temporal effects of finger sliding were recorded in the subsequent stage, as opposed to any residual viscoelastic effects during the compressive stage.
- Dynamic Translation – Finger skin model translated for 0.5 seconds across a distance of 10 mm at a velocity of 20 mm/s.

The interaction of the finger skin, polymer film and facial tissue is shown schematically in Figure 68. Throughout the translation period, the average strain energy density (SED) at each Type 1 mechanoreceptor site was recorded (Figure 68A) for each combination of polymer film (properties shown in Table 11, location shown schematically in Figure 68B).

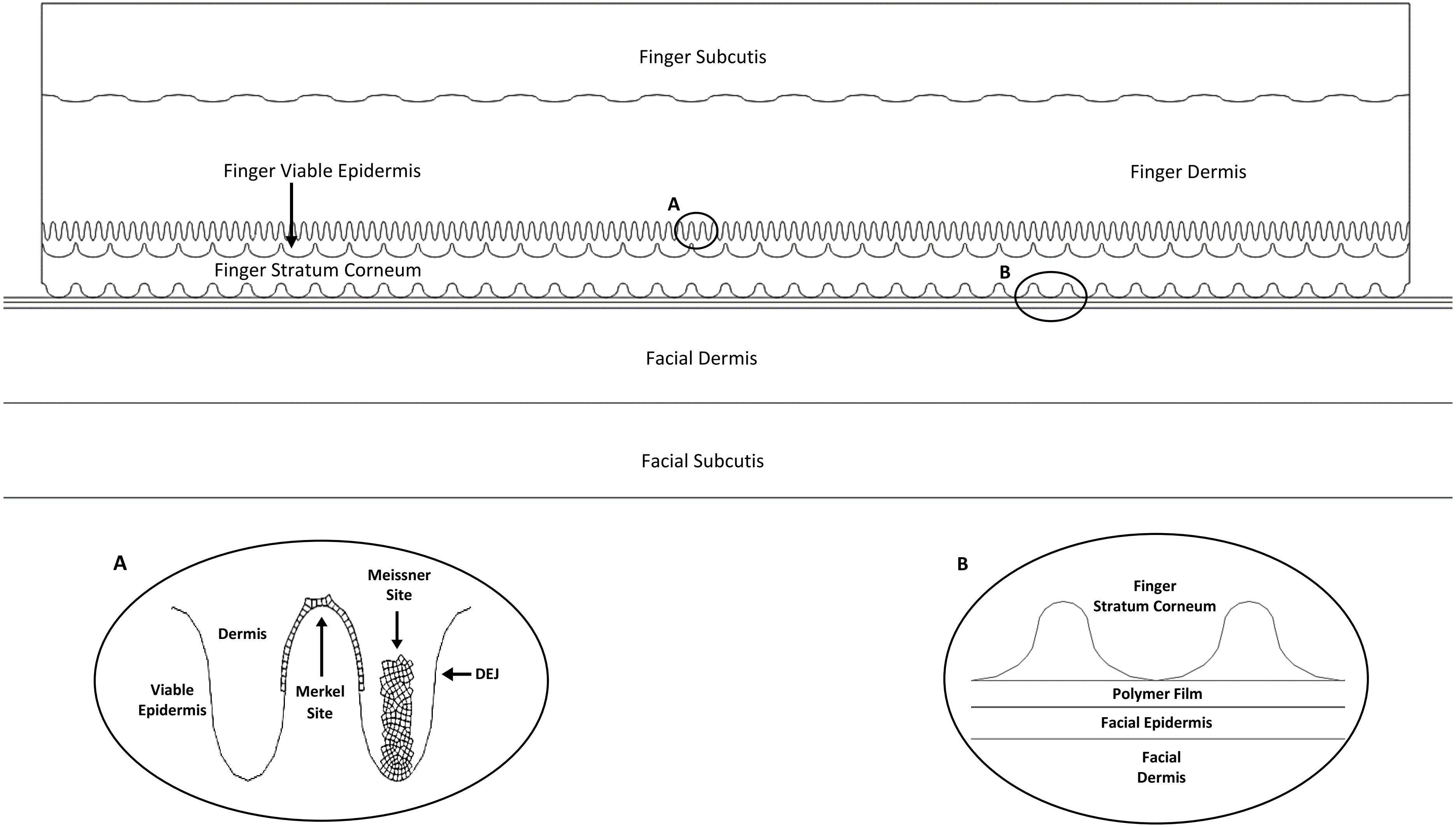

Figure 68: Schematic diagram of the finger and facial tissue models used in this study. Inset A: Schematic diagram of the finger's Type 1 mechanoreceptor sites along the Dermal Epidermal Junction (DEJ), where receptor excitation data will be extracted from in this study. Inset B: Schematic diagram of the cosmetic polymer film at the interface of the two skin models.

6.3. Results

In order to evaluate the effect of modifying cosmetic film properties on tactile perception, it was first necessary to understand the contact of the finger skin model against the facial skin model without the polymer film. Following this, the effect off applying the reference cosmetic film on mechanoreceptor excitation was analysed, before investigating the effects of modifying the polymer film.

6.3.1. Baseline Measurements

Figure 69 describes the strain energy density (SED) generated across each receptor site as the finger skin model was translated against the facial skin with (solid lines) and without (dotted lines) the applied reference cosmetic polymer film at the interface. Consistent with previous studies, the SED recorded at the Merkel site (red lines) was higher than that of the Meissner site (blue lines), which is attributed to its position atop the DEJ at a stress concentration site, compared to the Meissner site which is embedded within the dermal papillae (Figure 68A).

In both cases of an applied reference film and no film at all, the response of the Type 1 mechanoreceptors to the finger skin model sliding against the facial skin model can be characterised into three distinct Zones (Figure 69). Zone 1 describes the initial transient response as the finger skin model overcomes the initial static coefficient of friction at the inception of sliding. This Zone typically covers sliding distances from 0 mm to approximately 2 mm. The oscillatory SED response typically subsides by Zone 2, after which the SED at each site then stabilised and remained relatively constant until the finger model had been translated by approximately 6 mm. In Zone 3, further translation resulted in stresses propagating through the finger skin model across the Type 1 receptor sites, elevating SED values in the region. The stresses then subsided past the receptor site after approximately 8 mm of sliding, resulting in the stabilization of strain energy density in the region.

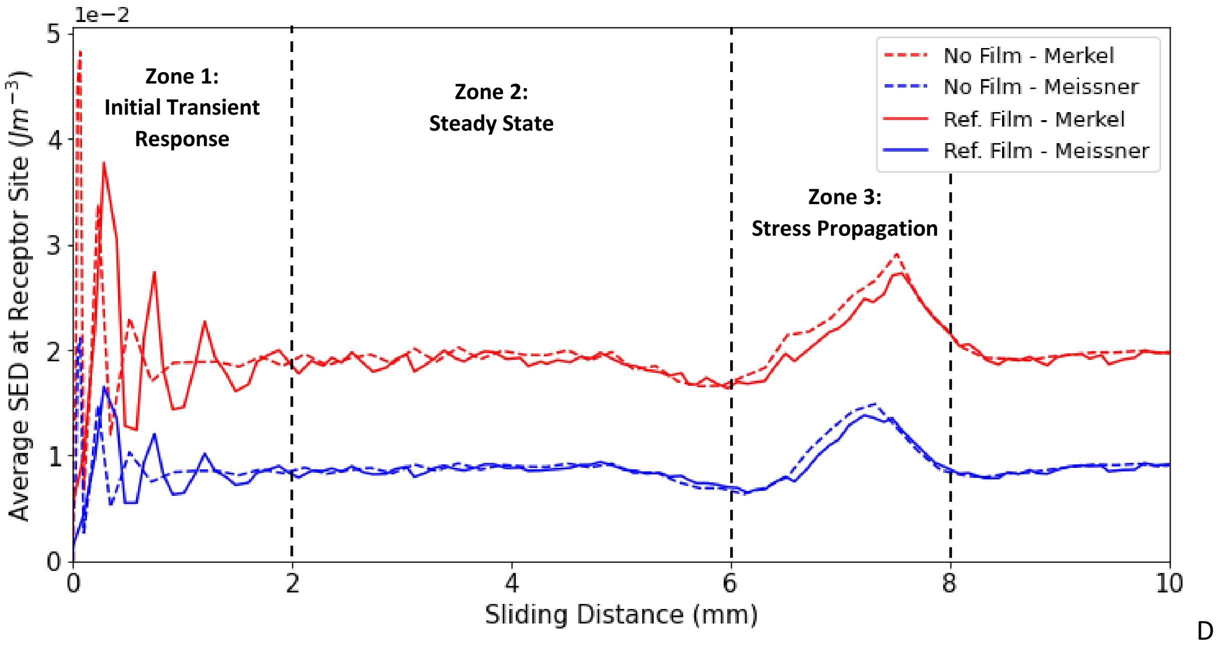

Figure 69: SED signal experienced at the Meissner (blue) and Merkel (red) receptor sites following the compression and translation of the finger skin against the facial tissue model with (solid line) and without (dotted line) an applied interfacial polymer film.

In Abaqus CAE, at the beginning of the translation stage, the size of the timesteps is dependent on the initial user-defined value. However, as the stage progresses, the resolution of the recorded time increments is defined by Abaqus CAE. The software attempts to incrementally increase the size of the timesteps up to a user-defined maximum value. The size of the timestep will only be increased if the previous increment has successfully converged, otherwise it is reduced. Whilst the user may implement a fixed time-step, if the timestep is too large the simulation will fail, and if it is too small the simulation duration will render the study no longer feasible. Therefore, variable timesteps were automatically defined by Abaqus CAE. However, as a result, an in depth, direct comparison of different simulations at exactly the same timestep was not always possible due to different increments failing within different simulations. This issue was particularly prevalent in Zone 1, where highly oscillatory SED signals at the receptor sites mean that outputting data at slightly different timesteps could result in the recording of vastly different stress-states. Therefore, any effect of polymer film modifications on the SED signal generated at the Type 1 receptor sites during Zone 1 will be stated, but firm conclusions will not be drawn. To establish such conclusions regarding Zone 1 behaviour, simulations with smaller, fixed timesteps in the initial stages of sliding would be required.

With regards to the initial transient response (Zone 1 – Figure 70), it was found that the presence of the reference film affected the magnitude of the oscillations of the SED signals generated at the receptor sites. Additionally, the distance required for the SED to stabilise was increased from approximately 1 mm for finger-facial contact, to 2 mm with the applied intermediate reference film. Neurologically, this initial oscillatory behaviour may be perceived by the rapidly adapting mechanoreceptors (Meissner and Pacinian corpuscles). Smaller, fixed time-steps at the inception of sliding would enable a more in-depth comparison of the effect of film presence at each of the receptor sites over the first few millimeters of sliding.

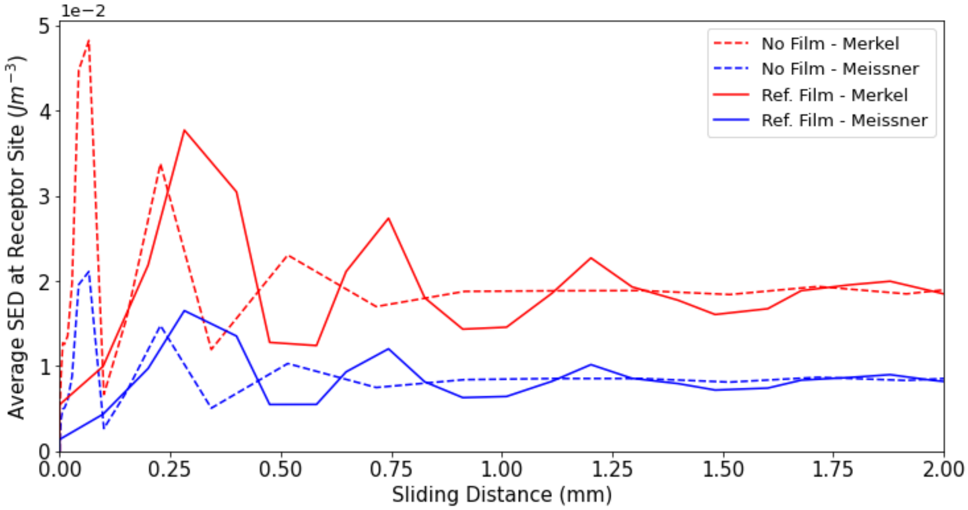

Figure 70: The initial transient response (Zone 1) of the receptors in response to the finger skin models contact with (solid line) and without (broken line) the reference polymer film.

Due to the propagation of stresses across the finger skin model, peak SED values migrate towards the site of the Type 1 mechanoreceptor sites during Zone 3 (Figure 71). Compared to direct contact of the finger skin model against the facial skin model, the presence of the reference film at the interface marginally reduced the magnitude of the strain energy density that propagated across each receptor site in Zone 3 (Figure 69).

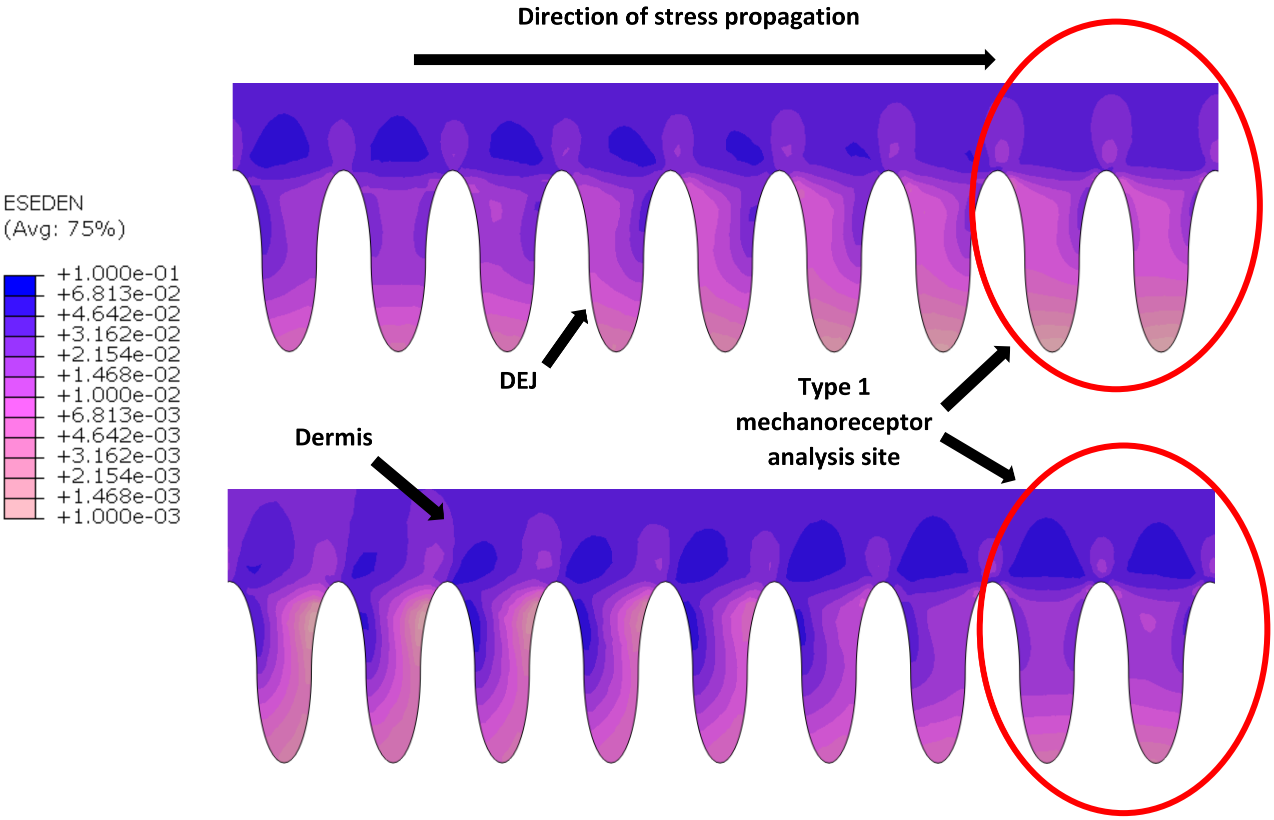

Figure 71: Stress induced SED propagation through the dermis of the finger skin model (top) to the Type 1 mechanoreceptor site (bottom) following contact with the facial skin model (without an applied polymer film).

6.3.2. Effect of Friction Coefficient on Mechanoreceptor Stimulation

To investigate the effect of tactile friction on the perception of cosmetic films, the interfacial friction coefficient between the stratum corneum of the finger and the polymer film adhered to the facial skin model was varied between μ = 0.1 and μ = 1.0. Figure 72 describes the effect of altering the friction from coefficient μ = 0.1 to μ = 0.6 on the SED excitation of the Meissner site.

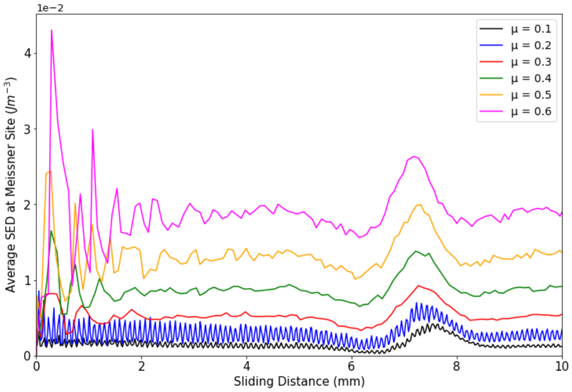

Figure 72: The effect of altering the interfacial friction coefficient between 0.1 - 0.6 on the SED recorded at the Meissner site.

It was found that increasing the interfacial friction coefficient from μ = 0.1 to μ = 0.6 resulted in SED values increasing by an increasing amount at the Meissner site, consistent with findings from section 5.3.1. Effect of Adhesive Friction on Type 1 Mechanoreceptor Stimulation. Despite exhibiting similar trends to the reference film, low friction coefficients (μ = 0.1 and μ = 0.2) resulted in highly oscillatory responses being recorded at the Meissner site. This oscillatory behaviour may be attributed to localised stick-slip between the fingerprint ridges and polymer surface and may represent vibrations propagating through the soft tissue, thereby offering additional stimulation of the rapidly adapting mechanoreceptors. Figure 73 shows the horizontal displacement of a single node at the tip of the fingerprint ridge as the skin is translated across a polymer film with an interfacial friction coefficient of μ = 0.2 (Figure 73A) and μ = 0.4 (Figure 73B). From Figure 73A, the oscillating horizontal displacement exhibited at the edge of the stratum corneum when μ = 0.2 is indicative of stick-slip, which is not the case when μ = 0.4 (Figure 73B). Higher interfacial friction coefficients between the fingerprint and polymer film results in increases in shear forces at the interface, which may restrict the oscillatory displacement of the fingerprint ridges, thus reducing the possibility of stick-slip. In order to develop smoother, more desirable products, further in-depth analysis of the effect of stick-slip on tactile perception would be required. This may include the use of simulations that incorporate joint dynamics and anisotropy, as well as velocity-dependent friction models.

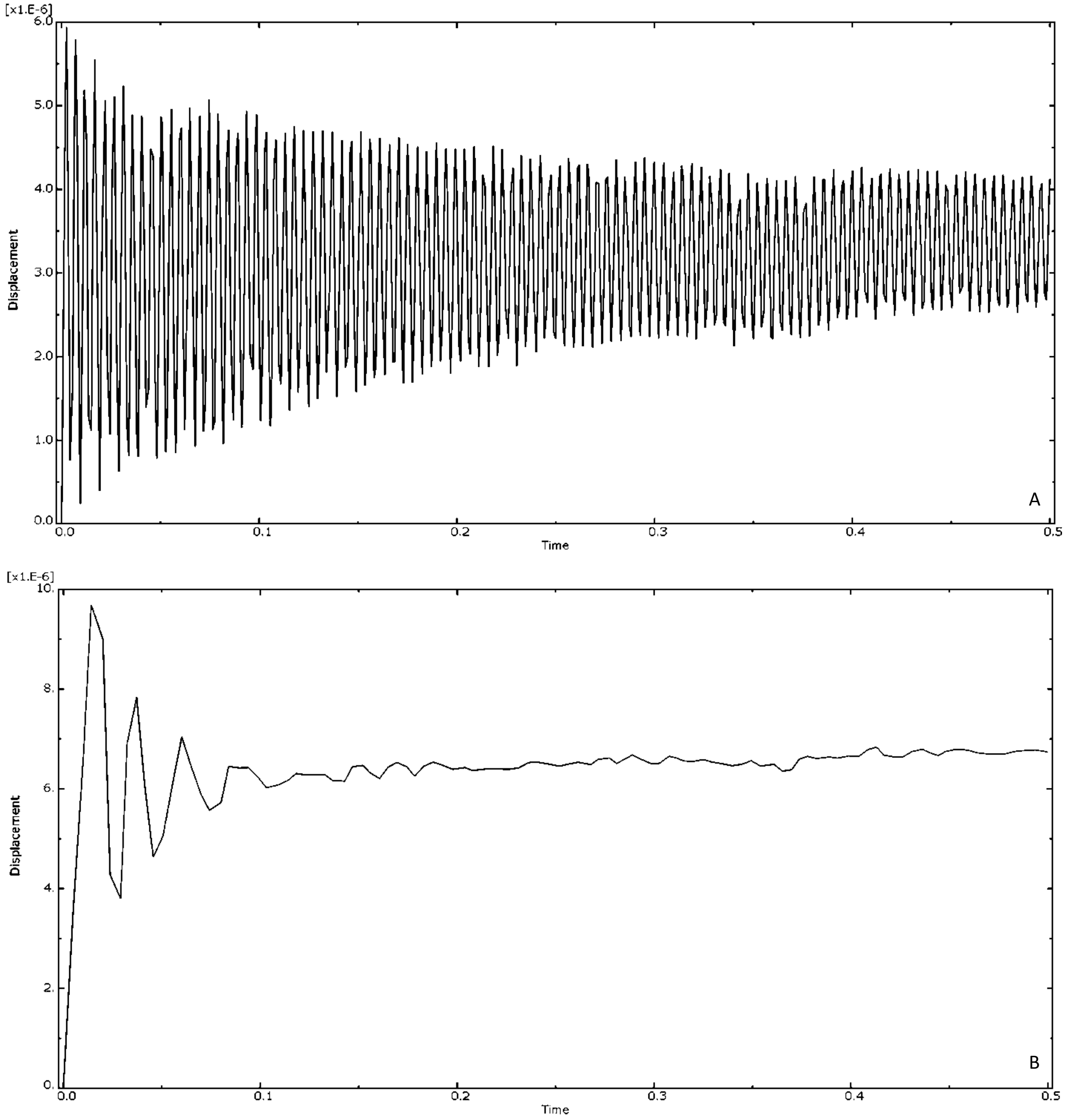

Figure 73: Displacement of a node at the edge of the fingerprint in response to translation against polymer film surfaces with friction coefficients of μ = 0.2 (A) and μ = 0.4 (B).

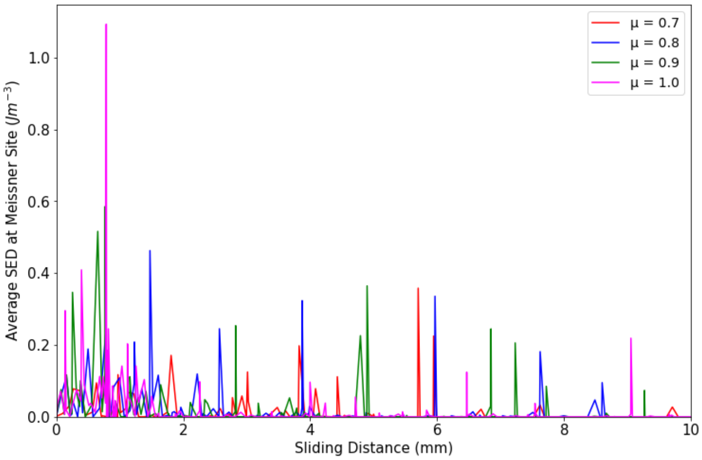

Figure 74: The effect of altering the interfacial friction coefficient between 0.7 - 1.0 on the SED recorded at the Meissner site.

Figure 74: The effect of altering the interfacial friction coefficient between 0.7 - 1.0 on the SED recorded at the Meissner site. describes the effect of increasing adhesive friction from μ = 0.7 to μ = 1.0 on the stimulation of the Meissner site. Larger frictional coefficients still result in higher peak SED values over the sliding duration e.g., when μ = 1.0, peak Meissner SED reaches approximately 1.1 Jm^{-3}, whilst for μ = 0.9, a peak value of 0.6 Jm^{-3} is recorded at the receptor site. However, the SED signal generated at the Meissner site differs considerably from the lower friction scenarios illustrated in Figure 72. Hamilton[240] has shown previously that extreme subsurface stresses can be achieved through contact between two solids when the interfacial friction coefficient exceeds 0.6. This effect is amplified in this investigation due to the many fingerprint ridges simultaneously contacting the polymer film, thereby exacerbating the subsurface SED distribution across the model.

Figure 75 describes the SED distribution across the Merkel site whilst the interfacial friction coefficient between the finger skin model and the polymer film is varied between μ = 0.1 and μ = 1.0. From Figure 75A, the magnitude of the SED distribution at the Merkel site is greater than that of the Meissner site for a given interfacial friction coefficient (note the scientific scale at the top of the graphs). However, the relative increase in SED caused by propagating stresses in Zone 3 is lower for the Merkel site than the Meissner site. The stresses propagate over the receptor sites after approximately 0.3 to 0.4 seconds of sliding (the time period corresponding to 6 to 8 mm of sliding). The 0.1 second duration of Zone 3 falls within the frequency range in which the Meissner receptor is most sensitive. This may indicate that the Meissner site is more ideally located to detect changes induced by stresses propagating through the tissue when the finger skin is translated across facial skin with applied cosmetics at the interface. Similar to the

Meissner site, increases in adhesive friction beyond 0.6 resulted in considerably larger variations in SED at the Merkel site (Figure 75B).

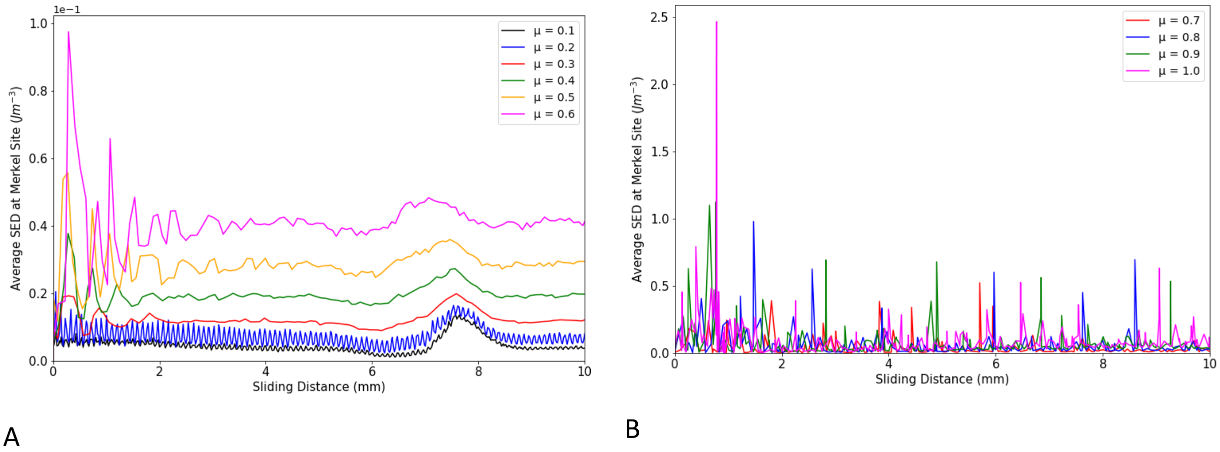

Figure 75: The effect of altering the interfacial friction coefficient between 0.1 - 0.6 (A) and 0.7 - 1.0 (B) on the SED recorded at the Merkel site.

6.3.3. Effect of Film Stiffness on Mechanoreceptor Stimulation

To investigate the effect of cosmetic polymer film stiffness on tactile sensations, the modulus of the film was varied between 1 kPa and 10 MPa whilst the SED distribution at the Merkel and Meissner site was recorded. Figure 76 displays the SED distribution at the Merkel site as the skin model was translated against a very soft polymer film (E = 1 kPa) and the reference film (E = 100 kPa).

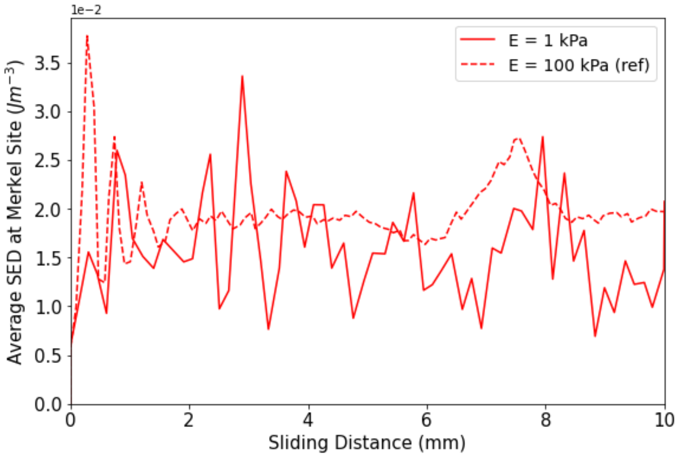

Figure 76: SED at the Merkel site following the translation of the skin against a 1 kPa polymer film (solid line) and the reference film (dashed line).

The considerable difference between the SED signals generated at the Merkel site upon contact with each of these films may be attributed to their compliance and time-dependency. Due to the viscoelasticity and low stiffness of the 1 kPa film, following compression of the fingerprint ridges against the cosmetic layer, the indentation grooves were not able to fully recover before the fingerprint ridges translated over them. This resulted in the finger skin model translating over an uneven surface (Figure 77), generating a highly oscillatory SED signal at the receptor sites for the entire duration of sliding as shown in Figure 76. As the polymer film stiffness increases further, its compliance decreases. By decreasing the deformability of the polymer film, the surface maintains its flatness, thereby decreasing SED variations experienced at the receptor sites during steady-state sliding (Zone 2).

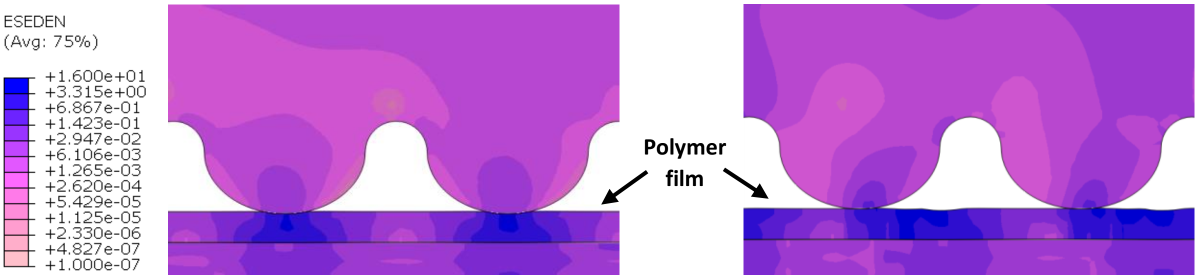

Figure 77: The indented 1 kPa polymer film surface prior to (left) and following (right) the commencement of finger sliding.

Figure 78 describes the SED response of the Merkel receptor following the translation of the skin model against stiffer polymer layers (5 kPa – 10 MPa, for clarity these are split up into two graphs). Figure 78A illustrates how as the polymer film is stiffened from 5 kPa to 100 kPa, the trend of the Merkel SED signal over the duration of sliding starts to approach that of the reference film (100 kPa). This is due a reduction in deformation of the polymer layers as stiffness increases, resulting in the surface becoming less uneven. Stiffer, smoother polymer surfaces reduced variation in the recorded SED signal at the Merkel site during steady state sliding (Zone 2 – sliding distances between 2 to 6 mm). Stiffer polymer layers (50 kPa and 100 kPa) also resulted in differences in the Zone 1 (sliding distances up to 2 mm) SED response at the Merkel site compared to softer polymer films (5 kPa and 10 kPa).

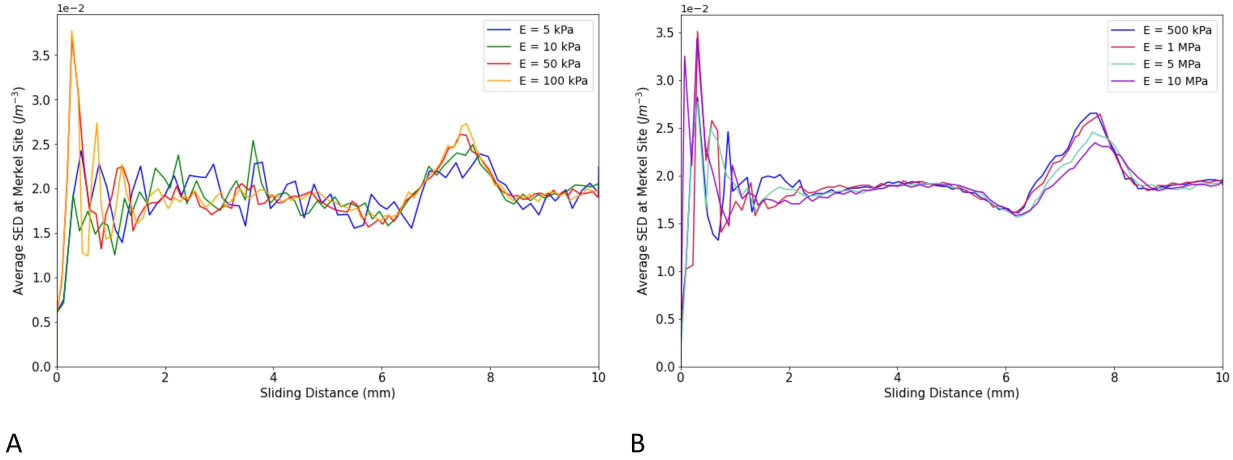

Figure 78: The effect of altering the stiffness of the cosmetic film from 5 kPa to 100 kPa (A) and from 500 kPa to 10 MPa (B) on the SED recorded at the Merkel site.

Figure 78B displays the SED signal recorded at the Merkel site as the cosmetic film is further stiffened from 500 kPa to 10 MPa. By considering both Figure 78 A & B, it was possible to analyse the effect of film modulus on the impact of stress propagation at the Merkel receptor site within Zone 3 (sliding distances between 6 – 8 mm). It was found that the maximum SED magnitude caused by stresses propagating over the receptor site reached a peak when polymer film stiffness was between 100 kPa and 500 kPa; with a maximum value of almost 0.0275 Jm^{-3} recorded when the polymer film stiffness is equal to 100 kPa. However, further increases in film stiffness results in a reduction in excitation of the Merkel site. This inverted U-shaped relationship between film modulus and maximum SED recorded at the Merkel site during Zone 3 is summarised in Figure 79. Overall, as the propagating stresses passed over the Merkel receptor site, the maximum SED experienced at the site fluctuated by approximately 15 % across the range of film moduli tested (5 kPa vs 100 kPa).

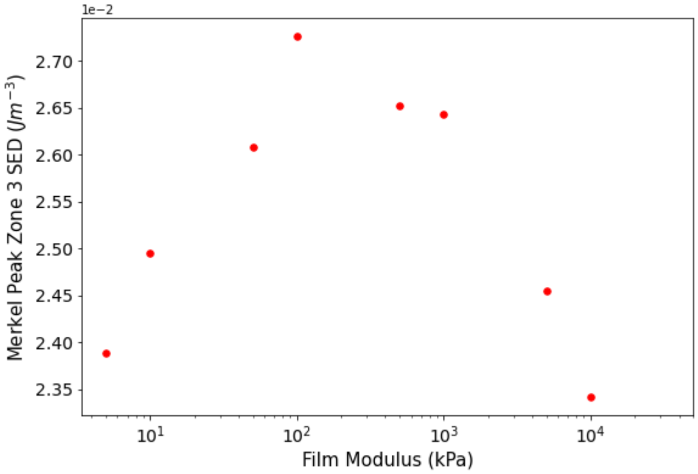

Figure 79: The inverted U-shaped relationship between polymer film stiffness and the peak SED generated whilst the stresses passed over the Merkel site.

As mentioned previously, strain energy density is a function of both stress and strain. Upon compression and translation of the finger skin model against a more compliant polymer film, the film will deform more whilst the skin will bear more load and exhibit higher stresses (Figure 80). The converse is true for the skin's compression against a stiffer polymer film. However, if the skin is compressed against a polymer film of intermediate stiffness, high values of stress and strain can be experienced within the tissue, elevating strain energy density values at the receptor sites, thereby generating the inverted U-shaped relationship between film stiffness and peak SED. Therefore, cosmetics companies should be conscious of the relative stiffness of deposited polymer films compared to surrounding skin tissue in order to influence the magnitude of SED generated at the receptor sites as stresses propagated over the receptor sites during finger sliding.

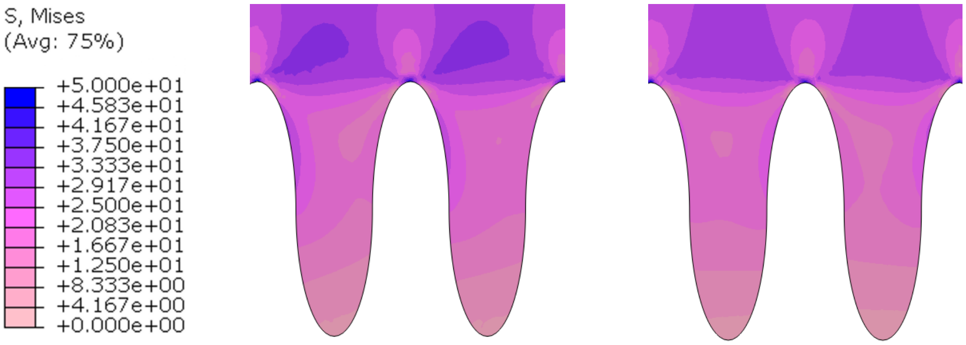

Figure 80: Deviatoric stress contours at the receptor site after 7.0 mm of the finger sliding against a 5kPa film (left) and a 10 MPa film (right).

Consistent with results found for the Merkel site, as the polymer film was stiffened from 5 kPa to 100 kPa, the oscillatory behaviour of the SED signal exhibited at the Meissner site within Zone 2 decreased. Additionally, during Zone 3, the peak SED magnitude exhibited an inverted U-shaped relationship with film modulus (Figure 81), with peak SED values generated upon the finger skin models contact with polymer films possessing stiffnesses between 100 kPa and 500 kPa. Overall, as stresses propagated over the Meissner receptor site, the maximum experienced SED fluctuated by up to almost 26% across the range of film moduli tested (5 kPa vs 500 kPa).

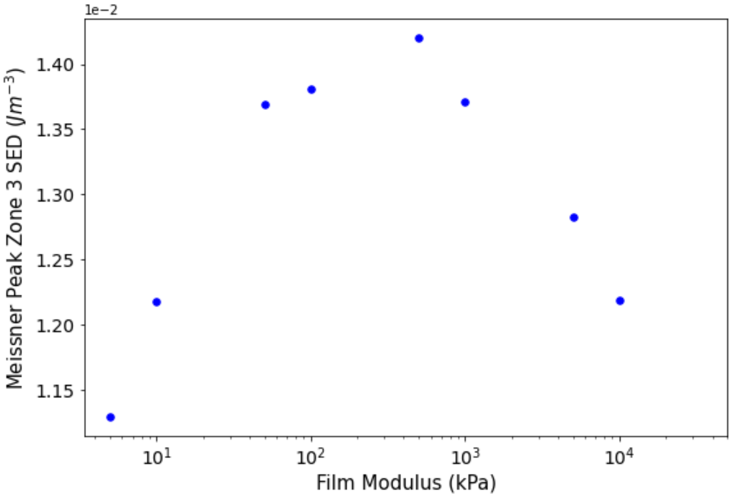

Figure 81: The inverted U-shaped relationship between polymer film stiffness and the peak SED generated whilst the stresses passed over the Meissner site.

6.3.4. Effect of Film Thickness on Mechanoreceptor Stimulation

The effect of cosmetic polymer film thickness on receptor stimulation was investigated by increasing the applied film thickness from 10 µm to 100 µm, in increments of 10 µm, before compressing and translating the finger skin model against it. For clarity, Figure 82 displays the SED signal experienced at the Merkel site following translation against alternating film thicknesses from 10 µm to 90 µm.

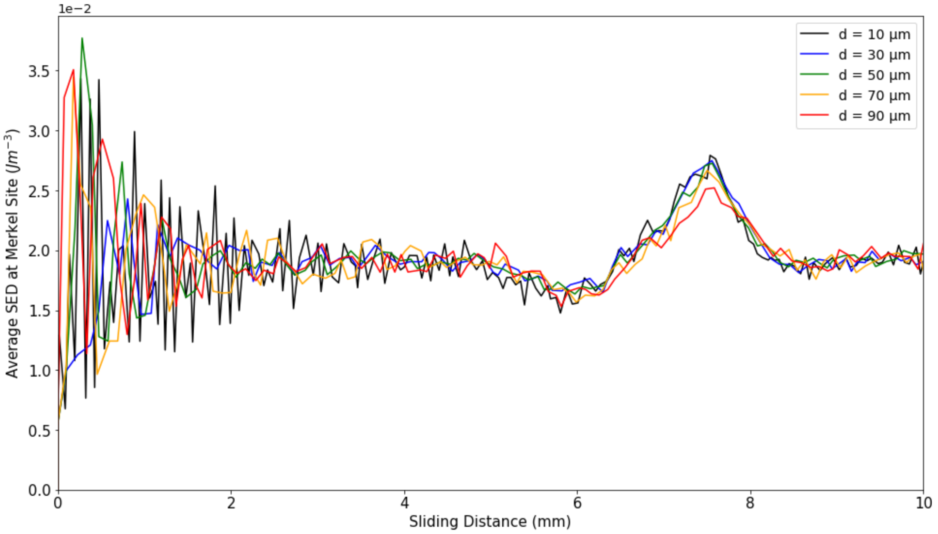

Figure 82: The effect of polymer film thickness on the SED signals generated at the Merkel site.

Figure 83 describes how film thickness had a noticeable effect on the initial transient response (Zone 1) and the stress propagation response (Zone 3) at the Merkel site. By reviewing the Merkel sites initial transient response (Zone 1), Figure 83A illustrates how changes in film thickness can influence the SED signal generated at the Merkel site at the inception of sliding. Due to the variable time-increments imposed by Abaqus, a detailed comparison of the Merkel SED exhibited for different polymer film thicknesses at the inception of sliding was not possible. However, a potential explanation for the differences between the SED signals in Zone 1 may involve the thicker polymer films deforming more around the fingerprint ridges, thereby influencing the contact area, which in turn effects the initial static frictional force that needs to be overcome for sliding to occur. It was found that changes in polymer film thickness had a negligible effect on the steady state SED signal generated at the Merkel site (Zone 2).

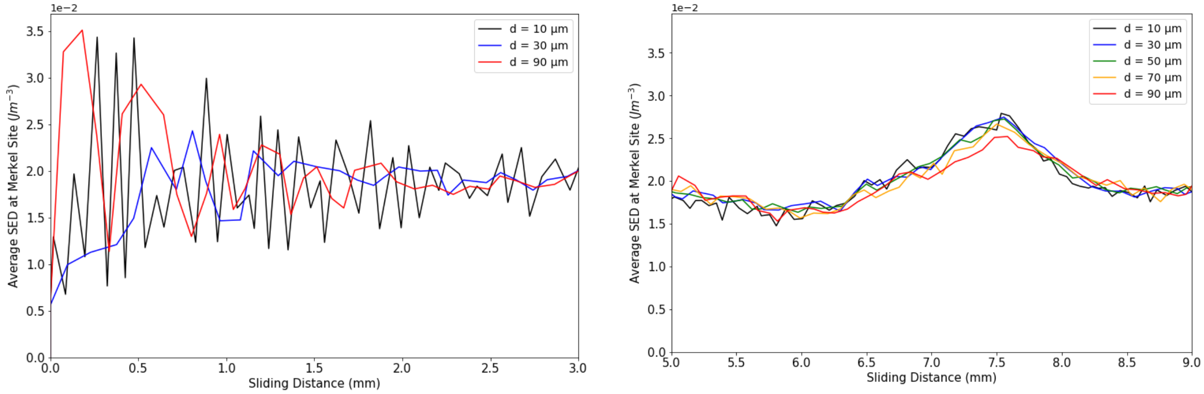

A

B

Figure 83: The effect of altering polymer film stiffness on the initial transient response (A - Zone 1) and the SED response during Zone 3 (B) at the Merkel site. For clarity, only thicknesses of 10 µm, 30 µm and 90 µm are shown in A.

Figure 83B includes the SED signal at the Merkel site whilst it experiences fluctuations caused by the stress propagation in Zone 3 (sliding distance from 6 to 8 mm). A negative correlation was found between the thickness of the polymer film and the peak SED generated whilst stresses propagated over the receptor sites during Zone 3 (Figure 84).

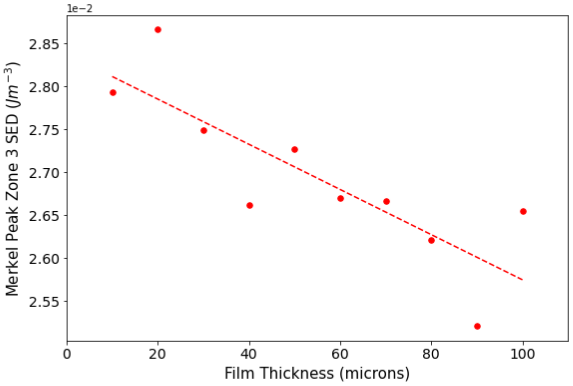

Figure 84: The effect of film thickness on the peak SED magnitude generated at the Merkel site as it was exposed to stresses in Zone 3.

This may be attributed to thinner films deforming less around the fingerprint ridges, resulting in lower contact areas between the two surfaces and thus higher localized stresses within the superficial layers of the skin. These thinner films resulted in higher stresses and strains propagating through the stratum corneum of the finger skin towards the sites of the Type 1 mechanoreceptors (Figure 85).

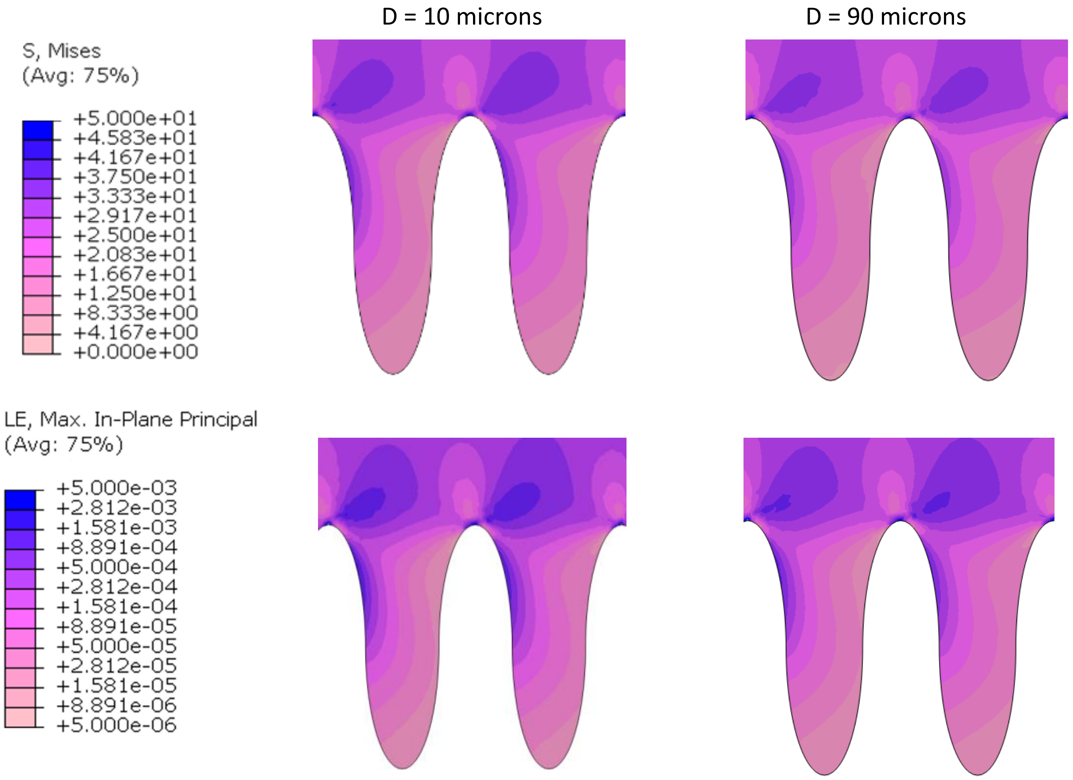

Figure 85: The deviatoric stress (top) and logarithmic strain (bottom) at the Type 1 mechanoreceptors sites following 7.4 mm of sliding against a 10 micron (left) and 90 micron (right) thick polymer film.

Similar trends were found with the Meissner site, where thicker polymer films were found to reduce the peak SED recorded at the Meissner site during Zone 3 (Figure 86).

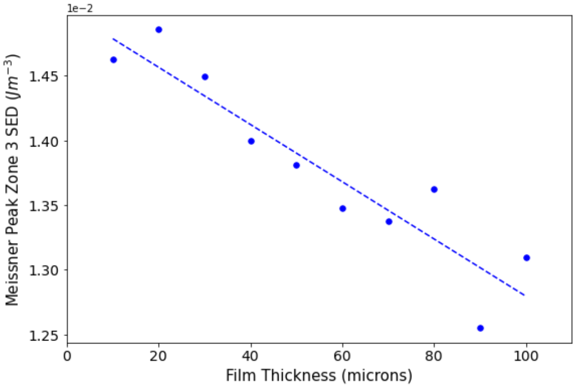

Figure 86: The effect of film thickness on the peak SED magnitude generated at the Meissner site during Zone 3.

6.3.5. Effect of Film Viscoelasticity on Mechanoreceptor Stimulation

As previously discussed, following the compression of the finger skin model against the polymer film, both the finger skin model and polymer film were given 10 seconds to relax before being translated for 0.5 seconds at a speed of 20 mm/s. Strain energy density (SED) is a function of both stress and strain. For the reference film, following 10 seconds of relaxation (prior to translation), it was found that whilst deviatoric stresses decreased during relaxation, strain increased by a greater than proportionate amount, leading to a subsequent rise in SED (Figure 87). A similar process is experienced within the polymer film.

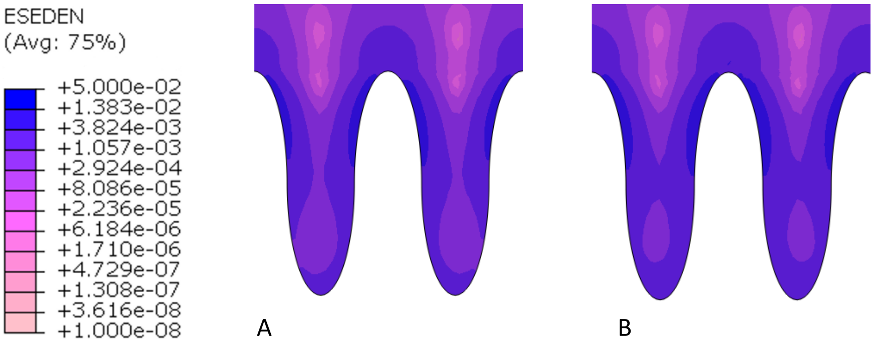

Figure 87: Rise in SED experienced in the vicinity of the Type 1 receptor sites pre- (A) and post- (B) relaxation.

In order to investigate the effect of altering the viscoelasticity of the polymer film on Type 1 mechanoreceptor stimulation during the translation stage, the dimensionless shear relaxation modulus (g_1) and time constant (T) were independently varied whilst the strain energy density was recorded at each receptor site.

6.3.5.1. Dimensionless Shear Modulus

Figure 88A illustrates the effect of altering the dimensionless shear modulus, g_1, of the interfacial polymer film between 0.1 and 0.4 on the SED signal exhibited at the Merkel site whilst the finger skin model was translated against the facial skin model. It was found that increases in g_1 had negligible effect on the Merkel site during both steady state sliding (Zone 2) and during the stress propagation phase (Zone 3). However, by examining Zone 1, (sliding distance 0 mm – 2 mm) it was found that modifying g_1 influenced the initial transient SED signal recorded at the Merkel site (Figure 88B). Similar trends were exhibited at the Meissner site.

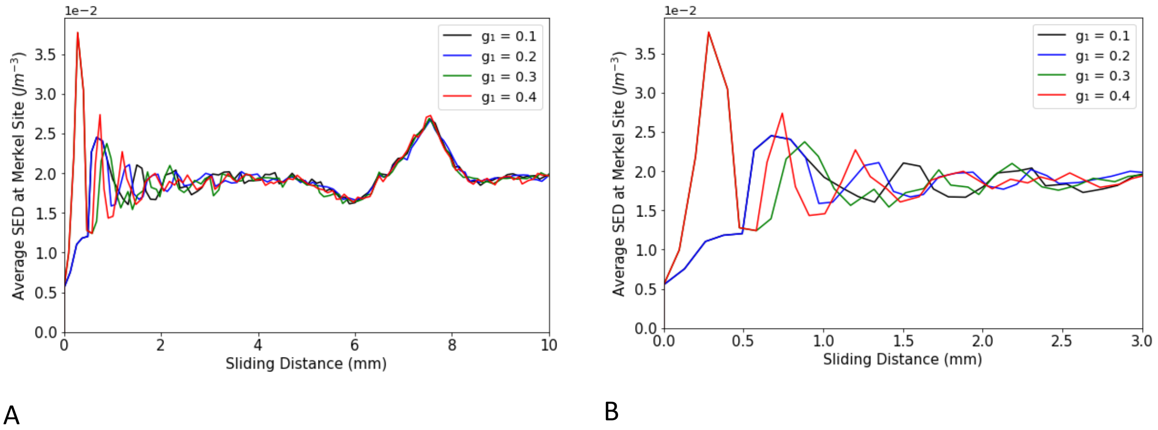

Figure 88: The effect of increasing dynamic shear modulus on the SED signal generated at the Merkel site for the whole 10 mm translation distance (A) and Zone 1 specifically (B).

A possible explanation is that the difference in initial transient response at the receptor sites is attributed to a difference in stiffness of the polymer film at the beginning of the translation stage. During the Dynamic Rest stage (relaxation for 10 seconds prior to translation), by using a first order Prony series, increases in the value of g_1 from 0.1 to 0.4 result in decreases in the time-dependent dimensionless shear relaxation modulus, g_t (Table 12). This relaxation term is then applied to the Young's modulus of the polymer layer, thereby reducing its stiffness. These more compliant polymer films may slightly increase the contact area with the fingerprint ridges, thereby increasing adhesive friction. Therefore, the SED generated at the receptor sites upon the inception of sliding may differ slightly as the finger tries to overcome the initial static coefficient of friction.

Table 12: The effect of altering g1 on the time-dependent dimensionless shear modulus.

g_1	g_t/g_0 (%)
0.1	90.4
0.2	80.7
0.3	71.1
0.4	61.4

6.3.5.1. Time Constant

Figure 89 illustrates the SED experienced at each receptor site following the translation of the finger skin model against polymer films with time constants varying from 0.3 seconds to 6 seconds. Figure 89A displays the effect of increasing the viscoelastic time constant of the polymer film on the SED response of the Merkel site. Similar to alterations in dimensionless shear relaxation modulus, changes in time constant had neglible effect on the steady state (Zone 2) or Zone 3 SED response of the Merkel site.

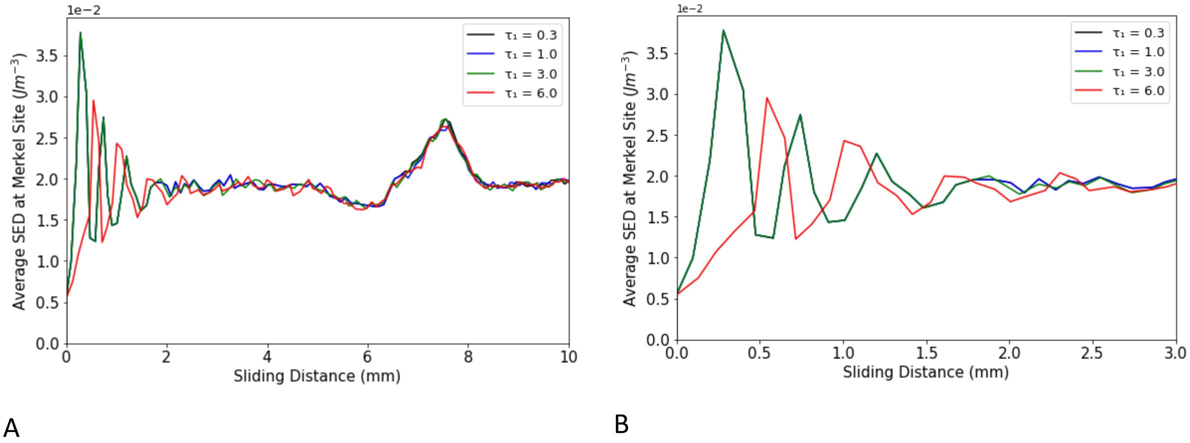

Figure 89: The effect of increasing viscoelastic time constant on the SED signal generated at the Meissner site for the whole 10 mm translation distance (A) and Zone 1 specifically (B). Similar graphs presented for the Merkel site also (C and D).

From Figure 89B, during Zone 1, the Merkel site appeared insensitive to increases in time constant from 0.3 seconds to 3 seconds; however further increases of the time constant affected the generated SED signal. A similar effect was recorded at the Meissner site. The difference in SED signal experienced at the receptor sites for polymer films with a time constant of 6 seconds may be attributed to the stiffness of the polymer layer. Using a first order Prony series, Table 13 illustrates the effect of increasing time constant from 0.3 to 6 seconds on the value of g_t following 10 seconds of rest after the fingers skin model was compressed against the polymer film (Dynamic Rest stage).

Table 13: The effect of increasing viscoelastic time constant on the time-dependent dimensionless shear modulus.

Time Constant (s)	g_t/g_0 (%)
0.3	60.0
1.0	60.0
3.0	61.4
6.0	67.6

Prior to translation, there is negligible difference in the time dependent shear modulus (and thus Ogden modulus) for polymer layers with time constants between 0.3 seconds and 3 seconds. However, a time constant of 6 seconds results in the polymer layer not being fully relaxed at the inception of sliding. Slightly stiffer polymer films would deform less at the inception of sliding and result in smaller contact areas forming against the fingerprint ridges. A reduction in contact area would reduce adhesive friction and thus lower the resistance to motion upon sliding, thereby prompting a smaller SED response from the receptor sites.

6.4. Discussion

With the year-on-year increase in the size of the global skincare market, developing premium products that can enhance sensorial experiences amongst consumers offers cosmetics companies the chance to gain a competitive edge. This study involved developing and utilizing finite element models to investigate the effect of altering the properties of cosmetic polymer films deposited on the face on their subsequent perception within the finger. Initially contact between the finger and facial skin was simulated by compressing and translating the skin models against each other. Following this, an intermediate reference cosmetic polymer film was applied to the facial tissue. The mechanical, geometric, and interfacial properties of the reference film were then independently varied whilst the strain energy density signals generated at the sites of the high spatial resolution (Type 1) mechanoreceptors within the finger skin model were recorded. Overall, it is hoped that the results of this study (summarised in Table 14) could be used to develop cosmetics that enhance tactile experience.

Table 14: Summary of the result of polymer film modifications on the excitation of Type 1 mechanoreceptors for each Zone.

Parameter	**Zone 1** **Initial transient response** **(approx. 0-2 mm)**	**Zone 2** **Steady state response** **(approx. 2-6 mm)**	**Zone 3** **Stress propagation response** **(approx. 6-8 mm)**
Friction	Reduction in friction resulted in substantial reduction in SED magnitude and (in extreme cases) increased oscillatory motion due to localised stick slip		
Stiffness	Modifications affected SED signals generated at each Type 1 receptor site; simulations with smaller, fixed initial time steps are required to draw firm conclusions	Films with stiffnesses below 50 kPa resulted in increased oscillatory behaviour in Zone 2	Inverted U-Shaped relationship
Thickness		Negligible	Increases in film thickness reduced peak SED
g_1		Negligible	Negligible
Time constant		Negligible	Negligible

From this study, altering interfacial friction coefficient had the largest effect on the SED signals generated at the Type 1 (Merkel and Meissner) receptor sites over the entire duration of sliding compared to the other polymer film modifications tested. It was found that modifying the material and geometric properties of the polymer film predominantly affected the SED signal generated in Zone 1 (initial transient response) and Zone 3 (stress propagation response). These modifications had negligible effect on the SED signal generated in Zone 2 (steady state sliding), with the exceptions of very compliant polymer films.

Smoother, low friction surfaces have frequently been correlated with pleasant or desirable sensations in literature[2,14,104,109,110]. Through examining the SED signals generated by low interfacial friction coefficients, it may be concluded that lower SED magnitude, with higher oscillatory responses, may stimulate the Type 1 receptors to produce these desirable sensations. If this is the case, then thicker, softer films should also be utilized to reduce the Zone 3 SED response and increase the oscillatory response during Zone 2. This result corroborates those found in literature, where increases in cream film thickness have been correlated with increases in smooth perception[244].

6.4.1. Limitations of This Study

In this investigation, during the Dynamic Rest stage, the finger and polymer film were held at constant loading conditions for 10 seconds prior to the translation, giving them sufficient time to almost completely relax. The exception to this was the polymer film with a time constant of 6 seconds (see section 6.3.5.1. Time Constant). As a result, the effect of viscoelasticity on film and finger modulus during the translation stage may be diminished due to the extensive relaxation that had already occurred prior to finger sliding. In the absence of the Dynamic Rest stage, both the finger skin and polymer film would have behaved with a higher stiffness as no relaxation would have occurred prior to the Translation stage. Due to the reduction in their compliance, it is hypothesized that the finger skin and polymer film would have experienced higher stress levels and lower strain values. It was found that by omitting viscoelasticity entirely from the simulation, the skin model was unable to relax, resulting in higher SED values at both receptor sites for the entire duration of sliding in both the presence and absence of the polymer film (Figure 90). Furthermore, with the polymer film present, it took slightly longer for the SED oscillations in Zone 1 to subside and progress into the steady state sliding phase (Zone 2). However, overall, the general trends observed in this investigation appear not to be largely affected by viscoelasticity, therefore the effects of the Dynamic Rest stage are assumed to be small.

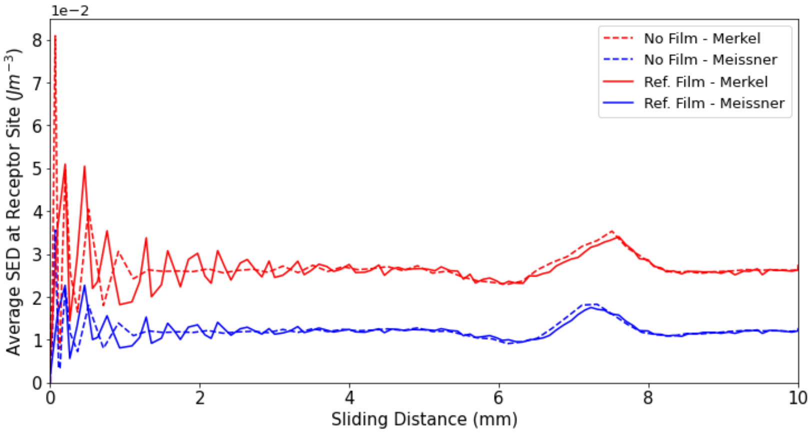

Figure 90: SED signal experienced at the Meissner (blue) and Merkel (red) receptor sites following the compression and translation of the finger skin against the facial tissue model with (solid line) and without (dotted line) an applied interfacial polymer film. Viscoelasticity was removed from both the finger skin and polymer film model for the entirety of these simulations.

As mentioned in section 6.3.1. Baseline Measurements, due to the unequal time increments implemented by Abaqus, direct comparison of the initial highly oscillatory transient response (Zone 1) between different simulations was not possible. In order to observe and compare the systems behaviour with sufficient granularity during Zone 1, very small, fixed timesteps would need to be defined with data outputted at every increment, thereby generating very large output files. This would potentially increase the duration of each simulation in the order of weeks and as a result was not feasible within the time constraints of this investigation. However, with advances in processing capability, it may become possible to use sufficiently small, fixed timesteps to enable the direct comparison of the effects of applying polymer films with different properties on their influence on Type 1 mechanoreceptor excitation at the inception of sliding. These SED signals could then be compared to experimental perceptive data to understand the importance of Zone 1 on our perception of cosmetic products.

6.4.2. Next steps

This investigation served as a pilot study to investigate the effect of different cosmetic polymer films deposited on the facial tissue and how these are perceived by the finger. Based on this study, through further research, high-performance computing could be used to provide further granularity to the Zone 1 response of the Type 1 mechanoreceptors at the inception of sliding. Following this, future work should focus on experimentally establishing the significance of Zones 1 – 3 on our perception of surfaces. Perceptions of Zone 1 may be recorded from observations at the inception of sliding, whilst Zones 2 and Zone 3 may be interpreted by changes in established observations whilst translating the finger across longer distances.

With respect to model development, four potential areas to further investigate include the effects of:

1) **Skin microrelief** – What effect would implementing the microscale topographical features of facial skin have on the perception of applied cosmetics?
2) **Moisture** – As mentioned in section 2.1.3.5. Effect of Hydration on Tactile Perception, moisture has been shown to influence the mechanical properties of skin as well as interfacial friction[248], thus influencing tactile perception. How would modelling these manifestations effect the strain energy density distributions at the Merkel and Meissner site?
3) **Relative movement of the polymer film** – In this investigation the polymer films were tied to the epidermis of the facial tissue (thus preventing any displacement of the film at the interface). What effect would the relative movement of the film (including delamination and film spreading) have on the excitation of Type 1 receptors?
4) **Embedded particles** – Particles and powders are frequently included within cosmetic products. Desirable qualities for selected cosmetic particles and powders include their pigment, covering power, adhesiveness against the face, spreadability or slip, and their ability to absorb natural skin secretions[249]. It has been shown that particle size, shape and concentration can have a significant effect on the tribological properties of cosmetics and tactile perception[250–252]. Current state-of-the-art numerical models have focused on simulating behaviour and interactions of individual particles or simulating granular flow[253,254]. To the best of the authors knowledge, there exists no computational model analysing the effect of altering particle properties on the tactile perception of cosmetics at the mechanoreceptor level.

7. Investigating the Effects of Respirator Mask Design on Facial Skin's Damage Propensity

This section contains work that has been published by Jobanputra et al in a peer reviewed journal[255].

7.1. Introduction

During the COVID-19 pandemic, medical professionals increased the duration of use of personal protective equipment (PPE), including respirator masks, visors and face shields. This increased skin irritations and injuries including urticaria, bruising and skin tears. The Tribology Group received funding from Imperial College COVID-19 Response Fund to investigate this phenomenon. A jointly computational and experimental approach was taking in this time-sensitive investigation to help mitigate injury[100,255,256]. This chapter the computational investigation, which surrounds the effect of altering the material, geometric and interfacial properties of PPE on the skin's damage propensity. Previous computational investigations on skin-PPE interaction have mainly focused on modelling the pressure that acts on the surface of the skin, with the objective of ensuring an appropriate seal and maintaining a level of user comfort[180,181,183]. However, the effects of PPE-skin interaction on the stresses and strains inside the tissue have not previously been investigated. Finite Element Analysis (FEA) is an efficient tool to model and visualise the local subsurface stress and strain levels within the tissue [191] and will be used to provide insight into the effects on the skin of interacting with PPE. The purpose of this investigation is to understand how the mechanical burden on the skin is affected by the characteristics of the PPE in terms of its material, geometric and interfacial properties. To enable this, the interaction between skin and a model respirator mask is examined using a parameterised finite element model. Following Oomens' work on skin loading and tissue damage[167,257], the strain energy density (SED) in the skin was taken as the quantitative measure representing local tissue failure. A series of simulations enabled the quantification of the efficacy of the respirator mask alterations and its interaction with facial skin, in order to provide information on how to reduce skin injury amongst PPE wearers. A set of readily implementable guidelines regarding the use and design improvements of PPE will be defined based on the obtained results.

7.2. Materials & Methods

7.2.1. Simulating and Varying Skin-PPE Contact

The parametric study was conducted using FEA to investigate the effects of independently altering the mask material, and its geometric and interfacial properties. Figure 91 shows a schematic diagram of the developed finite element model which comprises the contact between a respirator mask and facial skin tissue. A two-dimensional, isotropic finite element models was developed using Abaqus CAE 2019. The mask model was loaded with a uniform pressure of 1 N/mm along the 5 mm upper surface of the mask, thereby generating a 5 N applied load which was held constant throughout the study. This force caused the mask to indent the skin and generate a maximum pressure peak of 9.3 kPa at the edge of the mask (region $P_L$in Figure 92A), similar to pressures reported in literature [180,258–260]. The mask model was subsequently subjected to a lateral motion of 2 mm to represent the sliding and relative motion of tightened/fitted PPE during the execution day-to-day tasks, thus inflicting shear stresses on the skin. The facial injuries observed in users of PPE are representative of a combination of deep-tissue injury, such as bruising and more superficial injuries, such as blistering and abrasion. Using a combination of in-vivo experiments and finite element modelling, Oomens[257] related the extent of localised tissue breakdown to the amount of deformation energy at that site. This metric was therefore adopted in the present study, recording the maximum SED in the dermis during contact with the mask. As the exact damage threshold for skin has not been established and will vary interpersonally, the main purpose of this numerical investigation is to establish the effects and trends that a range of mask modifications have on the resulting subsurface SED distribution in the skin tissue, rather than attempting to obtain absolute values. The obtained results enable the recommendation of a range of potential mask modifications and help identifying the likely sites of skin failure.

7.2.2. Mask Model Development

The mask model represents the edge or rim of a respirator mask which is in contact with cheek skin. The mask comprises two components, a 2 mm thick substrate which is exposed to the environment, and an inner layer which is in contact with skin and for which the properties are varied in this study. The total width of the mask is 5 mm and the substrate material is modelled with an elastic modulus of 7 MPa and a Poisson's ratio of 0.4. The inner layer of the mask is perfectly adhered to this substrate and has a thickness of 1 mm. The edges were given a radius of curvature of 0.5 mm, which was varied later in the study to adjust the area of contact between the skin and the PPE. The mask model was given a coarser mesh than the skin, consisting of 971 quadratic plane strain elements.

Material characteristics that were varied within the study were the Young's modulus E and the Poisson's ratio ν of the respirator mask. The geometric properties varied include the contact length, L_c, representative of the contact area between the skin and PPE, and the thickness of the masks contacting layer, t. Finally, the interfacial properties altered in this investigation is the adhesive friction coefficient, μ. Whilst the material and the geometry can be directly controlled by the designer, the friction in the contact is affected by a wide range of parameters, including the material being used and the surface microgeometry or texture, personal traits such perspiration and hairiness, as well as the application topical creams or lubricants. Table 15 lists the reference values used in this work, as well as the range of values investigated[180,181,183]. The SED values in the tissue were recorded in order investigate the effects of these modified material, geometric and interfacial properties of the mask on the damage propensity of the skin. Subsequently, based on the obtained initial results, an improved PPE comprising the combined effects of a modified geometry, material and interface, was proposed and its effects on the skin SED values were investigated.

Table 15: The mask material, geometry and interfacial properties that were varied in this study.

Parameter	Reference value	Variations in study
Applied load [N]	5.0	-
Elastic modulus [kPa]	100	2 – 10,000
Poisson's ratio [-]	0.4	-0.2 – 0.49
Length of skin-ppe contact [mm]	4.0	3.0 – 4.8
Mask inner-layer thickness [mm]	1.0	0.5 – 2
Coefficient of friction [-]	0.5	0.1 – 1.1

7.2.3. Skin Model Development

The skin model consists of three layers, the epidermis, dermis and hypodermis or subcutaneous tissue, which were modelled as a continuum with flat interfaces between them. The model was developed as a single geometry before being partitioned into individual sections with different thicknesses and assigned material properties, thus simulating perfect adhesion between the skin layers. The skin comprises an epidermal layer with a thickness of 0.05 mm on top of a 1.3 mm thick dermal layer. This system is supported by a 1 mm subcutaneous tissue layer that provides a compliant boundary condition for the dermis by representing underlying tissue. The model was given material and geometric properties from literature[4,155,261,262] which are listed in Table 16.

Data on facial skin was used where available, complemented with properties of volar forearm skin, as research suggests there is no significant difference in thicknesses, stiffness, Poisson's ratios and frictional behaviour[133,263]. The modelled section of skin has a width of 15 mm, of which a 6 mm wide section is designated as the dermal analysis site. The additional width of the skin model will mitigate any edge effects on the dermal analysis site and allows sufficient room at the surface for translation of the PPE. The skin model comprised 40,014 quadratic plane strain elements.

Table 16: Material and geometric parameters of the simulated skin model.

Skin layer	E [kPa] [4]	ν [-] [262]	Thickness [mm][155,261]
Epidermis	1500	0.48	0.05
Dermis	20	0.48	1.3
Hypodermis/subcutis	2	0.48	1.0

As a form-fitting external barrier for the human body, the skin in its natural state is subject to tensile stresses. In order to keep the model of the skin taut, a pre-tensioning horizontal displacement of 0.1 mm was applied as a boundary condition on the left and right side of the finite element model. The base of the subcutis was restricted from vertical and rotational motion. Literature suggests adhesive friction is the main cause of macroscopic friction for unlubricated skin contacts[264]. Therefore, the surfaces were kept geometrically smooth, thus maximising the area of contact and consequently the adhesive friction acting on the interface. In the reference situation an interfacial coefficient of friction of 0.5 was applied between the mask and skin models. Following the translation of the skin, data was extracted from the dermal analysis site, underneath the mask-skin contact area. To reduce mesh effects, the reported maximum SED value is the average of the five elements with the highest SED values. Values are reported for the total skin, but also partitioned into an upper dermal segment (UD) and a mid-dermal segment (MD) both with a thickness of 0.4 mm and a lower dermal segment (LD) of 0.5 mm. These dimensions were chosen purely for analysis purposes and to provide insight, and do not refer to any specific anatomical dermal sublayers. A schematic diagram of the reference mask model, facial skin model and dermal analysis site (UD + MD + LD) simulated in this investigation is illustrated in Figure 91.

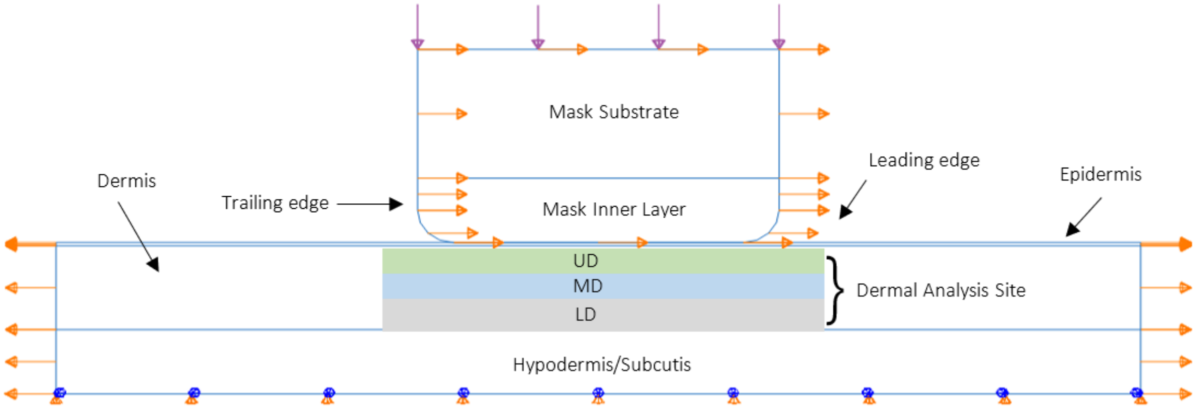

Figure 91: Schematic diagram detailing the compression and translation of a mask model against a skin model, in order to simulate PPE- Skin contact.

7.3. Results

Figure 92 displays the effect of altering the mask's geometric, material and interfacial properties on the dermal analysis site within the facial skin (illustrated in Figure 91). In all simulated cases the interface was fully closed, and there was no remaining gap between skin and PPE.

Figure 92A displays the SED distribution in the dermis resulting from contact between the facial skin model and the reference mask model described in Table 15. Figure 92 (B-I) illustrate the effects on the dermal SED distribution of varying the mask material, geometry and interfacial properties from the reference case. The SED distribution has a characteristic shape, with three main regions of interest:

- a sharp peak, P_L, in the upper dermis close to the skin surface, at the leading edge
- a sharp peak, P_T, in the upper dermis close to the skin surface, at the trailing edge,
- a larger region, A, of elevated SED values deeper into the tissue close to the boundary between the dermis and the hypodermis.

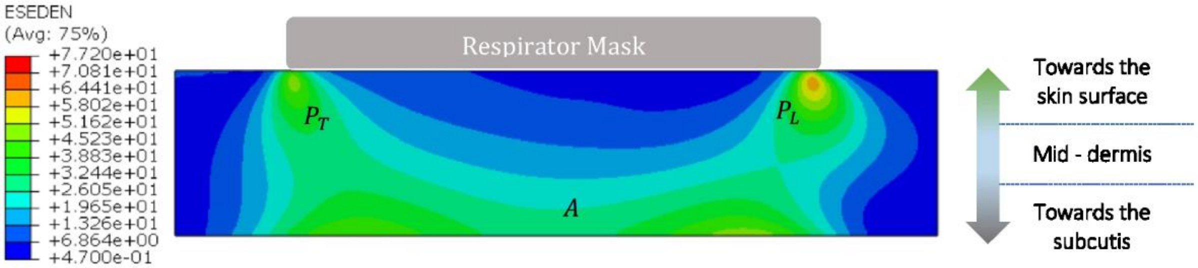

(A) The reference situation (E = 100 kPa, ν = 0.4, L_c *= 4 mm and μ = 0.5) shows a SED distribution that has two characteristic peaks in the upper dermis near the skin surface,* P_L *at the leading edge and* P_T *at the trailing edge of the contact with the PPE. Due to the friction in the PPE-skin interface, the distribution is asymmetrical and the value for the SED at the leading edge is elevated compared to the trailing edge. The typical SED distribution also includes a large area of elevated SED deeper within the dermis, marked* A*, towards the subcutis.*

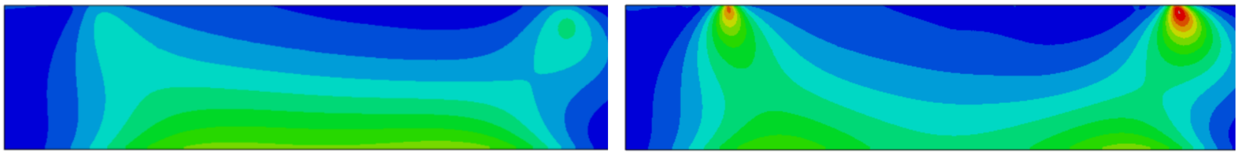

(B) When applying a compliant material (E = 5kPa) the SED reduces in the two peaks P_L and P_T. Deeper in the tissue, the SED appears elevated as marked by the larger area A.

(C) For a stiff mask material (E = 5 MPa), the SED at P_L and P_T is strongly increased whilst being reduced towards the central deeper tissue A.

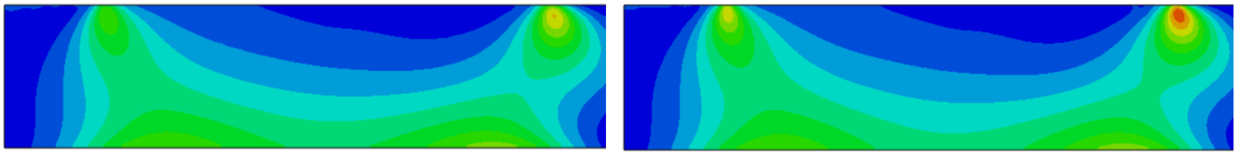

(D) A material with a Poisson's ratio ν= 0.1 results in a decreased SED in the upper dermisP_L, P_T with no substantial effect on the SED in the lower dermis A.

(E) A near incompressible material ν= 0.49 elevates SED at P_L and P_T. Whilst there is little effect on the SED in the lower dermis A, the SED in the region between P_L and A is elevated.

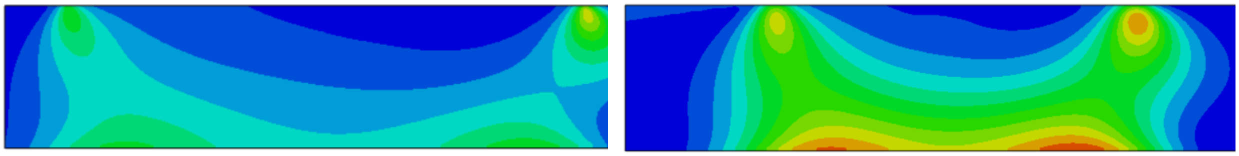

(F) When the load is distributed over a larger area of contact between the mask and the skin, in this case a contact length of 4.8 mm, the SED is distributed over a larger area and the SED is reduced throughout the skin.

(G) For a smaller contact area, in this case a contact length of 3 mm, the SED is strongly increased, particularly deeper into the skin at region A. Compared to the reference situation, the increase at P_L and P_T is marginal.

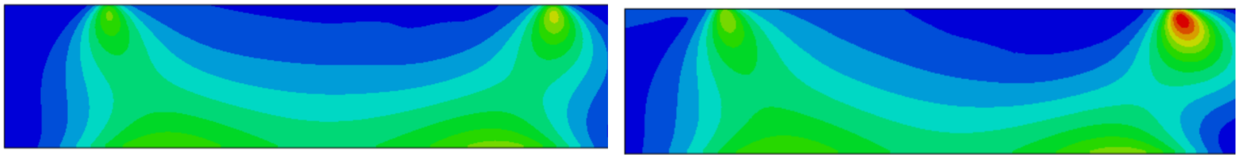

(H) Reducing the coefficient of friction (μ = 0.2) in the interface, reduces the SED values near the surface, particularly in P_L. The SED values between P_L and A increase slightly. No significant changes were observed for region A.

(I) Increasing the coefficient of friction (μ = 0.8) in the interface strongly increase SED at P_L. The effect deeper in the surface, in region A appears negligible. A minor decrease of SED values can be observed between P_L and A indicating a sharper, more isolated peak in P_L.

Figure 92: Close-up of the contact, showing the distribution of the SED in the dermis analysis site as a result of using PPE. Red indicates an elevated value. Distribution displayed overlayed over the undeformed tissue.

The various graphs show that increasing the stiffness of the material, the use of incompressible materials, and materials with a large coefficient of friction against skin all strongly increase the SED values, but mainly near the skin surface. Reducing the area of contact between the respirator mask and the skin strongly increases the SED deeper in the skin. From these results it can be concluded that to reduce the SED in the skin requires investigating a combination of effects. In terms of the design of optimised PPE, the stiffness or modulus of the mask material is arguably the main design parameter. A wide range of materials are available for mask design, and the stiffness directly affects the contact area and contact pressure, and thus the friction in the skin-PPE interface. Therefore, the results obtained in this study will be presented as a function of the modulus of the mask material.

7.3.1. Stiffness of the Mask Material

The effect of altering the stiffness of the mask material is clearly visible in all four graphs in Figure 93, which show the evolution of the maximum dermal SED as a function of the stiffness of the mask material for a variety of cases. Taking Figure 93A, which illustrates changes to the stiffness of the reference masks stiffness, the maximum SED in the skin increases following an S-shaped trend with increasing mask material stiffness. In general, a reduction of the mask stiffness leads to reduced maximum dermal SED in the upper dermis, as represented by the blue-coloured curve. The SED in the lower dermis is not sensitive to the stiffness of the mask material, except for highly compliant materials, $E < 10\ \mathrm{kPa}$, which result in a slight increase in SED (green curve in Figure 93A). Figure 93(B-D), show that the SED appears have a minimum level for compliant mask materials ($E \leq 50\ \mathrm{kPa}$), whilst the SED plateaus at a maximum value for stiff mask materials with $E \geq 10^3\ \mathrm{kPa}$.

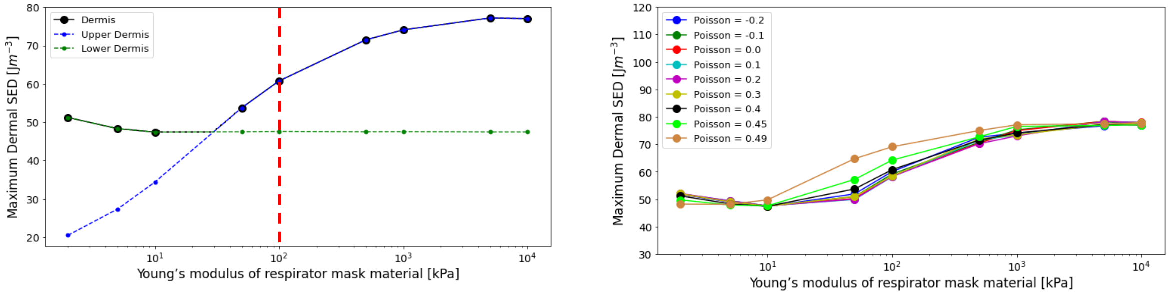

(A) With all other parameters held constant, stiffer mask materials result in the maximum dermal SED to be located in the upper dermis (blue). Below E » 30 kPa the maximum SED occurs in the lower dermis and its value increases with reducing mask stiffness. Reference model indicated by the red line.

(B) Nearly incompressible materials (v à 0.5) with intermediate levels of stiffness (10 kPa < E < 1000 kPa) result in increases in maximum SED.

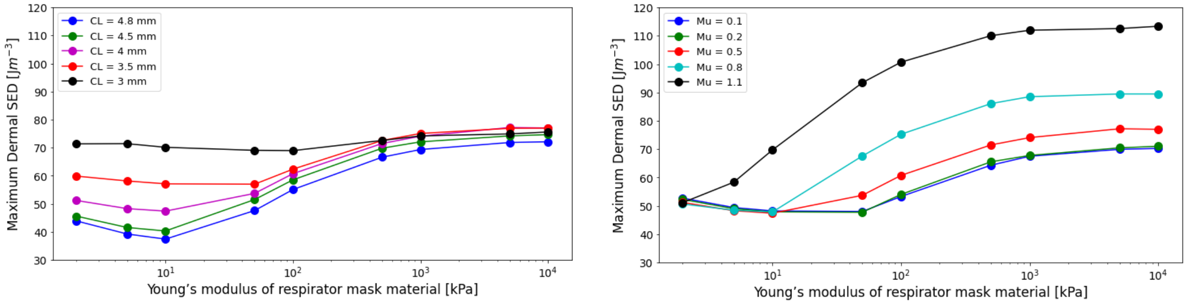

(C) A larger contact area between the skin and mask results in lower maximum SED values in the dermis. This effect is particularly pronounced for softer materials.

(D) For mask material stiffnesses above 10 kPa an increased interfacial friction coefficient results in substantially higher SED values in the upper dermis, particularly at the leading edge of the contact, P_L.

Figure 93: The effects of independently altering the mask properties on the maximum SED in the tissue. (A) Mask material stiffness, (B) Poisson's ratio, (C) area of contact, and (D) interfacial friction coefficient.

7.3.2. Poisson's Ratio

The Poisson's ratio describes the extent of deformation of a material perpendicular to the direction of loading, in this case the deformation of the mask material parallel to the skin surface when compressed against the skin. If the resulting deformation of the material is different than the deformation of the skin, an additional shear component is introduced in the interface. Therefore, the Poisson's ratio of the mask material is a potentially interesting parameter to take into account during the design phase of respirators. Figure 93B illustrates that in general the effect of changing the Poisson's ratio on the SED in the skin is small and may be ignored. However, for mask materials with an intermediate stiffness $(10\ kPa < E < 500\ kPa)$ the near incompressibility of rubber materials ($\nu = 0.49$) may result in an increase of the SED. For example, for a mask with a Young's modulus of 50 kPa, this increase is more than 20%, from $\Xi = 53.7$ J m^{-3} when $\nu = 0.40$ to $\Xi = 64.8$ J m^{-3} when $\nu = 0.49$.

7.3.3. Size of the Contact Interface

Figure 93C shows that an increase of the contact area between the skin and the PPE results in decreased maximum SED values. For very soft materials this effect is quite pronounced; for $E = 10\,\mathrm{kPa}$ the maximum SED reduces 47%, from $\Xi = 70.1$ J m^{-3} for a contact length $L = 3$ mm, to $\Xi = 37.5$ J m^{-3} for a contact length $L = 4.8$ mm. For stiff mask materials ($E > 500\ \mathrm{kPa}$) the SED and approach a value of about $\Xi \sim 70$ J m^{-3}, irrespective of the contact length. For very small contact sizes ($L \sim 3$ mm) the maximum value of the SED in the skin appears to be relatively insensitive to the stiffness of the mask material, with the curve being nearly horizontal. It was found that increases in contact significantly reduced SED values in region A, whilst having a much smaller effect on the upper dermis (Figure 94).

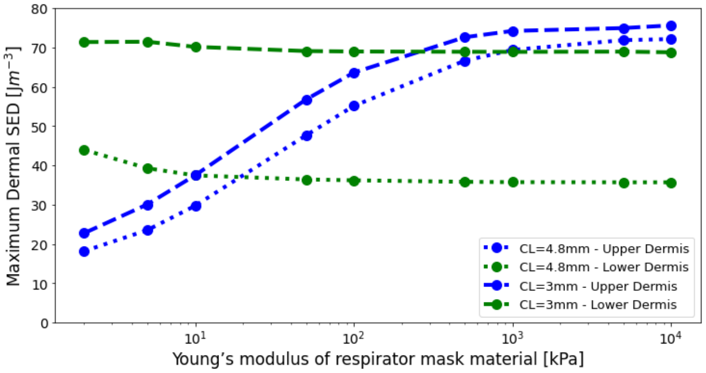

Figure 94: Evolution of SED in the tissue as a function of mask material modulus for contact lengths of 4.8 mm and 3 mm. Changes in contact length had a substantial effect on maximum SED in the lower dermis compared to the upper dermis.

7.3.5. Coefficient of Friction in the Skin-PPE Interface

Figure 93D summarises the effects of the interfacial friction on the SED in the skin. The coefficient of friction has a large effect on maximum dermal SED, compare Figure 92 H & I, which represent μ = 0.2 and μ = 0.8 respectively. Elevated friction increases the maximum SED in the upper dermis, particularly at location P_L, with little to no effect on the values in the lower dermis. At elevated levels of friction, the value of the SED increases more with increasing friction. Overall, lower friction values can lead to a strong reduction of the SED in the dermis. There appears to be a minimum friction level of approximately $\mu = 0.2$, where a further reduction does not substantially maximum dermal SED.

7.4. Discussion

The presented results provide a general overview of the relationships between the characteristics of the respirator masks and the resulting burden on the skin as quantified using SED. The dermal SED distributions provide some insights into the underlying tissue damage mechanisms, and thus can be used to develop PPE design guidelines to reduce the likelihood of dermal injury. With this in mind, it is worth noting that whilst in this work the SED was used as the indicator for tissue damage and has been related to the onset of tissue injury under sustained loading[257], similar trends were obtained when analysing engineering parameters such as shear stress and deviatoric stress.

7.4.1. Limiting the Stressing of the Skin

Figure 92 displays a range of dermal SED distributions in the skin as a result of combined compression and translation of the mask against the face. Elevated SED values in the upper dermis towards the skin surface may indicate an increased risk of superficial skin injury, such as abrasions, surface rupture and tearing as well as delamination of the dermal-epidermal junction. Elevated values of the SED deeper in the skin may indicate an increased likelihood of deep tissue injuries such as bruising, full skin rupture and delamination of the skin from the underlying tissue.

7.4.2. Contact Area

The effect the area of contact between the PPE and the skin is clearly visible when comparing Figure 92 (A,F,G) Reducing the contact area means the load is distributed over a smaller area, meaning the SED is strongly increased throughout the skin, and particularly deeper in the skin at the region marked A (Figure

92G & Figure 94). These results illustrate the importance of distributing the loads over a larger area, and thus the risk of pressure related injuries.

7.4.3. Stiffness

Materials with a reduced Young's modulus, often referred to as 'softer' materials, deform more under the same load than stiffer materials. As a result, the area of contact between the PPE and the skin increases and the strapping force of the PPE is distributed over a larger area. This supports the convention of softer materials being used in PPE with the aim of reducing discomfort and preventing injury. An additional effect of the increased area of contact between skin and PPE is that the maximum shear stress moves deeper into the tissue[265]. In Figure 93A it can be seen that reducing the stiffness of the PPE from 10 kPa to 2 kPa results in a modest but noticeable increase of the SED in the skin, driven by the lower dermis. When the stiffness of the mask material is larger than 1 MPa, i.e., significantly stiffer than the dermis, it was found that the maximum SED in the dermis did not vary significantly with further increasing stiffness. In that case the contact behaviour is dominated by the deformation of the skin whilst the PPE does not significantly deform.

7.4.4. Poisson's ratio

The Poisson's ratio of the mask material quantifies the extent to which the material displays the Poisson effect, i.e. its deformation in lateral direction following compression of the mask material against the skin. Theoretically, values for the Poisson's ratio range from $-1 < \nu < 0.50$ and typical engineering materials have a Poisson's ratio of approximately $\nu = 0.3$. Some cork materials do not display Poisson's effect-like behaviour and thus have $\nu = 0$. Most rubber materials have a value of $\nu \rightarrow 0.50$. This means that rubber, whilst highly deformable, has a constant volume which does not change when loaded or pressurised. Therefore, materials with $\nu = 0.5$ are referred to as incompressible. If the lateral deformation is different from the lateral deformation of the skin, a shear stress may be generated in the interface. The results indicate that the SED is relatively insensitive to this phenomenon, except for the specific combination of the mask comprising a material with intermediate stiffness ($10\ \mathrm{kPa} < E < 500\ \mathrm{kPa}$) and near incompressible behaviour ($\nu = 0.49$). Stiffer materials will only show a small deformation under loading, meaning that even for high values of ν the low strain of the mask material will not exert a substantial stress onto the skin surface. For highly compliant materials this effect is also minimal; whilst in this case the strains may be large, the modulus is low and therefore the resulting stress introduced into the interface will be too low to substantially affect the SED in the skin. These results, however, illustrate a potential issue for the typical softer materials used in respirator masks, which are often rubbery materials with a Young's modulus that falls in the "intermediate" range. This means that the use of these materials in PPE may possibly need further consideration.

7.4.5. Friction in the Interface

A high interfacial friction coefficient between mask and skin results in increased levels of SED close to the skin surface. This is in agreement with literature, where high friction has been related to the development of superficial tissue injury[148,168,257], whilst deep tissue injury appears to be related to the direct application of pressure[168]. In addition, friction may cause delamination of the dermal-epidermal junction, resulting in blisters and skin tearing [266–269]. Therefore, reducing the level of friction should be of primary concern when designing respirator masks. It is worth noting that friction in the skin-PPE interface is not a parameter that can easily be designed or optimised. The overall friction between the skin and PPE is a system parameter that depends on the mask material, the characteristics of the skin, as well as the loading and interfacial conditions. However, the literature mentions various ways to reduce friction, including the use of custom surface microgeometry or textures on the respirator masks, controlling the moisture in the contact and the use of specialised lubricants[100,144,256]. The application of a (micro-)texture to the surface of a device may be an effective measure to reduce the shear forces [21,234,270]. However, this may interfere with the sealing capability of the respirator.

Following mask usage, moisture levels in the skin are reported to increase [271]. The frictional response of skin is strongly dependent on humidity [139,217,272] and a moist environment macerates the skin and locally disrupts the skin barrier function [166,273]. Therefore, moisture control is an effective means of reducing friction and preventing injury. Breathable materials could be utilised, and inspiration may be drawn from the materials used in diapers and sanitary towels, both of which make contact with skin for extended periods of time in warm, humid conditions. An additional solution that may be considered, particularly by users that suffer from high friction or 'sticky' skin, is the use of a topical creams to alleviate the shear stresses in the skin-PPE interface[100,256].

7.4.6. Mask Thickness

From Figure 95, it was found that changes in the thickness of the mask's inner layer had negligible effect on the maximum dermal SED within the facial tissue across the range of mask moduli tested. Softer mask layers exhibited substantial deformation along the side edges of the mask, as opposed to conferring significant increases in contact area at the mask-skin interface. Therefore, as the contact areas remained relatively similar regardless of mask thickness, negligible change in maximum dermal SED was observed. According to this analysis, mask thickness may not play as large a role as other tested parameters do in reducing PPE-related skin injuries.

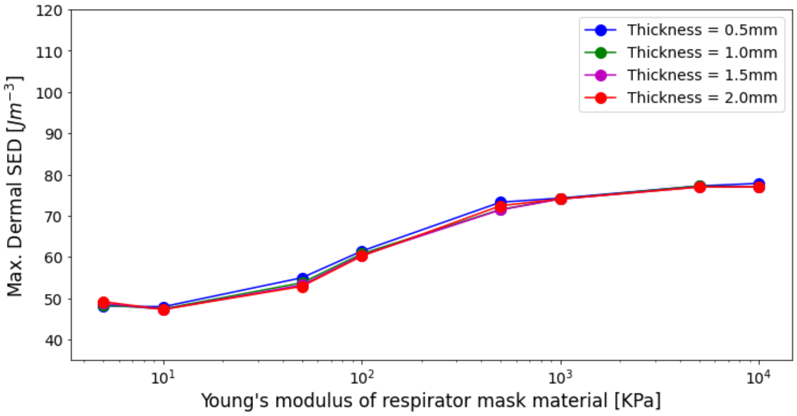

Figure 95: The effect of mask inner layer thickness on the maximum dermal SED.

7.4.7. Design Considerations

The results presented provide insight into the relative importance of the various investigated parameters. These results can be used to extract design guidelines for facial PPE. Figure 96 shows the potential reduction in skin loading resulting from the use of alternative geometrical, interfacial and material parameters, taking a silicone-based face mask as the starting point[274]. The results confirm that interfacial and material alterations have a substantial effect on skin loading near the surface, whilst geometric alterations mainly effected the subsurface response.

Figure 96 also presents results obtained for an improved PPE, comprising an alternative material with increased contact area and reduced friction. The SED levels in the upper dermis reduce for every single alteration, resulting in an overall reduction of 46.6% for the improved model. The SED levels deeper in the tissue can only be reduced by changing the geometry of the mask. This enables the targeted augmentation of PPE to reduce the likelihood of injuries at specific dermal locations, deep tissue injury requires geometrical changes, whilst superficial injury may be alleviated through interfacial and material interventions.

Model/parameter	E **[kPa]**	ν **[-]**	L_C **[mm]**	μ **[-]**
Silicone	210	0.49	4	0.6
Geometry altered	210	0.49	4.8	0.6
Interface altered	210	0.49	4	0.2
Materials altered	50	0.4	4	0.6
Improved PPE	50	0.4	4.8	0.2

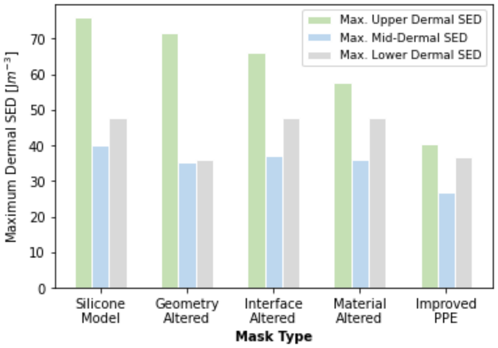

Figure 96: Table (left) showing different mask modifications compared to a silicone-based model. Graph (right) showing the SED in the upper (green), middle (blue) and lower dermis (grey) in response to the modifications.

Elastomeric materials are often used in respirator masks as the contacting layer against the skin. The low modulus of these materials distributes the pressure over a larger area, providing a degree of comfort whilst permitting a tight seal to form around the face to prevent leakage and viral exposure. However, the combination of the stiffness ($E < 1\ MPa$) and near incompressibility ($\nu \rightarrow 0.5$) of these materials may result in an elevated SED in the skin, as shown in Figure 93B. More significantly, in contact against skin, elastomers exhibit friction coefficients that exceed 1[100,256,275] which significantly elevates dermal SED values. In terms of defining optimal materials to be used for facial PPE, three parameters to consider are:

- a modulus of about 100 kPa. Elastomers with a lower modulus would be beneficial from a pressure point of view, but many exhibit adhesive behaviour, which may elevate shear stresses in the skin
- a Poisson's ratio below 0.45 to reduce compression-induced shear stress
- a coefficient of friction against skin of approximately 0.2, but definitely not exceeding 0.5

Whilst a single material with these properties may not be available, such a combination of characteristics may be achieved by using a soft, compressible inner layer (such as polymer foams or gels) covered with a thin, low-friction, breathable outer layer. Such a solution would confer beneficial bulk and interfacial properties to the user, reducing the risk of discomfort and injury. Although this study is focussed on respirator masks for COVID-19 healthcare staff, there are several conditions in which patients also are fitted respirator or ventilator masks for extended periods of time. Future work could consist of testing a variety of material combinations that fit the design recommendation above in order to reduce the skin's damage propensity for both healthcare staff and patients.

7.4.8. Strengths and Limitations to the Study

The objective of the developed model was to record the strain energy density in the dermis when in contact with PPE with a variety of properties, in order to indicate the propensity for tissue failure. The accuracy of the obtained results depends on how representative the model and input parameters are. Whilst geometric data is available for facial tissue, there is a lack of data accurately describing its topography and mechanical properties. Consequently, a generalised skin model was developed, comprising a smooth surface and typical geometric and mechanical properties. The effects of these assumptions on the results are limited; skin topography would result in locally elevated contact pressures on the epidermis, but the high stiffness of the epidermis prevents these pressures to be translated into elevated SED values into the subsurface tissue. Changing the geometry will affect the absolute values obtained, but not the trends observed. The mechanical properties of facial skin as reported in literature[157] and used in this model are linearly elastic, whilst this is sufficient for the purposes of this study, any further optimisation will require a better understanding of the nonlinearity and time-dependent behaviour of each layer of the skin.

Additionally, the properties of facial tissues and craniofacial dimensions differ significantly between ages, ethnicities and sexes[276,277] and therefore further work is required to enable differentiation and optimization of PPE design for different demographics in order to ensure functionality and fitting whilst preventing injury and viral exposure[278]. Finally, damage thresholds for skin have not yet been established and these would provide useful insight into the likelihood of failure at different facial locations.

8. Conclusions

The purpose of the research presented in this thesis was to use computational models to help deliver insight into skin-product interaction. A computational approach confers the benefits of delivering results repeatably, inexpensively, and non-invasively. Due to the highly individualized nature of the skin, parameterized finite element skin models were used to establish generalized conclusions surrounding the effects and trends of parametric studies performed on the skin, substrate and interfacial properties.

This work was conducted in conjunction with researchers at L'Oréal Research & Innovation and aimed to understand the effect of modifying the mechanical, geometric, and interfacial properties of cosmetic products on their subsequent perception at mechanoreceptor sites within the finger. To meet this objective, three constituent parametric studies were conducted:

- A non-linear, time-dependent, two-dimensional, parameterized, finite element finger skin model was first developed. This was then used in order to investigate the effect of age-related biomechanical skin changes on tactile perception.
- The finger skin model was compressed and translated against various rigid, textured surfaces in order to investigate the effect of surface topography on the stimulation of mechanoreceptor sites.
- The finger skin model was compressed and translated against a newly developed facial skin model whilst the properties of an interfacial cosmetic polymer film was varied.

Furthermore, a secondary objective was defined following the emergence of the COVID-19 virus. During the pandemic, healthcare workers were fitted with high-grade personal protective equipment (PPE) for extended periods of time, resulting in facial skin irritation and injury. As this thesis focused on skin-product interaction, the fourth and final investigation fell within the remit of the defined research objectives and was thus included:

- Contact between respirator masks and facial tissue was first simulated. A parametric study was then conducted to investigate the effect of altering the mask's material, geometric and interfacial properties on the skin's damage propensity.

This section summarises the key conclusions of the four parametric studies, before reviewing the computational methods utilized in this thesis and outlining key areas of focus for future research.

8.1. Effect of Biomechanical Skin Ageing on Tactile Perception

The conclusions presented here have been published by Jobanputra et al in a peer reviewed journal[223]*.*

Our sense of fine touch deteriorates as we age, a phenomenon typically associated with neurological changes within the skin, such as reductions in mechanoreceptor density. However, geometric and material changes to the skin may also play an important role on tactile perception and have not previously been investigated in detail. In this study, a finite element model was utilised to assess the extent to which age-related structural skin changes influence the tactile stimuli experienced by the mechanoreceptors.

A numerical, hyperelastic, four-layered skin model was developed to simulate sliding of the finger against a rigid surface. The strain, deviatoric stress and strain energy density were recorded at the sites of the Merkel and Meissner receptors, whilst parameters of the model were systematically varied to simulate age-related geometric and material skin changes. The simulations comprise changes in skin layer stiffness, flattening of the dermal-epidermal junction and thinning of the dermis.

It was found that the stiffness of the skin layers has a substantial effect on the stimulus magnitudes recorded at mechanoreceptors. Additionally, reducing the thickness of the dermis has a substantial effect on the Merkel disc whilst the Meissner corpuscle is particularly affected by flattening of the dermal epidermal junction. In order to represent aged skin, a model comprising a combination of ageing manifestations revealed a decrease in stimulus magnitudes at both mechanoreceptor sites. The result from the combined model differed from the sum of effects of the individually tested ageing manifestations, indicating that the individual effects of ageing cannot be linearly superimposed. Each ageing manifestation resulted in a decreased stimulation intensity at the Meissner Corpuscle site, potentially reducing the proportion of stimuli meeting the receptor's amplitude detection threshold.

This model therefore offers an additional biomechanical explanation for tactile perceptive degradation amongst the elderly. Future work could focus on the development and evaluation of cosmetics products aimed at mitigating the effects of ageing, e.g., through skin hydration and administration of antioxidants, as the design of products with improved tactile sensation, e.g., through the optimisation of materials and surface textures.

8.2. Effect of Surface Textures on Tactile Perception

The purpose of this investigation was to simulate the contact between the finger and different surface textures in order to evaluate their effect on Type 1 mechanoreceptor excitation. To the best of the authors knowledge, a parametric study on the effect of surface topography on our sense of fine touch has not been previously conducted. In this investigation, a parameterised finite element finger skin model was compressed and translated against a counter surface with a sinusoidal surface texture, whilst the amplitude and wavelength of the sinusoid were independently varied during a parametric study. The strain energy density (SED) at the Type 1 (Merkel and Meissner) receptor sites were recorded in order to analyse mechanoreceptor excitation.

Upon contact with smooth, rigid surfaces, it was found that increases in adhesive friction coefficient resulted in non-linear increases in SED at the mechanoreceptor sites. When analysing rough surfaces during the parametric study, it was found that surface amplitude played a less significant role in influencing receptor excitation than surface wavelength. Both average SED and SED range at each receptor site did not vary substantially as the finger skin model was translated against rough surfaces whose wavelengths were dissimilar to that of the fingerprint. However, when the surface and fingerprint wavelengths were commensurate, large increases in average and range SED values were observed. Furthermore, in these scenarios, increases in amplitude resulted in the finger skin model exhibiting greater physical resistance when sliding due to the increase in height of the counter surface texture, thereby elevating SED at the receptor sites.

The developed model enables the comparison of the subsurface stress-state within the skin with experimental perception tests to provide a link between the different processes involved in tactile perception. Future work could focus on using the computational model to compare the receptor excitation levels generated with upon contact with different surfaces with perceptive data obtained during psychophysical tests. This may enable product designers and ergonomists to design surfaces that can help deliver specific tactile sensations to the user.

8.3. Effect of Cosmetic Polymer Film Modifications on Tactile Perception

The purpose of this study was to investigate the effect of altering the properties of cosmetic polymer films on their subsequent perception within the finger. In this study, the previously developed finger skin model was compressed and translated against a facial skin model, whilst the material, geometric and interfacial properties of a polymer film residing at the interface was altered. The strain energy density (SED) signal recorded at the Type 1 (Merkel and Meissner) receptor sites was recorded during finger sliding.

It was found that the SED signals generated during contact comprised three distinct stages or Zones: an initial transient response as the surfaces overcome the initial static coefficient of friction, steady state sliding, and finally a peak generated as stresses propagated over the site of the receptors. Independently altering the interfacial polymer film stiffness, thickness, viscoelasticity, and adhesive friction coefficient affected each of the stages in different ways; with high levels friction being the dominant parameter in elevating the SED signals at each of the receptor sites.

Low friction, low roughness tactile interactions are often correlated with increases in pleasantness[13,14,110]. In this study, reducing the interfacial friction coefficient attenuated the SED signal generated at each receptor site as the finger was translated against the polymer film. Therefore, if lower-magnitude SED signals are correlated to desirability, the results of this study indicate that thicker, more compliant films should also be developed by cosmetics manufacturers to help reduce the magnitude of stresses propagating over the receptor sites.

This investigation served as a pilot study to computationally analyse the effect of film properties on the excitation of tactile mechanoreceptors. These results provide a foundation to develop premium cosmetic products designed to deliver enhanced sensorial experiences to consumers. Future work can focus on better understanding the importance of each of the distinct SED signal stages on our sense of perception. Additionally, more advanced models may evaluate the significance of skin microrelief, moisture, relative film movement and embedded particles on our sense of fine touch.

8.4. Effect of PPE Design Modifications on the Facial Skin's Damage Propensity

The conclusions presented here have been published by Jobanputra et al in a peer reviewed journal [255].

The use of close-fitting PPE is essential to prevent exposure to dispersed airborne matter, including the COVID-19 virus. The current pandemic has increased pressure on healthcare systems around the world, leading to medical professionals using high-grade PPE for prolonged durations, resulting in device-induced skin injuries.

This study focuses on computationally improving the interaction between skin and PPE to reduce the likelihood of discomfort and tissue damage. A finite element model is developed to simulate the movement of PPE against the face during day-to-day tasks. Due to limited available data on skin characteristics and how these vary interpersonally between sexes, races and ages, the main objective of this study was to establish the effects and trends that mask modifications have on the resulting subsurface strain energy density distribution in the skin. These modifications include the material, geometric and interfacial properties.

Overall, the results show that skin injury can be reduced by using softer mask materials, whilst friction against the skin should be minimised, e.g. through use of micro-textures, humidity control and topical creams. Furthermore, the contact area between the mask and skin should be maximised, whilst the use of soft materials with incompressible behaviour (e.g. many elastomers) should be avoided.

The results of this investigation are also relevant to patients who require respiratory aid for other medical conditions. Future work could focus on establishing the mechanical properties and damage thresholds of different anatomical regions of facial skin more accurately; designing masks with a soft, compressible inner layer (such as polymer foams or gels) covered with a thin, low-friction, breathable outer layer; and ensuring these masks can be fitted to both healthcare staff and patients of different ages, sexes and ethnicities.

8.5. Looking Forwards

It was found that the developed numerical skin models enabled the subsurface stress-state of soft tissue to be observed and analysed quickly, repeatably, inexpensively and non-invasively. As with any modelling initiative, simplifications and assumptions were made to provide a balance of accuracy and computational expenditure. These simplifications include the use of parameterized skin models, which proved useful for conducting parametric studies to establish and isolate the general trends and effects of modifying the properties of the skin, substrate and interface.

Future improvements in computational processing capability will increase the feasibility of simulating skin contact scenarios with increased complexity. These models may include more accurate, multiscale biological and mechanical representations, including intralayer variations in skin properties and structure; multiphase models to simulate the presence of skin secretions on the surface, such as sweat and sebum; and extending the current two-dimensional model in to the third dimension.

However, before developing and utilizing more advanced finite element skin models, three key areas of focus are identified as being necessary to improve our understanding and analysis of tactile perception and skin injury:

- Measuring and modelling the skin’s mechanical properties
- Correlating micro-scale cellular damage to macroscale skin injury
- In-situ analysis of skin deformation during contact

In the following section these three areas will be discussed in more detail.

8.5.1. Measuring and Modelling the Skin's Mechanical Properties

In order to improve our understanding of the relationship between the mechanical, neurological and psychological stages of tactile perception, it is first necessary to improve our understanding of the mechanical behaviour of the skin. Further experimental testing is required to better understand the non-linearity, time-dependency and anisotropy of the skin across different anatomical sites.

Presently, experimental data describing the non-linear behaviour of the human finger pad is scarce. Non-invasive testing could include analysing the deformation of the finger pad over time as it is compressed and translated against counter surfaces, with different applied loads. This would enable the development of an overall, non-linear stress-strain curve for the finger pad. However, this curve would only be able to model the macroscopic effective modulus of the finger and may not provide sufficient granularity to model mechanical stimuli propagation from the skin-surface boundary to the mechanoreceptor sites.

Invasive methods offer the benefit of obtaining more representative results; however, they are frequently performed *ex vivo*, potentially resulting in a change in the mechanical properties of the skin. Boyle et al used atomic force microscopy (AFM) to characterize the stress-strain relationship of individual layers of sectioned plantar foot skin[5]. An Ogden model was then fitted to the obtained data to establish the hyperelastic properties of the skin layers. Similar methods could be utilized to evaluate the non-linear properties of each layer of the finger skin.

Due to the complexity of soft tissue and the rise in computational processing capability, multiscale modelling is becoming an increasingly popular method to help deliver insight into biomechanical processes[279]. When subjected to mechanical loading, the skin's non-linear behaviour is attributed to the presence and distribution of collagen and elastin fibres embedded within the dermal matrix. The orientation of these fibres also confers anisotropic mechanical properties to the skin. Constitutive equations to describe the behaviour of these fibres are well documented in literature[6,51,52,280]. However, to the best of the author's knowledge, there exists no multi-layered, hyperelastic, numerical finger skin models that incorporates fibre-level mechanics. It is worth noting; however, that efforts have been made to do so in other applications[281–284]. Implementation of fibre-level mechanics within more complex FE finger skin models may help obtain more representative, directional, multiscale perspectives on the propagation of stresses, strains and vibrations from the skin-surface boundary to the sites of our tactile mechanoreceptors.

8.5.2. Correlating Microscale Cellular Damage with Macroscale Skin Injury

A better understanding of skin damage thresholds on the cellular level can help explain irritation and injury on the macroscale, thereby enabling the development of more targeted preventative measures.

Presently, much of our knowledge on tissue damage derives from animal studies, offering results that may not be representative of human skin damage[285]. Non-invasive efforts to assess skin damage amongst humans include the analysis of erythema (skin redness) amongst patients following prolonged exposure of the skin to counter surfaces; however, variations in skin pigment can obscure results[286].

Another popular non-invasive method involves the analysis of inflammatory biomarkers. These biomarkers can normally be obtained from a variety of body fluids (e.g. blood, sweat, sebum and urine) and are used as early detection indicators of pressure ulcers and other forms of skin injury[287,288]. Cytokines are small proteins that are used in cell signaling. Interleukins (a subgroup of cytokines) are associated with our immune and inflammatory response, more specifically IL-1α[289–293]. Elevated presence of IL-1α has been detected following prolonged exposure of the skin to compressive and shear forces[293–298] and has been identified as a precursor to skin irritation and damage[299], as have sebum lactate and sweat lactate – biomarkers used to detect skin ischemia[292,300–303].

Bader et al reviewed attempts by researchers to establish skin damage thresholds through the development of risk curves, describing limiting values of pressure that can be applied to the skin for a given period of time before pressure ulcers may develop (Figure 97)[285,304]. Many of these studies were conducted experimentally through indenting animal tissue. Through analysing the effect of applied load and exposure time on inflammatory biomarker concentration, it may be possible to non-invasively develop more representative skin damage thresholds for humans. This data can then be compared to subsurface strain energy density (SED) distributions[167] within finite element skin models in order to more accurately simulate the skin’s damage propensity over a wider variety of scenarios.

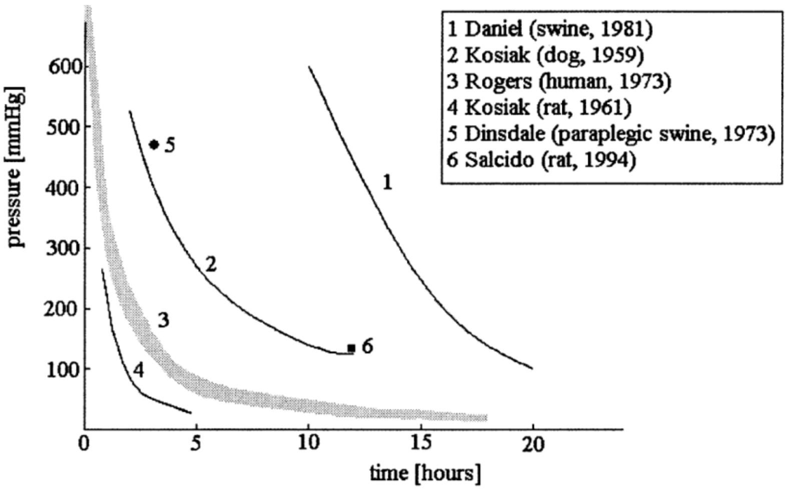

Figure 97: Risk curves with regards to pressure ulcers. Time/Pressure combinations above the curve result in tissue breakdown [285,304].

8.5.3. In-situ Analysis of Skin Deformation During Contact

In order to improve and validate numerical skin models, non-invasive optical methods can be utilized to observe skin contact in greater detail and develop our understanding of skin deformation.

On the macroscale, digital image correlation (DIC) can be used to generate a speckle pattern on the surface of the skin. Analysed temporally, as the skin is mechanically loaded, the movement of each node of the speckle pattern can be used to track deformations of the skin surface and changes in contact area due to tactile friction[305].

On the microscale, ultrasound techniques can be used to visualize soft tissue at a high penetration depth but offers poor resolution. In contrast, optical coherence tomography (OCT) offers higher resolution but lower penetration depth. As a result, high resolution imaging of the dermal skin layer and mechanoreceptor sites within plantar skin is not currently possible (Figure 98 shows an OCT scan of the finger pad in which the dermal skin layer is not fully resolved[306]). Increases in the penetration depth and resolution of optical methods would enable the visualization of the skin's inhomogeneity and mechanoreceptor sites within the finger pad.

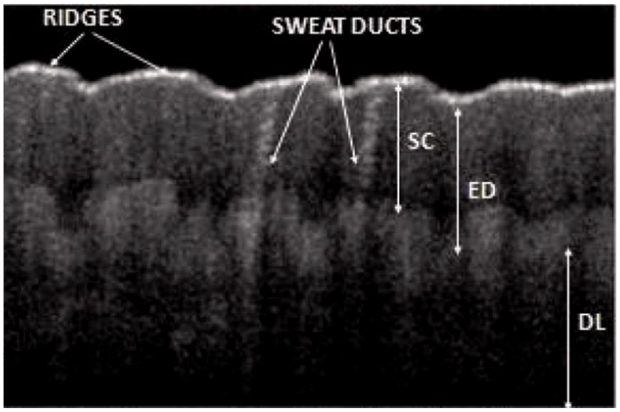

Figure 98: OCT image of the finger pad (SC: stratum corneum; ED: epidermis; DL: dermis)[306].

Coupled with DIC, it may become possible to observe the deformation of the individual skin layers and the propagation of mechanical stimuli to the receptor site following contact between the finger pad and counter surfaces. This could then be compared to the subsurface stress, strain and energy fields within finite element finger skin models for validation purposes. Furthermore, for a given applied load, analysis of the deformation of the subsurface skin layers could also yield information about the effective mechanical properties of the finger skin as a whole[4].

8.6 Final Remarks

The computational models developed in this PhD thesis describe the contact between skin and a counter surface, focusing on tactile perception and facial tissue damage. Due to the skin's complexity, cutaneous biomechanical phenomena are not fully understood. The developed models provide insight into the key drivers involved in skin-surface interaction, enabling the development of improved products.

9. References

1. Limbert, G. *et al.* Biotribology of the ageing skin—Why we should care. *Biotribology* **17**, (2019).

2. van Kuilenburg, J. A Mechanistic Approach to Tactile Friction. vol. PhD Thesis (University of Twente, Enschede, The Netherlands, 2013).

3. Dzidek, B. M., Adams, M. J., Andrews, J. W., Zhang, Z. & Johnson, S. A. Contact mechanics of the human finger pad under compressive loads. *J R Soc Interface* **14**, (2017).

4. van Kuilenburg, J., Masen, M. A. & van der Heide, E. Contact modelling of the human skin: What value to use for the modulus of elasticity? *Journal of Engineering Tribology* **227**, 349–361 (2012).

5. Boyle, C. J. *et al.* Morphology and composition play distinct and complementary roles in plantar skin's tolerance to load. *Sci Adv* **5**, (2019).

6. Joodaki, H. & Panzer, M. B. Skin mechanical properties and modeling: A review. *Journal of Engineering in Medicine* **232**, (2018).

7. Bergmann Tiest, W. M. Tactual perception of material properties. *Vision Res* **50**, (2010).

8. Lederman, S. J. & Taylor, M. M. Fingertip force, surface geometry, and the perception of roughness by active touch. *Percept Psychophys* **12**, 401–408 (1972).

9. Pasqualotto, A., Ng, M., Tan, Z. Y. & Kitada, R. Tactile perception of pleasantness in relation to perceived softness. *Sci Rep* **10**, 11189 (2020).

10. Ellenbecker, T. S., Davies, G. J. & Bleacher, J. Proprioception and Neuromuscular Control. in *Physical Rehabilitation of the Injured Athlete* (eds. Andrews, J. R., Harrelson, G. L. & Wilk, K. E.) 524–547 (Elsevier, 2012).

11. Reuter, E. M., Voelcker-Rehage, C., Vieluf, S. & Godde, B. Touch perception thoughout working life: effects of age and expertise. *Exp Brain Res* **216**, 287–297 (2012).

12. Zhou, X., Mo, J. L. & Jin, Z. M. Overview of finger friction and tactile perception. *Biosurf Biotribol* **4**, 99–111 (2018).

13. Kitada, R., Sadato, N. & Lederman, S. J. Tactile Perception of Nonpainful Unpleasantness in Relation to Perceived Roughness: Effects of Inter-Element Spacing and Speed of Relative Motion of Rigid 2-D Raised-Dot Patterns at Two Body Loci. *Perception* **41**, 204–220 (2012).

14. Essick, G. K. *et al.* Quantitative assessment of pleasant touch. *Neurosci Biobehav Rev* **34**, 192–203 (2010).

15. Zingaretti, P., Petta, A. M., Cruciani, G. & Spitoni, G. F. Tactile sensitivity, tactile acuity, and affective touch: from childhood to early adolescence. *Somatosens Mot Res* **36**, 90–96 (2019).

16. Fagiani, R., Massia, F., Chateleta, E., Berthier, Y. & Akay, A. Tactile Perception by Friction Induced Vibrations. *Tribol Int* **44**, 1100–1110.

17. www.statista.com/statistics/254612/global-skin-care-market-size/. Size of the global skin care market from 2012 to 2025. *Trefis.com* (2019).

18. Mihaela, P. & Sergachev, D. Touch - Perception. *TriboNet* https://www.tribonet.org/news/touch-perception/ (2021).

19. Feher, J. Cutaneous Sensory Systems. in *Quantitative Human Physiology* (Elsevier, 2016).

20. Fagiani, R. & Barbieri, M. A contact mechanics interpretation of the duplex theory of tactile texture perception. *Tribol Int* **101**, 49–58 (2016).

21. van Kuilenburg, J., Masen, M. A. & van der Heide, E. The role of the skin microrelief in the contact behaviour of human skin: Contact between the human finger and regular surface textures. *Tribol Int* **65**, 81–90 (2013).

22. Derler, S. & Gerhardt, L.-C. Tribology of Skin: Review and Analysis of Experimental Results for the Friction Coefficient of Human Skin. *Tribol Lett* **45**, 1–27 (2012).

23. van Kuilenburg, J., Masen, M. A. & van der Heide, E. A review of fingerpad contact mechanics and friction and how this affects tactile perception. *Proceedings of the Institution of Mechanical Engineers, Part J: Journal of Engineering Tribology* **229**, 243–258 (2015).

24. Geerligs, M. *et al.* In vitro indentation to determine the mechanical properties of epidermis . *J Biomech* **44**, 1176–1181.

25. Agache, P. & Humbert, P. Skin Structural Components: Physiology and Metrology. in *Measuring the Skin* (Springer, 2004).

26. Leyva-Mendivila, M. F., Page, A., Bressloffd, N. W. & Limbert, G. A mechanistic insight into the mechanical role of the stratum corneum during stretching and compression of the skin. *J Mech Behav Biomed Mater* **49**, 197–219 (2015).

27. Flynn, C. O. The Design and Validation of a Multi-Layer Model of Human Skin. vol. PhD Thesis (Dept. Mechanical and Electronic Engineering, School of Engineering, Institute of Technology, Sligo, 2007).

28. Geerligs, M. Skin Layer Mechanics. *Universty of Eindhoven, Netherlands* (Universiteitsdrukkerij TU Eindhoven, 2009).

29. New York University School of Medicine. Cell Biology of Tissue and Organs: Skin Histology. http://education.med.nyu.edu/Histology/courseware/modules/skin/ (2005).

30. Peckham, M., Knibbs, A. & Paxton, S. Skin Functions and Layers - The Histology Guide, Faculty of Biological Sciences, University of Leeds. Preprint at https://www.histology.leeds.ac.uk/skin/skin_layers.php (2003).

31. Swenson, R. S. Thick Skin Histology, Anatomy - Dartmouth Medical School. Preprint at https://www.dartmouth.edu/~anatomy/Histo/lab_4/skin/DMS033/popup.html (7AD).

32. Roberson, K. & Rees, J. L. Variation in Epidermal Morphology in Human Skin at Different Body Sites as Measured by Reflectance Confocal Microscopy. *Acta Derm Venereol* **90**, 368–373 (2010).

33. Adams, M. J. *et al.* Finger pad friction and its role in grip and touch. *J R Soc Interface* **10**, 20120467 (2013).

34. Shao, F., Childs, T. H. C., Barnes, C. J. & Henson, B. Finite element simulations of static and sliding contact between a human fingertip and textured surfaces. *Tribol Int* **43**, 2308–2316 (2010).

35. Prevost, A., Scheibert, J. & Debrégeas, G. Effect of fingerprints orientation on skin vibrations during tactile exploration of textured surfaces. *Commun Integr Biol* **2**, 422–424 (2009).

36. Scheibert, J., Leurent, S., Prevost, A. & Debrégeas, G. The Role of Fingerprints in the Coding of Tactile Information Probed with a Biomimetic Sensor. *Science (1979)* **323**, 1503–1506 (2009).

37. David, T. J. Distribution, Age and Sex Variation of the Mean Epidermal Ridge Breadth. *Hum Hered* **31**, 279–282 (1981).

38. Cummins, H., Waits, W. J. & McQuitty, J. T. The breadths of epidermal ridges on the finger tips and palms: A study of variation. *American Journal of Anatomy* **68**, 127–150 (1941).

39. Sharma, S., Shrestha, R., Krishan, K. & Kanchan, T. Sex estimation from fingerprint ridge density. A review of literature. *Acta Biomedica* **95**, (2021).

40. Abdouni, A. *et al.* Biophysical properties of the human finger for touch comprehension: influences of ageing and gender. *R Soc Open Sci* **4**, 170321 (2017).

41. Abdouni, A., Moreau, G., Vargiolu, R. & Zahouani, H. Static and active tactile perception and touch anisotropy: aging and gender effect. *Sci Rep* **8**, 14240 (2018).

42. Soanboon, P., Nanakorn, S. & Kutanan, W. Determination of sex difference from fingerprint ridge density in northeastern Thai teenagers. *Egypt J Forensic Sci* **6**, 185–193 (2016).

43. Sánchez-Andrés, A., Barea, J. A., Rivaldería, N., Alonso-Rodríguez, C. & Gutiérrez-Redomero, E. Impact of aging on fingerprint ridge density: Anthropometry and forensic implications in sex inference. *Science & Justice* **58**, 323–334 (2018).

44. Peters, R. M., Hackeman, E. & Goldreich, D. Diminutive Digits Discern Delicate Details: Fingertip Size and the Sex Difference in Tactile Spatial Acuity. *Journal of Neuroscience* **29**, 15756–15761 (2009).

45. Abdouni, A., Vargiolu, R. & Zahouani, H. Impact of finger biophysical properties on touch gestures and tactile perception: Aging and gender effects. *Sci Rep* **8**, 12605 (2018).

46. Morganti, P., Ruocco, E., Wolf, R. & Ruocco, V. Percutaneous Absorption and Delivery Systems. *Clin Dermatol* **19**, 489–501.

47. Flynn, C. O. & McCormack, B. A. O. Finite element modelling of forearm skin wrinkling. *Skin Research and Technology* **14**, 261–269.

48. Flynn, C. O. & McCormack, B. A. O. A three-layer model of skin and its application in simulating wrinkling. *Comput Methods Biomech Biomed Engin* **12**, 125–134 (2009).

49. Hendriks, F. M., Brokken, D., Oomens, C. W. J., Bader, D. L. & Baaijens, F. P. T. The relative contributions of different skin layers to the mechanical behaviour of human skin in vivo using suction experiments. *Med Eng Phys* **28**, 259–266.

50. Wex, C., Arndt, S., Stoll, A., Bruns, C. & Kupriyanova, Y. Isotropic incompressible hyperelastic models for modelling the mechanical behaviour of biological tissues: a review. *Biomed. Eng.-Biomed. Tech.* **60**, 577–592 (2015).

51. Marino, M. Constitutive Modeling of Soft Tissues. *Encyclopedia of Biomedical Engineering* **2**, 81–110 (2019).

52. Limbert, G. Mathematical and computational modelling of skin biophysics: a review. *Proceedings of The Royal Society A Mathematical Physical and Engineering Sciences* **473**, (2017).

53. Benítez, J. M. & Montáns, F. J. The mechanical behavior of skin: Structures and models for the finite element analysis. *Comput Struct* **190**, 75–107 (2017).

54. Miller-Young, J. E., Duncanb, N. A. & Baroud, G. Material properties of the human calcaneal fat pad in compression: experiment and theory. *J Biomech* **35**, 1523–1531 (2002).

55. Halata, Z., Grim, M. & Baumann, K. I. Current understanding of Merkel cells, touch reception and the skin. *Expert Rev Dermatol* **5**, 109–116 (2010).

56. Hamann, W. Mammalian Cutaneous Mechanoreceptors. *Prog Biophys Mol Biol* **64**, 81–104 (1995).

57. Gerling, G. J. SA-I mechanoreceptor position in fingertip skin may impact sensitivity to edge stimuli. *Appl Bionics Biomech* **7**, 19–29 (2010).

58. Chen, X., Shao, F., Barnes, C., Childs, T. & Henson, B. Exploring Relationships between Touch Perception and Surface Physical Properties and . *Institute of Engineering Systems and Design, School of Mechanical Engineering* **3**, 67–76 (2009).

59. Fagiani, R., Massi, F., Chatelet, E., Costes, J. P. & Berthier, Y. Contact of a finger on rigid surfaces and textiles: Friction coefficient and induced vibrations. *Tribol Lett* **48**, 145–158 (2012).

60. Ergen, E., Ulkar, B. & Eraslan, A. Proprioception and Coordination. *Journal of Sports Medicine* **42**, 57–83 (2007).

61. Johnson, K. O. The roles and functions of cutaneous mechanoreceptors. *Curr Opin Neurobiol* **11**, (2001).

62. Wu, J. Z., Krajnaj, K., Welcome, D. E. & Dong, R. G. Analysis of the dynamic strain in a fingertip exposed to vibrations: Correlation to the mechanical stimuli on mechanoreceptors. *J Biomech* **39**, 2445–2456 (2006).

63. Fagiani, R. Tribological activation of tactile receptors by vibrations induced at the finger contact surface. vol. PhD Thesis (Institut National des Sciences appliquées de Lyon, 2011).

64. Strzalkowski, N. Tactile Perception Across the Human Foot Sole as Examined by the Firing Characteristics of Cutaneous Afferents and Mechanical Properties of the Skin . (The University of Guelph, 2015).

65. Wang, Q. I. & Hayward, V. Tactile Synthesis and Perceptual Inverse Problems Seen from the Viewpoint of Contact Mechanics. *ACM Trans Appl Percept* **5**, (2008).

66. Gescheider, G. A. & Wright, J. H. Roughness perception in tactile channels: Evidence for an opponent process in the sense of touch. *Somatosens Mot Res* **30**, 120–132 (2013).

67. Pham, T. Q., Hoshi, T., Tanaka, Y. & Sano, A. Effect of 3D microstructure of dermal papillae on SED concentration at a mechanoreceptor location. *PLoS One* **12**, (2017).

68. Sripati, A. P., Bensmaia, S. J. & Johnson, K. O. A continuum mechanical model of mechanoreceptive afferent responses to indented spatial patterns. *J Neurophysiol* **95**, 3852–3864. (2006).

69. Hamasaki, T. & Iwamoto, M. Computational analysis of the relationship between mechanical state and mechanoreceptor responses during scanning of a textured surface. *Advances in Mechanical Engineering* **11**, 168781401988526 (2019).

70. Vallbo, A. B. & Johansson, R. S. Properties of cutaneous mechanoreceptors in the human hand related to touch sensation. *Hum Neurobiol* **3**, 3–14 (1984).

71. Pitts-Yushchenko, S. Mechanisms of Mechanotransduction in the Pacinian corpuscle. (University of Exeter, 2013).

72. Haeberle, H. & Lumpkin, E. A. Merkel Cells in Somatosensation. *Chemosens Percept* **1**, 110–119 (2008).

73. Fagiani, R. & Barbieri, M. Modelling of finger-surface contact dynamics. *Tribol Int* **74**, 130–137 (2014).

74. Biology, L. L. B. Somatosensation. Preprint at https://courses.lumenlearning.com/boundless-biology/chapter/somatosensation/ (2013).

75. Farage, M. A., Miller, K. W., Elsner, P. & Maibach, H. I. Structural Characteristics of the Aging Skin: A Review. *Cutan Ocul Toxicol* **26**, 343–357 (2007).

76. Amaied, E., Vargiolu, R., Bergheau, J. M. & Zahouni, H. Aging effect on tactile perception: Experimental and modelling studies. *Wear* **332–333**, 715–724 (2015).

77. Norman, J. F. *et al.* Aging and the haptic perception of 3D surface shape. *Atten Percept Psychophys* **73**, 908–918 (2011).

78. Skedung, L. *et al.* Mechanisms of tactile sensory deterioration amongst the elderly. *Sci Rep* **8**, (2018).

79. Decorps, J., Saumet, J. L., Sommer, P., Siguado-Roussel, D. & Fromey, B. Effect of ageing on tactile transduction processes. *Ageing Res Rev* **13**, 90–99 (2014).

80. Shaffer, S. W. & Harrison, A. L. Aging of the Somatosensory System: A Translational Perspective. *Phys Ther* **87**, 193–207 (2007).

81. Venkatesan, L., Barlow, S. M. & Kieweg, D. Age and sex-related changes in vibrotactile sensitivity of hand and face in neurotypical adults. *Somatosens Mot Res* **32**, 44–50 (2015).

82. Metze, D. & Luger, T. Nervous system in the skin. in *The Biology of the Skin* (eds. Frienkel, R. K. & Woodley, D. T.) 153–176 (The Parthenon Publishing Group, 2001).

83. Garcia-Piqueras, J. *et al.* Ageing of the somatosensory system at the periphery: age-related changes in cutaneous mechanoreceptors. *J Anat* **234**, 839–852 (2019).

84. Abdouni, A. *et al.* Biophysical properties of the human finger for touch comprehension: influences of ageing and gender. *R Soc Open Sci* **4**, (2017).

85. Thornbury, J. M. & Mistretta, C. M. Tactile Sensitivity as a Function of Age. *J Gerontol* **26**, 34–39 (1981).

86. Edwards, C., Heggie, R. & Marks, R. A study of differences in surface roughness between sun-exposed and unexposed skin with age. *Photodermatol Photoimmunol Photomed* **19**, 169–174 (2003).

87. Trojahn, C. *et al.* Relation between skin micro-topography, roughness, and skin age. *Skin Research and Technology* **21**, 69–75 (2015).

88. Care, S. S. C. S. How does skin get old? Preprint at http://silkah.com/stemcell/howtouse/.

89. Pawalaczyk, M., Lelonkiewicz, M. & Wieczorowski, M. Age-dependent biomechanical properties of the skin. *Postepy Dermatol Alergol* **30**, 302–306 (2013).

90. Kruglikov, I. L. & Scherer, P. E. Skin aging as mechanical phenomenon: The main weak links. *Nutr Healthy Aging* **4**, 291–307 (2018).

91. Schulze, C. *et al.* Stiffening of Human Skin Fibroblasts with Age. *Biophys J* **99**, 2434–2442 (2010).

92. Lynch, B. *et al.* How aging impacts skin biomechanics: A multiscale study in mice. *Sci Rep* **7**, (2017).

93. Flynn, C. O. & McCormack, B. A. O. Simulating the wrinkling and aging of skin with a multi-layer finite element model. *J Biomech* **43**, 442–448 (2010).

94. McGrath, J. A., Eady, R. A. J. & Pope, F. M. Anatomy and Organisation of Human Skin. in *Rook's Textbook of Dermatology* (Springer, 2004).

95. Adams, M. J. *et al.* Finger pad friction and its role in grip and touch. *J R Soc Interface* **10**, (2013).

96. Skedung, L. *et al.* Tactile perception: Finger friction,surface roughness and perceived coarseness. *Tribol Int* **44**, 505–512 (2011).

97. Smith, A. M., Chapman, C. E., Deslandes, M., Langlais, J.-S. & Thibodeau, M.-P. Role of friction and tangential force variation in the subjective scaling of tactile roughness. *Exp Brain Res* **144**, 211–223 (2002).

98. Leyva-Mendivila, M. F., Lengiewicz, J. & Limbert, G. Skin friction under pressure. The role of micromechanics. *Surf Topogr* **6**, (2018).

99. Kadiric, A., Sayles, R. S., Zhou, X. B. & Ioannides, E. A Numerical Study of the Contact Mechanics and Sub-Surface Stress Effects Experienced Over a Range of Machined Surface Coatings in Rough Surface Contacts. *J Tribol* **125**, 720–730 (2003).

100. Masen, M. A. *et al.* Evaluating lubricant performance to reduce COVID-19 PPE-related skin injury. *PLoS One* **15**, (2020).

101. Tomlinson, S. E., Carre, M. J., Lewis, R. & Franklin, S. E. Human finger ocntact with small, triangular ridged surfaces. *Wear* **279**, 2349–2353 (2010).

102. Lee, S. C. & Ren, N. The Subsurface Stress Field Created by Three-Dimensionally Rough Bodies in Contact with Traction. *Tribology Transactions* **37**, 615–621 (1994).

103. Tomlinson, S. E., Carre, M. J., Lewis, R. & Franklin, S. E. Human finger friction in contacts with ridged surfaces. *Wear* **301**, 330–337 (2020).

104. Arvidsson, M., Ringstad, L., Skedung, L., Duvefelt, K. & Rutland, M. W. Feeling fine - the effect of topography and friction on perceived roughness and slipperiness. *Biotribology* **11**, (2017).

105. Derler, S., Gerhardt, L.-C., Lenz, A., Bertaux, E. & Hadad, M. Friction of human skin against smooth and rough glass as a function of the contact pressure. *Tribol Int* **42**, 1565–1574 (2009).

106. Kwiatkowska, M., Franklin, S. E., Hendriks, C. P. & Kwiatkowski, K. Friction and deformation behaviour of human skin. *Wear* **267**, 1264–1273 (2009).

107. Limbert, G. *et al.* Biotribology of the ageing skin - Why we should care. *Biotribology* **17**, 75–90 (2019).

108. Voyer, J., Ausserer, F., Klien, S., Velkavrh, I. & Diem, A. Reduction of the Adhesive Friction of Elastomers through Laser Texturing of Injection Molds. *Lubricants* **5**, 45 (2017).

109. T. Verrillo, R., Bolanowski, S. J. & McGlone, F. P. Subjective magnitude of tactile roughness. *Somatosens Mot Res* **16**, 352–360 (1999).

110. Klöcker, A., Wiertlewski, M., Théate, V., Hayward, V. & Thonnard, J.-L. Physical Factors Influencing Pleasant Touch during Tactile Exploration. *PLoS One* **8**, e79085 (2013).

111. Tang, W. *et al.* From finger friction to brain activation: Tactile perception of the roughness of gratings. *J Adv Res* **21**, 129–139 (2020).

112. Liao, X. *et al.* Effects of contact method and acclimation on temperature and humidity in touch perception. *Textile Research Journal* **88**, 1605–1615 (2018).

113. Lawrence, M. A., Kitada, R., Klatzky, R. L. & Lederman, S. J. Haptic Roughness Perception of Linear Gratings via Bare Finger or Rigid Probe. *Perception* **36**, 547–557 (2007).

114. Cesini, I., Ndengue, J. D., Chatelet, E., Faucheu, J. & Massi, F. Correlation between friction-induced vibrations and tactile perception during exploration tasks of isotropic and periodic textures. *Tribol Int* **120**, 330–339 (2018).

115. Hollins, M., Fox, A. & Bishop, C. Imposed Vibration Influences Perceived Tactile Smoothness. *Perception* **29**, 1455–1465 (2000).

116. Hollins, S. J. B. S. W. M. Vibrotactile adaptation impairs discrimination of fine, but not coarse, textures. *Somatosens Mot Res* **18**, 253–262 (2001).

117. Strzalkowski. Tactile Perception Across the Human Foot Sole as Examined by the Firing Characteristics of Cutaneous Afferents and Mechanical Properties of the Skin. (2015).

118. MAENO, T., KOBAYASHI, K. & YAMAZAKI, N. Relationship between the Structure of Human Finger Tissue and the Location of Tactile Receptors. *JSME International Journal Series C* **41**, 94–100 (1998).

119. Gueorguiev, D., Bochereau, S., Mouraux, A., Hayward, V. & Thonnard, J. L. Touch uses frictional cues to discriminate flat materials. *Sci Rep* **6**, (2016).

120. Connor, C., Hsiao, S., Phillips, J. & Johnson, K. Tactile roughness: neural codes that account for psychophysical magnitude estimates. *The Journal of Neuroscience* **10**, 3823–3836 (1990).

121. Gescheider, G. A., Bolanowski, S. J., Greenfield, T. C. & Brunette, K. E. Perception of the tactile texture of raised-dot patterns: A multidimensional analysis. *Somatosens Mot Res* **22**, 127–140 (2005).

122. Gescheider, G. A. & Wright, J. H. Effects of receptor density on the tactile perception of roughness: implications for neural mechanisms of texture perception. *Somatosens Mot Res* **38**, 202–213 (2021).

123. Connor, C. & Johnson, K. Neural coding of tactile texture: comparison of spatial and temporal mechanisms for roughness perception. *The Journal of Neuroscience* **12**, 3414–3426 (1992).

124. Weber, A. I. *et al.* Spatial and temporal codes mediate the tactile perception of natural textures. *Proceedings of the National Academy of Sciences* **110**, 17107–17112 (2013).

125. Konyo, M., Maeno, T., Yoshida, A. & Tadokoro, S. Roughness Sense Display Representing Temporal Frequency Changes of Tactile Information in Response to Hand Movements. in *First*

Joint Eurohaptics Conference and Symposium on Haptic Interfaces for Virtual Environment and Teleoperator Systems 609–610 (IEEE). doi:10.1109/WHC.2005.113.

126. Yoshioka, T., Bensmaïa, S. J., Craig, J. C. & Hsiao, S. S. Texture perception through direct and indirect touch: An analysis of perceptual space for tactile textures in two modes of exploration. *Somatosens Mot Res* **24**, 53–70 (2007).

127. Tanaka, Y., Bergmann Tiest, W. M., Kappers, A. M. L. & Sano, A. Contact Force and Scanning Velocity during Active Roughness Perception. *PLoS One* **9**, e93363 (2014).

128. Zhou, X. *et al.* Correlation between tactile perception and tribological and dynamical properties for human finger under different sliding speeds. *Tribol Int* **123**, (2018).

129. Zhou, X. *et al.* Effect of Finger Sliding Direction on Tactile Perception, Friction and Dynamics. *Tribol Lett* **68**, 85 (2020).

130. Masen, M. A. A systems based experimental approach to tactile friction. *J Mech Behav Biomed Mater* **4**, 1620–1626 (2011).

131. Dinc¸, O. S., Ettles, C. M., Calabrese, S. J. & Scarton, H. A. Some Parameters Affecting Tactile Friction. *J Tribol* **113**, 512–517 (1991).

132. Sasada, T. The friction of human skin. in *Proceedings of the 21st Biotribology Symposium* 46–52 (JSME, 2000).

133. Hendriks, C. P. & Franklin, S. E. Influence of Surface Roughness, Material and Climate Conditions on the Friction of Human Skin. *Tribol Lett* **37**, (2010).

134. Liu, X., Lu, Z., Lewis, R., Carré, M. J. & Matcher, S. J. Feasibility of using optical coherence tomography to study the influence of skin structure on finger friction. *Tribol Int* **63**, 34–44 (2013).

135. Savescu, A. v., Latash, M. L. & Zatsiorsky, V. M. A Technique to Determine Friction at the Fingertips. *J Appl Biomech* **24**, 43–50 (2008).

136. Seo, N. J. & Armstrong, T. J. Friction coefficients in a longitudinal direction between the finger pad and selected materials for different normal forces and curvatures. *Ergonomics* **52**, 609–616 (2009).

137. Hyun-Yong H., Shimada, A. & Kawamura, S. Analysis of friction on human fingers and design of artificial fingers. in *Proceedings of IEEE International Conference on Robotics and Automation* 3061–3066 (IEEE). doi:10.1109/ROBOT.1996.509177.

138. Pasumarty, S. M., Johnson, S. A., Watson, S. A. & Adams, M. J. Friction of the Human Finger Pad: Influence of Moisture, Occlusion and Velocity. *Tribol Lett* **44**, 117–137 (2011).

139. Gerhardt, L.-C., Strässle, V., Lenz, A., Spencer, N. D. & Derler, S. Influence of epidermal hydration on the friction of human skin against textiles. *J R Soc Interface* **5**, (2008).

140. Gueorguiev, D., Vezzoli, E., Mouraux, A., Lemaire-Semail, B. & Thonnard, J.-L. The tactile perception of transient changes in friction. *J R Soc Interface* **14**, 20170641 (2017).

141. André, T., Lefèvre, P. & Thonnard, J.-L. Fingertip Moisture Is Optimally Modulated During Object Manipulation. *J Neurophysiol* **103**, 402–408 (2010).

142. Klöcker, A., Arnould, C., Penta, M. & Thonnard, J.-L. Rasch-Built Measure of Pleasant Touch through Active Fingertip Exploration. *Front Neurorobot* **6**, (2012).

143. Zhou, N.-Y. *et al.* Prevention and Treatment of Skin Damage Caused by Personal Protective Equipment: Experience of the First-Line Clinicians Treating SARS-CoV-2 Infection. *Int J Dermatol Venereol* **3**, (2020).

144. Gefen, A. Skin Tears, Medical Face Masks, and Coronavirus. *Wound Manag Prev* **66**, (2020).

145. Zulkowski, K. Understanding Moisture-Associated Skin Damage, Medical Adhesive-Related Skin Injuries, and Skin Tears. *Adv Skin Wound Care* **30**, (2017).

146. Payne, A. Covid-19: skin damage with prolonged wear of FFP3 masks. *BMJ* (2020) doi:10.1136/bmj.m1743.

147. Dhandapani, M., Jose, S. & Cyriac, M. C. Health Problems and Skin Damages Caused by Personal Protective Equipment: Experience of Frontline Nurses Caring for Critical COVID-19 Patients in Intensive Care Units. *Indian Journal of Critical Care Medicine* **25**, (2021).

148. Woo, K. Y., Beeckman, D. & Chakravarthy, D. Management of Moisture-Associated Skin Damage. *Adv Skin Wound Care* **30**, (2017).

149. Park, J. PPE Skin Protection during COVID. *Tea with MD* https://www.teawithmd.com/2020/04/ppe-skin-protection/ (2020).

150. Corniani, G. & Saal, H. P. Tactile innervation densities across the whole body. *J Neurophysiol* **124**, 1229–1240 (2020).

151. Kalra, A., Lowe, A. & Al-Jumaily, A. Mechanical Behaviour of Skin: A Review. *Journal of Material Science & Engineering* **5**, (2016).

152. Seidenari, G. P. S. Variations in Facial Skin Thickness and Echogenicity with Site and Age. *Acta Derm Venereol* **79**, 366–369 (1999).

153. Griffin, M. F., Leung, B. C., Premakumar, Y., Szarko, M. & Butler, P. E. Comparison of the mechanical properties of different skin sites for auricular and nasal reconstruction. *Journal of Otolaryngology - Head & Neck Surgery* **46**, 33 (2017).

154. Warburton, M. & Maddock, S. Physically-based forehead animation including wrinkles. *Comput Animat Virtual Worlds* **26**, 55–68 (2015).

155. Chopra, K. *et al.* A Comprehensive Examination of Topographic Thickness of Skin in the Human Face. *Aesthet Surg J* **35**, (2015).

156. Kuwazuru, O., Saothong, J. & Yoshikawa, N. Mechanical approach to aging and wrinkling of human facial skin based on the multistage buckling theory. *Med Eng Phys* **30**, 516–522 (2008).

157. Luboz, V., Promayon, E. & Payan, Y. Linear Elastic Properties of the Facial Soft Tissues Using an Aspiration Device: Towards Patient Specific Characterization. *Ann Biomed Eng* **42**, (2014).

158. Donovan, J., Kudla, I., Holness, L. D., Skotnicki-Grant, S. & Nethercott, J. R. Skin Reactions Following Use of N95 Facial Masks. *Dermatitis* **18**, (2007).

159. al Badri, F. Surgical mask contact dermatitis and epidemiology of contact dermatitis in healthcare workers. *Current Allergy and Clinical Immunology* **30**, 183–188 (2017).

160. Donovan, J. & Skotnicki-Grant, S. Allergic Contact Dermatitis from Formaldehyde Textile Resins in Surgical Uniforms and Nonwoven Textile Masks. *Dermatitis* **18**, (2007).

161. Lan, J. *et al.* Skin damage among health care workers managing coronavirus disease-2019. *J Am Acad Dermatol* **82**, (2020).

162. Yan, Y. *et al.* Consensus of Chinese experts on protection of skin and mucous membrane barrier for health-care workers fighting against coronavirus disease 2019. *Dermatol Ther* **33**, (2020).

163. Sernicola, A. *et al.* Treatment of nasal bridge ulceration related to protective measures for the COVID-19 epidemic. *Int Wound J* **17**, (2020).

164. Jiang, Q. *et al.* The Prevalence, Characteristics, and Prevention Status of Skin Injury Caused by Personal Protective Equipment Among Medical Staff in Fighting COVID-19: A Multicenter, Cross-Sectional Study. *Adv Wound Care (New Rochelle)* **9**, (2020).

165. Thorfinn, J., Sjöberg, F. & Lidman, D. Sitting can cause ischaemia in the subcutaneous tissue of the buttocks, which implicates multilayer tissue damage in the development of pressure ulcers. *Scand J Plast Reconstr Surg Hand Surg* **43**, (2009).

166. Hua, W. *et al.* Short-term skin reactions following use of N95 respirators and medical masks. *Contact Dermatitis* **83**, (2020).

167. Loerakker, S. *et al.* Temporal Effects of Mechanical Loading on Deformation-Induced Damage in Skeletal Muscle Tissue. *Ann Biomed Eng* **38**, 2577–2587 (2010).

168. Bouten, C. v., Oomens, C. W., Baaijens, F. P. & Bader, D. L. The etiology of pressure ulcers: Skin deep or muscle bound? *Arch Phys Med Rehabil* **84**, (2003).

169. Mimura, M., Ohura, T., Takahashi, M., Kajiwara, R. & Ohura Jr., N. Mechanism leading to the development of pressure ulcers based on shear force and pressures during a bed operation: Influence of body types, body positions, and knee positions. *Wound Repair and Regeneration* **17**, (2009).

170. Wu, Y., van der Schaft, D. W. J., Baaijens, F. P. & Oomens, C. W. J. Cell death induced by mechanical compression on engineered muscle results from a gradual physiological mechanism. *J Biomech* **49**, (2016).

171. Jagannathan, N. S. & Tucker-Kellogg, L. Membrane permeability during pressure ulcer formation: A computational model of dynamic competition between cytoskeletal damage and repair. *J Biomech* **49**, (2016).

172. Oomens, C. W. J., Bressers, O. F. J. T., Bosboom, E. M. H., Bouten, C. V. C. & Bader, D. L. Can Loaded Interface Characteristics Influence Strain Distributions in Muscle Adjacent to Bony Prominences? *Comput Methods Biomech Biomed Engin* **6**, 171–180 (2003).

173. Gefen, A. *et al.* Device-related pressure ulcers: SECURE prevention. *J Wound Care* **29**, (2020).

174. Reichel, S. M. Shearing force as a factor in decubitus ulcers in paraplegics. *J Am Med Assoc* **166**, (1958).

175. Bader, D. L., Worsley, P. R. & Gefen, A. Bioengineering considerations in the prevention of medical device-related pressure ulcers. *Clinical Biomechanics* **67**, (2019).

176. Manorama, A., Meyer, R., Wiseman, R. & Bush, T. R. Quantifying the effects of external shear loads on arterial and venous blood flow: Implications for pressure ulcer development. *Clinical Biomechanics* **28**, (2013).

177. Bishopp, A. *et al.* The preventative effect of hydrocolloid dressings on Nasal bridge pressure ulceration in acute non- invasive ventilation. *Ulster Med J.* **88**, 17–20 (2019).

178. Moore, Z. E. & Webster, J. Dressings and topical agents for preventing pressure ulcers. *Cochrane Database of Systematic Reviews* **12**, (2018).

179. Kantor, J. Behavioral considerations and impact on personal protective equipment use: Early lessons from the coronavirus (COVID-19) pandemic. *J Am Acad Dermatol* **82**, (2020).

180. Lei, Z., Yang, J. (James) & Zhuang, Z. Headform and N95 Filtering Facepiece Respirator Interaction: Contact Pressure Simulation and Validation. *J Occup Environ Hyg* **9**, 46–58 (2012).

181. Lei, Z., Yang, J. & Zhuang, Z. Contact Pressure Study of N95 Filtering Face-piece Respirators Using Finite Element Method. *Comput Aided Des Appl* **7**, 847–861 (2010).

182. Lei, Z. *et al.* Simulated Effects of Head Movement on Contact Pressures Between Headforms and N95 Filtering Facepiece Respirators Part 1: Headform Model and Validation. *Ann Occup Hyg* 1175–1185 (2014) doi:10.1093/annhyg/meu051.

183. Lei, Z., Ji, X., Yang, J., Zhuang, Z. & Rottach, D. Simulated Effects of Head Movement on Contact Pressures between Headforms and N95 Filtering Facepiece Respirators Part 2: Simulation. *Ann Occup Hyg* (2014) doi:10.1093/annhyg/meu064.

184. Software, I. E. BEM and FEM: A Comparison. Preprint at https://www.integratedsoft.com/Technology/bemvsfem.aspx.

185. Hansen, U. *ME3/4 Finite Element Analysis & Applications*. (Department of Mechanical Engineering - Imperial College London, 2017).

186. Simulia, D. S.-. Abaqus CAE. Preprint at https://www.3ds.com/products-services/simulia/products/abaqus/ (2017).

187. Simulia, D. S.-. *Abaqus 6.12 - Getting Started with Abaqus: Interactive Edition*. (2012).

188. Simulia. Abaqus CAE - 4.1 Element formulation and integration. in *Abaqus Theory Manual* (Dassault Systemes, 2019).

189. Simulia. Abaqus CAE - 3.2.5 Continuum elements with incompatible modes. in *Abaqus Theory Manual* (Dassault Systemes, 2019).

190. Simulia. Abaqus CAE - 3.2.3 Hybrid incompressible solid element formulation. in *Abaqus Theory Manual* (Dassault Systemes, 2019).

191. Rausch, M. K., Karniadakis, G. E. & Humphrey, J. D. Modeling Soft Tissue Damage and Failure Using a Combined Particle/Continuum Approach. *Biomech Model Mechanobiol* **16**, (2017).

192. Balint, D. *Computational Continuum Mechanics*. (Imperial College London, 2018).

193. Department of Mechanical Engineering. *Data & Formula Book*. (Imperial College London, 2014).

194. Ogden, R. W. *Non-Linear Elastic Deformations*. *Mathematics And Its Applications* (Ellis Horwood Limited, 1984).

195. Malvern, L. E. *Introduction to the Mechanics of a Continuous Medium*. *Engineering of the Physicsal Sciences* (Pretence-Hall, 1969).

196. Kim, N. *Introduction to Nonlinear Finite Element Analysis*. (Springer, 2015).

197. Kim, B. *et al.* A Comparison Among Neo-Hookean Model, Mooney-Rivlin Model, and Ogden Model for Chloroprene Rubber. *International Journal of Precision Engineering and Manufacturing* **13**, 759–764 (2012).

198. Bergstrom, J. S. Elasticity/Hyperelasticity. in *Mechanics of Solid Polymers: Theory and Computational Modeling* (Elsevier, 2015).

199. Rackl, M. Curve Fitting for Ogden, Yeoh and Polynomial Models. *7th International Scilab Users Conference*.

200. Martins, P. A. L. S., Natal Jorge, R. M. & Ferreira, A. J. M. A Comparative Study of Several Material Models for Prediction of Hyperelastic Properties: Application to Silicone-Rubber and Soft Tissues. *Strain* **46**, 135–147 (2006).

201. Groves, R. B. Quantifying the Mechanical Properties of Skin In Vivo and Ex Vivo to Optimise Microneedle Device Design. vol. PhD Thesis (Cardiff University, 2011).

202. Berselli, G., Vertechy, R., Pellicciari, M. & Vassura, G. Hyperelastic Modeling of Rubber-Like Photopolymers for Additive Manufacturing Processes. in *Rapid Prototyping Technology – Principles and Functional Requirements* (InTech, 2011).

203. Lapeer, R. J., Gasson, P. & Karri, V. Fitting hyperelastic material models to stress-strain data from an in-vitro experiment on human skin. *Conference: Polymers and Moulds Innovations (PMI)* **127–133**, (2015).

204. Meyers, M. A. & Chawla, K. K. *Mechanical Behavior of Materials*. vol. 1 (Cambridge University Press, 2008).

205. Meyers, M. A. & Chawla, K. K. Mechanical Behavior of Materials - Section 13.11. in *Mechanical Behavior of Materials* (Cambridge University Press, 2008). doi:10.1017/CBO9780511810947.

206. Taylor, A. & Wong, J. Stress Analysis of Polymers. in *Structure, Properties and Applications of Polymers* (Imperial College London, 2017).

207. Epaarachchi, J. A. The effect of viscoelasticity on fatigue behaviour of polymer matrix composites. in *Creep and Fatigue in Polymer Matrix Composites* 492–513 (Elsevier, 2011). doi:10.1533/9780857090430.3.492.

208. WANG, L. One-Dimensional Visco-Elastic Waves and Elastic-Visco-Plastic Waves. in *Foundations of Stress Waves* 219–264 (Elsevier, 2007). doi:10.1016/B978-008044494-9/50006-8.

209. Gefen, A. & Shaked, E. Modeling the effects of moisture-related skin-support friction on the risk for superficial pressure ulcers during patient repositioning in bed. *Front Bioeng Biotechnol* **1**,.

210. Hendriks, F. M. *et al.* A numerical-experimental method to characterize the non-linear mechanical behaviour of human skin. *Skin Research and Technology* **9**, (2003).

211. Bischoff, J. E. & Arruda, E. M. Finite element simulations of orthotropic hyperelasticity. *Finite Elements in Analysis and Design* **38**, 983–998.

212. Shergold, O. A. & Fleck, N. A. Mechanisms of deep penetration of soft solids, with application to the injection and wounding of skin. *The Royal Society* **460**,.

213. Flynn, C. O., Taberner, A. J., Nielsen, P. M. F. & Fels, S. Simulating the three-dimensional deformation of in vivo facial skin. *Journal of the Mechanical Behaviour of Biomedical Materials* **28**, 484–494 (2013).

214. Manan, N. F. A. *et al.* Determining Hyperelastic Parameters of Human Skin Using 2D Finite Element Modelling and Simulation. *Conference: IEEE Symposium on Humanities, Science and Engineering Research*.

215. Mahmud, J., Holt, C., Evans, S., Manan, N. & Chizaric, M. A Parametric Study and Simulations in Quantifying Human Skin Hyperelastic Parameters. *Procedia Eng* **41**, 1580 – 1586.

216. Koutroupi, K. S. & Barbenal, J. C. Mechanical and failure behaviour of the stratum corneum. *J Biomech* **23**, 281–287 (1990).

217. Geerligs, M., Oomens, C., Ackermans, P., Baaijens, F. & Peters, G. Linear shear response of the upper skin layers. *Biorheology* **48**, 229–245.

218. Magnenat-Thalmann, N. *et al.* A computational skin model: fold and wrinkle formation. *IEEE Transactions on Information Technology in Biomedicine* **6**, 317–323 (2002).

219. Leveque, J. L. & Audoly, B. Influence of Stratum Corneum on the entire skin mechanical properties, as predicted by a computational skin model. *Skin Research and Technology* **19**, (2012).

220. Wu, K. S., van Osdol, W. W. & Dauskardt, R. H. Mechanical Properties of Human Stratum Corneum: Effect of Temperature, Hydration, and Chemical Treatment. *Biomaterials* **27**, 785–795 (2006).

221. Delalleau, A. In vivo analysis of the skins mechanical properties. vol. PhD Thesis (University Jean Monnet - Saint Etienne, 2007).

222. Hull, D. & Clyne, T. W. *An introduction to Composite Materials*. (Cambridge University Press, 1996).

223. Jobanputra, R. D., Boyle, C. J., Dini, D. & Masen, M. A. Modelling the effects of age-related morphological and mechanical skin changes on the stimulation of tactile mechanoreceptors. *J Mech Behav Biomed Mater* **112**, (2020).

224. Liu, X. *et al.* The contributions of skin structural properties to the friction of human finger-pads. *Proceedings of the Institution of Mechanical Engineers, Part J: Journal of Engineering Tribology* **229**, 294–311 (2015).

225. Fruhstorfer, H., Abel, U., Garthe, C. D. & Knuttel, A. Thickness of the Stratum Corneum of the Volar Fingertips. *Clinical Anatomy* **13**, 429–433 (2000).

226. Pan, L., Zan, L. & Foster, F. S. Ultrasonic and viscoelastic properties of skin under transverse mechanical stress in vitro. *Ultrasound Med Biol* **24**, 995–1007 (1998).

227. Wan Abas, W. A. Biaxial tension test of human skin in vivo. *Biomed Mater Eng* **4**, 473–86 (1994).

228. Yong-Ping Zheng & Mak, A. F. T. An ultrasound indentation system for biomechanical properties assessment of soft tissues in-vivo. *IEEE Trans Biomed Eng* **43**, 912–918 (1996).

229. Piccinin, M. A., Miao, J. H. & Schwartz, J. Histology, Meissner Corpuscle. in *StatPearls[Internet]* (Treasure Island (FL): StatPearls Publishing, 2020).

230. Norman, J. F. *et al.* Ageing and curvature discrimination from static and dynamic touch. *PLoS One* **8**, (2013).

231. Zhang, S. & Duan, E. Fighting against Skin Aging: The Way from Bench to Bedside. *Cell Transplant* **27**, 729–738 (2018).

232. Jobanputra, R. Touch & Perception: Numerical Modelling of Finger Interaction. (Imperial College London, 2018).

233. Morey, P. Skin Tears: A Literature Review. *The Australian Journal of Wound Management* **15**, 122–124, 126–129 (2007).

234. Klaassen, M., de Vries, E. G. & Masen, M. A. Friction in the contact between skin and soft counter material: Effects of hardness and surface finish. *Journal of the Mechanical Behaviour of Biomedical Materials* **92**, 137–143 (2019).

235. Bicchi, A., Buss, M., Ernst, M. & Peer, A. *The Sense of Touch and its Rendering*. vol. 45 (Springer Berlin Heidelberg, 2008).

236. Sripati, A. P., Bensmaia, S. J. & Johnson, K. O. A Continuum Mechanical Model of Mechanoreceptive Afferent Responses to Indented Spatial Patterns. *J Neurophysiol* **95**, 3852–3864 (2006).

237. Pham, T. Q., Hoshi, T., Tanaka, Y. & Sano, A. Effect of 3D microstructure of dermal papillae on SED concentration at a mechanoreceptor location. *PLoS One* **12**, e0189293 (2017).

238. Nonomura, Y. *et al.* How to identify water from thickener aqueous solutions by touch. *J R Soc Interface* **9**, 1216–1223 (2012).

239. Simulia. Abaqus CAE - 6.3.2 Implicit dynamic analysis using direct integration. in *Abaqus CAE User Manual* (2019).

240. Hamilton, G. M. & Goodman, L. E. The Stress Field Created by a Circular Sliding Contact. *J Appl Mech* **33**, 371–376 (1966).

241. Tang, W. *et al.* Investigation of mechanical responses to the tactile perception of surfaces with different textures using the finite element method. *Advances in Mechanical Engineering* **8**, 1–9 (2016).

242. Almagirby, A., Rongong, J. A. & Carré, M. J. The development of a new artificial model of a finger for assessing transmitted vibrations. *J Mech Behav Biomed Mater* **78**, 20–27 (2018).

243. Dohrn, M. Fingerprint Skin Ridges - Science Photo Library. *Pixels* (2018).

244. Tang, W. *et al.* Tactile Perception of Skin and Skin Cream. *Tribol Lett* **59**, 24 (2015).

245. Zhao, Y., Feng, B., Lee, J., Lu, N. & Pierce, D. M. A multi-layered model of human skin elucidates mechanisms of wrinkling in the forehead. *J Mech Behav Biomed Mater* **105**, 103694 (2020).

246. Bader, D. & Bowker, P. Mechanical characteristics of skin and underlying tissues in vivo. *Biomaterials* **4**, 305–308 (1983).

247. Krupička, A., Johansson, M. & Hult, A. Viscoelasticity in Polymer Films on Rigid Substrates. *Macromol Mater Eng* **288**, 108–116 (2003).

248. Liu, X. *et al.* The contributions of skin structural properties to the friction of human finger-pads. *Proceedings of the Institution of Mechanical Engineers, Part J: Journal of Engineering Tribology* **229**, 294–311 (2015).

249. Mohiuddin, A. K. An Extensive Review of Face Powder Formulation Considerations. *Dermatology and Dermatitis* **4**, 01–18 (2019).

250. Myant, C. Experimental Techniques for Investigating Lubricated Compliant Contacts. (Imperial College London, 2010).

251. Timm, K., Myant, C., Spikes, H. A. & Grunze, M. Particulate lubricants in cosmetic applications. *Tribol Int* **44**, 1695–1703 (2011).

252. Timm, K. *et al.* Cosmetic powder suspensions in compliant, fingerprintlike contacts. *Biointerphases* **6**, 126–134 (2011).

253. Wilson, R., Dini, D. & van Wachem, B. The influence of surface roughness and adhesion on particle rolling. *Powder Technol* **312**, 321–333 (2017).

254. Cremonesi, M., Franci, A., Idelsohn, S. & Oñate, E. A State of the Art Review of the Particle Finite Element Method (PFEM). *Archives of Computational Methods in Engineering* **27**, (2020).

255. Jobanputra, R. D., Hayes, J., Royyuru, S. & Masen, M. A. A numerical analysis of skin–PPE interaction to prevent facial tissue injury. *Sci Rep* **11**, (2021).

256. Yap, K. K. *et al.* Wax-Oil Lubricants to Reduce the Shear Between Skin and PPE. *Sci Rep* **11**, (2021).

257. Oomens, C. W. J., Bader, D. L., Loerakker, S. & Baaijens, F. Pressure Induced Deep Tissue Injury Explained. *Ann Biomed Eng* **43**, (2015).

258. Xu, M. & Yang, J. Contact Pressure Sensitivity Analysis in N95 Filtering Facepiece Respirator With Strap Location, Friction, and Headform Material Property. in *Volume 1A: 35th Computers and Information in Engineering Conference* (American Society of Mechanical Engineers, 2015). doi:10.1115/DETC2015-46465.

259. Lei, Z. *et al.* Simulated Effects of Head Movement on Contact Pressures Between Headforms and N95 Filtering Facepiece Respirators Part 1: Headform Model and Validation. *Ann Occup Hyg* (2014) doi:10.1093/annhyg/meu051.

260. Brill, A.-K., Moghal, M., Morrell, M. J. & Simonds, A. K. Randomized crossover trial of a pressure sensing visual feedback system to improve mask fitting in noninvasive ventilation. *Respirology* **22**, (2017).

261. Xu, M. & Yang, J. Human Facial Soft Tissue Thickness and Mechanical Properties: A Literature Review. in *Volume 1A: 35th Computers and Information in Engineering Conference* (American Society of Mechanical Engineers, 2015). doi:10.1115/DETC2015-46363.

262. Zahouani, H. *et al.* Characterization of the mechanical properties of a dermal equivalent compared with human skin in vivo by indentation and static friction tests. *Skin Research and Technology* **15**, (2009).

263. Maiti, R. *et al.* Morphological parametric mapping of 21 skin sites throughout the body using optical coherence tomography. *J Mech Behav Biomed Mater* **102**, (2020).

264. Adams, M. J., Briscoe, B. J. & Johnson, S. A. Friction and lubrication of human skin. *Tribol Lett* **26**, (2007).

265. Johnson, K. L. *Contact Mechanics*. (Cambridge University Press, 1985). doi:10.1017/CBO9781139171731.

266. Xing, M., Pan, N., Zhong, W. & Maibach, H. Skin friction blistering: computer model. *Skin Research and Technology* **13**, (2007).

267. Polliack, A. A. & Scheinberg, S. A New Technology for Reducing Shear and Friction Forces on the Skin: Implications for Blister Care in the Wilderness Setting. *Wilderness Environ Med* **17**, (2006).

268. Aumailley, M. & Rousselle, P. Laminins of the dermo–epidermal junction. *Matrix Biology* **18**, (1999).

269. Hatje, L. K., Richter, C., Blume-Peytavi, U. & Kottner, J. Blistering time as a parameter for the strength of dermoepidermal adhesion: a systematic review and meta-analysis. *British Journal of Dermatology* **172**, (2015).

270. Tang, W., Zhou, Y., Zhu, H. & Yang, H. The effect of surface texturing on reducing the friction and wear of steel under lubricated sliding contact. *Appl Surf Sci* **273**, 199–204 (2013).

271. Aly, R., Shirley, C., Cunico, B. & Maibach, H. I. Effect of Prolonged Occlusion on the Microbial Flora, pH, Carbon Dioxide and Transepidermal Water Loss on Human Skin. *Journal of Investigative Dermatology* **71**, (1978).

272. Klaassen, M., Schipper, D. J. & Masen, M. A. Influence of the relative humidity and the temperature on the in-vivo friction behaviour of human skin. *Biotribology* **6**, (2016).

273. Kleesz, P., Darlenski, R. & Fluhr, J. W. Full-Body Skin Mapping for Six Biophysical Parameters: Baseline Values at 16 Anatomical Sites in 125 Human Subjects. *Skin Pharmacol Physiol* **25**, (2012).

274. Zhang, M. & Mak, A. F. T. In vivo friction properties of human skin. *Prosthet Orthot Int* **23**, (1999).

275. Seo, N. J., Armstrong, T. J. & Drinkaus, P. A comparison of two methods of measuring static coefficient of friction at low normal forces: a pilot study. *Ergonomics* **52**, (2009).

276. Farkas, L. G., Katic, M. J. & Forrest, C. R. International Anthropometric Study of Facial Morphology in Various Ethnic Groups/Races. *Journal of Craniofacial Surgery* **16**, (2005).

277. Dong, Y. *et al.* Influence of sex and body mass index on facial soft tissue thickness measurements of the northern Chinese adult population. *Forensic Sci Int* **222**, (2012).

278. Ascott, A., Crowest, P., de Sausmarez, E., Khan, M. & Chakladar, A. Respiratory personal protective equipment for healthcare workers: impact of sex differences on respirator fit test results. *Br J Anaesth* **126**, (2021).

279. Bhattacharya, P. & Viceconti, M. Multiscale modeling methods in biomechanics. *WIREs Systems Biology and Medicine* **9**, (2017).

280. ALDIERI, A., TERZINI, M., BIGNARDI, C., ZANETTI, E. M. & AUDENINO, A. L. A CONSTITUTIVE FRAMEWORK FOR HUMAN DERMIS MECHANICAL MODELLING. in 367–378 (2017). doi:10.2495/MC170381.

281. Pond, D., McBride, A. T., Davids, L. M., Reddy, B. D. & Limbert, G. Microstructurally-based constitutive modelling of the skin – Linking intrinsic ageing to microstructural parameters. *J Theor Biol* **444**, 108–123 (2018).

282. Guissouma, I., Hambli, R., Rekik, A. & Hivet, A. A multiscale four-layer finite element model to predict the effects of collagen fibers on skin behavior under tension. *Proc Inst Mech Eng H* **235**, 1274–1287 (2021).

283. Witt, N. J., Woessner, A. E., Quinn, K. P. & Sander, E. A. Multiscale Computational Model Predicts Mouse Skin Kinematics Under Tensile Loading. *J Biomech Eng* **144**, (2022).

284. Groves, R. B., Coulman, S. A., Birchall, J. C. & Evans, S. L. An anisotropic, hyperelastic model for skin: Experimental measurements, finite element modelling and identification of parameters for human and murine skin. *J Mech Behav Biomed Mater* **18**, 167–180 (2013).

285. Stekelenburg, A., Oomens, C. & Bader, D. Compression-Induced Tissue Damage: Animal Models. in *Pressure Ulcer Research* 187–204 (Springer-Verlag, 2005). doi:10.1007/3-540-28804-X_12.

286. Edsberg, L. E. *et al.* Revised National Pressure Ulcer Advisory Panel Pressure Injury Staging System. *Journal of Wound, Ostomy & Continence Nursing* **43**, 585–597 (2016).

287. Bader, D. & Oomens, C. The Potential of Biomarkers in the Early Detection of Pressure Ulcers. in *Science and Practice of Pressure Ulcer Management* 1–15 (Springer London, 2018). doi:10.1007/978-1-4471-7413-4_1.

288. Soetens, J. F. J. Mechanical and biochemical response of human skin to diverse loading conditions. (Technical University of Eindhoven, 2019).

289. Klaassen, M. The static friction behaviour of skin with relevance to pressure ulcer prevalence. (University of Twente, 2018). doi:10.3990/1.9789036546072.

290. Worsley, P. R., Stanger, N. D., Horrell, A. K. & Bader, D. L. Investigating the effects of cervical collar design and fit on the biomechanical and biomarker reaction at the skin. *Medical Devices: Evidence and Research* **Volume 11**, 87–94 (2018).

291. Worsley, P., Prudden, G., Gower, G. & Bader, D. Investigating the effects of strap tension during non-invasive ventilation mask application: a combined biomechanical and biomarker approach. *Medical Devices: Evidence and Research* **Volume 9**, 409–417 (2016).

292. Hemmes, B. *et al.* Cytokine IL1α and lactate as markers for tissue damage in spineboard immobilisation. A prospective, randomised open-label crossover trial. *J Mech Behav Biomed Mater* **75**, 82–88 (2017).

293. de Wert, L. A. *et al.* A new method to evaluate the effects of shear on the skin. *Wound Repair and Regeneration* **23**, 885–890 (2015).

294. Bronneberg, D. Biochemical markers for early detection of superficial pressure ulcers. (2007).

295. Bronneberg, D., Bouten, C. V. C., Oomens, C. W. J., van Kemenade, P. M. & Baaijens, F. P. T. An in vitro Model System to Study the Damaging Effects of Prolonged Mechanical Loading of the Epidermis. *Ann Biomed Eng* **34**, 506–514 (2006).

296. Cornelissen, L. Modeling the transport of biochemical markers in skin. (Technical University of Eindhoven, 2008).

297. Cornelissen, L. H., Bronneberg, D., Bader, D. L., Baaijens, F. P. T. & Oomens, C. W. J. The Transport Profile of Cytokines in Epidermal Equivalents Subjected to Mechanical Loading. *Ann Biomed Eng* **37**, 1007–1018 (2009).

298. Bronneberg, D. *et al.* Cytokine and chemokine release upon prolonged mechanical loading of the epidermis. *Exp Dermatol* **16**, 567–573 (2007).

299. Perkins, M. A., Osterhues, M. A., Farage, M. A. & Robinson, M. K. A noninvasive method to assess skin irritation and compromised skin conditions using simple tape adsorption of molecular markers of inflammation. *Skin Research and Technology* **7**, 227–237 (2001).

300. van Heyningen, R. & Weiner, J. S. The effect of arterial occlusion on sweat composition. *J Physiol* **116**, 404–413 (1952).

301. Ferguson-Pell, M. & Hagisawa, S. Biochemical changes in sweat following prolonged ischemia. *J Rehabil Res Dev* **25**, 57–62 (1988).

302. Polliack, A., Taylor, R. & Bader, D. Sweat analysis following pressure ischaemia in a group of debilitated subjects. *J Rehabil Res Dev* **34**, 303–8 (1997).

303. Knight, S. L., Taylor, R. P., Polliack, A. A. & Bader, D. L. Establishing predictive indicators for the status of loaded soft tissues. *J Appl Physiol* **90**, 2231–2237 (2001).

304. Reswick, J. B. & Rogers, J. E. Experience at Rancho Los Amigos Hospital With Devices and Techniques to Prevent Pressure Sores. in *Bed Sore Biomechanics* 301–310 (Macmillan Education UK, 1976). doi:10.1007/978-1-349-02492-6_38.

305. Liu, X. Understanding the effect of skin mechanical properties on the friction of human finger-pads. (2013).

306. Liu, X. *et al.* The contributions of skin structural properties to the friction of human finger-pads. *Proceedings of the Institution of Mechanical Engineers, Part J: Journal of Engineering Tribology* **229**, 294–311 (2015).